



UNIVERSITY OF LEEDS

Asymmetric Boundary Layer Dynamics in Tropical Cyclones

Amethyst Annie Johnson

**Submitted in accordance with the requirements for the degree
of Doctor of Philosophy**

**The University of Leeds
Faculty of Environment
School of Earth and Environment**

March 2024

Abstract

This thesis aims to investigate asymmetric boundary layer dynamics of tropical cyclones using convection-permitting ensemble forecasts to address the relatively slow progress of intensity forecast improvements. Tropical cyclones are regularly approximated as being axisymmetric, although storm-scale asymmetries and smaller-scale stochastic processes can contribute to intensity change. This thesis presents contributions to the study of asymmetric tropical cyclone boundary layers, including improved use of observations, development of full-physics model parametrisations, and development of new theories to explain asymmetric dynamics. First, we develop a novel framework for evaluating the 3D structure of tropical cyclones in forecasts, focusing on azimuthal variability, rather than the simple surface based metrics typically used operationally. Next, we show that reducing the turbulent mixing in the free troposphere of asymmetric, sheared tropical cyclones can improve intensity forecasts by contributing to a more efficient downdraft ventilation weakening process, which offers a mechanism by which free-tropospheric turbulence can impact intensity change. Finally, we examine the asymmetric boundary layer wind structure of a landfalling tropical cyclone, showing that large-scale vorticity gradients can produce external forcing which leads to the asymmetric re-distribution of winds, and rainbands can also exert their own influence on the primary and secondary circulations. This thesis demonstrates the significance of different asymmetric boundary layer structures in tropical cyclones, and their impact on flow and intensity, which contributes to the expanding research on representing complex storm dynamics.

Intellectual Property

The candidate confirms that the work submitted is his/her own and that appropriate credit has been given where reference has been made to the work of others.

This copy has been supplied on the understanding that it is copyright material and that no quotation from the thesis may be published without proper acknowledgement.

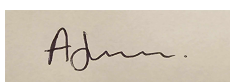
I confirm that the work submitted is my own, except where work which has formed part of jointly authored publications has been included. My contribution and the other authors to this work has been explicitly indicated below. I confirm that appropriate credit has been given within the thesis where reference has been made to the work of others.

Chapter 5, and part of Chapter 3, are based on the following article: Johnson, A. A., Schwendike, J., Ross, A. N., Lock, A., Edwards, J. M., Kepert, J. D. (Submitted: 2023, Revised: 2024). Impacts of Free Tropospheric Turbulence Parametrisation on a Sheared Tropical Cyclone. Quarterly Journal of the Royal Meteorological Society. (In Review)

The candidate is the lead author of the article and performed all of the simulations, analysis, as well as writing the manuscript. The co-authors were involved in the discussing the results, suggesting analysis techniques, and editorial corrections to the manuscript.

© 2024 The University of Leeds, Amethyst Annie Johnson

Signed

A rectangular box containing a handwritten signature in cursive script, which appears to read "Amethyst".

Acknowledgements

I would like to start by thanking my supervisors based at Leeds, Dr Andrew Ross and Dr Juliane Schwendike, for continually supporting me throughout the past 3.5 years, not only academically but also through my personal trials and tribulations. My supervisors at the Met Office, Dr John Edwards and Dr Adrian Lock, have provided a tremendous amount of support during my PhD, particularly when I was on a steep learning curve of getting to grips with running the MetUM and understanding how it works. My one-on-one time with John when I visited the Met Office was invaluable and I made substantial progress in my work by being there. Finally, Dr Jeff Kepert at the Bureau of Meteorology has provided an incredible level of supervisory support, especially during the write-up of my final results chapter, when we would have weekly meetings for over a year despite the time difference. Thank you.

Aside from my supervisors, Professor David Schultz has remained a pillar of support for me since finishing my undergraduate degree. When things got difficult during my PhD, Dave was always there to tell me to keep going and that he believed in me. These words have kept me going through all of challenges life has had to throw at me over the past few years.

For technical support, I want to thank Dr Simon Peatman, Dr Richard Rigby, Dr Will Torgerson, Dr Stuart Webster, Dr Richard Jones and Veryan Horne. For mathematical support, thanks to Erin Raif and Jonathan Coney. For moral support, thanks to Ruza, Amanda, Sarah, Fran, Olivia, Seherish, Leah, Sunny, Reece, Cam, and my family.

Thank you to various scientists across the Hurricane Research Division and the University of Miami for always answering my emails for discussion, and for hosting me in a recent visit: Professor David Nolan, Professor Sharanya Majumdar, Shirley Murillo, Dr Frank Marks, Dr Jun Zhang, Dr Andrew Hazelton, Dr Robert Rogers, Dr Paul Reasor, Dr Michael Fischer. Thank you also to the Hurricane Research Division for making all the data from flight missions

publicly available (e.g. radar and dropsonde).

This work used Monsoon2, a collaborative High-Performance Computing facility funded by the Met Office and the Natural Environment Research Council. The analysis for this work was undertaken on ARC4, part of the High Performance Computing facilities at the University of Leeds, UK. This work was supported by the Panorama Natural Environment Research Council (NERC) Doctoral Training Partnership (DTP), under grant NE/S007458/1. There was also financial support provided by CASE partnership with the Met Office.

Dedication

For my closest and deepest friend, Alex Ryan Cook, who left the world as I was starting this journey. Thank you for always believing in me.

Contents

| | | |
|----------|---|-----------|
| 1 | Introduction | 1 |
| 2 | Literature Review | 7 |
| 2.1 | Introduction | 7 |
| 2.2 | Observation and Modelling | 9 |
| 2.2.1 | Observations | 9 |
| 2.2.2 | Modelling: Full-Physics | 11 |
| 2.2.3 | Modelling: Idealised | 14 |
| 2.3 | Intensification Mechanisms | 16 |
| 2.4 | Deep Layer Vertical Wind Shear | 20 |
| 2.5 | Role of Turbulence | 27 |
| 2.6 | Landfall | 31 |
| 2.7 | Summary and Thesis Outlook | 34 |
| 3 | Data and Methods | 36 |
| 3.1 | Case Studies | 37 |
| 3.2 | Met Office Unified Model | 38 |
| 3.3 | ERA5 Reanalysis Dataset | 43 |
| 3.4 | Idealised Models | 44 |
| 3.5 | Observational Data | 45 |
| 3.6 | Metric Calculations | 48 |
| 3.7 | Summary | 51 |
| 4 | Using Airborne Observations for the Evaluation of Tropical Cyclone Asymmetry | 53 |

| | | |
|----------|--|------------|
| 4.1 | Introduction | 53 |
| 4.2 | Methods | 55 |
| 4.2.1 | MetUM Simulations | 55 |
| 4.2.2 | Dropsonde Analysis Technique | 55 |
| 4.2.3 | Radar Analysis | 57 |
| 4.2.4 | Ensemble Skill and Spread | 59 |
| 4.2.5 | Evaluating Asymmetry | 61 |
| 4.3 | Results | 63 |
| 4.3.1 | Combining Methods | 68 |
| 4.4 | Discussion | 71 |
| 4.4.1 | Ensemble Rankings | 73 |
| 4.4.2 | Performance Indicators | 74 |
| 4.5 | Concluding Remarks | 75 |
| 5 | Impacts of Free Tropospheric Turbulence Parametrisation on a Sheared Tropical Cyclone | 77 |
| 5.1 | Introduction | 77 |
| 5.2 | Data and Methods | 80 |
| 5.2.1 | Met Office Unified Model | 80 |
| 5.2.2 | Distinguishing Ensemble Intensity Divergence Points | 81 |
| 5.2.3 | Observations | 82 |
| 5.3 | Results and Discussion | 83 |
| 5.3.1 | Synoptic Overview | 83 |
| 5.3.2 | Model Evaluation | 86 |
| 5.3.3 | Asymmetric Storm Structure | 90 |
| 5.3.4 | Vertical Mixing | 92 |
| 5.3.5 | Downdraft Ventilation | 96 |
| 5.4 | Concluding Remarks | 102 |
| 6 | The Asymmetric Boundary Layer Wind Structure of a Landfalling Tropical Cyclone | 105 |
| 6.1 | Introduction | 105 |
| 6.2 | Data and Methods | 107 |

| | | |
|----------|--|------------|
| 6.2.1 | Observations | 107 |
| 6.2.2 | Reanalysis Dataset | 108 |
| 6.2.3 | Full-Physics Model | 108 |
| 6.3 | Synoptic history | 110 |
| 6.4 | Results | 113 |
| 6.4.1 | Model Evaluation | 113 |
| 6.4.2 | Simulated Storm Evolution | 116 |
| 6.4.3 | Contribution of Rainband, Landfall and Shear | 121 |
| 6.4.4 | Vorticity Analysis | 128 |
| 6.5 | Discussion | 136 |
| 6.5.1 | Thermodynamic Contribution | 141 |
| 6.5.2 | Other Theories and Cases | 142 |
| 6.6 | Conclusion | 144 |
| 7 | Conclusions | 147 |
| 7.1 | Addressing the Research Questions | 148 |
| 7.2 | Wider Context | 151 |
| 7.3 | Limitations and Future Work Recommendations | 153 |
| 7.4 | Closing Remarks | 155 |
| A | Appendix | 157 |
| | References | 158 |

List of Figures

| | | |
|-----|---|----|
| 1.1 | Average decadal National Hurricane Center official operational forecasting errors for a) Track, and b) Intensity. Taken from Gopalakishnan et al. (2021). | 2 |
| 2.1 | Schematic of a northern hemisphere storm (a) and a southern hemisphere storm (b). The grey arrows denote the direction of the primary circulation. In this example, the storms are translating northward. The red arrows show where there would be a local enhancement of the tangential wind speed, based on the alignment of the motion vectors. | 9 |
| 2.2 | Average biases for different model simulations for the 2020 Atlantic basin tropical cyclones. Adapted from Hazelton et al. (2022). | 13 |
| 2.3 | Conceptual representation of a nested CM1 LES domain (white square) within a larger tropical cyclone model simulation. Taken from Bryan et al. (2017). . . . | 15 |
| 2.4 | (a) and (b) adapted from Shimada et al. (2024), showing the radar-derived asymmetric vorticity field (coloured; 10^{-4} s^{-1}) and wind vectors at 2 km altitude, for (a) intensifying cases and (b) steady state cyclones. (c) Radar-derived wavenumber-1 component of vorticity (coloured; 10^{-5} s^{-1}) at 2 km for Hurricane Rita (2005), adapted from Boehm and Bell (2021). (d) Radar-derived wavenumber-1 asymmetry of vorticity (shaded; 10^{-4} s^{-1}) at 5 km for Hurricane Guillermo (1997), adapted from Reasor and Eastin (2012). | 24 |

| | | |
|-----|--|----|
| 2.5 | Schematic depicting the dynamics of intensifying (a) and non-intensifying (b) tropical cyclones under vertical wind shear, taken from Rios-Berrios et al. (2023). The colour of the surface represents relatively warmer (red) or cooler (blue) sea surface temperatures. The red arrows depict surface fluxes. The black circular arrows represent the eyewall updraft, which is more tilted in the non-intensifying cases. The blue arrows represent the secondary circulation. The brown regions are dry air. The grey cloud-like features represent the eyewall cloud. | 26 |
| 2.6 | Schematic of TKE distribution within a tropical cyclone axisymmetric framework, where r_{MW} is the radius of maximum wind and r is the radial distance from the storm centre. Taken from Lorsolo et al. (2010). | 29 |
| 2.7 | Schematic from Hlywiak and Nolan (2022) demonstrating how the wind speed changes as the storm interacts with land. The broad circle is the radius of tropical storm force winds. The storm is translating westwards, where the green area denotes land and the blue area is sea. The region of maximum inflow is shown in dark blue and the maximum tangential winds are shown in red. Azimuthal circulation is denoted by the arrows. | 32 |
| 3.1 | The tracks (black line) and 10-m wind speed (coloured dots) of: (a) Hurricane Maria, and (b) Tropical Cyclone Veronica. The white dotted box outlines the approximate study periods for the thesis. | 37 |
| 3.2 | Examples of grid-aligned numerical noise discovered in MetUM simulations of tropical cyclones. a) and b) show the shear of the eastward wind component between model levels 13-14 (approximately 740 - 640 m above sea level); the simulations were performed by the current author and John Edwards respectively. c) is the stress tensor + eddy diffusivity, from a simulation run by Sam Hardy. . . | 41 |
| 3.3 | Hurricane Maria simulations in the MetUM, showing the shear of the eastward wind component between model levels 13-14 (approximately 740 - 640 m above sea level). Each subplot shows the shear field with a different model timestep. . . | 42 |

| | | |
|-----|---|----|
| 3.4 | Hurricane Maria simulations in the MetUM, showing the shear of the eastward wind component between model levels 13-14 (approximately 740 - 640 m above sea level). Each subplot shows the shear field with a different value for the implicit solver for the unstable boundary layer column, which is denoted in the top right annotation. | 43 |
| 3.5 | The locations of all of the automatic weather stations used for the Tropical Cyclone Veronica (2019) case study. The surface elevation (m) is shown in filled contours. | 46 |
| 4.1 | An example of how adjusting the radius (km) to the r/RMW affects model evaluation. a) and c) the tangential wind field (m s^{-1}) derived from NOAA TDR (mission 210926H1), and b) and d) the corresponding model tangential wind field from ensemble member 0. For a) and b), which are plotted in absolute radius, the dashed lines denote every 25 km radius and the thick black lines denote 50 km radius. For c) and d), which are plotted in the normalised radius (r/RMW) the dashed lines and the solid black lines denote every 0.5 r/RMW and 1 r/RMW respectively. | 58 |
| 4.2 | An example of unique member pairings (shown in green) used to calculate the ensemble spread following Flack (2023). | 60 |
| 4.3 | Ensemble mean errors (solid line) and spread (filled) for a MetUM simulation of Hurricane Maria, using the NHC Best Track as the control. For a) track, b) minimum sea level pressure, c) maximum 10 m wind speed. Initialised at 22 September 2017 00 UTC. | 64 |
| 4.4 | Hovmöller time-height diagram of ensemble mean errors (ensemble mean - radar) for Hurricane Maria (2017) within the inner core (0.5 - 1.5 r/RMW). a) Tangential wind (m s^{-1}), b) radial wind (m s^{-1}), c) vertical wind (m s^{-1}), and d) radar reflectivity. Hatching denotes regions where the ensemble spread captures the observed values. Gaps are evident where the data is sparse. | 65 |
| 4.5 | Inner core vertical profiles for the mean tangential and radial wind speed (m s^{-1}), for the ensemble (blue) and dropsondes (red) across the study period. The transparent fill denotes the spread. n is the number of dropsondes used. The quadrants are represented as follows: a) northwest, b) northeast, c) southwest, d) southeast. | 66 |

- 4.6 (a,b) Contoured Frequency by Azimuth Diagrams (CFAzDs) for the radial wind at the RMW and 1.5 km altitude in Hurricane Maria across the entire study period. (a) airborne tail Doppler radar, and (b) 18-member ensemble mean. (c) Azimuth-time Hovmöller plot of the corresponding radial wind errors (ensemble mean - observations). The same data points are used to produce the top and bottom row of plots. 67
- 4.7 a) The standard deviation of the tangential wind speed (m s^{-1}) for the ensemble. b) Number of standard deviations between the ensemble mean tangential wind speed and radar-derived wind speed. Solid black lines denote 1 r/RMW and dotted black lines denote 0.5 r/RMW. Radar swathes were used from 26 September 2017 for demonstration purposes. Gaps in (b) show regions where observational data was not collected. 69
- 4.8 An ensemble member ranking system, demonstrated using Hurricane Maria data for T+46. From top to bottom, the ranked diagnostics are: v_{10} - the maximum wind speed at surface level, evaluated against the Best Track; MSLP - minimum sea level pressure, evaluated against the Best Track; the track; v_{1500} - the tangential wind speed at 1500 m, evaluated against radar; u_{1500} - the radial wind speed at 1500 m, evaluated against radar; radar reflectivity at 1500 m, evaluated against radar; and θ_e , evaluated against dropsonde. The boundary layer diagnostics are averaged within the inner core. 70

- 5.1 Storm metrics of simulations with a high (λ_{high}) and low (λ_{low}) free tropospheric mixing length turbulence parametrisation. Solid lines represent the ensemble means for simulations initialised on 22 September 2017 00 UTC, dashed lines represent the ensemble means for the simulations initialised on 23 September 2017 00 UTC. The black lines denote ‘observations’, which are taken from the NOAA Best Track for a), b), c) and e). The observed translational speed in panel d) is calculated from the latitude and longitude values from the Best Track. The deep layer wind shear in panel g) is calculated from the ERA-5 reanalysis dataset, in a 200-800 km annulus from the storm centre. There is not enough data to calculate a timeseries of observed storm tilt for panel f), but observed point values are discussed in section 5.3.1. Panel a) includes white circle markers every 12 hours from 25 September 2017 00 UTC for the Best Track. 84
- 5.2 A qualitative overview of model performance at T+19 to T+23. (a,b,c) The tangential wind field at 2 km altitude (m s^{-1} ; filled). (d,e,f) The vertical velocity field at 2 km altitude (m s^{-1} ; filled). The dotted circles represent 50 km intervals from the storm centre; the solid circle is 100 km. The complete radius is 200 km. The model data (a,b,d,e) is produced of a mean from 22 September 2017 19:00 UTC and 23:00 UTC. The tail Doppler radar fields (c,f) are produced using the flight missions spanning between the same time period. 88
- 5.3 Time-height Hovmöller diagrams of the absolute tangential wind errors (ensemble mean - observations). (a) The λ_{high} ensemble mean, regions in which the ensemble spread captures the observations are hatched. (b) The same as (a), but for λ_{low} . (c) $\lambda_{high} - \lambda_{low}$, where the hatching denotes the regions in which λ_{low} has a lower absolute error than λ_{high} 89
- 5.4 Time-height Hovmöller diagrams of the absolute radial wind errors (m s^{-1} ; ensemble mean - observations). (a) The λ_{high} ensemble mean, regions in which the ensemble spread captures the observations are hatched. (b) The same as (a), but for λ_{low} . (c) $\lambda_{high} - \lambda_{low}$, where the hatching denotes the regions in which λ_{low} has a lower absolute error than λ_{high} 89

- 5.5 Model simulations evaluated against dropsondes, methodology described in-text. (a,b) The tangential and radial wind components respectively (m s^{-1}) between 22 September 2017 1200 UTC and 25 September 2017 00 UTC. For this period, 9 dropsondes were classified as being within the eywall. (c,d) As in (a,b), but between 25 September 2017 00 UTC and 27 September 00 UTC, using 8 dropsondes. The solid line denotes the mean and the transparent fill is the spread. 90
- 5.6 Storm-relative radial velocity (m s^{-1}) at different heights at the intensity divergence point (approx T+18) for a representative ensemble member. The high mixing scheme (λ_{high}) is shown in (a)-(d); the low mixing scheme (λ_{low}) in (e)-(h). Dashed contours are at intervals of 25 km radius. The wind barbs represent the deep layer vertical wind shear. 92
- 5.7 (a) Minimum sea level pressure (hPa). (b) Maximum 10-m wind speed (m s^{-1}). The black line is the NHC best track. $\lambda_{high,3D}$ corresponds to a simulation with a high 3-dimensional mixing length. $\lambda_{low,3D}$ is the same, but for a reduced mixing length (described in-text). $\lambda_{high,1D}$ is the same as $\lambda_{high,3D}$ but with no lateral mixing (only vertical). 93
- 5.8 Ensemble composite of azimuthally averaged vertical turbulent moisture flux ($\overline{w'q'_t}$) in $\text{g m}^{-2} \text{ s}^{-1}$ in two mixing length (λ) schemes. Negative values (blue) indicate downward transport of moisture. The black solid contour represents the cloud liquid water content at 0.01 g kg^{-1} . The hatching indicates a statistically significant difference in the vertical turbulent moisture flux using the Wilcoxon Rank Sum test, between the experiments. The composite is averaged over the 6 hours prior to intensity divergence. The normalised radius is produced using the surface RMW. 94
- 5.9 Ensemble composites of azimuthally averaged (a-c) θ_e (K) and (d-f) mixing ratio (g kg^{-1}), over a period of 6 hours before intensity divergence. For the θ_e plots in a and b, the black contours indicate a threshold of cloud liquid water cumulative frequency (> 0.001), to provide context into where the cloud layer is. In c and f, the black contours indicate regions of statistically significant difference between the simulations according to a Wilcoxon Rank Sum Test ($p < 0.05$). The unfilled white contours represent vertical velocity $\geq 0.2 \text{ m s}^{-1}$, for λ_{high} (solid) and λ_{low} (dotted). The radius is normalised by the surface RMW. 95

- 5.10 Mixing ratio (g kg^{-1}) at 1.5 km for a representative ensemble member. Black contours indicate downward motion of -0.5 m s^{-1} . Three simulation times are shown: time of intensity divergence (t), 1 hour before intensity divergence (t-1) and 2 hours before intensity divergence (t-2). The deep layer vertical wind shear is shown as a wind barb. Dashed white lines denote 50 km radius intervals, beginning with 50 km from the storm centre. 97
- 5.11 An ensemble composite of the radial ventilation in the 6 hours before the intensity divergence point, performed over the inner 50-150 km of the storm. Subplots (a) and (b) are the full field of radial ventilation ($\text{kg K m}^{-2} \text{ s}^{-1}$). (c) The difference between (a) and (b), with the grey line denoting the 0 contour. Positive values represent the inward transport of anomalously low θ_e 99
- 5.12 An ensemble composite of the downdraft ventilation in the 6 hours before the intensity divergence point, performed over the inner 150 km of the storm. Subplots a) and b) are the full field of downdraft ventilation ($\text{kg K m}^{-2} \text{ s}^{-1}$), where the black contour is the 0 line and subplots c) and d) are the wavenumber-1 components ($\times 10^{-1} \text{ kg K m}^{-2} \text{ s}^{-1}$), where black contours indicate regions of statistically significant ($p < 0.05$) differences between the two simulations. The radius is normalised by the surface RMW. 100
- 5.13 An ensemble composite in the 6 hours before the intensity divergence point, performed at 1 km height over the inner 150 km of the storm, removing the inner 50 km to ensure the results were not skewed by the eye. a) and b) are contoured frequency by altitude diagrams of vertical velocity (m s^{-1}) for the λ_{high} and λ_{low} ensemble members respectively. d) and e) 2d histograms, to show the frequency distribution (K m s^{-1}) of θ_e in the downdrafts. c) and f) the probability density function of vertical velocity (m s^{-1}) and θ_e (K) respectively. 101
- 6.1 Vorticity (10^{-3} s^{-1}). (a,d) The MetUM vorticity field. (b) The MetUM vorticity field with all anticyclonic vorticity exceeding $2.5 \times 10^{-4} \text{ s}^{-1}$ enhanced by 50%. (c) a-b. (e) The MetUM vorticity field with all anticyclonic vorticity exceeding $2.5 \times 10^{-4} \text{ s}^{-1}$ masked and interpolated over. (f) d-e. 109

- 6.2 a) Best track storm position (black) and modelled storm position (blue) with circles denoting every 6 hours starting at 23 September 2019 00 UTC, where the first point is denoted by a square. b) Best track (black), deterministic (blue) and ensemble mean (red) maximum wind speed (m s^{-1}), with the ensemble spread filled in red. c) Simulated 200-850 hPa wind shear magnitude (m s^{-1} ; solid; left axis) and direction using meteorological convention ($^{\circ}$; dotted; right axis). d) Best track (black), deterministic (blue) and ensemble mean (red) minimum sea level pressure (hPa), with the ensemble spread filled in red. 112
- 6.3 MetUM global deterministic forecast at 23 March 2019 00:00 UTC ($T + 24$). (a) Relative vorticity at 850 hPa (filled; s^{-1}), mean sea level pressure (hPa; unfilled contours). (b) Steering-level flow (filled; m s^{-1}) and streamlines. 112
- 6.4 (a) Satellite 91 H brightness temperature (K) from the Naval Research Lab on 23 March 2019 20:15 UTC. (b) Satellite 91 GHz polarization-corrected temperature (K) from the Naval Research Lab, on 23 March 2019 22:20 UTC. (c) Satellite-derived SAR 10-m wind speed (m s^{-1} ; Mouche et al., 2019) on 24 March 2019 10:38 UTC. (d) Modelled 10-m wind speed (m s^{-1}) on 24 March 2019 15:00 UTC. 114
- 6.5 Evaluation of MetUM deterministic forecast (red) against the surface observation sites (black). In east to west order (since east is closest to the initial storm landfall), the columns represent: Port Hedland, (a,e,i,m), Roebourne (b,f,j,n), Karratha (c,g,k,o), Varanus (d,h,l,p). (a,b,c,d) Surface temperature (solid; $^{\circ}\text{C}$), dewpoint temperature (dotted, $^{\circ}\text{C}$). (e,f,g,h) Wind speed (solid; m s^{-1}) and wind direction (dotted; $^{\circ}$). (i,j,k,l) Mean sea level pressure (hPa). (m,n,o,p) Precipitation rate (mm hr^{-1}). There were no precipitation measurements available in Port Hedland (m) due to instrument malfunction. 116
- 6.6 Tangential wind (filled contours; m s^{-1}) at 950 hPa, with positive vertical wind in black and downward vertical wind in white contours, at $\pm 0.5 \text{ m s}^{-1}$ 116
- 6.7 6-hourly rainfall accumulation (filled; mm), with 950 hPa vertical velocity in black contours at 0.5 m s^{-1} . The thick black line denotes the coastline. The y-axis is the latitude in $^{\circ}\text{N}$ and the x-axis is the longitude in $^{\circ}\text{E}$. The plot domain follows the storm centre. 117

- 6.8 Equivalent potential temperature (θ_e ; K) averaged between 0 - 1.5 km (a) and 1.5 - 3 km (d). (b,e) The same as (a,d) but for temperature (K). (c,f) The same as (a,d) but for mixing ratio ($g\text{ kg}^{-1}$). During a period of prominent eyewall break (T + 59; 25 September 2019 11:00 UTC). The black contours are the positive vertical velocity (averaged in the same layers) at 0.25 m s^{-1} 118
- 6.9 Total wind speed (m s^{-1}), vertical wind speed (m s^{-1}), relative vorticity (s^{-1}) and divergence (s^{-1}) for ensemble member 0 at 900 hPa, at 25 March 2019 1200 UTC. The thick black contour denotes the MetUM determined land-sea boundary, where the north side is sea. The thinner contour is the wind speed at 40 m s^{-1} 119
- 6.10 (a,b,c) Cross-sections at the RMW (12 km) at 25 March 2019 1200 UTC for tangential wind (m s^{-1}), radial wind (m s^{-1}) and vertical wind (m s^{-1}) respectively. The unfilled contour denote 0 m s^{-1} . (d,e,f) The same fields as (a,b,c) but in a plan-view averaged across the lowest 1.5 km. The coastline is shown as a thick black line. Streamlines correspond to the earth-relative wind field. The shear-relative quadrants are labelled as UL: upshear left, DL: downshear left, DR: downshear right, UR: upshear right. Faint dashed circles denote the radius at 25 km intervals. 122
- 6.11 Wind fields outputted from the KW01 model at 10 m. (a) - (f) tangential wind (filled; m s^{-1}) with a black contour denoting the 40 m s^{-1} contour level. (g) - (l) The radial wind component (filled; m s^{-1}). (m) - (r) The vertical velocity (filled; m s^{-1}). The thick black line denotes the angle and position of the coastline. Units for the x- and y- axis are in km from the storm centre. 123
- 6.12 As in Figure 6.11, for 298 m altitude. The black contour in (g) - (r) is the vertical velocity at 0.1 m s^{-1} 123
- 6.13 As in Figure 6.11, for 1648 m altitude. The black contour in (g) - (r) is the vertical velocity at 0.1 m s^{-1} 124

- 6.14 Schematic demonstrating the calculation of the eyewall break ratio (EWB). (a) an example asymmetric tangential wind field (v ; filled). The black lines are radials from the storm centre, with a white circle denoting where the maximum wind is. (b) Idealised asymmetric maximum winds from each radial, plotted by azimuth. The eyewall break ratio is the ratio of the minimum tangential wind ($\min(v)$) to the mean (\bar{v}). 127
- 6.15 Azimuth-time Hovmöller diagram of the wavenumber-2 asymmetry of the 900 hPa relative vorticity (s^{-1}) at the RMW (12.1 km). Times correspond to 24 March 2019, prior to the eyewall break which occurred distinctly in the simulations on 25 March 2019. 129
- 6.16 (a) Relative vorticity at ($10^{-6}s^{-1}$) input from the MetUM simulations at T + 59; 25 September 2019 11:00 UTC. (b) Relative vorticity (s^{-1}) calculated from the wind field in (d). (c) Divergence (s^{-1}) calculated from the wind field in (d). (d) Wind speed (filled; $m s^{-1}$) and streamlines from the MetUM at the same forecast time as (a), where the thick black contours denote the wind speed at $45 m s^{-1}$. (e) The rotational flow (filled; $m s^{-1}$) and associated streamlines, calculated from the vorticity field in (b), where the thick black contours denote the wind speed at $45 m s^{-1}$. (f) The divergent flow (filled; $m s^{-1}$) and associated streamlines, calculated as the residual of (d)-(e). Units for the x- and y- axis are in km from the storm centre and all fields are taken at 900 hPa. 131
- 6.17 Fourier decomposition of the relative vorticity (s^{-1}) at T+59; 25 September 11:00 UTC, during prominent eyewall break (as shown in Figure 6.16). The top row, (a,b,c,d) represent: wavenumber-0, wavenumber-1, waveumber-2, and the residual, respectively. The bottom row (e,f,g,h) as in (a,b,c,d) with the symmetric field (wavenumber-0) included. Each dashed line denotes 50 km radius. 132
- 6.18 (a) Idealised symmetric relative vorticity field (s^{-1}) with a reference contour at $-0.0005 s^{-1}$. (b) Idealised north-south vorticity gradient (s^{-1}). (c) The sum of (a) and (b) with a reference contour at $-0.0005 (s^{-1})$ for (a) (solid) and (c) (dotted). (d) The symmetric rotational flow (s^{-1}) calculated from (a). (e) The rotational flow (s^{-1}) calculated from (b). (f) The rotational flow calculated from (c) (s^{-1}). 134

| | | |
|------|---|-----|
| 6.19 | (a),(c),(e),(g) Idealised relative vorticity gradients (10^{-3} s^{-1}) with their overall north-south vorticity ratio annotated. (b),(d),(f),(h) The rotational flow calculated from the asymmetric vorticity field the symmetric field (e.g. Figure 6.18c). The eyewall break ratio is annotated. Calculations for the eyewall break ratio and vorticity ratio are described in-text. | 135 |
| 6.20 | Correlation between the north-south relative vorticity gradient (ζ ratio) and the eyewall break (EWB) ratio. Correlation coefficient (annotated) is calculated using Pearson's correlation coefficient (Pearson, 1901) with a confidence level of $> 99.9\%$ | 136 |
| A.1 | Hurricane Idalia (2023) radar fields at 1.5 km, composited using five swathes from a NOAA reconnaissance mission on 29 August 2023 over a four hour period from 21:44 UTC. a) Tangential wind, b) radial wind, c) relative vorticity | 157 |

List of Tables

| | | |
|-----|---|-----|
| 3.1 | Model set-up for different storms. Every row corresponds to an 18-member ensemble with 1-hourly output, aside from the 1.5 km resolution run of Veronica which was performed for a single member with 10-minute output. T_0 denotes the initialisation time (DD/MM/YYYY HH), T_{total} is the total run-time in hours, δx is the horizontal grid spacing. | 41 |
| 5.1 | Ensemble averages of minimum sea level pressure (MSLP; hPa) and maximum 10 m wind speed (u_{10} ; m s^{-1}) forecast error and standard deviation for two tropospheric mixing schemes at $T + 72$ | 86 |
| 6.1 | The eyewall break (at 1648 m) and radial wind (at 298 m) metrics, calculated within 150 km of the storm centre. The angle, denoted by ϕ , is the azimuth of the eyewall break, the inflow maximum, and the outflow maximum for each dual column respectively. | 128 |

List of Acronyms

| | |
|--------------------------|---|
| 4DVAR | Four-dimensional data assimilation technique |
| ACCESS | Australian Community Climate and Earth System Simulator |
| BoM | Bureau of Meteorology |
| CAPE | Convective available potential energy |
| CFAD/CFAzD | Contoured Frequency by Altitude (or Azimuth) Diagram |
| CISK | Conditional Instability of the Second Kind |
| CM1 | Cloud Model 1 (Bryan and Fritsch, 2002) |
| DL | Downshear left |
| DR | Downshear right |
| ECMWF | European Centre for Medium-Range Weather Forecasts |
| GPS | Global positioning system |
| HAFS | Hurricane Analysis and Forecast System |
| HRD | Hurricane Research Division |
| IBTrACS | The International Best Track Archive for Climate Stewardship |
| KW01 | The boundary layer model of Kepert and Wang (2001) |
| LES or LEM | Large eddy simulation or large eddy model |
| MetUM | Met Office Unified Model |
| MAE | Mean absolute error |
| MIMIC | Morphed Integrated Microwave Imagery at the Cooperative Institute for Meteorological Satellite Studies |
| MSLP | Minimum sea level pressure |
| NOAA | National Oceanic and Atmospheric Administration |
| NWP | Numerical Weather Prediction |
| PDF | Probably density function |

| | |
|--------------|---|
| RMSE | Root mean square error |
| RMW | Radius of maximum winds |
| SFMR | Stepped Frequency Microwave Radiometers |
| SHIPS | Statistical Hurricane Intensity Prediction Scheme |
| SLP | Sea level pressure |
| TC | Tropical cyclone |
| TDR | Tail Doppler radar |
| TKE | Turbulent kinetic energy |
| TRACK | The storm tracking algorithm of Hodges (1994) |
| UAS | Unmanned aircraft system |
| UL | Upshear left |
| UR | Upshear right |
| VHT | Vortical hot towers |
| VRW | Vortex Rossby waves |
| VWS | Vertical wind shear (850 - 200 hPa) |
| WISHE | Wind-Induced Surface Heat Exchange |
| WRF | Weather Research and Forecasting Model |

Chapter 1

Introduction

Tropical cyclones are among the most destructive natural disasters, producing heavy rainfall and high wind speeds, having a direct influence on wave height and storm surges (Needham and Keim, 2014). Coastal communities are especially vulnerable to landfalling tropical cyclones. Flooding and extreme winds can threaten infrastructure, potentially causing displacement and loss of life in severe cases. The level of preparedness relies heavily on the quality of tropical cyclone track, size and intensity forecasts, as well as the efficacy of the meteorological organisations to communicate warnings to coastal communities.

While forecast quality depends on effective communication and user response, a substantial component is the quality of numerical weather prediction (NWP), which relies on three main components: i) knowledge of the current state of the atmosphere (through observation, including data assimilation), ii) our understanding of the physical processes that govern the weather, and iii) the numerical application of the physics to the observations. All three components have limiting factors. Following the ‘Chaos Theory’ of Lorenz (1963), small perturbations in the initial conditions (or even the representation of the physics) can amplify over time, leading to distinct end results. Therefore, a perfect weather forecast would require an infinite number of accurate and precise observations, a flawless understanding of the physics to the molecular level, and an infinite number of model grid-points. This conundrum leads to the ‘limit of predictability’, whereby the deficiencies in observations, physical understanding and modelling, combined with Chaos Theory, mean that there is an inherent limit on our capability to accurately predict the weather.

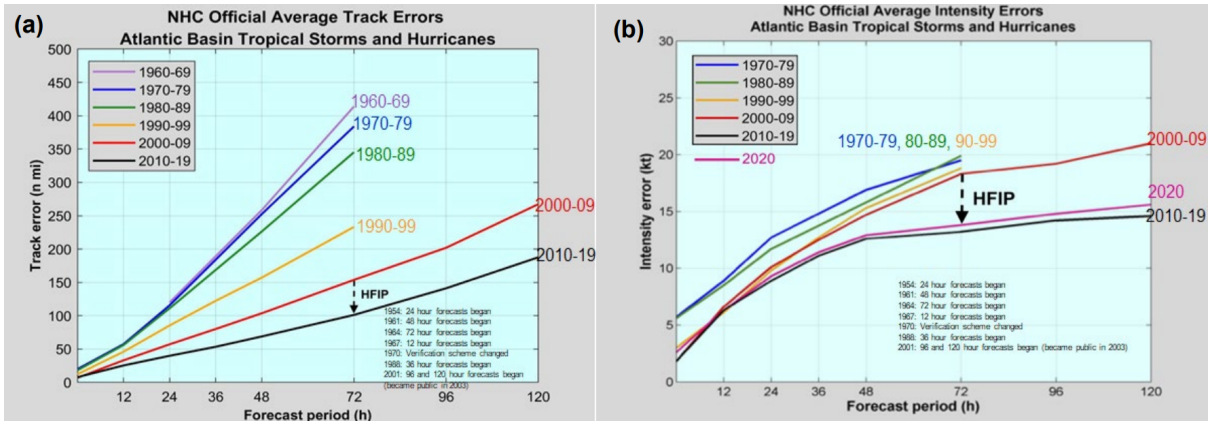


Figure 1.1: Average decadal National Hurricane Center official operational forecasting errors for a) Track, and b) Intensity. Taken from Gopalakishnan et al. (2021).

However, despite the seemingly unattainable target of a perfect forecast, good progress has been made in recent years to produce reliable weather forecasts, particularly in well-observed regions. The general consensus is that as a global meteorology community, we gain about one day of reliable weather forecasting per decade. For example, the quality of a 6-day forecast by European Centre for Medium-Range Weather Forecasts (ECMWF) in 2010 matched the quality of their 3-day forecast in 1980 (Magnusson and Källén, 2013). Improvements in NWP can be attributed to each of the three points listed above. For example, Magnusson and Källén (2013) state that the biggest improvements in ECMWF forecast quality came from a higher availability of observations (primary from satellite) and better assimilation into the model, as well as the improved understanding and implementation of physics into the model.

Tropical cyclone forecasting and modelling, in particular, have seen advancements in recent years. For example, between 1990 and 2016, the National Hurricane Center (NHC) tropical cyclone 72-hour track forecasts improved by around 50% (Figure 1.1a; Landsea and Cangialosi, 2018). Again, this progress has been widely attributed to the factors mentioned above. However, the accuracy of tropical cyclone intensity forecasts (Figure 1.1b) has not progressed at the same rate as it has for the track (Cangialosi et al., 2020).

The track is largely dominated by larger-scale features such as the monsoon trough and subtropical ridge (Harr and Elsberry, 1991) which can be better captured by satellite observations and predicted by global atmospheric models. Conversely, intensity forecasts are more challenging since storm intensity is highly dependent on internal small-scale processes in the troposphere. As I will discuss in Section 2.3, the boundary layer plays a key role in intensity change; it is widely accepted that the provision of heat and moisture to the storm system via the sea surface

is crucial to intensification (e.g. Charney and Eliassen, 1964; Ooyama, 1969; Emanuel, 1986; Montgomery and Smith, 2014), and that such air-sea interactions are driven by turbulent enthalpy fluxes (Riehl, 1950). Radial turbulence within the boundary layer has been shown to have substantial impacts on storm intensity (Bryan, 2012), linked to the transport of entropy and momentum into the inner core.

Turbulent mixing takes place across the whole storm system. For example, the eyewall itself contains extreme turbulence (Zhang et al., 2010), and rainbands can contain turbulence that contributes significantly to the overall transport of momentum (Zhao et al., 2020). Mixing within the low-mid troposphere can also lead to detrimental effects on storm intensity, such as weakening induced by the downward transport of low entropy air from the mid-levels (e.g. Tang and Emanuel, 2012a; Riemer et al., 2010; Alland et al., 2021a). This means that the observation, modelling, and physical understanding of turbulent mixing, both within and above the boundary layer, are key for forecasting intensity change.

Such turbulent mixing and other contributors to intensity change are highly dependent on asymmetric processes, which need to be studied in three-dimensional space. For example, the mixing of low entropy air into the inner core typically occurs within tilted vortexes (e.g. Tang and Emanuel, 2012a; Riemer et al., 2010; Alland et al., 2021a) and small asymmetrically-distributed updrafts can produce cyclonic vorticity to intensifying vortexes (e.g. Van Sang et al., 2008; Montgomery et al., 2006; Fang and Zhang, 2011; Montgomery and Smith, 2014).

Thus, tropical cyclones challenge all three pillars of NWP. For example, observations are needed throughout the lower troposphere of a tropical cyclone to inform models of the initial conditions, but it is difficult to attain in-situ observations of the boundary layer for several reasons. Firstly, during genesis and intensification, tropical cyclones are usually over the open ocean, so there is a lack of surface observation sites. While The National Oceanographic and Oceanic Administration (NOAA) routinely fly aircraft into tropical cyclones for research and operational purposes, the extreme weather conditions of the lower troposphere mean it is too dangerous for them to fly into the boundary layer for direct in-situ measurements. To maximise the value from the research missions, NOAA deploy dropsondes (e.g. Hock and Franklin, 1999; Zhang et al., 2011; Zhang et al., 2013) and make use of aircraft-mounted Doppler radar (e.g. Fischer et al., 2022) to sample the boundary layer. A full review of tropical cyclone boundary layer observation techniques is given in Section 2.2, but overall these methods are limited in their

temporal and spatial distribution capabilities. Additionally, these research flights are generally contained to the basins around the US, meaning there is a global disparity in the quality of tropical cyclone observations in the lower troposphere.

Developing a comprehensive understanding of the physical processes within the low levels of tropical cyclones is made more difficult by the lack of observations. Weather models can be a good tool to investigate physical processes, but only if these processes are well represented by the pre-existing equations in the model. Models must be evaluated and scrutinised using observations to highlight flaws and systematic biases in the physical representation. Furthermore, current regional operational NWP uses kilometre-scale grids (e.g. Bush et al., 2023), which are fundamentally unable to resolve smaller scale processes such as microphysical processes and turbulence mixing. These are important and have to be parametrised, but to develop and test such parametrisations requires observations and models which operate at ‘turbulence-resolving’ resolutions (≤ 100 m). Therefore, observations are necessary but not sufficient to improve our understanding of the underlying science, especially at small scales.

So, there are challenges in the observation and physical understanding of tropical cyclones, but also in the numerical representation. The horizontal grid spacing of NWP models introduces a limitation. Generally, current regional operational forecasts of tropical cyclones operate at a resolution that is ‘convection-permitting’, meaning that convective processes are explicitly represented at the grid-scale and do not need to be parameterised. However, smaller-scale processes such as microphysics and some turbulence (as mentioned above) must be represented implicitly in the model using parameterisations.

Convection-permitting models demonstrated that explicit representation of the physics can improve forecast quality (Clark et al., 2016; Judt et al., 2021), but a completely explicit model would require a grid-size comparable to the Kolmogorov microscale (≈ 1 mm; Kolmogorov, 1941) and much more compute power than is currently possible. As technology advances, improvements in computation will be made, but parametrisations will be unlikely to disappear.

The overarching aims of this thesis will be to contribute to each of the three pillars of NWP for tropical cyclone applications, with a focus on asymmetric boundary layer dynamics. Chapter 2 will contain a literature review which will explore observational techniques, modelling, and the fundamental science which underpins the rest of the thesis. Chapter 3 will describe the data and methods used, and the results chapters will be structured as follows:

- (i) Chapter 4 will address the effective use of airborne observations such as tail Doppler radar and dropsondes in evaluating forecasting models, including ensemble forecasts. This chapter will lay the foundation and provide context for the proceeding chapters. New techniques are developed in this chapter, designed to inspire a more creative approach to model evaluation by focusing on the representation of storm structure rather than single-value metrics. Using the Met Office Unified Model (MetUM) to exemplify this, two main questions will be answered:
- 1) How can in-flight tropical cyclone observations be used to evaluate tropical cyclone intensity and structure within the lower troposphere?
 - 2) To what extent can an evaluation of the surface metrics be used to infer the quality of the ensemble within the boundary layer?
- (ii) Chapter 5 will build on the use of observations in model evaluation to aid in improving model physics in the MetUM. This chapter focuses on the development of the turbulent mixing parametrisation in the free troposphere and the impact it has on storm intensity in a sheared tropical cyclone. These changes to the mixing parametrisation were subsequently added to the newest version of the MetUM, being implemented into operational weather forecasts. In this chapter, I aim to answer:
- 1) To what extent does tropospheric mixing above the boundary layer influence the intensity forecasts of Hurricane Maria (2017) during a period of weakening and moderate to high vertical wind shear?
 - 2) How does the choice of sub-grid turbulence parametrisation in the free troposphere contribute to the thermodynamic processes associated with weakening tilted tropical cyclones?
- (iii) Chapter 6, the final results section, aims to enhance our understanding of the physical dynamics of tropical cyclones by analysing a case study of a tropical cyclone making land-fall. This cyclone developed an asymmetric structure which disproportionately impacted the inland quadrants of the storm, whilst weakening more rapidly over the sea. I use the term ‘eyewall break’ to refer to an eyewall with a static, pronounced region of reduced intensity. We develop a novel theory to explain eyewall breaks in tropical cyclones, using observations, the MetUM, a boundary layer model, and simple numerical methods.

I also show that the theory can be reasonably applied to other case studies. I aim to answer the following questions, of which the second question will be answered by a novel vorticity-based analysis of the dynamics and kinematics of the eyewall break:

- 1) How do landfall, environmental vertical wind shear and rainband dynamics contribute to the eyewall break of Tropical Cyclone Veronica (2019)?
- 2) To what extent, and by what mechanism, can eyewall breaks be explained by the synoptic environment?

The final chapter will summarise the results chapters, placing them back into the context of developments in NWP. The potential impact of the results will be discussed, and avenues for future work will be explored.

Chapter 2

Literature Review

2.1 Introduction

To address the questions set out in Chapter 1, we must first explain the various definitions of a ‘boundary layer’. First, I will introduce generic definitions, often used in NWP systems, and then I will go on to overview the tropical cyclone boundary layer more specifically.

In fluid dynamics, the boundary layer is the layer of a fluid that is affected by the friction of a boundary surface. In meteorology, the atmospheric boundary layer is the lowest part of the troposphere, typically capped by a temperature inversion (Stull, 1988) and often characterised by a ‘mixed layer’, in which the atmospheric turbulence leads to a uniform mixing. Historically, the bulk Richardson number (Ri_b), which considers both the buoyant suppression and shear-generated turbulence, has been used to quantify a boundary layer depth (Stull, 1988; Zhang et al., 2011) based on these principles. This quantity can be defined by:

$$Ri_b = \frac{(g/T_v)\Delta\theta_v\Delta z}{(\Delta U)^2 + (\Delta V)^2} \quad (2.1)$$

where g is the gravitational acceleration, T_v is the virtual temperature, $\Delta\theta_v$ is the change in the virtual potential temperature, Δz is the change in height, and ΔU and ΔV are the change in the eastward and northward wind components respectively. To obtain an approximate boundary layer depth, Ri_b must be calculated across thin slices of the atmosphere, depending on the vertical resolution of the available data. Once the number reaches a ‘critical’ value - usually 0.25 (Stull, 1988; Lock et al., 2000) - the boundary layer top has been reached. The Richardson

number can also be applied to numerical models to determine the depth over which to apply boundary layer parametrisations. In the MetUM, the Richardson number is used to determine the depth of turbulent layers in the free troposphere, and the depth of the stable boundary layer, as described in Lock et al. (2000).

The tropical cyclone boundary layer is accepted to be a vital component of storm intensification by all of the major published theories (Charney and Eliassen, 1964; Ooyama, 1969; Emanuel, 1986; Smith et al., 2009), but it is not well captured by the depth of the mixed layer (Zhang et al., 2011; Kepert et al., 2016) or the critical Richardson number (Zhang et al., 2011). There is also typically no temperature inversion capping the tropical cyclone boundary layer top (e.g. Nicholls, 1985). While sub-critical Ri_b and a mixed layer do exist in the tropical cyclone boundary layer (Zhang et al., 2011), the most compelling effect of the surface friction is the inflow layer. The inflow layer, which is vital for importing moisture, enthalpy and absolute angular momentum into the eyewall, is induced due to the surface frictional sink of momentum (Montgomery and Smith, 2014) and the retardation of the tangential wind (Montgomery and Smith, 2014), which causes an imbalance in the pressure gradient force and results in an inward velocity. Sometimes, the height of the maximum tangential winds is used as a proxy to determine the depth of the boundary layer (Zhang et al., 2011), since it is believed that the maximum tangential winds reside at the top of this layer (Smith et al., 2009). Furthermore, all definitions of the boundary layer noted here have been found to be asymmetric across the storm system (Zhang et al., 2013).

There are several mechanisms by which a tropical cyclone may become asymmetric. For example, it has been well documented (e.g. Shapiro, 1983; Kepert and Wang, 2001; Kepert, 2001) that storm translation can modulate the dynamical structure of a tropical cyclone. Convergence in the front quadrants is enhanced due to the increased frictional drag, leading to local increases in vertical motion and consequent precipitation. Tangential wind speeds tend to reach a maximum right-of-motion in northern hemisphere storms, and left-of-motion in southern hemisphere storms. This is explained in detail by Smith et al. (1990) but can be summarised in Figure 2.1, which shows how the coincidence of the steering flow vectors and the tangential wind vectors can enhance the local circulation.

The most relevant asymmetry mechanisms for this thesis are vertical wind shear and landfall. As such, they will be explored individually in Section 2.4 and Section 2.6, respectively. However,

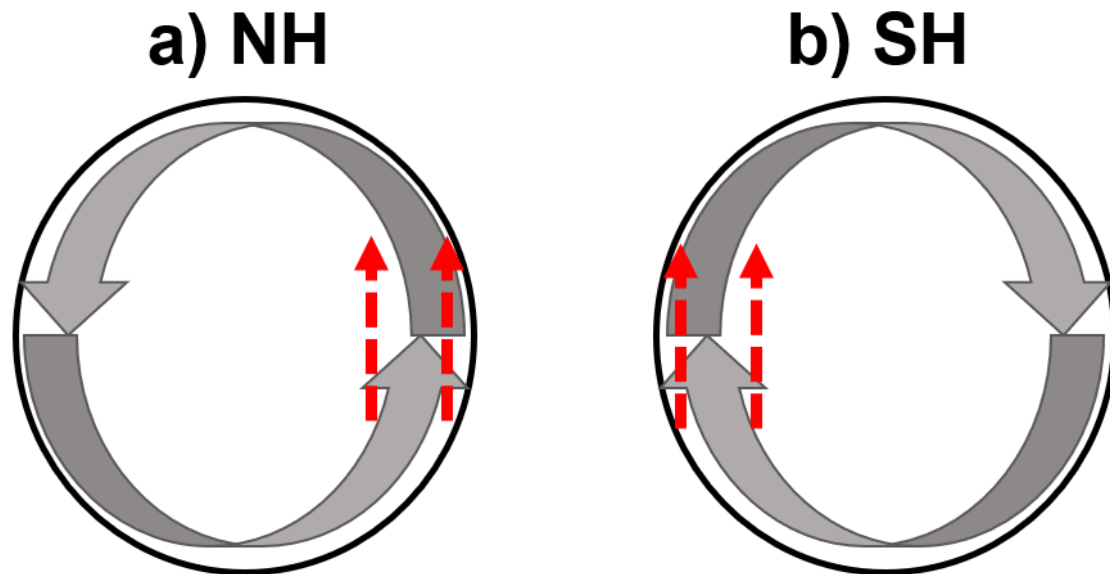


Figure 2.1: Schematic of a northern hemisphere storm (a) and a southern hemisphere storm (b). The grey arrows denote the direction of the primary circulation. In this example, the storms are translating northward. The red arrows show where there would be a local enhancement of the tangential wind speed, based on the alignment of the motion vectors.

it is important to note that there may be other contributors to storm asymmetry, such as asymmetries in surface temperature and moisture.

The next section will overview observations and modelling of the tropical cyclone boundary layer (Section 2.2). After that, I will lay the foundation for the rest of the paper, analysing the major storm intensification theories (Section 2.3), including the role of the boundary layer and convective asymmetries in spin-up. Next, I will investigate three major factors contributing to asymmetric tropical cyclone dynamics, including deep layer vertical wind shear (Section 2.4), turbulence (Section 2.5), and landfall (Section 2.6).

2.2 Observation and Modelling

2.2.1 Observations

While tropical cyclones are often captured by satellite observations, this section will focus mainly on in-situ observations of the lower troposphere and boundary layer due to the relevance to the rest of the thesis.

The main source of observational data in the lower troposphere of tropical cyclones comes from research flight missions, such as the reconnaissance flight missions run by NOAA, which have

been used extensively for research purposes (e.g. Lorsolo et al., 2010; Rogers et al., 2012; Reasor et al., 2013; Rogers and Zhang, 2023; Fischer et al., 2024). NOAA tend to use the WP-3D Turboprop Aircraft for these missions, which are mounted with specialised tail Doppler radar (TDR). The TDR operates in the X-band and scans vertically, allowing for vertical profiling of the lower troposphere (NOAA, 2014). This technology allows for the derivation of wind speeds, including the vertical wind, and the reflectivity. The major drawback of the TDR is that Doppler radar wind measurements are dependent on precipitation, meaning that data cannot be collected in non-precipitating regions. Furthermore, NOAA flight missions tend to fly above the boundary layer to avoid the most dangerous high-wind conditions, so although the TDR scans vertically, data in the lowest 500 m is often patchy or unreliable.

While research flights at 3 km provide useful insight into the lower troposphere through dropsondes, SFMR, and Doppler radar measurements, they are still limited in their ability to sample the lowest levels of the atmosphere. It is widely accepted that the tropical cyclone boundary layer modulates storm intensity, so gathering data here is important for operational intensity forecasts and model evaluation, but this region also contains the strongest wind speeds and extreme turbulence, making it extremely dangerous to enter.

In 2014, NOAA deployed the first unmanned aircraft system (UAS) into a hurricane, from a P-3 aircraft (Cione et al., 2016). After two successful flight missions into major Hurricane Edouard (2014) using the Coyote UAS, Cione et al. (2016) found an agreement with dropsondes within 0.5 m s^{-1} for wind speed, $0\text{-}0.4 \text{ }^\circ\text{C}$ for air temperature, and $0.7\text{-}1.3 \text{ }^\circ\text{C}$ for dewpoint temperature. The authors also found an agreement with the P-3 Doppler radar-derived wind speeds within $\pm 1 \text{ m s}^{-1}$.

Deeming this mission a success, NOAA went on to deploy the Coyote UAS into several more Atlantic basin tropical cyclones (Cione et al., 2020), such as Hurricane Maria (2017) and Hurricane Michael (2018). From these missions, for the first time in history, NOAA were able to get measurements of the momentum flux and turbulent kinetic energy within the low levels of the tropical cyclone eyewall with good agreement with the higher altitude measurements taken by the P-3 (Cione et al., 2020).

A few years later, NOAA began testing on two novel UASs (Cione et al., 2024) which are designed to withstand the extreme environmental conditions of the tropical cyclone boundary layer. For reference, the Coyote has a flight time of 90 minutes, a wingspan of 1.5 m and a

weight of 6.4 kg (Cione et al., 2020). Of the new systems, the bigger UAS is the Altius-600 which has a longer flight time of up to 4 hours, a wingspan of 2.5 m, and weighs 12.25 kg (Airforce Technology, 2021). While a larger UAS may be more capable of withstanding turbulence, NOAA is also trialling a lightweight UAS called the Black Swift S0 (Cione et al., 2024), which has been specifically designed for manoeuvres within the boundary layer of the inner core of tropical cyclones. The S0 has a comparable flight time and wingspan to the Coyote, but is significantly lighter at 1.6 kg (BlackSwift, 2024).

Currently, these UAS missions run by NOAA seem to be the only missions of their kind, worldwide. These missions provide novel data of the tropical cyclone boundary layer to inform numerical models and develop scientific research. However, they also have potential to improve operational forecasts through data assimilation. Preliminary results using the Coyote data (Sellwood et al., 2023) suggest that assimilating UAS data into operational forecasting models can improve intensity forecasts. However, they also found that the quality of the improvements was partially dependent on having a symmetric distribution of observations around the inner core.

2.2.2 Modelling: Full-Physics

There are several different types of modelling techniques used to forecast and study tropical cyclones. In this section, we will address full-physics models which are typically used for operational forecasting and case study research, and then we will go on to discuss some more idealised models which are often used to explore the impacts of specific processes on tropical cyclone dynamics.

Full-physics models work on a variety of scales. At the top-level, there are global models which currently typically operate at ≈ 10 km horizontal resolution. Although there are efforts among meteorological agencies to increase the resolution (e.g. Sandu and Stevens, 2021), operational global models still use a lower resolution than regional models due to the computational expense. As a result, these global models are largely unable to capture storm intensity (e.g. Hodges and Klingaman, 2019; Magnusson et al., 2019).

Regional models usually operate at a convection-permitting resolution, which produces better results than the lower-resolution global models (Judt et al., 2021). There are several regional models that provide operational tropical cyclone forecasting. For example, the Australian Com-

munity Climate and Earth System Simulator (ACCESS; Puri et al., 2013) produced by the Australian Bureau of Meteorology (BoM) is an implementation of the Met Office Unified Model (Davidson et al., 2014), and has a specific version for the operational forecasting of tropical cyclones (ACCESS-TC). ACCESS-TC has a relocatable grid at a horizontal resolution of 0.036° (Bureau of Meteorology, 2020).

Although ACCESS-TC is nested inside of the lower resolution global model (similar to other regional models), BoM has developed a tropical cyclone initialisation technique called ‘vortex specification’ (Davidson et al., 2014) to reduce the impact of low-intensity biases inherited from the global model. Vortex specification produces a tropical cyclone idealised three-dimensional axisymmetric inner-core profile following Chan and Williams (1987), tuned on observations made by the NOAA flight missions discussed in the previous section. The idealised vortex is merged with the larger-scale analysis following the methodology of Davidson and Weber (2000) to generate a more realistic initialisation for the regional model.

Further supporting the role of observations, ACCESS-TC uses four-dimensional variational data assimilation (4DVAR; Rawlins et al., 2007; Davidson et al., 2014) using all of the standard available observational data. This data assimilation process iterates over the 24-hour period preceding the forecast initialisation time to optimise the initial conditions.

One of the most globally recognisable tropical cyclone forecasting models is the Hurricane Weather Research and Forecast model (HWRF; Tallapragada et al., 2015) which was developed by NOAA for operational forecasting of tropical cyclones for all global basins. The smallest nested grid in HWRF is 2 km resolution, which is relatively higher than ACCESS-TC.

Similarly to ACCESS-TC, in some circumstances (when a storm is above 20 m s^{-1} or is underestimated in the global model compared to the observations), HWRF uses a ‘bogus vortex’ (Tallapragada et al., 2015). The HWRF bogus vortex is two-dimensional and based on a small, axisymmetric pre-forecasted vortex, and then the two-dimensional profile is smoothed to match the observed intensity or size of the target storm. Additionally, HWRF uses a 4DVAR data assimilation method based on Gridpoint Statistical Interpolation (GSI; Kleist et al., 2009).

However, recently NOAA have been operationally trialling a next generation model called the Hurricane Analysis and Forecast System (HAFS; Gopalakishnan et al., 2021). This model is being developed with the aim of breaking through the stagnation of intensity prediction

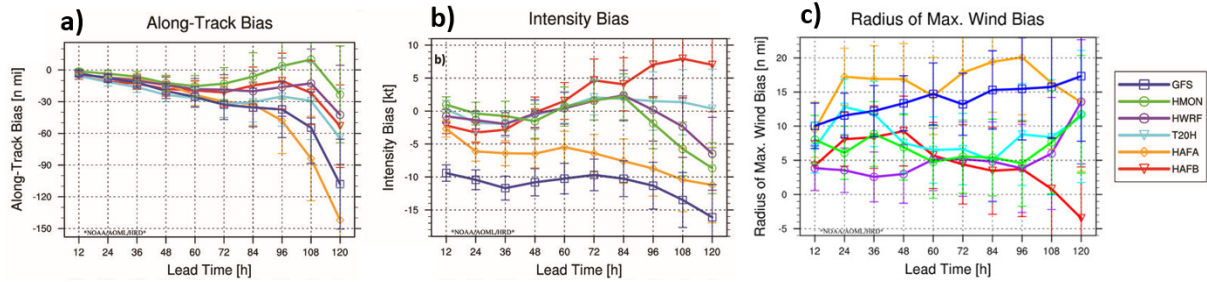


Figure 2.2: Average biases for different model simulations for the 2020 Atlantic basin tropical cyclones. Adapted from Hazelton et al. (2022).

improvements shown in Figure 1.1. According to Hazelton et al. (2021) and Hazelton et al. (2022), HAFS has a fully compressible nonhydrostatic dynamical core which is a two-way-nested version of the finite-volume cubed sphere (FV3; Harris and Lin (2013)). Similar to other models (and HWRF), HAFS is a regional domain nested within a larger, lower resolution domain. However, HAFS is planned to be ocean and wave coupled, and coupled to the parent grid (Gopalakishnan et al., 2021), allowing full interaction between the regional grid and the environment.

Further upgrades (relative to HWRF; Gopalakishnan et al. (2021)) include increased resolution of the smallest nested grid to 1 km; an ensemble version of 4DVAR (En4DVAR; Zhu et al. (2022) to represent variability; an improved physics suite with additional surface layer and boundary layer parametrisations; and improved vortex initialisation procedures, which are still in development. Despite these developments, an evaluation study by Hazelton et al. (2022) demonstrated using 2020 Atlantic basin storms that there is still a lot of work to do in order to achieve the forecast improvement ambitions.

The results of Hazelton et al. (2022) are summarised in Figure 2.2. Two configurations of HAFS are shown, HAFA and HAFB, which represent slightly different model physics and nesting setups. At the 120-hour mark, although HAFB performs the best for the radius of maximum wind (RMW) bias, both HAFS configurations perform worse than HWRF for the along-track bias and intensity bias. NOAA has an ambition that HAFS will be able to reliably forecast tropical cyclone intensity and track up to the 7-day mark (Gopalakishnan et al., 2021), but it seems that there is a long way to go for models to have this capability.

2.2.3 Modelling: Idealised

So far, operational forecasting models have been discussed. However, it was mentioned previously that models are also important for developing an understanding of the physics. While operational models can be used for these purposes, more experimental models may be better equipped to answer specific scientific questions.

For example, while operational models tend to operate on the kilometre scale, there are processes such as smaller-scale turbulence which cannot be explicitly represented. So, ‘turbulence-resolving’ models, known as Large Eddy Models (LEM) or Large Eddy Simulations (LES), were developed in the range of $\lesssim 100$ m resolution. Work has gone into adapting well-established models such as the NOAA Weather Research and Forecasting model (WRF; e.g. Ronda et al., 2017; Liu et al., 2021) and MetUM (e.g. Boutle et al., 2014a; Hanley et al., 2016; Brown et al., 2020) to perform effectively at these scales.

Some idealised models can also perform LES. Idealised models tend to be individual- or community-owned, with vastly reduced physics suites which require much less compute power. Usually, idealised models of tropical cyclones are initialised using either an idealised axisymmetric wind profile (e.g. Kepert and Wang, 2001; Bryan and Fritsch, 2002) or an asymmetric distribution which can be taken from a real case study (e.g. Kepert, 2018).

One of the most well-known idealised models is Cloud Model 1 (CM1; Bryan and Fritsch, 2002). This model, which has been proven to work at LES scales for tropical cyclone boundary layers (e.g. Bryan et al., 2017; Chen et al., 2021a), has the option to nest an idealised LES domain within a larger model simulation. This is demonstrated in Figure 2.3. Due to current constraints making LES simulations of entire tropical cyclones unfeasible due to their size, this two-way interactive nest allows for the targeted study of a specific region of a tropical cyclone, with reasonable compute times and manageable data output.

Another idealised model, developed specifically for the study of tropical cyclone boundary layers, is that of Kepert and Wang (2001) (hereafter KW01). This was adapted by Kepert (2018) to take in a nonlinear balanced pressure field, providing an asymmetric forcing. With many additional environmental and vortex parameters available, KW01 has allowed for many targeted boundary layer studies, for example on secondary eyewall formation (Kepert, 2013; Zhang et al., 2017a; Yu et al., 2021), boundary layer wind structure (Schwendike and Kepert, 2008; Fei et al., 2021),

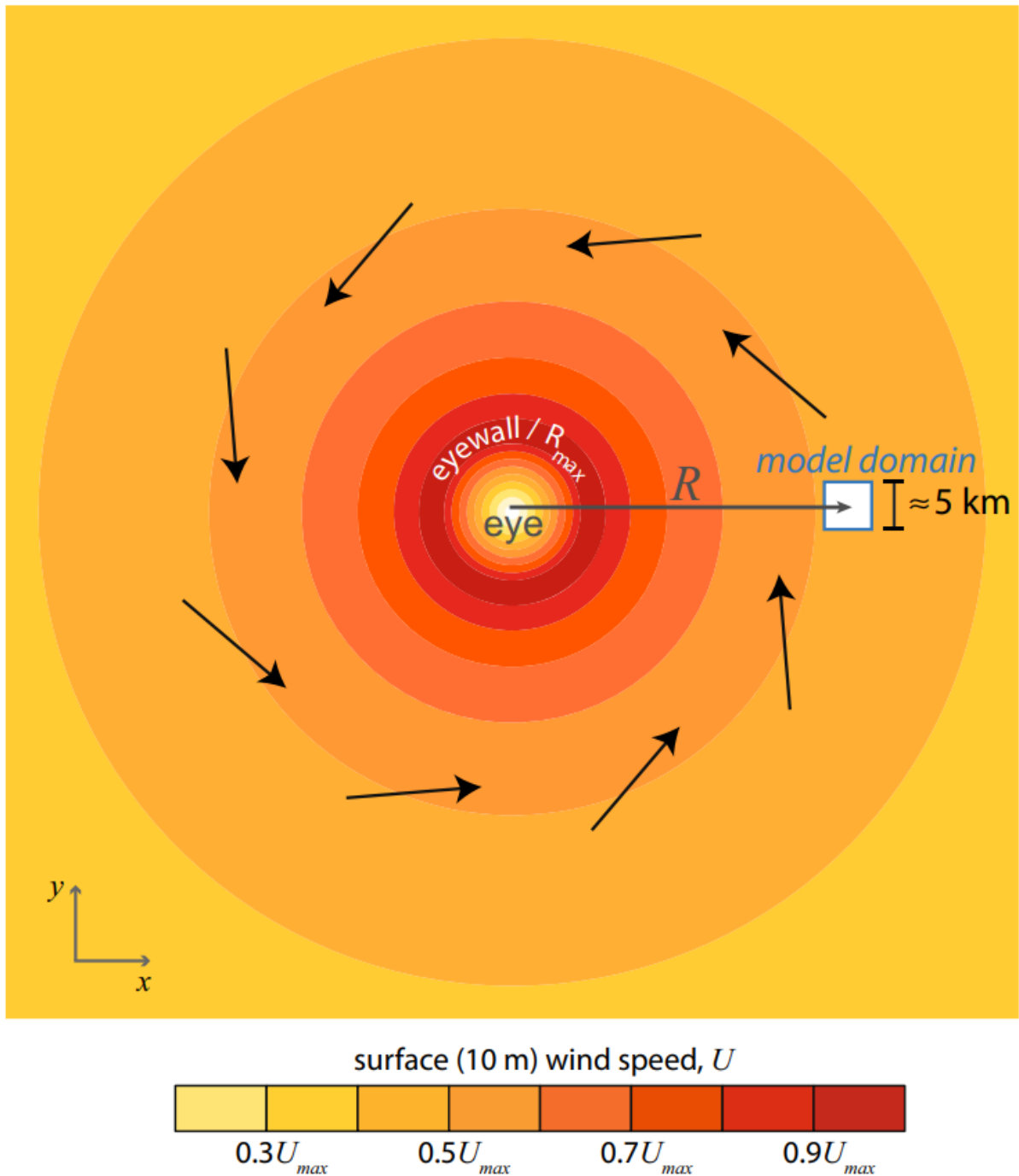


Figure 2.3: Conceptual representation of a nested CM1 LES domain (white square) within a larger tropical cyclone model simulation. Taken from Bryan et al. (2017).

and rainband dynamics (Kepert, 2018).

Idealised studies, using either CM1 or KW01, are not expected to be a perfect representation of reality due to the reduction in model physics and lack of detail in the initial conditions. However, such models can provide a good framework for isolating the effects of physical processes within tropical cyclones. For the remainder of the literature review, we will move on to the final and arguably most important pillar of tropical cyclone forecasting - the underpinning physics.

2.3 Intensification Mechanisms

The importance of the boundary layer in tropical cyclone intensity change is not contended. It is widely agreed that the provision of heat and moisture to the atmosphere by the sea surface is a critical factor in the modulation of intensity change. However, there is some contention regarding the specific mechanisms by which tropical cyclones intensify. In this section, we will explore three main paradigms in chronological order: Conditional Instability of the Second Kind (CISK; Charney and Eliassen, 1964), the Ooyama cooperative intensification theory (Ooyama, 1969), and Wind-Induced Surface Heat Exchange (WISHE; Emanuel, 1986). The most well-known of the three is WISHE, which puts the most emphasis on the boundary layer fluxes. The former theories, CISK and cooperative intensification, revolve around similar ideas on the importance of convective organisation in an axisymmetric framework. All three of them rely on the existence of an incipient vortex. The early stages of cyclogenesis will not be discussed here. After summarising these three theories, a more recently proposed intensification mechanism called the ‘rotating-convective updraft paradigm’ (Montgomery and Smith, 2014) will be considered.

In CISK, Charney and Eliassen (1964) propose a linear model with positive feedback system whereby the latent heat released by localised cumulus convection aloft would drive moisture convergence in the boundary layer of an incipient vortex. Increasing moisture convergence would lead to enhanced diabatic heating, thus fuelling the deep convective cumulus clouds. As the vortex intensifies, this process becomes more aggressive. Ooyama (1969) argued that a developing warm core within a vortex would become progressively less sensitive to convection, due to the basic principles of atmospheric instability. Building on CISK, Ooyama (1969) generated a basic non-linear model in which a vertical mass flux is initiated in regions of low-level convergence. The model introduces radial entrainment of environmental air, and a diabatic heating rate that is proportional to the convective instability, represented by the convective available potential

energy (CAPE). The radial entrainment, which is key to Ooyama’s cooperative intensification theory, would cause mid-level convergence leading to enhanced vortex spin-up (Ooyama, 1982).

In order to continually produce CAPE as it is being used up in the vortex, the cooperative intensification theory points to the importance of heat and moisture provision from the sea surface, but this is secondary to the convective mass flux process. An alternate theory, WISHE, proposed by Emanuel (1986) suggests the surface fluxes are the primary driver of tropical cyclone intensification and that the theories proposed by Charney and Eliassen (1964) and Ooyama (1969) are necessary secondary processes for redistributing mass.

The WISHE paradigm introduces a different positive feedback system, still framed around convection and diabatic heating in an axisymmetric framework, and based on similar assumptions to the previous models (such as gradient wind and hydrostatic balance). WISHE has a distinct convection closure compared to the cooperative intensification theory; while the latter assumes upright ascent and the mid-level entrainment, WISHE assumes pseudo-adiabatic ascent along surfaces of constant absolute angular momentum (M) surfaces with no entrainment.

As the name (‘Wind-Induced Surface Heat Exchange’) suggests, the WISHE feedback is based on wind speed dependent surface enthalpy fluxes. In this model, the horizontal gradient of equivalent potential temperature (θ_e , commonly used as a proxy for entropy) across the entire troposphere is controlled by the fluxes within the boundary layer. Emanuel (1986) argued that surface latent heat fluxes are the primary fuel for tropical cyclone intensification, and that these fluxes increase with increasing surface tangential wind speeds. Consequently, an incipient vortex becomes more intense due to the increasing radial gradient of the moist entropy, which facilitates the convective mass flux detailed above. As a result, the increased surface wind speeds become stronger and the process continues. This is the positive feedback mechanism that underpins the WISHE paradigm.

Emanuel (1986) claimed that “the intensification and maintenance of tropical cyclones depend exclusively on self-induced heat transfer from the ocean,” which has been a source of contention in the literature. The importance of enthalpy fluxes to tropical cyclone intensification is not disputed - the contention lies in the words ‘exclusively’ and ‘self-induced’. In response, Montgomery et al. (2009) and Montgomery et al. (2015) conducted experiments in which the wind speed for the surface enthalpy fluxes was capped, and found that the idealised vortices intensified at a comparable rate to the uncapped control experiment. They argued that while surface

enthalpy fluxes are important to tropical cyclone development, the feedback process between increased tangential wind speed and surface fluxes is not essential. Acknowledging these results, Zhang and Emanuel (2016) agreed that the wind speed dependence is not essential for intensification in idealised environments; however, they showed that the suggested WISHE feedback mechanism has the potential to spin-up tropical cyclones in less favourable environments in which the development may be otherwise stunted. The relevance of WISHE in environments with vertical wind shear and real sea surface temperatures was investigated by Cheng and Wu (2020) and supported the suggestion by Zhang and Emanuel (2016).

Other criticisms for the WISHE paradigm, and which are applicable to CISK and the cooperative intensification theory, is that they are based on axisymmetric, idealised storms. This allows no space for rotating, asymmetric convective structures, such as strong updrafts and cool downdrafts (Molinari et al., 2004). To address these shortcomings, Montgomery and Smith (2014) presented an alternate theory developed in three-dimensions, which they coined the ‘rotating-convective updraft paradigm’. While still acknowledging the importance of surface enthalpy fluxes, the authors take a double-edged approach to storm intensification, tackling the asymmetric and axisymmetric components.

In some ways, the rotating-convective updraft paradigm is similar to CISK and the co-operative intensification theory, in that convective updrafts are acknowledged to play a key role in intensification. However, Montgomery and Smith (2014) propose a different mechanism by which this occurs. Firstly, the authors focus on smaller scale updrafts which occur with a level of randomness and stochasticity, thus being inherently asymmetric. Such updrafts are referred to as ‘vortical hot towers’ (VHT; Hendricks et al., 2004) by the authors, which refer to vorticity dipoles generated by the tilting and stretching effects of deep convection. The authors claim that these VHTs tend to have a stronger cyclonic component than anticyclonic and the cyclonic components are propagated cyclonically inwards, slowly converging towards the storm centre. Montgomery and Smith (2014) suggest that the anticyclonic components are propagated outward, losing intensity and eventually becoming consumed by axisymmetrisation. As a result, there is a proposed net positive impact on the cyclonic vorticity from convective updrafts.

The foundations for the rotating-convective updraft paradigm were laid by the idealised simulations in Van Sang et al. (2008) and Montgomery et al. (2006), which support the inward propagation of the cyclonic components and outward propagation of their anticyclonic coun-

terparts. However, Fang and Zhang (2011) found that the convectively-produced anticyclonic perturbations can also propagate radially inward, rather than being expelled. Without the separation of the dipole as suggested by Montgomery and Smith (2014), the positive and negative effects would begin to cancel each other out. In addressing this conundrum, Fang and Zhang (2011) found that the horizontal convergence of the cyclonic vorticity flux can produce such an effect that the anticyclonic vorticity anomalies dissipate during their inward transport, and their impact is compensated by the importation of cyclonic vorticity. So, although Fang and Zhang (2011) propose a different mechanism for the removal of the anticyclonic anomalies, their work does support the broader idea that the inward transport of small-scale asymmetric vorticity perturbations can lead to spin-up of the storm system.

Now that the asymmetric component of the rotating-convective updraft paradigm has been addressed, the axisymmetric component can be considered. It relates to the spin-up of tropical cyclones via the radial convergence of M , which was first presented in Smith et al. (2009). While the authors touch on two spin-up processes, here we will focus primarily on the one based on convergence within the boundary layer which contributes to the spin-up of the inner core. The other mechanism is based on convergence of M above the boundary layer, induced by convection, which claims to explain increases in storm size. To understand the significance of M on the tangential wind speeds, the relation is presented by:

$$v = \frac{M}{r} - \frac{1}{2}fr, \quad (2.2)$$

where v is the tangential wind speed, r is the radius, and f is the Coriolis parameter. This relation implies that when M is materially conserved, the tangential wind speed will increase as the radius decreases. Within the tropical cyclone boundary layer, however, M is not materially conserved. Smith et al. (2009) suggest that despite this, the maximum tangential wind speeds (and supergradient wind speeds) can be found within the boundary layer due to the inflow velocity being strong enough to transport parcels inward fast enough to offset the loss of M . This process is dependent on a temporally increasing radial pressure gradient which is supported by the aforementioned spin-up above the boundary layer. As the vortex intensifies, the boundary layer inflow velocity is expected to increase, contributing to the increased radial convergence of M in the boundary layer and acting to spin-up the mean tangential winds.

While all four of the proposed intensity paradigms presented here have merit, it is difficult to say which is ‘right’ or ‘best’. It is likely that the truth lies between these theories, with aspects of all of them being important for intensification. CISK, Ooyama’s cooperative intensification theory and WISHE are all based on an idealised, axisymmetric incipient vortex. Montgomery and Smith (2014) introduced the component of asymmetry, which is invaluable as all real-world developing tropical cyclones experience a degree of asymmetry throughout their intensification process. The effects of asymmetry on intensity and structure will be discussed in the upcoming sections, and will further support the need for an intensification paradigm that considers such asymmetries.

Despite the differences, all of the theories agree on the importance of several main aspects of tropical cyclone intensification. These include:

- Surface enthalpy fluxes are a necessary fuel source for tropical cyclones.
- Convective updrafts aid in spin-up, via several proposed mechanisms.

The following sections are underpinned by these two basic principles. First, deep layer vertical wind shear will be discussed in the context of causing asymmetries and contributing to intensity change via the boundary layer. Next, a review of tropical cyclone boundary layer dynamics would not be complete without consideration of landfall, which relates to asymmetry and shear, and commonly spells the end of life for many storms.

2.4 Deep Layer Vertical Wind Shear

There are many different ways to calculate vertical wind shear in tropical cyclones. The most widely used definition in studying tropical cyclones is that the vertical wind shear is the vector difference between the mean horizontal wind at 850 and 200 hPa across a radius (Tang and Emanuel, 2012a; Wang et al., 2015; Ahern et al., 2019). While this does not address the variability of the full vertical profile, it is generally accepted to be a good approximation of the deep layer shear (Tang and Emanuel, 2012a). However, the radius over which to calculate the shear can be more subjective and is dependent on context.

Previous studies vary in their approach. Environmental shear may be more effectively calculated using distances at least 500 km from the storm centre, often extending to 800 or 900 km (Wang et al., 2015), although some begin the calculations from as close as 200 km (Zehr, 2003; Ahern

et al., 2019). Using further radial distances can help to eliminate the internal properties of the storm itself, which may produce a ‘re-balancing’ effect to resist the environmental shear and preserve the vortex (Dai et al., 2021). On the other hand, calculating the shear within the inner radii - from the centre to around 200 km (Ahern et al., 2019) - can produce a good generalisation of the state of the inner core, and may be an appropriate metric when considering vortex tilting.

Asymmetry

Deep layer vertical wind shear (VWS) is one of the primary mechanisms by which tropical cyclones can become asymmetrical (e.g., Corbosiero and Molinari, 2003; Corbosiero et al., 2006; Hence and Houze, 2012). Most detrimentally, VWS-related asymmetry can present as vortex tilt, where the vortex is differentially advected across the troposphere, leading to tilt across the entire vortex including the eyewall and the vorticity patterns (e.g. DeMaria, 1996; Reasor et al., 2004; Boehm and Bell, 2021). Due to the impacts on intensity (which are discussed in detail below), there is scientific interest in the ability of cyclones to resist VWS-related tilting.

While the first three intensification paradigms described in Section 2.3 focus on thermodynamic processes, the theories around vortex resilience to tilting relate more closely to the rotating-convective updraft paradigm presented by Montgomery and Smith (2014), with a more dynamic approach. It is generally accepted that moist convective processes in the inner core can contribute to resilience; however, there have been many theories (e.g., Jones, 1995; DeMaria, 1996; Corbosiero and Molinari, 2002; Reasor et al., 2004) which suggest the importance of circulation and vorticity in re-aligning the vortex. For example, Jones (1995) suggested that in a tilted vortex, potential vorticity anomalies become vertically displaced from each other which causes vortex precession and small-scale circulations that act to cyclonically advect the anomalies, combating the impacts of VWS.

In a similar line of thought, Reasor et al. (2004) discussed the potential role of potential vorticity asymmetries produced by VWS. In fact, the authors suggested that interaction of VWS with a tropical cyclone can produce vortex Rossby waves (VRW) which can act to re-stabilise and re-align the vortex through a process which they coined ‘VRW damping’. Reasor et al. (2004) suggest that vortex re-alignment can occur either through precession caused by quasi-mode propagating VRWs or the dispersal of the vortex asymmetry by cyclonically propagating VRWs,

which will act to resist the tilting by differential advection.

In a large-scale analysis, DeMaria (1996) found that a tropical cyclone's ability to resist tilting was positively correlated to the latitude (through the Coriolis force), storm size, and storm intensity. There can also be notable differences in the wind field - for example, Zhang et al. (2013) suggested that in the northern hemisphere, the depth of the inflow layer is highest in the downshear quadrants, particularly in the downshear-right (DR), while the depth of the mixed layer is highest to the left-of-shear. In the southern hemisphere, the upshear/downshear relationships are the same as in the northern hemisphere, but the left-of-shear/right-of-shear relationships are flipped.

Shear-related asymmetries can typically present as convective asymmetries (Hence and Houze, 2012; Barron et al., 2022), in which the convective precipitation tends to be concentrated in the right-of-shear quadrants, whereas the stratiform rainfall occurs to the left-of-shear (in the northern hemisphere). The idea is that convection initiates in the downshear right quadrant and then intensifies as it is propagated azimuthally to the downshear left quadrant (DeHart et al., 2014). This is related to the previous argument about the wind asymmetries. Increased inflow in the downshear right quadrant enhances the local CAPE (following the WISHE intensification paradigm of Emanuel (1986)), which in turn fuels deep convection.

A detailed analysis of dropsonde composites by Zhang et al. (2013) further strengthened this argument, relating the highest surface equivalent potential temperature (θ_e) to the downshear right (DR) quadrant, and the lowest surface θ_e to the upshear left (UL). Since θ_e is logarithmically proportional to the entropy (Emanuel et al., 1994), it follows that the most convective regions would have relatively enhanced levels of θ_e . On the other hand, in regions of stratiform precipitation, there should be larger-scale evaporative cooling in the downdrafts, which would lead to thermodynamic depletion of the descending air, resulting in a lower surface θ_e .

It is more difficult to give generalised statements about the horizontal distribution of vorticity under shear. Figure 2.4 summarises the results of three radar studies of vorticity under shear. One similarity of all of these studies (which are all using radar observations), is that the sign of the vorticity flips between the left-of-shear and right-of-shear quadrants. Note that all of these studies (Reasor and Eastin, 2012; Boehm and Bell, 2021; Shimada et al., 2024) are based on Northern Hemisphere storms, so consistency would be expected if the vorticity asymmetry was highly dependent on the orientation of shear.

The difficulty in relating these results is that the vorticity flips several times in some cases. For example, there are three horizontal dipoles of vorticity in Figure 2.4c - within the eye, cyclonic vorticity is oriented to the left-of-shear, with the anticyclonic component right-of-shear. At approximately 20 km radius, this dipole flips sign, and then it reverts back at 40 km radius.

To an extent, this behaviour is consistent with the findings in Figure 2.4d, where the cyclonic vorticity is left-of-shear within the inner core and then flips at larger radii. However, Reasor and Eastin (2012) only showed two distinct vorticity dipoles, whereas Boehm and Bell (2021) showed three. While it is possible that another dipole would exist in Figure 2.4d if the radial plot limits were extended, it would be unjustified to make this assumption based on the results presented by the authors. Thus, it must be noted as an inconsistency. Another inconsistency is that the magnitude of the vorticity seems to be matched between the two inner dipoles in Figure 2.4c, whereas the innermost dipole in Figure 2.4d has a higher maximum vorticity than its counterpart.

The findings by Shimada et al. (2024), shown in Figures 2.4a and 2.4b, complicate this even further. Figure 2.4a suggests that the inner core asymmetric cyclonic vorticity is situated to the left-of-shear in intensifying tropical cyclones, whereas in steady state cyclones (Figure 2.4b) it is more of an upshear-downshear relationship. In the steady state composite, it seems that the cyclonic vorticity is more oriented to the right-of-shear in the inner core, which contrasts to the rest of the findings. Note, however, that there does seem to be a weak flipping of the vorticity sign at larger radii in the intensifying composite (Figure 2.4a) which is consistent with Reasor and Eastin (2012) and Boehm and Bell (2021).

While Figures 2.4a and 2.4d represent intensifying tropical cyclones, Figure 2.4c shows the vorticity field of Hurricane Rita (2005) as it was weakening, and these results still contrast more with the steady-state cyclones in Figure 2.4b. Therefore, it is not simple enough to conclude that shear dominates the asymmetric vorticity distribution consistently across a range of storm systems, or that intensification rate is the dominating factor. Furthermore, it is possible that vorticity may be affected by other factors such as storm translation and larger-scale interactions with the environment.

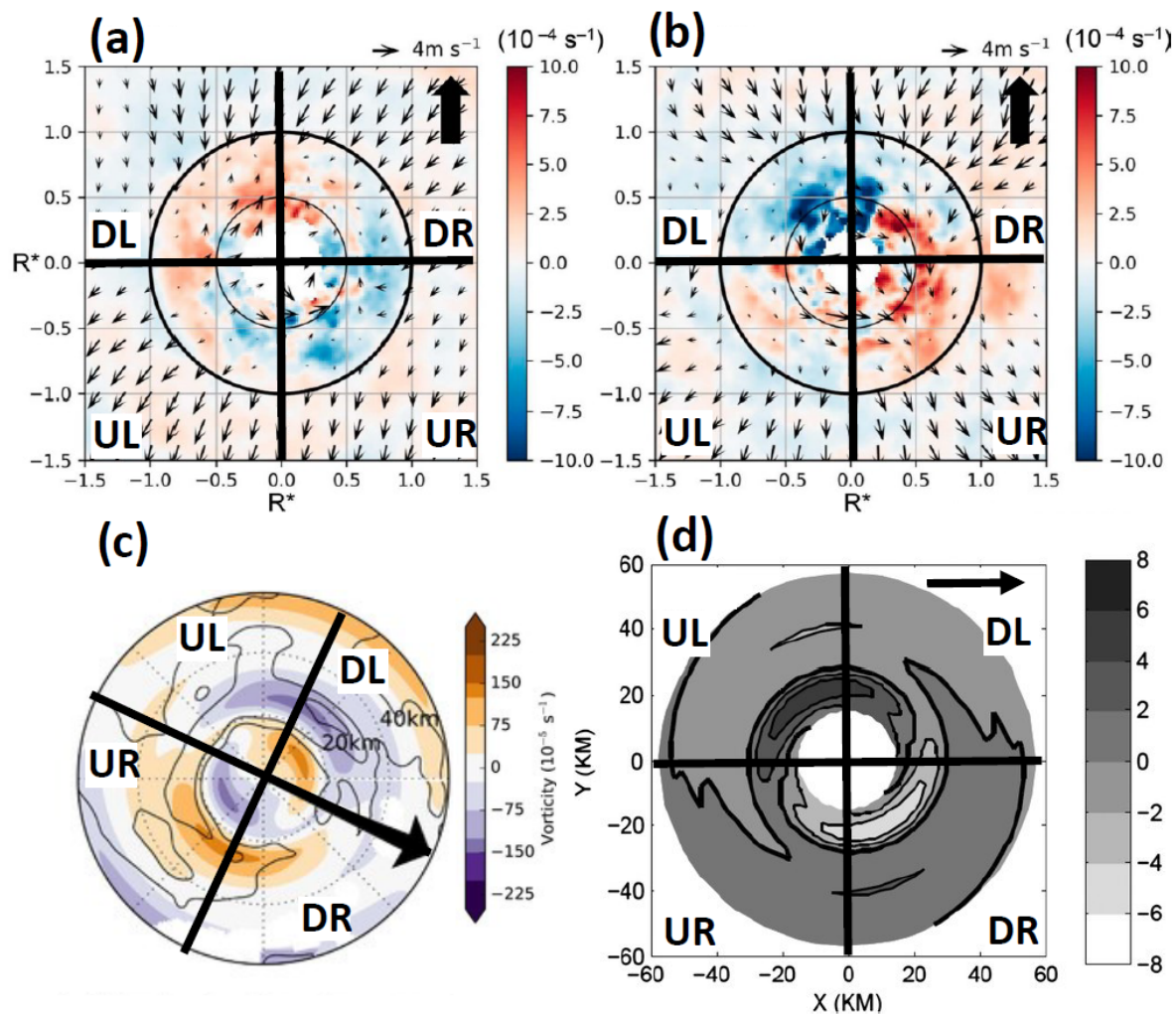


Figure 2.4: (a) and (b) adapted from Shimada et al. (2024), showing the radar-derived asymmetric vorticity field (coloured; 10^{-4} s^{-1}) and wind vectors at 2 km altitude, for (a) intensifying cases and (b) steady state cyclones. (c) Radar-derived wavenumber-1 component of vorticity (coloured; 10^{-5} s^{-1}) at 2 km for Hurricane Rita (2005), adapted from Boehm and Bell (2021). (d) Radar-derived wavenumber-1 asymmetry of vorticity (shaded; 10^{-4} s^{-1}) at 5 km for Hurricane Guillermo (1997), adapted from Reasor and Eastin (2012).

Intensity

Vertical wind shear can have varied impacts on intensity. Typically, high-moderate shear is associated with storm weakening (e.g. DeMaria and Kaplan, 1999; Paterson et al., 2005; Wang et al., 2015), with storms being able to intensify when the deep layer shear is $\lesssim 7\text{--}10\text{ m s}^{-1}$ depending on the study, at which point they begin to weaken. DeMaria and Kaplan (1999) found that the extent to which wind shear has a negative impact on the intensity of tropical cyclones in the north Atlantic basin is partially related to the latitude; higher latitude storms seem to have a greater resistance to the detrimental effects, suggesting a contribution from the Coriolis force. While this result was supported by Zeng et al. (2010) in regards to deep layer vertical wind shear, their statistical analysis implied that higher-latitude storms are more susceptible to low-level shear, which they define as 600–800 hPa rather than 200–850 hPa.

The primary mechanisms by which vertical wind shear is thought to negatively impact storm intensity relate to the asymmetry discussed above. In Section 2.3, the importance of high- θ_e for storm intensification was summarised - such asymmetries can lead to thermodynamically depleted (dry and/or cool) air being introduced into the inner core (e.g. Tang and Emanuel, 2012a; Riemer et al., 2010; Alland et al., 2021a; Alland et al., 2021b; Finocchio and Rios-Berrios, 2021; Wadler et al., 2021; Rios-Berrios et al., 2023). This phenomenon is conceptualised in Figure 2.5b, in which the vortex is substantially tilted, the convection is asymmetrically distributed between the upshear and downshear quadrants, and thermodynamically depleted air is entering the storm core via the disrupted secondary circulation.

For low- θ_e air which is introduced by a strong radial inflow in the low to mid-levels, this process is named ‘radial ventilation’ (Alland et al., 2021b; Rios-Berrios et al., 2023). If it is introduced to the boundary layer by convectively-induced downdrafts, it is named ‘downdraft ventilation’ (Alland et al., 2021a). Both types of ventilation can co-exist (Riemer et al., 2010) and the end result is the same - thermodynamic depletion of the inner core, which reduces the buoyancy of the eyewall (Tang and Emanuel, 2012a). With the eyewall being the region of maximum vertical motion and diabatic heating, following the intensification principles from Section 2.3, reducing the buoyancy inevitably comes at a cost to the overall intensity. The extent to which tropical cyclones can resist the detrimental effects of ventilation depends on their ability to recover their θ_e (Wadler et al., 2021), which would generally require the air–sea enthalpy fluxes to offset the depletion (Molinari et al., 2013; Wadler et al., 2018).

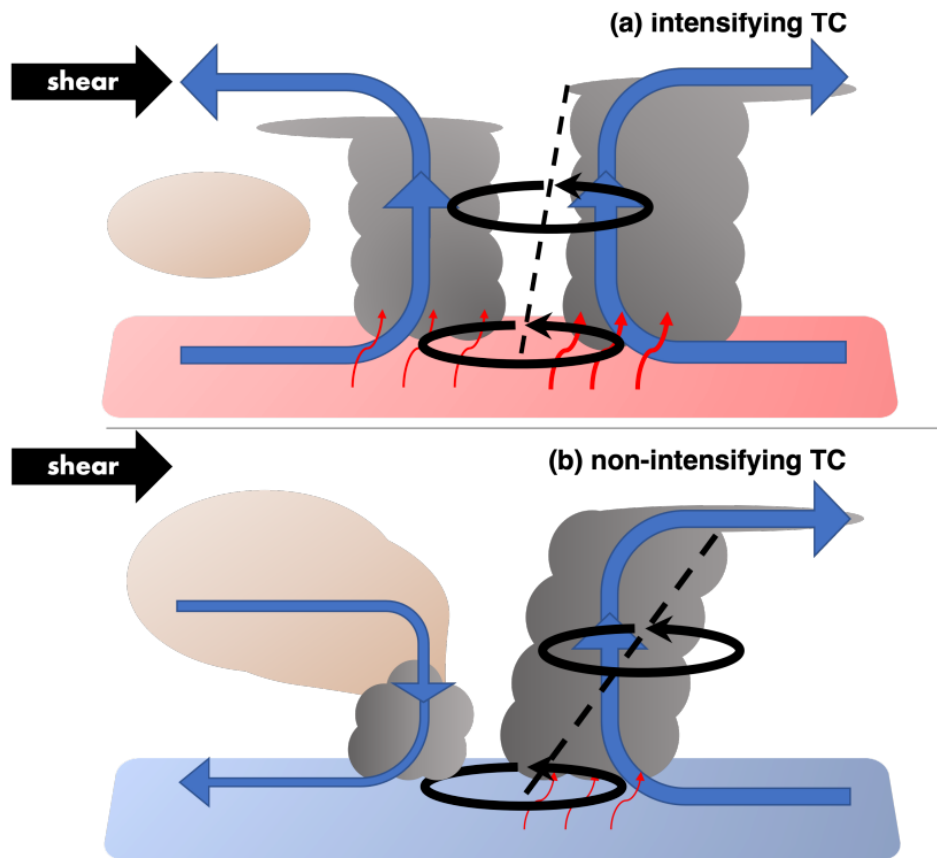


Figure 2.5: Schematic depicting the dynamics of intensifying (a) and non-intensifying (b) tropical cyclones under vertical wind shear, taken from Rios-Berrios et al. (2023). The colour of the surface represents relatively warmer (red) or cooler (blue) sea surface temperatures. The red arrows depict surface fluxes. The black circular arrows represent the eyewall updraft, which is more tilted in the non-intensifying cases. The blue arrows represent the secondary circulation. The brown regions are dry air. The grey cloud-like features represent the eyewall cloud.

In some cases, tropical cyclones can not only resist weakening in moderate-high wind shear, but they can also intensify or even rapidly intensify. While the factors contributing to intensification in the presence of deep layer shear are still not perfectly understood, there is a growing body of literature emerging. The structural differences in intensifying and non-intensifying tropical cyclones under shear are shown in Figure 2.5. In a review, Rios-Berrios et al. (2023) summarised that intensifying tropical cyclones tend to have a lower vortex tilt, more symmetric convection, warmer surface temperatures (and stronger surface fluxes), and a reduced impact of ventilation. Ryglicki et al. (2018) found that rapidly intensifying storms under shear can counteract the effects of ventilation by developing a stronger mid-level outflow upshear, which diverts the dry environmental air away from the inner core (Ryglicki et al., 2021).

Another possible mechanism by which tropical cyclones may be able to resist shear enough to intensify, is the axisymmetrisation of precipitation (Rios-Berrios et al., 2023). As mentioned above, wind shear can cause asymmetric distributions of precipitation, concentrated downshear and reaching a maximum in the downshear left quadrant (DeHart et al., 2014). Tao et al. (2017) found a relationship between stratiform precipitation and intensification rate in sheared tropical cyclones. The results showed that in the storms that rapidly intensified, there was a correlation with an increase in upshear inner core stratiform precipitation, which the authors link to an increase in inner core moisture. Again, this can be related to resisting ventilation.

Clearly, there is a complex relationship between deep layer vertical wind shear and tropical cyclone dynamics. Here, a few of the main concepts were summarised, but there are still many questions to be answered. The following sections on turbulence and landfall will be underpinned by the ideas presented here and in Section 2.3, which will further demonstrate the complexity of tropical cyclone dynamics.

2.5 Role of Turbulence

A common theme between intensity and wind shear in tropical cyclones is turbulence; previous studies have suggested using observations (Zhang et al., 2010; Ming et al., 2014) and models (Zhu, 2008; Bryan et al., 2017) that much of the turbulence within the tropical cyclone boundary layer is driven by shear. However, turbulence is known to be produced by local shear rather than the deep layer VWS discussed in the previous section. Turbulent kinetic energy (TKE), which is a measure of turbulent intensity (Stull, 1988), can be broken down into a shear-generated

component (Stull, 1988):

$$-\overline{u'_i u'_j} \frac{\delta \overline{U}_i}{\delta x_j}, \quad (2.3)$$

and a buoyancy-generated component (Stull, 1988):

$$\delta_{i3} \frac{g}{\theta_v} (\overline{u'_i \theta'_v}), \quad (2.4)$$

where overbars represent the mean and primes denote the eddy flux. Equations 2.3 and 2.4 make use of Einstein's summation notation (Einstein et al., 1916).

The produced TKE can then be dissipated, advected and transported within a system (Zhu, 2008) - it is not conserved (Stull, 1988). From the shear-driven (Eq. 2.3) and buoyancy-driven (Eq. 2.4) terms, turbulence can be related to storm intensity. For example, all of the major theories (Charney and Eliassen, 1964; Ooyama, 1969; Emanuel, 1986) give importance to inner-core buoyancy in the intensification of tropical cyclones, and the rotating convective updraft paradigm presented by Montgomery and Smith (2014) implies that smaller-scale asymmetric buoyant updrafts play a key role in storm spin-up by providing the storm with vorticity. Some examples of local shear-producing mechanisms in tropical cyclones include shear caused by the frictional effects of the surface, convergence and divergence (related to the updrafts), and horizontal shear between the eyewall and eye or between the eyewall and outer-radii.

In Section 2.3, we discussed the key role of enthalpy fluxes from the sea surface in the intensification of tropical cyclones. These fluxes are inherently turbulent (Riehl, 1950) - the evaporation of water from the sea surface leads to a dissipation of TKE into heat, which is transported into the inner core of the storm (Emanuel et al., 2023). This relation is an example of how TKE can be used to infer the transport of heat, moisture and momentum around the storm and the direct relation between this transport and TKE is described in full detail in Stull (1988).

The distribution of TKE across tropical cyclones was mapped by Lorsolo et al. (2010) using airborne radar observations, and the results are summarised in the schematic in Figure 2.6. While there is some TKE in the boundary layer, linked to the surface enthalpy fluxes and surface shear, the eyewall region has the highest values. Kepert (2012) theorised that the high observed TKE in the eyewall could be produced by local buoyancy. However, in idealised simulations,

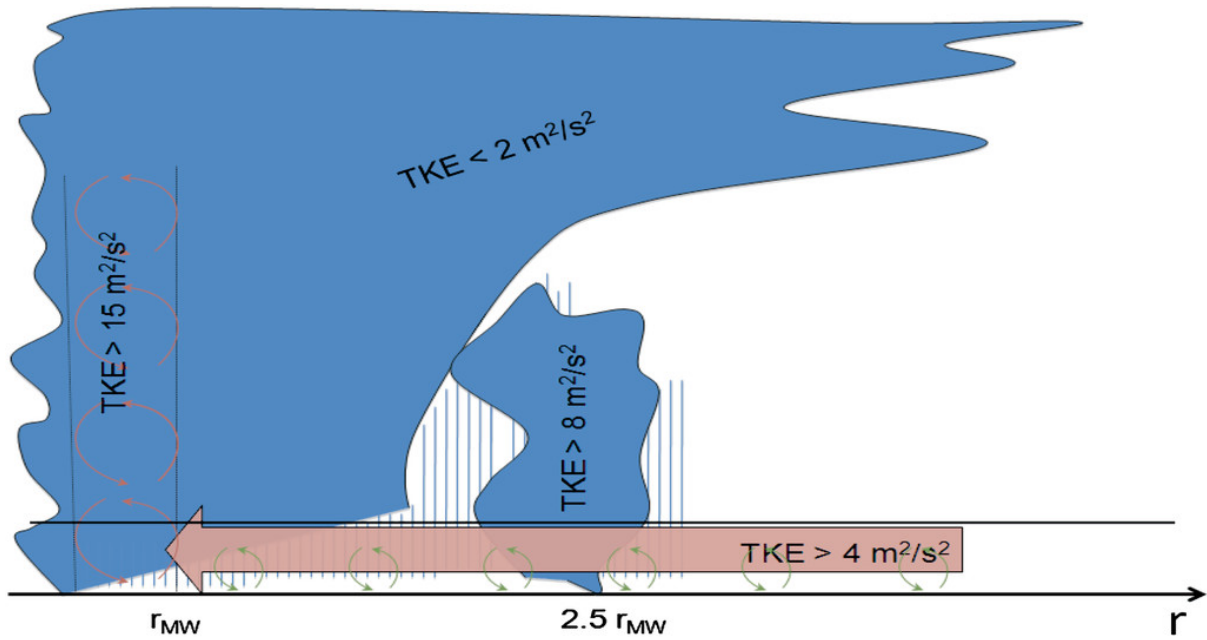


Figure 2.6: Schematic of TKE distribution within a tropical cyclone axisymmetric framework, where r_{MW} is the radius of maximum wind and r is the radial distance from the storm centre. Taken from Lorsolo et al. (2010).

Chen and Bryan (2021) found that there was a negative buoyancy production of TKE within the eyewall, despite still diagnosing high values of TKE. An alternate theory, presented by Smith and Thomsen (2010) and Smith and Montgomery (2010), is that the high TKE within the eyewall can be attributed to lofting or vertical advection of TKE. Dynamically, this is logical since the eyewall is a broad region of updraft and so the high TKE could be directly related to the transport from the boundary layer. Despite this, the vertical advection hypothesis is inconsistent with the study performed by Kepert (2012), in which the turbulence schemes did not advect TKE. As it stands, the source of high TKE within the eyewall remains to be an open question, although Lorsolo et al. (2010) suggested that it could be being mechanically produced by the horizontal shear of the updraft itself.

Turbulent eddy processes within the eyewall can contribute to storm intensification via the redistribution of moist entropy (Montgomery et al., 2019). Emanuel (2012) and Emanuel et al. (2023) proposed a mechanism whereby this entropy is further redistributed by the turbulent processes within upper tropospheric outflow, which causes a local thermal stratification. The authors state that such thermal stratification would retain sub-criticality in the Richardson number (Eq. 2.1), meaning that the layer would remain turbulent and thus drive the amplification of the tangential wind above the boundary layer. Montgomery et al. (2019) performed simulations that contested this hypothesis, showing that the turbulent redistribution of moist

entropy was attributed to asymmetric deep convection rather than a reliance on the Richardson number.

On the other hand, turbulence can be related to weakening mechanisms in tropical cyclones. In Section 2.4, we discussed convective asymmetries produced by VWS. Following the equations describing TKE production through local horizontal shear (Eq. 2.3) and buoyancy (Eq. 2.4), it follows that convective asymmetries would produce pockets of turbulent mixing. For example, convergence into an updraft would lead to a horizontal wind shear, and convective updrafts are inherently buoyant. Additionally, the small-scale vorticity dipoles associated with convection that were discussed in Section 2.3 would contribute to the local turbulent mixing.

Furthermore, we discussed in Section 2.4 that VWS can modulate the distribution of precipitation. Zhang et al. (2009) found that turbulence produced in between tropical cyclone rainbands is predominantly shear-driven, which fits with observational (Powell, 1990; Skwira et al., 2005) and idealised (Kepert, 2018) studies which suggest that rainbands produce local perturbations in the wind speed.

In Section 2.4, we discussed the downdraft and radial ventilation storm weakening processes (e.g. Tang and Emanuel, 2012a; Riemer et al., 2010; Alland et al., 2021a; Alland et al., 2021b; Finocchio and Rios-Berrios, 2021), and observed VWS-induced asymmetries. Namely, Zhang et al. (2013) showed that in sheared storms, the depth of the inflow layer is the highest in the downshear quadrants. Similarly, DeHart et al. (2014) showed that convection is initiated in the downshear right quadrants and propagated to the downshear left as it strengthens. This alignment between the maximum inflow layer depth and the regions of convection mean that this region becomes especially vulnerable to ventilation, since convective and precipitation can also contribute to mixing via the turbulence.

In the next section, the dynamics of tropical cyclone landfall will be considered. An observational study by Zhao et al. (2022) found that due to the increasing drag of the land surface, landfalling cyclones produce much more near-surface TKE than those over the ocean but also produce more vertical eddy diffusivity. The impact of landfall turbulence on tropical cyclone intensity remains an open question, although following the intensification mechanisms in Section 2.3, it would seem that the turbulent mixing of dry surface air into the boundary layer would not be beneficial for intensification.

2.6 Landfall

Interaction between the earth's surface and the atmosphere is what defines the boundary layer. While the sea surface is largely accepted to fuel tropical cyclone intensity via the provision of heat and moisture, it is important to consider how the dynamics change once the surface changes. Landfall is the most destructive part of a tropical cyclone's life cycle, but it can also result in rapid weakening and asymmetric changes to the overall structure.

Asymmetry

Typically, the tropical cyclone wind field is detrimentally impacted by the sudden increase in surface friction, but more work is needed to develop a comprehensive understanding of how the wind distribution changes during landfall, and how this may be affected by factors such as storm translation and environmental wind shear. Recent work by Hlywiak and Nolan (2022) made progress in filling these gaps using idealised simulations of a landfalling tropical cyclone with varying translation speeds and land surface characteristics. Notably, Hlywiak and Nolan (2022) found that the effect of the surface roughness discontinuity produced by the coast dominated the asymmetric response when compared to the effect of the storm motion.

At landfall, Hlywiak and Nolan (2022) found that the primary and secondary circulations were both directly impacted by the changing surface characteristics. The authors studied an idealised northern hemisphere storm and observed an enhancement of the offshore inflow velocity, linked to the sudden decrease in friction from land to sea as the winds are propagated azimuthally. The convergence produced by the inflow within this region encourages vertical motion upstream. As a consequence of the increased inflow, the radial advection of momentum is increased, leading to a boundary layer tangential wind maximum to the rear quadrants (following Montgomery and Smith (2014)). The relationship remains the same regardless of the hemisphere, and is based just on the orientation of the storm to land. Of course, the region of maximum inflow will be on opposite sides of the storm depending on the hemisphere, but following Hlywiak and Nolan (2022), it should always be on the immediate offshore flow. This wind structure is illustrated in the schematic given by Hlywiak and Nolan (2022), shown in Figure 2.7.

The enhancement of the offshore inflow velocity has been supported by previous idealised simulations (Li et al., 2014) and an observational study by Rogers and Zhang (2023), in which an aircraft flew parallel to the coast during a tropical cyclone eye penetration. The onshore bound-

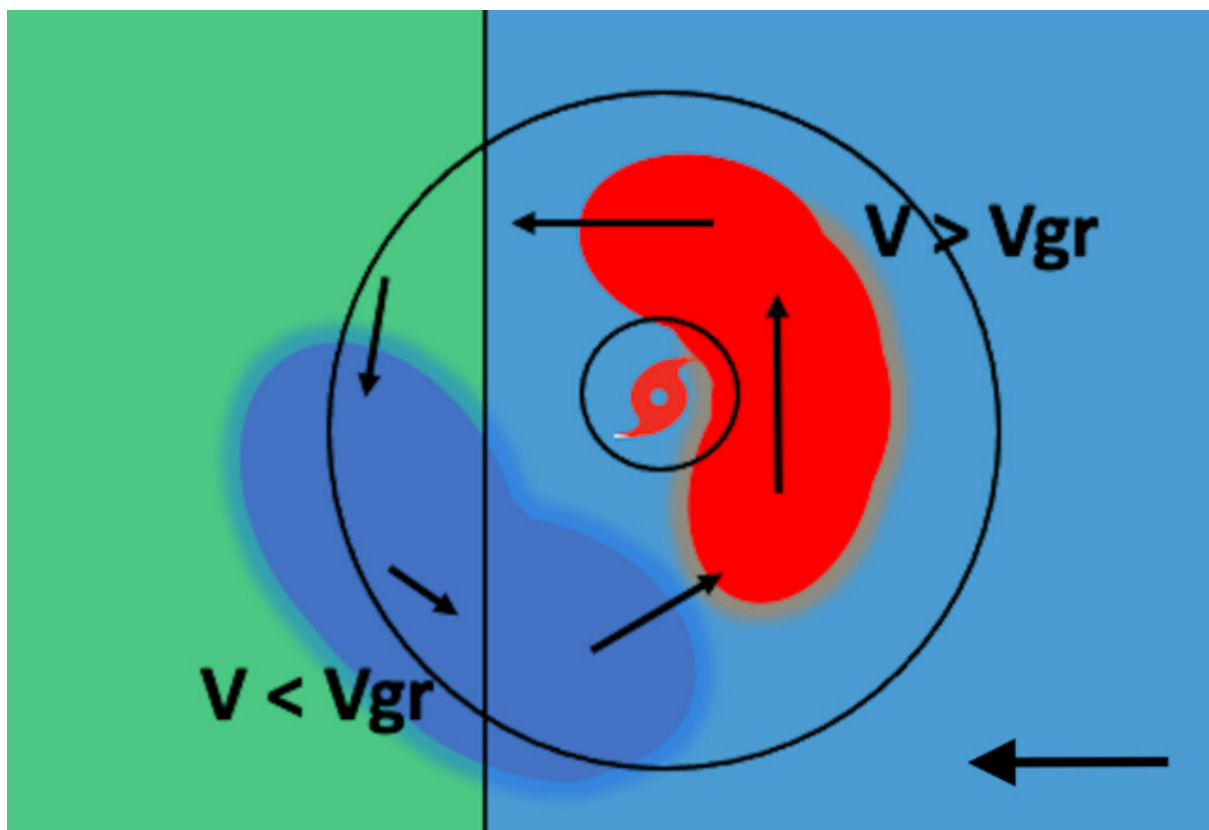


Figure 2.7: Schematic from Hlywiak and Nolan (2022) demonstrating how the wind speed changes as the storm interacts with land. The broad circle is the radius of tropical storm force winds. The storm is translating westwards, where the green area denotes land and the blue area is sea. The region of maximum inflow is shown in dark blue and the maximum tangential winds are shown in red. Azimuthal circulation is denoted by the arrows.

ary layer tangential wind maximum found by Hlywiak and Nolan (2022) was also corroborated by these observational findings.

Another asymmetric impact of landfall is the distribution of convection and rainfall, which are linked to the VWS discussed in the previous section. As the cyclone makes landfall, the magnitude of wind shear tends to increase (Li et al., 2014), which would modulate the distribution of precipitation to be maximised downshear. Numerous composite studies of observed tropical cyclone landfalls (Xu et al., 2014; Wen et al., 2019) have found that while storm motion, topography, sea surface temperatures, and total precipitable water did contribute to the distribution of precipitation, the major controlling factor was the deep layer VWS.

In landfall cases, frictional convergence must be considered. Frictional convergence occurs when air parcels are slowed over land due to the increased surface drag. Low-level convergence can enhance upward motion. In fact, enhanced convergence ahead of translating tropical cyclones was shown by Shapiro (1983) to increase the precipitation in the front quadrants. However, idealised studies suggest that the convergence produced by the frictional effects of landfall have a limited effect on precipitation distribution (Chan and Liang, 2003).

To summarise, asymmetric dynamics of tropical cyclones are complex to predict in landfalling cases, due to the impacts of VWS, translation, environmental moisture and topography. In general, landfall reduces the near-surface wind speed onshore and increases the inflow velocity offshore (e.g. Li et al., 2014; Hlywiak and Nolan, 2022; Rogers and Zhang, 2023). While convergence (either through frictional effects or translation) can impact vertical motion, it has limited impact on the distribution of precipitation (Chan and Liang, 2003). The dominating factor in modulating the distribution of precipitation is VWS (Xu et al., 2014; Wen et al., 2019), further supporting the motivation to study VWS in the context of tropical cyclone asymmetry.

Intensity

Storm intensity is negatively affected by landfall, according to the arguments presented above. Since tropical cyclone intensity is typically measured by the 10 m wind speed (e.g. Camelo and Mayo, 2021), and wind speeds tend to peak in the front quadrants of the storm (e.g. Shapiro, 1983), the intensity of the storm is directly impacted by friction from land, which leads to an immediate reduction in surface wind speeds in the front quadrants of the storm (Hlywiak and Nolan, 2022; Chen and Chavas, 2021). The enhancement in the offshore inflow velocity (Li

et al., 2014; Hlywiak and Nolan, 2022; Rogers and Zhang, 2023) is likely to introduce dry air from the coast into the inner core circulation, reducing the moist entropy of the eyewall.

The Carnot heat engine theory for tropical cyclone intensification presented by Emanuel (1986) is fundamentally disrupted by landfall. As has been discussed, all of the major theories for intensification (Charney and Eliassen, 1964; Ooyama, 1969; Emanuel, 1986; Montgomery and Smith, 2014) are dependent on fluxes of heat and moisture from the sea surface. It is generally agreed that tropical cyclones are fuelled by diabatic heating. When this moisture source is removed by the relatively dry land surface, the inflow layer ventilates dry air into the inner core, leading to a reduction in CAPE, diabatic heating, and ultimately storm intensity.

However, in rare cases, tropical cyclones can re-intensify over land (e.g. Emanuel et al., 2008; Arndt et al., 2009; Laureano Bozeman et al., 2012). Usually, this occurs in storms that encounter warm, moist conditions inland. Emanuel et al. (2008) showed that storms can re-intensify over hot sand, such as in northern Australia, particularly when the surface has been pre-moistened by the incoming tropical cyclone.

2.7 Summary and Thesis Outlook

This literature review has summarised the key concepts of asymmetric boundary layer dynamics in tropical cyclones, including recent developments in observations, modelling and scientific understanding. By establishing the fundamentals of tropical cyclone intensification, we were able to contextualise the current knowledge of how asymmetric processes impact intensity change.

The main results indicate that wind shear is a key factor in modulating the asymmetry of the inflow layer depth, precipitation, and convection. Such asymmetries can drive turbulent processes within the boundary and the troposphere, which contribute to intensity change by various mechanisms, such as transporting momentum into the inner core (which has a positive effect on intensification), or alternatively - encouraging the transport of low-entropy air into the boundary layer (which has a potential weakening effect).

However, many questions still remain, partially due to the lack of available data to verify turbulence representation in numerical models, and the lack of focus on asymmetric dynamics during model verification processes. Even with these two points addressed, it can be difficult to investigate the impact of asymmetry on storm evolution due to the complexity of the natural

environment. For example, in meteorology it is difficult to attribute an outcome to a particular process in observations or full-physics modelling because the atmosphere is constantly evolving and is subject to numerous physical processes at any given point in time. A good example of this is Figure 2.4, which demonstrated a diversity of results from observational studies that used similar analysis techniques.

To address these gaps in the literature, although it is not within our capability to collect new observations, I will present a new framework for the routine model evaluation of storm asymmetry. Next, I will investigate the turbulence parametrisation in the mid-troposphere of a sheared tropical cyclone and how changing this affects the boundary layer and storm intensity. Finally, idealised models and simple numerical models will be used alongside full-physics models and observations to disentangle atmospheric processes relating to asymmetry. Specifically, I will consider how shear, landfall, rainband dynamics and large-scale environmental vorticity gradients can contribute to boundary layer wind asymmetries.

Chapter 3

Data and Methods

Tropical cyclones are physically extensive, often spanning hundreds of kilometres in radius. In the current technological climate, tropical cyclones are always captured by geostationary and/or polar-orbiting satellites due to their vast size, and can be recognised even in coarse ($\gtrsim 10$ km) global forecasting models, though higher resolution ($\lesssim 5$ km) is often needed to accurately represent intensity.

While these approaches can provide useful information to understand the global synoptic situation and to construct climatologies, studying the meteorology of the tropical cyclone boundary layer requires more advanced methods. Visible and infrared satellite channels can rarely reliably penetrate the thick tropical cyclone cloud layer, which means they cannot relay useful information about the boundary layer profile. In Section 3.5, alternative sources of observational data will be explored, which allows for a more robust study of the boundary layer.

In terms of modelling, global models are often too coarse to represent the fine-scale structure of tropical cyclones. For example, a global model of grid-length 12 km would not be able to represent a tropical cyclone that had an eye of diameter 10 km, and this conundrum extends across the system, into the rainbands. Furthermore, current global models rarely operate on ‘convection-permitting’ resolutions, which means a large proportion of the tropical cyclone convection is parameterised. Convection-permitting simulations, which are used throughout this work, are widely accepted to perform better than those with parameterisations.

This chapter will explore all of the modelled data and observations used to perform in-depth analysis of the tropical cyclone boundary layer, including the techniques by which this data was

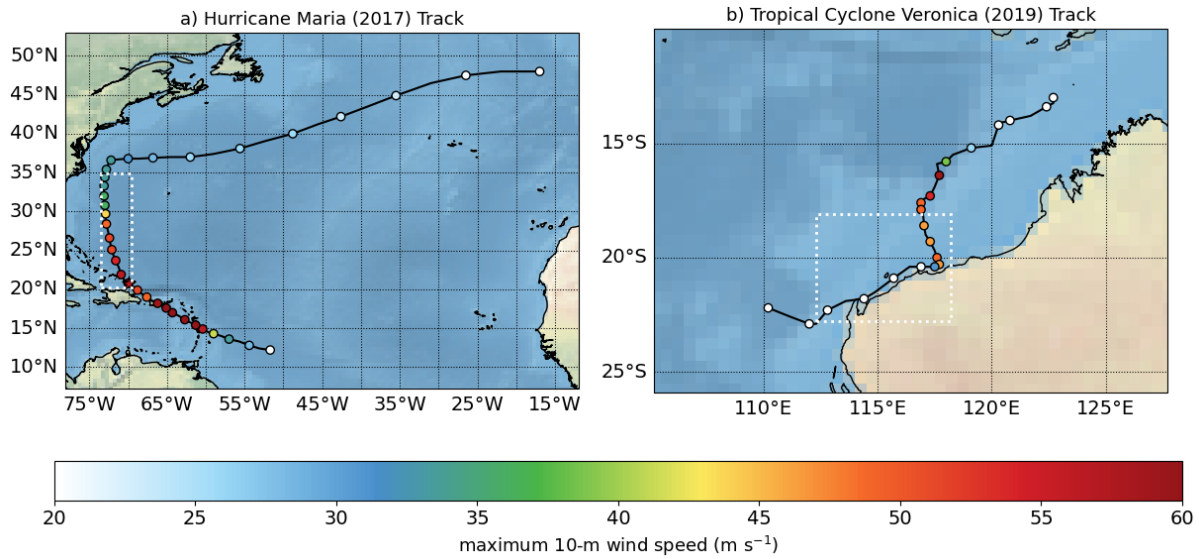


Figure 3.1: The tracks (black line) and 10-m wind speed (coloured dots) of: (a) Hurricane Maria, and (b) Tropical Cyclone Veronica. The white dotted box outlines the approximate study periods for the thesis.

processed.

3.1 Case Studies

Two case studies will be presented in this thesis. These are Hurricane Maria (2017) and Tropical Cyclone Veronica (2019). A short summary of the synoptic history, impacts, and reason that these case studies were selected will now be given. Their respective tracks and intensities are shown in Figure 3.1, with the study periods highlighted by a white dashed box.

Hurricane Maria (2017) was a Category 5 hurricane according to the Saffir-Simpson scale (Saffir and Simpson, 1974; Pasch et al., 2019). Maria was the second Category 5 hurricane impacting the Atlantic basin in 2017 (the first being Hurricane Irma), the tenth most intense hurricane on record in this region (NOAA, 2017). Maria made landfall in Puerto Rico two weeks after Irma. Almost all of the Caribbean’s emergency supplies had already been deployed following Irma and had not been replenished before Maria’s landfall, leading to a death toll of almost 3,000 in Puerto Rico and an estimated cost over USD\$90 billion (NOAA, 2024). In some regions of Puerto Rico, the two-day rainfall accumulation reached over 950 mm (NOAA, 2024).

Maria was selected as a case study for this thesis in 2020. Understanding the tropical cyclone boundary layer and performing in-depth model evaluation is not possible without in-situ observations. NOAA undertook several flight missions into Hurricane Maria, making it one of the

most well-observed recent storms (at the time of selection). The number of successful flight missions increased as Maria approached the mainland United States. Our study period (22 - 27 September 2017) is based on the period which maximises the number of observations and does not contain a landfall, since this would significantly complicate the analysis.

The second case study, Tropical Cyclone Veronica (2019), made landfall in northwest Australia as a Category 4 on the Australian scale (Paterson, 2019), although its maximum intensity was a Category 5. Veronica was less impactful than Maria, partly due to the area having a much lower population density than Puerto Rico, and the substantially lower amount of precipitation (with three-day rainfall accumulation reaching a maximum of 468 mm). Even so, there was widespread flooding which led to an estimated industry loss of AUD\$2 billion (Paterson, 2019; approximately USD\$1.3 billion).

There were several reasons that Veronica was selected as a case study. The homogeneous land surface and relatively flat terrain in northwestern Australia paired with the low translation speeds of Veronica presented a good opportunity to study a real landfall while limiting the variables. For example, complex terrain can modulate tropical cyclone structure such as local gusts (e.g. Ramsay and Leslie, 2008) and storm translation can cause asymmetries in the wind field and distribution of convection (e.g. Shapiro, 1983; Kepert, 2001). There were four consecutive passes of a polar-orbiting satellite that provided good imagery of the storm as it approached land, and a good spread of automatic weather stations to validate the model. These observations will be discussed more in Section 3.5.

3.2 Met Office Unified Model

The Met Office Unified Model (MetUM) is an operational numerical weather prediction model used by numerous meteorological agencies across the world, which operates by solving the equations for a deep fully compressible, non-hydrostatic atmosphere (Wood et al., 2014) in a semi-Lagrangian advective framework. The variables and diagnostic outputs are projected onto staggered grids, according to Charney-Phillips staggering (Charney and Phillips, 1953) in the vertical, and an Arakawa-C grid (Arakawa and Lamb, 1977) in the horizontal.

To provide a realistic initialisation, the MetUM uses a four-dimensional variational data assimilation method described by Rawlins et al. (2007), which is based on the 4DVAR technique

of Courtier et al. (1994). Observational data is assimilated onto a global ‘background’ state, which is taken from the previous 6-hour forecast. The deterministic forecast is initialised from the unperturbed, data-assimilated base state.

Perturbations can then be applied to represent uncertainty and determine a range of possible outcomes. The regional ensemble is nested in the MetUM global ensemble (‘MOGREPS-G’, Bowler et al. 2008) which has 70 vertical levels up to 80 km altitude, and a 20 km horizontal resolution. To generate the perturbations, the global model applies an Ensemble Transform Kalman Filter to the unperturbed single member (Bowler et al., 2008) and each regional ensemble member is initialised from the corresponding global member perturbations.

While the MetUM contains a large collection of schemes to represent different aspects of the atmosphere, the most relevant for this work is the boundary layer scheme (Lock et al., 2000), which will be described in the following subsection.

The Boundary Layer Scheme

There are seven diagnosed boundary layer types in the MetUM, which determine the type and scale of mixing; the full details of the first six boundary layer type classifications can be found in Lock et al. (2000). A seventh type was subsequently added - the unstable boundary layer dominated by wind shear, which can produce deeper kinematic mixing than the thermodynamic profile would imply.

Diagnosing the base and top of the boundary layer is particularly important due to the style of turbulence parametrisation used in the MetUM. When stable, the mixing is determined by the local scheme, which is a first-order mixing length closure dependent on the Richardson number (Ri), according to:

$$K = \lambda^2 S f(Ri) \quad (3.1)$$

where λ is the mixing length, S is the vertical wind shear and $f(Ri)$ is a stability dependence function. In the boundary layer and other unstable layers of the atmosphere, λ is calculated from the depth of the layer.

Non-local mixing in unstable boundary layers is determined by a K -profile closure in which K

is calculated using the magnitude of the turbulent forcing and the depth of the layer.

For this thesis, I perform regional MetUM simulations at convection-permitting resolutions. At such fine-scale resolution, the turbulence parametrisation uses a blending scheme following Boutle et al. (2014a), within a three-dimensional Smagorinsky-like closure. The Smagorinsky scheme also uses Eq. 3.1 but with its mixing length (λ_{max}) given by:

$$\lambda_{max} = C_s \times \Delta x \quad (3.2)$$

where C_s is the Smagorinsky constant (0.2) and Δx is the horizontal resolution of the model.

The blending scheme, given in Boutle et al. (2014a), is scale-dependent and allows for seamless transition between regions of different turbulence-resolving capabilities. In well resolved environments, the blending scheme preferentially weights towards the Smagorinsky mixing, and toward the Lock et al. (2000) scheme in less well resolved regions. Since the only difference between these schemes is the mixing length, a relatively simple weighting function can be defined Boutle et al. (2014a):

$$W_{1D} = 1 - \tanh\left(\beta \left(\frac{z_{turb}}{\Delta x}\right) \max\left[0, \min\left[1, r_f \left(l_0 - \frac{\Delta x}{z_{turb}}\right)\right]\right]\right) \quad (3.3)$$

where β is a scaling parameter, z_{turb} is the turbulence length scale, $r_f = \frac{1}{3.75}$, and $l_0 = 4$.

The weighting function is defined such that when $W_{1D} = 0$ (the turbulence is fully resolved), the Smagorinsky scheme is used, whilst when $W_{1D} = 1$, the Lock et al. (2000) scheme is used. There is some uncertainty in determining the length scale (z_{turb}) outside of turbulent layers.

Model Set-up

The MetUM is used in the regional tropical configuration (RA2-T; Bush et al. 2023) to provide retrospective ensemble forecasts for several tropical cyclone case studies, which will be detailed in Chapter 4 and Chapter 6.

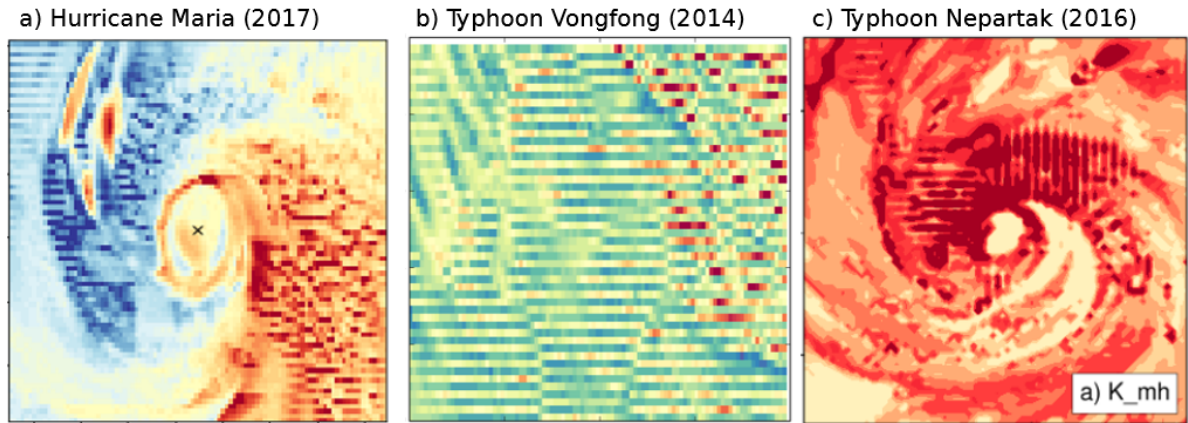


Figure 3.2: Examples of grid-aligned numerical noise discovered in MetUM simulations of tropical cyclones. a) and b) show the shear of the eastward wind component between model levels 13-14 (approximately 740 - 640 m above sea level); the simulations were performed by the current author and John Edwards respectively. c) is the stress tensor + eddy diffusivity, from a simulation run by Sam Hardy.

Table 3.1: Model set-up for different storms. Every row corresponds to an 18-member ensemble with 1-hourly output, aside from the 1.5 km resolution run of Veronica which was performed for a single member with 10-minute output. T_0 denotes the initialisation time (DD/MM/YYYY HH), T_{total} is the total run-time in hours, δx is the horizontal grid spacing.

| Storm name | T_0 | T_{total} | δx | Mixing scheme | Model version | Chapter |
|------------|---------------|-------------|-------------------|-------------------------------------|---------------|------------|
| Maria | 22/09/2017 00 | 120 | 4.4 km | λ_{low} λ_{high} | RA2T | 5 4 & 5 |
| Maria | 23/09/2017 00 | 72 | 4.4 km | λ_{low} λ_{high} | RA2T | 5 5 |
| Veronica | 22/03/2019 00 | 120 | 2.2 km 1.5 km* | λ_{low} | RA2T | 6 |

Model Adjustments

Early on in the Maria study, it became apparent that MetUM simulations sometimes produce grid-aligned numerical noise in the tropical cyclone boundary layer wind fields, demonstrated by several storms in Figure 3.2. This was documented previously internally at the Met Office by John Edwards, using the simulation shown in Figure 3.2b. Noise in the eastward (northward) wind component is exhibited in straight lines in the x-direction (y-direction). Since this noise was most obvious in the boundary layer, the hypothesis was that the winds travel too far within a timestep.

To address this issue, I performed tests of several different model timesteps on a deterministic forecast of Hurricane Maria (2017), detailed in Table 3.1. The results are shown in Figure 3.3 in the shear of the eastward wind component. The larger model timestep of 60 seconds (Figure

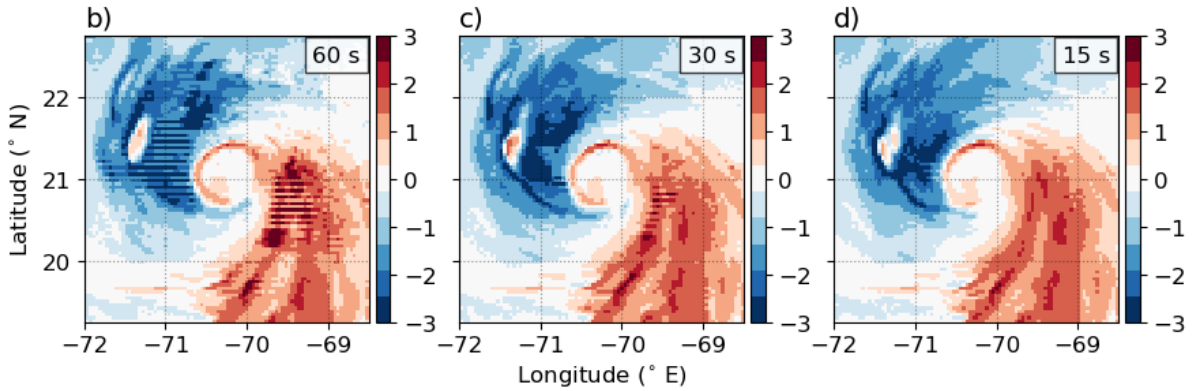


Figure 3.3: Hurricane Maria simulations in the MetUM, showing the shear of the eastward wind component between model levels 13-14 (approximately 740 - 640 m above sea level). Each subplot shows the shear field with a different model timestep.

3.3a) qualitatively displays the most extensive grid-aligned noise. As the timestep is reduced, the noise seems to dissipate. There is still some evidence of noise in the 15-second timestep (Figure 3.3c), but it is vastly reduced.

Unfortunately, reducing the model timestep can have significant consequences on the model efficiency, leading to a drain on compute resources. While this may be acceptable for regional deterministic forecasts, it would be too costly to use a 15 second timestep on all of the ensemble forecasts in Table 3.1.

To address the issue of computational expense, I experimented with an alternate method, whereby I altered the implicit numerical method used to solve the diffusion equation in unstable columns. The solver follows the vertical diffusion scheme of Wood et al. (2007) and is dependent on a prescribed estimate of the non-linearity of the diffusion coefficient. In the stable boundary layer column the implicit measure is set to 2, since the mixing is controlled by the Richardson number and expected to be non-linear. In unstable columns, the non-local scheme (described in Section 3.2) tends to dominate, producing a more linear dependence on the model profile. Thus, by default the implicit solver for the unstable boundary layer column (‘puns’) is set to 0.5. In previous internal work at the Met Office, John Edwards found that increasing this number above 1 - and thereby increasing the non-linearity of the diffusion dependence on the model profile - can smooth out some of the numerical noise found in tropical cyclone wind fields.

Using the 60 second timestep shown in Figure 3.3a, I performed tests of: $puns = 0.5$, $puns = 1.5$, and $puns = 2.0$, and these results are displayed in Figure 3.4. From this analysis, it seems that

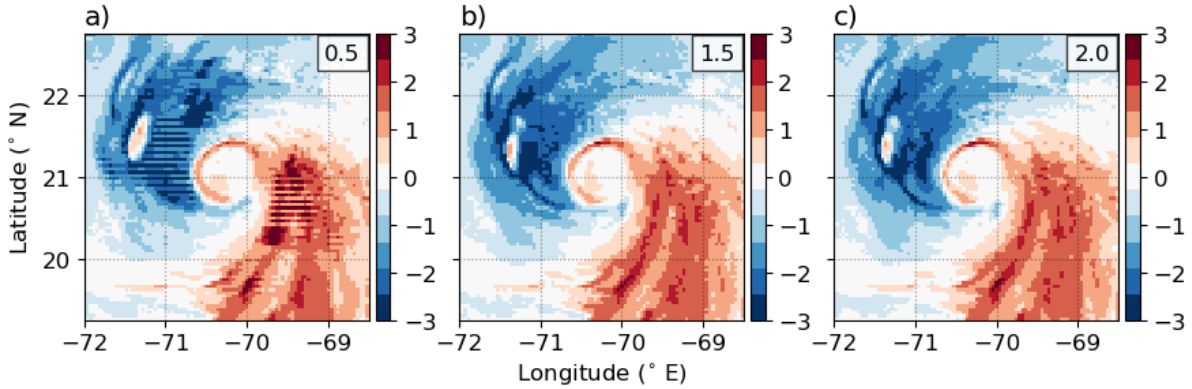


Figure 3.4: Hurricane Maria simulations in the MetUM, showing the shear of the eastward wind component between model levels 13-14 (approximately 740 - 640 m above sea level). Each subplot shows the shear field with a different value for the implicit solver for the unstable boundary layer column, which is denoted in the top right annotation.

increasing the implicit measure can drastically reduce grid-aligned noise in the MetUM. By just increasing the number to 1.5, the noise was (qualitatively) almost completely removed, with little change when increasing to 2.0.

Further analysis of the vertical profiles (not shown) proved an increase to $puns = 1.5$ was more effective at reducing the noise than a reduction to a timestep of 15 seconds, which was a best case scenario in terms of optimising compute resources and simulation quality. Sensitivity tests showed no change in overall storm intensity when these changes were implemented.

The final decision was to complete all simulations in Table 3.1 with an unstable column implicit measure of 1.5, and a model timestep of 60 seconds.

3.3 ERA5 Reanalysis Dataset

All of the following work in this thesis is based on real case studies. While the MetUM can provide high quality, high resolution forecasts, it is unlikely to perfectly capture reality. Although reanalysis datasets tend to be lower resolution, they can provide a more realistic representation of what really happened, due to the intensive post-processing and data assimilation. Reanalyses can serve as a ‘best guess’ of the true environmental conditions at a given point in time and space, and are therefore useful tools to evaluate general model performance, calculate large-scale variables that are unavailable from the observations (such as environmental wind shear), and investigate the synoptic environment beyond the regional MetUM domain.

The current ‘gold-standard’ atmospheric reanalysis is the European Centre for Medium-Range

Weather Forecasts (ECMWF) ERA5 dataset (Hersbach et al., 2020), which spans from 1950 to the current date. ECMWF’s Integrated Forecasting System (IFS) is used for the numerical weather prediction aspect of the reanalysis, with a horizontal resolution of 0.25° and 137 vertical levels from the surface to 0.1 hPa. For the data assimilation, ERA5 also uses a 4D-Var method described in Bonavita et al. (2016), and makes use of a large variety of observational sources. The full details of the observations can be found in Hersbach et al. (2020), but it includes over 200 sources of satellite and other conventional data.

ERA5 appears to perform well for tropical cyclones, on average. A recent study by Slocum et al. (2022) suggests that within 1000-500 hPa, the reanalysis tends to produce errors less than 0.5° for temperature, less than 8.5% for relative humidity; and less than 1.6 m s^{-1} and 0.26 m s^{-1} for the u and v wind components respectively. These values are particularly impressive considering ERA5 does not operate at convection-parametrising resolutions.

3.4 Idealised Models

Full-physics models, such as the MetUM, are useful tools for representing the atmosphere in its full complexity; however, sometimes complexity can be a scientific conundrum. Meteorological research often presents chicken-and-egg situations, where it is difficult to disentangle cause and effect, correlation and causation. Furthermore, there is such a large range of atmospheric variables and processes that it can become difficult to attribute an outcome to any single process.

Simpler, ‘idealised’ models can isolate different atmospheric phenomena to provide a clearer insight into the individual effects. For the case study in Chapter 6, I make use of an idealised model alongside the MetUM to investigate the dynamics of landfall. Here, I use the boundary layer model of KW01: Kepert and Wang (2001), as modified by Kepert (2012). The model of KW01 estimates the low-level vortex structure by taking an input of the gradient wind field at the top of the boundary layer. Unlike ‘slab’ models (e.g. Shapiro, 1983; Smith, 2000) which are vertically averaged, KW01 is a non-linear model which retains the vertical dimension, making it particularly useful for analysing surface effects. Parametrisations of the vertical turbulent mixing are included and are detailed in Kepert and Wang (2001).

KW01 also retains the azimuthal dimension of the cyclone, allowing for a 3-dimensional view of the vortex. It is common for idealised models to work in an axisymmetric (azimuthally averaged)

framework, but KW01 allows the analysis of asymmetric storms, which are more representative of reality. I acknowledge that idealised models such as KW01 are unlikely to produce results as close to observation as the MetUM, which is why they are used in conjunction. In this work, KW01 simply complements the MetUM simulations by reducing the complexity.

3.5 Observational Data

Best Track

Individual meteorological centres around the world produce their own official tropical cyclone tracks. These tracks are maintained and obtained from The International Best Track Archive for Climate Stewardship (Knapp et al., 2010). For the Atlantic basin, I use the National Hurricane Center (NHC) Best Track from the ‘HURDAT’ dataset (Landsea et al., 2008). In Chapter 6, an Australian storm is studied, and in that case the Best Track refers to that which is maintained by the Bureau of Meteorology (Courtney et al., 2021).

All available observational data sources are utilised by these organisations in order to provide the most accurate results, although tropical cyclones are never perfectly observed from the surface. Data coverage is highly variable depending on the track of the storm, orbit of satellites, and flight missions. Despite these limitations, the values published in the Best Track datasets are the best approximations, and are generally accepted by the meteorological community.

The main metrics included in the Best Track are the latitude and longitude of the storm centre; the 10 m maximum sustained wind speeds, the maximum wind gust, and the minimum sea level pressure. In more sophisticated datasets such as the NHC Extended Best Track Dataset (Landsea et al., 2008), metrics such as the radius of maximum wind (RMW), eye diameter, storm direction, and radius of gale-force winds, may also be published.

Ground-level

In general, ground-level observation stations are relatively sparse for tropical cyclones, particularly in storms translating over the open ocean. Even in cases which make landfall, the destructive winds and storm surge can cause instrument failure or measurement anomalies. In all of the cases studied in this thesis, the best ground-based radar observation was in Puerto Rico ahead of the Hurricane Maria landfall on 20th September 2017. In this case, the radar

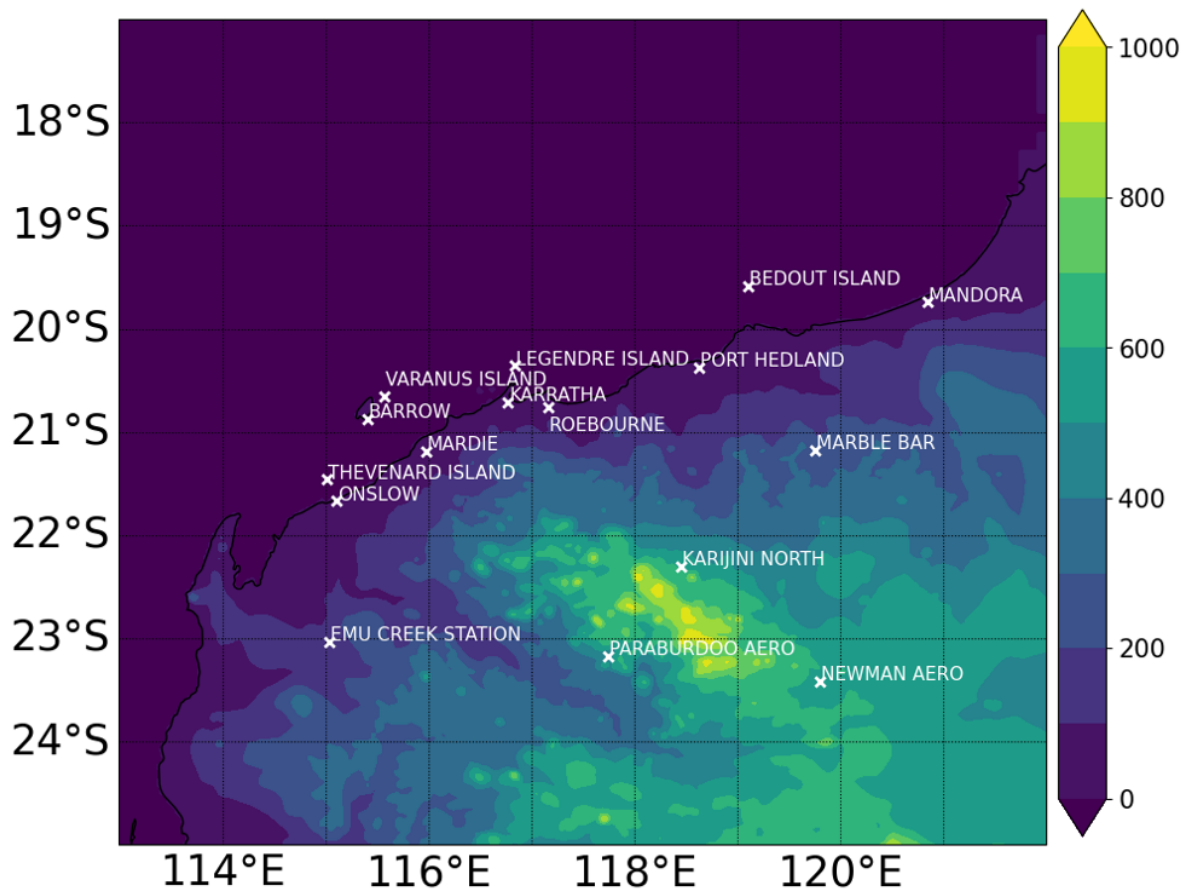


Figure 3.5: The locations of all of the automatic weather stations used for the Tropical Cyclone Veronica (2019) case study. The surface elevation (m) is shown in filled contours.

was destroyed by the storm just before landfall. No ground-based observations were used to evaluate the Atlantic storms in this thesis due to a lack of data.

Chapter 6 investigates a major landfalling tropical cyclone in northwest Australia. Despite the relatively low population in this region, there are several industrial sites, shipping ports and airports which allow for a good coverage of automatic weather station data - the distribution of surface observation sites is shown in Figure 3.5. At these sites, data is available at least every 30 minutes and at 10 minute intervals in some cases. Veronica made landfall between Karratha and Port Hedland, and I retrieved observations for all surface sites within 500 km of Karratha. The main variables analysed from these surface sites were: surface air temperature, dewpoint temperature, surface wind speed, surface wind direction, mean sea level pressure, and precipitation rate.

Flight-level Observations

All flight-level data used in this thesis comes from NOAA reconnaissance flight missions. The data is publicly available from the HRD Hurricane Field Program webpages. There are two main sources of data from flight missions that I will explore and discuss, starting with the dropsondes and moving on to the radar. There are several common flight paths used by NOAA to study tropical cyclones. Perhaps the most valuable for inner core boundary layer studies is the ‘butterfly’ flight path, in which the aircraft makes several passes directly through the centre of the storm at different angles (mimicking butterfly wings). By using this pattern, the radar can observe broad swathes of data from different quadrants of the storm, producing a more cohesive overall picture. Dropsondes collected from different quadrants can also be very valuable to explore the kinematic and thermodynamic asymmetry.

Other frequently used flight patterns include ‘synoptic’, in which the aircraft is flown in circles around the storm, but never directly through the eyewall into the eye; and ‘ferry’, which is a straight line through the storm. The synoptic pattern is also very useful to analyse storm asymmetry and may be more suitable for conditions in which the eyewall makes it dangerous to cross into the eye.

Most of the flights operate at a cruising altitude of approximately 3 km, although some missions take an undulating vertical path. As a result, the dropsondes tend to be released from around 3 km and provide a good profile of the boundary layer structure.

Much of the analysis for Chapters 4 and 5 is based on dropsondes deployed by NOAA on reconnaissance flight missions, which use the Vaisala Dropsonde RD94 (Young et al., 2015). According to Vaisala (2017), the dropsondes can measure to around 5-6 m above the sea surface, and are accurate to 0.2 °C, 2% and 0.4 hPa for temperature, relative humidity and pressure respectively. The dropsondes are fitted with standard GPS receivers to measure wind speed, which are accurate to 0.15 m s⁻¹ for the horizontal wind speed (Vaisala, 2013), although derivation of the vertical wind speed can produce a higher error due to the temporal resolution and variations in fall rate. Each sonde goes through a quality control process (Young et al., 2015) before being archived by NOAA, ensuring that each measurement is a realistic representation of the atmosphere. Further detail on the dropsonde analysis technique can be found in Chapter 4, where it comprises a significant contribution to the chapter.

One of the most useful instruments onboard the aircraft is the Tail Doppler Radar (TDR), which is mounted on both primary aircraft used for these research missions: the Gulfstream IV and WP-3D Turboprop Aircraft (NOAA, 2014). Data from TDR has formed the basis of many tropical cyclone studies (e.g. Rogers et al., 2012; Reasor et al., 2013; Lorsolo et al., 2010; Barron et al., 2022) due to its capability to profile the boundary layer where remote instruments such as satellites are limited by the cloud layer. However, data retrieval is limited by the distribution of precipitation, due to the derivation of the wind components being reliant on the reflection of radio signals from water droplets.

Satellite

Satellite imagery is available for every tropical cyclone in the current technological age; however, satellite data is of limited use to boundary layer studies due to the obstruction caused by the cloud layer. In this work, the main way in which I use satellite images in the visual and infrared wavelengths is to quantitatively assess whether the general size and cloud structure of the cyclone is accurately represented in the model.

Passive microwave imagery can provide more information on the convective organisation of tropical cyclones, but can be limited by the lack of coincidental passage of polar-orbiting satellites. One of the best resources for analysing the convective structure of tropical cyclones via microwave imagery comes from the post-processed products called Morphed Integrated Microwave Imagery at the Cooperative Institute for Meteorological Satellite Studies (MIMIC; Wimmers and Velden, 2007). MIMIC contains two main products, the first is MIMIC-TC which functions in the 85-92 GHz range and performs very similarly to ground-based radar observations; and MIMIC-IR, which imposes a tropical cyclone precipitation field onto an infrared base picture. For this thesis, MIMIC-TC is used most frequently to discern spatial asymmetry and the distribution of convective features. All MIMIC products are freely and publicly available on their official webpage.

3.6 Metric Calculations

Once the data has been obtained, one of the first and most important steps is to track the cyclone, which usually includes finding the storm centre, along with the maximum 10 m wind speed and minimum sea level pressure. There are many different ways to determine the storm

centre of a tropical cyclone, which vary in complexity depending on the nature of the available data.

When given wind data from flight missions, the Hurricane Research Division (HRD) calculate a track of the aircraft-derived wind centres at high temporal resolution (usually 2 minute intervals), using the least squares method described by Willoughby and Chelmow (1982). While it serves as a good estimation of the storm centre, being within 3 km for intense tropical cyclones (Willoughby and Chelmow, 1982), its intended use is for the direct analysis of flight data such as dropsondes. The accuracy of the wind centres is influenced by the frequency of flight missions, which tends to be lower further from the US coast, and does not give information about vertical displacement of the storm centre. However, due to all of the storms in Chapter 4 being well-observed by flight missions, and the temporal resolution being much higher than the Best Track, the HRD wind centre fixes are used for determining storm-relative dropsonde positions in Chapter 4.

For all of the other observation work, the NHC Best Track dataset (Landsea et al., 2008) is used for all of the Atlantic basin storms studied hereafter (Chapters 4 and 5). For the Australian storm, studied in Chapter 6, the Best Track refers to that which is maintained by the Bureau of Meteorology (Courtney et al., 2021). As the names imply, these tracks are regarded as the best estimates for the storm centres for their respective regions and are obtained from the The International Best Track Archive for Climate Stewardship (Knapp et al., 2010).

To calculate the track from the model data, several different techniques were evaluated. The Met Office use the 850 hPa relative vorticity and the MSLP (Heming, 2017). First, the search is initialised with an observed track position, and then at each 6-hour interval, the algorithm finds the maximum 850 hPa relative vorticity within a pre-determined radius (usually 3°), and then finds the MSLP within the same radius from the maximum vorticity location. This tracking method, described by Heming (2017), is made more robust by a ‘closed isobar check’, which checks eight points around the MSLP to ensure that it is the local minimum, before continuing to the next forecast time.

While the Met Office method performs well enough to verify the coarser global model and to provide some insight into the performance of the ensemble, our analysis showed that the algorithm performed less well for data of higher temporal resolution (≤ 1 hour) and higher horizontal grid resolution (≤ 2.2 km). The noisy result from this method could potentially be

attributed to finer scale features such as local pressure minima within the eye itself. While slight imperfections in the centre-finding algorithm can be usable for operational forecasts and verification, it is important to find the best possible centre for scientific studies which evaluate the boundary layer structure. Throughout this thesis, storms will be analysed in a cylindrical, Lagrangian coordinate system (r, ϕ) . Calculations of components such as the radial and tangential wind speed can be highly sensitive to the TC centre. Furthermore, it is important to get the meridional and zonal storm translation vectors correct, so that storm translation can be removed from the Lagrangian wind components.

A successful technique adopted in this thesis, which forms the primary centre-finding algorithm for Chapters 4 and 5, is the iterative pressure centroid method, described by Nguyen et al. (2014). Known for its robustness in producing a consistent, smooth track that is relatively unaffected by shear and tilt (Nguyen et al., 2014), the pressure centroid method has been adopted as the preferential storm-tracking technique for high resolution tropical cyclone forecasts across the field (e.g. Hlywiak and Nolan, 2019; Zhang and Rogers, 2019; Ashcroft et al., 2021; Nolan et al., 2021). As in the previous method, the NOAA Best Track from the International Best Track Archive for Climate Stewardship (IBTrACS; Knapp et al. 2010) dataset is used for the ‘first guess’ centre location to initialise the pressure centroid algorithm.

The pressure centroid method (Nguyen et al., 2014) works well for storms with well defined, circular eyewalls and closed isobars, which functions well for all of the Atlantic storms studied in this thesis at the relevant study periods. However, Chapter 6 introduces a more complex case study, which requires further fine-tuning of the tracking algorithm.

We first tried to track the more complex storm, which will be described in Chapter 6 but generally consists of a broken eyewall with elevated surface winds and a pressure minimum lining up with a rainband, using the TRACK algorithm presented by Hodges et al. (2017). Similar to the Met Office method (Heming, 2017), TRACK uses the vorticity field at 6-hourly intervals. Rather than using the 850 hPa level, TRACK vertically averages between the 850, 700, and 600 hPa relative vorticity to reduce noise. There are several further steps, which are described in full detail in Hodges (1994), Hodges (1995), and Hodges (1999) and Hodges et al. (2017). Again, I found this method largely unsuccessful for accuracy and precision on data of 10-minute intervals, and with a small storm of such distorted organisation. I thank Kevin Hodges for his assistance on implementing this tracking algorithm. It is likely that the

highly atypical vorticity structure, which will be described in Chapter 6, rendered this method unsuitable. There was also a distinct displacement of the pressure and wind field at some times during the simulation, which complicated the tracking even further.

Going back to basics, the most effective way to find the wind centre (which is most appropriate for the kinematic studies), was to locate the minimum sea level pressure and simply find the minimum 10 m wind speed within a prescribed radius. Gaussian smoothing of the wind speed field helped to eliminate local minima. This simple method was used for the analysis of Tropical Cyclone Veronica (Chapter 6). All other storms (in Chapters 4 and 5) were tracked using the pressure centroid method of (Nguyen et al., 2014).

To estimate the extent of the storm tilt, the same tracking algorithm is applied to the storm at 1 km, 3 km, 7 km and 10 km altitude. The tilt is then the distance between the low pressure centre or wind centre at both height levels (1-10 km or 3-7 km). This method is similar to those detailed in idealised (Riemer et al., 2010) and full-physics (Ahern et al., 2021) studies of sheared tropical cyclones.

The model vertical wind shear is calculated as the vector difference between the winds at 850 and 200 hPa. Many previous studies (Ahern et al., 2021; Riemer et al., 2010; Tang and Emanuel, 2012a) use this metric, acknowledging that it does not represent the complete vertical structure but is a good general approximation of the environmental deep layer shear. The radius over which to calculate the shear is more context dependent and subjective. For consistency with previous studies (Ahern et al., 2021; Dai et al., 2021; Slocum et al., 2022), along with the widely used Statistical Hurricane Intensity Prediction Scheme (SHIPS; DeMaria and Kaplan 1994) I use an environmental wind shear, calculated between 200 - 800 km from the storm centre and a local shear calculated within a 200 km annulus. Recent idealised simulations (Dai et al., 2021) have shown that the impact of altering the definition of environmental shear is small, but SHIPS tends to use the 200 - 800 km radius to limit the impact of an imperfect centre estimate (Slocum et al., 2022).

3.7 Summary

Throughout this chapter, I have described several different datasets and analysis methods that will be used throughout the thesis. The MetUM and observations play a key role throughout

each results chapter, allowing for a comprehensive investigation into storm dynamics while verifying that the model is a realistic representation of the environment. Although full-physics models and observational sources of data lay the foundation for this work, reanalysis datasets are needed to provide information on the larger-scale environment that cannot always be represented by observational methods, particularly in-situ observations. also make use of an idealised boundary layer model to disentangle the complex dynamics of tropical cyclones, which is not possible in full-physics models. In summary, the framework for this thesis is built on full-physics model simulations and observations, but is complemented by reanalyses and idealised models.

Chapter 4

Using Airborne Observations for the Evaluation of Tropical Cyclone Asymmetry

4.1 Introduction

Tropical cyclone forecasts are often evaluated based on their performance at the surface level, using the tropical cyclone track, minimum sea level pressure (MSLP) and maximum wind speed, but there is a wealth of in-situ observations in the Atlantic basin which are rarely used in ensemble evaluations due to their relative complexity. For instance, it can be challenging to condense three-dimensional (3D) observational data into concise and meaningful analyses for ensemble evaluation without generating a large volume of overwhelming data for analysis and interpretation. In-situ observations add another layer of complexity due to their irregular spacing and temporal sampling patterns, requiring extra consideration when applied to model simulations. Furthermore, simulated storms may be of different sizes and locations to the observed storm, so it is important to make sure the data is adjusted appropriately to ensure similar storm regions are being compared. How much value can really be added from analysing the 3D structure obtained from airborne observations, and is it worth the extra effort?

The track and surface wind speed are considered amongst the most relevant metrics for operational applications, as the high wind speeds in the inner core can have devastating impacts on

infrastructure, and it is the surface wind speeds that are used to categorise storm intensity (e.g. Saffir and Simpson, 1974). It is well established from in-situ observations Kepert, 2006; Zhang et al., 2013; Young et al., 2015 that tropical cyclone wind speeds peak above the surface but within the kinematic boundary layer, often accompanied by a strong near-surface vertical wind shear. While the surface wind speed is important, the stronger wind speeds within the lower boundary layer have the potential to be destructive, especially in built-up urban landscapes. The boundary layer winds are also relevant for the maintenance of the secondary circulation, which can modulate storm intensity via the inflow of dry environmental air.

Forecasts require the quantification of precipitation probability and storm surge risk, which are major contributors to displacement and infrastructure damage, when the storm is approaching landfall. However, moisture is rarely considered in tropical cyclone forecast evaluations prior to landfall, likely because it is difficult to quantify the total moisture within a storm system from standard observational techniques.

Track and surface intensity are arguably the most important diagnostics for determining risks to communities, and are extensively used for model evaluation (e.g. Goldenberg et al., 2015; Alaka Jr et al., 2017; Cangialosi, 2022); however, such evaluations fail to address the asymmetric performance of forecasts, despite the well-established view that asymmetry directly impacts storm intensity (e.g. Tang and Emanuel, 2012a; Tao et al., 2017; Ahern et al., 2021; Wadler et al., 2023).

While model evaluations are common in research and operations, and asymmetric and vertical boundary layer structures have been studied in models (e.g. Reasor et al., 2013; Fischer et al., 2022; Shimada et al., 2024) and observations (e.g. Corbosiero and Molinari, 2002; Corbosiero et al., 2006; Zhang et al., 2013) independently, they are rarely used in tandem to produce in-depth analyses of model performance. For example, the National Hurricane Centre (NHC) does not consider asymmetry when verifying forecasts for the previous season (Cangialosi, 2022). In NOAA's real-time product viewer (available at <https://storm.aoml.noaa.gov/research/>), models are evaluated against the radar data using single plan-view plots and cross-sections, but provide no detailed analysis of the asymmetry or altitude biases.

In this study, I aim to demonstrate the value of integrating in-situ observations into ensemble evaluation more holistically to represent asymmetry and altitude biases, considering temporal change. This toolkit will fill a gap, where previous studies and current operational practices are

limited in their model evaluations.

We aim to answer two main questions:

- How can in-flight tropical cyclone observations be used to evaluate tropical cyclone intensity and structure within the lower troposphere?
- To what extent can an evaluation of the surface metrics be used to infer the quality of the ensemble within the boundary layer?

4.2 Methods

4.2.1 MetUM Simulations

To demonstrate the ensemble evaluation techniques, simulations using the Met Office Unified Model (MetUM) will be used. The full specifications of the MetUM are described in Chapter 3. For this study, I use 120 hour retrospective forecast simulations for Hurricane Maria (2017), spanning from 22 September 2017 00 UTC to 27 September 2017 000 UTC. The output frequency is every hour and the horizontal resolution of the regional grid is 0.04° (approximately 4.4 km). There are 551 total latitude points, between $16.02 - 37.98^\circ$, and 380 longitude points ($280.02 - 295.18^\circ$). This grid provides a border of more than 4° from the observed track position at all times, allowing for the simulated storms to deviate and remain generally unaffected by the edge effects of the grid.

4.2.2 Dropsonde Analysis Technique

A large proportion of the observations of the vertical structure of the boundary layer come from dropsondes deployed by National Oceanic and Atmospheric Administration (NOAA) on reconnaissance flight missions. Measurement uncertainties are described in Section 3.5. While individual sondes may have slightly higher errors, particularly if they are released in high wind environments, composites tend to produce robust results (e.g. Zhang et al., 2011; Zhang et al., 2013; Ren et al., 2019).

To analyse the dropsondes alongside the model, a storm-relative coordinate system is required due to the difference in track between the observations and model simulations. An estimate of the dropsonde storm centre is taken from the Hurricane Research Division (HRD) wind centre fixes, which has a temporal resolution of 2 minutes and is derived from flight missions following

the methodology described in Willoughby and Chelmon (1982). The wind centre at the closest time to the dropsonde deployment is used to convert the position from a Eulerian to a Lagrangian coordinate system, centred on the storm.

To account for differences between the observed and simulated storm sizes, a normalised radius (r/RMW , where RMW is the radius of maximum winds) is used. The RMW is estimated from the National Hurricane Center (NHC) Extended Best Track (Landsea et al., 2008), which is output every 6 hours and interpolated to the relevant dropsonde deployment time. Multiple data sources are used by the National Hurricane Center (NHC) to estimate the RMW in the Atlantic basin, but Stepped Frequency Microwave Radiometers (SFMR) mounted on reconnaissance flight missions contribute a large amount of surface data (Klotz and Nolan, 2019). Since the SFMR data relies heavily on the frequency and duration of the flight missions, and because the SFMR measures surface wind speeds directly below the flight path, the areal coverage of the data is limited. There has also been some investigation into the quality of the data derived from SFMR (Klotz and Uhlhorn, 2014), which suggested a high wind speed bias within regions of high precipitation. Despite these limitations, SFMR is still the richest data source for estimations of surface wind speeds in tropical cyclones over the open ocean. When calculating the RMW from flight mission and satellite data, the error is estimated to be approximately ± 8 km for storms exceeding Category 3 on the Saffir-Simpson scale, and ± 14.5 km for hurricanes of lower intensity.

For each dropsonde, the closest model gridpoint is located based on the bearing (relative to north) and r/RMW . An average of the neighbouring gridpoints is calculated to allow for some discrepancy in the position-finding method and drift of the dropsonde during its descent. The tangential and radial wind components are then calculated, with the model ‘pseudo-simulated’ sonde directly compared to the relevant dropsonde. Simulated dropsondes are possible, but would require data outputted at a much higher temporal resolution (every 1 minute or less, demonstrated by Stern and Bryan, 2018) and is not feasible for this experiment due to the high volume of data required. Therefore, the next most appropriate solution is an average of the vertical profile of the closest and nine adjacent gridpoints to that of which the sonde’s descent was initiated.

4.2.3 Radar Analysis

Tail Doppler Radar (TDR) is a useful tool for analysing the vertical and horizontal structure of the boundary layer, but it is often under-used in ensemble evaluation due to complexities which will be discussed in Section 4.4.2. More easily accessible metrics such as the maximum 10-m wind speed and minimum sea level pressure tend to be used to evaluate ensemble forecasts, but this omits much of the detail that can be gained from flight missions.

A similar method to the dropsonde analysis is used for the in-flight radar data collected by the NOAA reconnaissance flight missions. Aircraft used by NOAA for tropical cyclone research missions include the Gulfstream IV which is mounted with TDR, and more often the WP-3D Turboprop Aircraft, which contains a TDR, Lower Fuselage Radar, and cloud physics sensors (NOAA, 2014). The TDR is a commonly used aircraft radar for researching tropical cyclones (e.g. Lorsolo et al., 2010; Rogers et al., 2012; Reasor et al., 2013; Cha et al., 2021). Both the radar and model data are projected onto storm-relative Lagrangian co-ordinates, and interpolated to the normalised radius (r/RMW) from 0 to 3 r/RMW , with an interval of 0.05. This means that if the RMW is 100 km, the interval would be 5 km. While this method may not always reflect the resolution of the model and/or radar data, normalising the radius accounts for the difference in storm size between model and observations, which are not always well correlated. Thus, the calculated errors over r/RMW annuli will be more representative of characteristic storm regions (e.g. eye, eyewall, rainbands, outer radii) when compared to using the raw radius. To demonstrate this effect, Figure 4.1 shows an example of the difference between the tangential wind field when represented at the km scale (Figure 4.1a and 4.1b) and when normalised using the r/RMW (4.1c and 4.1d).

In the observations, this storm has a very small eye. The entire eyewall is contained within 25 km of the storm centre in Figure 4.1a, whereas the modelled eye has a maximum diameter of approximately 25 km. If evaluation were to be carried out on these fields, the model may seem to have a negative wind bias due to the modelled eye overlaying the observed eyewall. The normalisation in Figures 4.1c and 4.1d produce much more comparable results. Now it can be seen that the model has a positive wind bias at the RMW (the first solid black line), and the general wind fields are in much closer alignment, although they are still not in full agreement due to differences in the overall storm structure. Figure 4.1 exemplifies the impact of normalising the radius and this justifies the method to be used across the analysis.

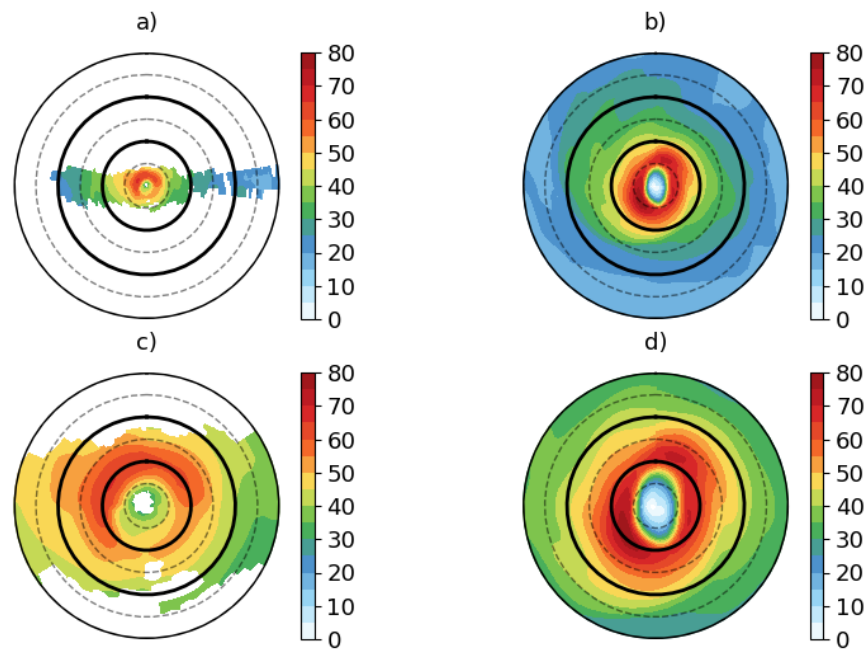


Figure 4.1: An example of how adjusting the radius (km) to the r/RMW affects model evaluation. a) and c) the tangential wind field (m s^{-1}) derived from NOAA TDR (mission 210926H1), and b) and d) the corresponding model tangential wind field from ensemble member 0. For a) and b), which are plotted in absolute radius, the dashed lines denote every 25 km radius and the thick black lines denote 50 km radius. For c) and d), which are plotted in the normalised radius (r/RMW) the dashed lines and the solid black lines denote every 0.5 r/RMW and 1 r/RMW respectively.

To determine the radar RMW, the radar data is used instead of the NHC wind centres described in Section 4.2.2. Where available, the RMW is calculated from the 500-m level, taking the radius of the maximum azimuthally averaged tangential wind. There are several assumptions made for this RMW calculation (and for previous estimations, from the Best Track), which are: that the eye is circular, there is limited vortex tilting, and that the storm centre is well determined. Since the radar data is derived from flight missions which fly directly through the eye, and are post-processed by NOAA to be storm-centred at different levels, it is one of the most accurate methods of determining the location of the storm centre. The post-processing to centre the storm at each height level also accounts for storm tilt.

The coverage of data from the TDR instruments is likely to be asymmetric, particularly in storms which have an asymmetric precipitation distribution, due to the radar being unable to derive wind speeds in the absence of precipitation (Zhang et al., 2018). In storm quadrants with low precipitation, the dropsondes complement the analysis, partially compensating for the asymmetric radar coverage.

4.2.4 Ensemble Skill and Spread

In order to evaluate the ensemble against the observations, evaluation metrics are needed. There are two main metrics in general use for ensemble forecasting: skill and spread. Skill is commonly quantified as the mean absolute error (MAE) or the root mean square error (RMSE). These metrics are calculated by (Chai and Draxler, 2014):

$$MAE = \frac{1}{n} \sum_{i=1}^n |y_i - \hat{y}_i|, \quad (4.1)$$

$$RMSE = \sqrt{\frac{1}{n} \sum_{i=1}^n (y_i - \hat{y}_i)^2}, \quad (4.2)$$

where n is the number of: observations (y) and model predictions (\hat{y}).

Spread can be defined in a various ways, for example the standard deviation of the ensemble or the absolute difference about the ensemble mean. For this work, I use the standard Met Office practices described in Bain et al. (2022) and Flack (2023), which are to use the mean absolute error as a measure of ensemble skill, and the difference between every unique ensemble member pairing as a measure of ensemble spread. Unique ensemble member pairings are demonstrated

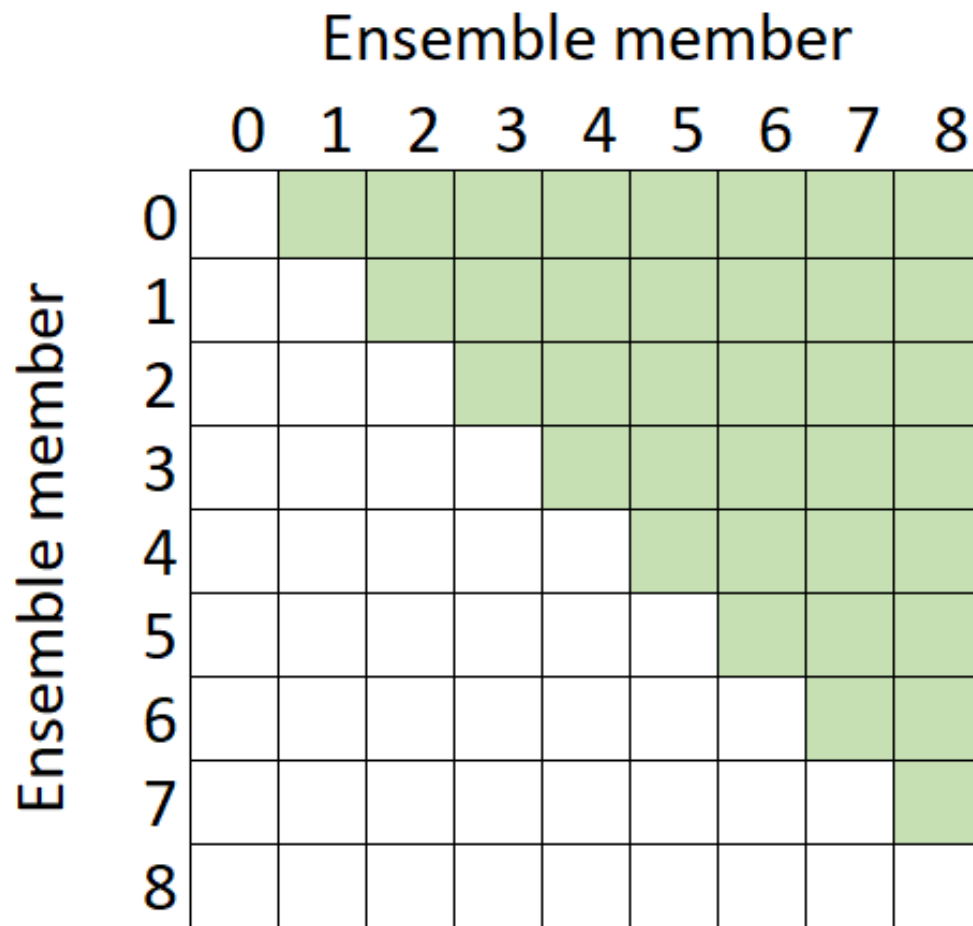


Figure 4.2: An example of unique member pairings (shown in green) used to calculate the ensemble spread following Flack (2023).

the green boxes in Figure 4.2.

When there are multiple data points to evaluate at once, for example through a radar data swathe at a given altitude, the mean of all relevant points is used to evaluate the ensemble. Generally, the evaluation will take place over the ‘inner-core’ of the storm, which I define as being within 0.5 - 1.5 of the normalised radius (r/RMW ; dimensionless). This method assumes that the distance between the storm centre and the RMW can be used to infer a general distribution for the overall storm structure, and implies some level of axisymmetry. While I acknowledge that this is not strictly true for all cases, some level of automation is needed to handle the large amounts of data associated with ensemble simulations. Using a range of 0.5 - 1.5 r/RMW should be able to capture the main characteristics of the acute inner core structure regardless of storm heterogeneity, due to the maximum tangential winds being found within the eyewall. Figures 4.1c and 4.1d further support this inner core range, with the majority of the eyewall structure being contained within 0.5 - 1.5 r/RMW (the two inner-most dashed lines) in both

the observations and model.

4.2.5 Evaluating Asymmetry

The tendency to overlook storm asymmetry when assessing tropical cyclone forecasts is common, particularly when using entire ensembles. In some cases, asymmetry is neglected due to a lack of data - for example, while satellite imagery can imply asymmetries in convection and moisture, it is difficult to quantify the kinematic aspects using remote sensing methods. Ensembles add another level of complexity due to the increased data volume. A standard practice to evaluate storm asymmetry in an ensemble is to produce stamp plots and compare those with satellite imagery. However, is there a better, more quantitative method?

There are some simple, quick metrics that could be calculated to estimate the overall ability of the ensemble in replicating an asymmetrical storm. For example, to calculate asymmetry, one could take the absolute difference between the maximum and minimum value of a diagnostic at a given radius. Other metrics, such as the standard deviation, could provide some measure of variability within an annulus. While these calculations would work on an overall basis (and the skill/spread could be calculated as discussed above), they do not provide any practical information about how the asymmetry is different between the observations and simulations.

In order to maximise the rich spatial wind data obtained from TDR, in which I can infer differences in various relevant fields including boundary layer radial and tangential winds, more experimental methods are needed. Several ideas will now be briefly discussed, before concluding with the methods that were selected to produce the best results.

To quantify the similarity between the azimuthal distributions of a variable, one suggestion is to normalise the model to the observations to ensure the maximum values are the same, and then calculate the distance or area between two azimuthal profiles at a given height and radius. Normalisation could be achieved by adjusting to the maximum winds, for example:

$$v_{norm} = v_{mod} \times \frac{\max(v_{obs})}{\max(v_{mod})}, \quad (4.3)$$

where v_{mod} is the modelled wind speed and v_{obs} is the observed wind speed.

The distance could be estimated by calculating the Fréchet distance (Eiter and Mannila, 1994), which is an approximation of the shortest cord lengths joining the points of each curve. Alterna-

tively, the area between the curves may be calculated as described in Jekel et al. (2019), whereby the data is discretised and then quadrilaterals are constructed between the curves. While these algorithms provide information about the similarity between the observed and modelled curves, giving some indication of how well the overall asymmetry is reproduced, they do not provide any spatial information relevant for operational or scientific use. Furthermore, small displacements in the curve can result in high areal/distance values even if the distributions are overall well represented.

A simpler method is to calculate the correlation between the two datasets, such as in a Pearson correlation (Pearson, 1901). Using the correlation would provide information on how well the asymmetry is represented by proxy, although this method is subject to the same drawbacks as the difference and area algorithms described above - there is no location information and small shifts in the distribution may lead to the asymmetry error being overestimated.

In order to retain the spatial information, two analysis techniques will be presented that can be used with any observational source as long as the data is in a storm-centred coordinate system. The first method is an alteration of the Contoured Frequency by Altitude Diagram (CFAD) which is commonly used in the atmospheric sciences to demonstrate change in a variable with altitude. For this work, I suggest picking a constant height level and replacing the altitude coordinate with azimuth, producing a ‘Contoured Frequency by Azimuth Diagram’ (CFAzD). Essentially, this is a two-dimensional (2D) histogram representing the frequency of a variable’s magnitude at every azimuth. Any variable could be interrogated using this method, with wind speed and reflectivity being of higher relevance for operational forecasters. I suggest that the most appropriate use would be to produce the CFAzD for the observations and for the average points separately, and then compare them qualitatively. Differences in the storm asymmetry should be immediately observable.

While the CFAzD retains spatial information, no temporal information is used. Several CFAzDs can be produced for different stages of the forecast time, but histogram style plots work best with maximal data points, so it may be more appropriate to use all of the available data to get an overall picture of the asymmetry differences.

The second technique is an azimuth-time or altitude-time Hovmöller diagram. Hovmöllers are commonly used to diagnose temporal changes over the radial or azimuthal axis within tropical cyclones, for example in diagnosing and calculating the propagation of vortex Rossby waves

(Wang, 2002; Corbosiero et al., 2006; Otto and Soderholm, 2012). However, they can also be used to track biases (via the mean absolute error) in tropical cyclone structure and the evolution through time. This method can be adjusted based on the interests of the user. For example, presenting errors in a radius-time Hovmöller diagram could give some information about biases in horizontal extent of rainfall, convection, or even wind speed. For the purposes presented here, I choose the azimuth-time Hovmöller to demonstrate systematic biases in the representation of horizontal storm asymmetry, and the altitude-time Hovmöller to uncover variability in model performance in the vertical dimension.

4.3 Results

To demonstrate the analysis methods, Hurricane Maria (2017) will be used as the model case study. Maria was a relatively well-observed storm with several flight missions, equipped with TDR and dropsonde deployments. During the simulation period (between 22 September 2017 00 UTC and 27 September 2017 00 UTC), Hurricane Maria was translating north-northwest and was observed to weaken due to entering a region of moderate southwesterly vertical wind shear (Pasch et al., 2019). According to the official NHC report (Pasch et al., 2019), Maria retained major hurricane status until 24 September 0600 UTC and retained hurricane status until 28 September, although the eyewall began degrading on 25 September. Whilst the purpose of this work is to demonstrate new techniques rather than to perform an in-depth evaluation, it is important to understand the context of the storm.

As previously discussed, many tropical cyclone evaluations tend to focus on the surface metrics provided by the Best Track. These type of results are typically presented similarly to Figure 4.3, showing the mean errors and spread for the track, MSLP and maximum wind speed. For the simulations shown here, the storm intensity was overestimated from approximately T+72 hours, and the track error increased significantly after this point. For the first 72 hours, the track error was relatively low and on average the wind speeds were within 5 m s^{-1} of the Best Track.

Now, I will exemplify the techniques that were earlier discussed to evaluate the structure of the boundary layer more thoroughly, using TDR and dropsondes.

Temporal and spatial coverage of TDR is not perfect, so in Figure 4.4 (which shows the ensemble

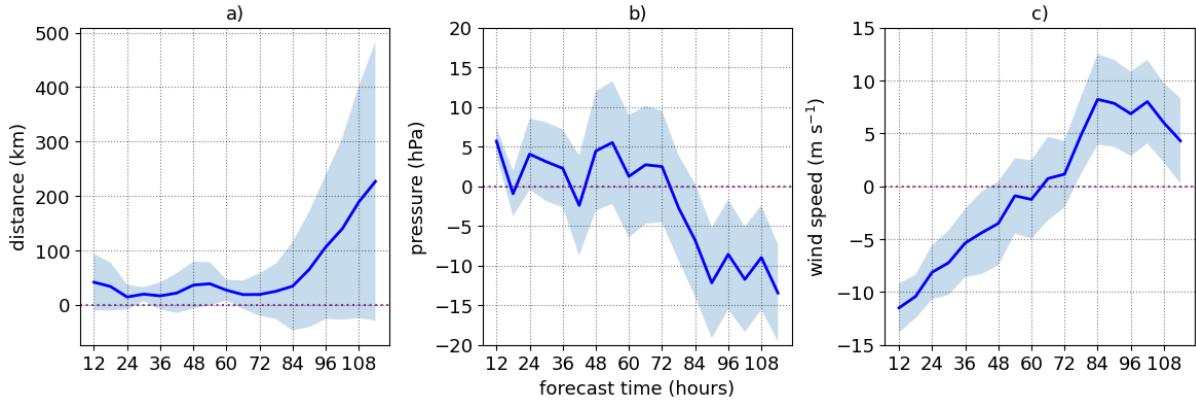


Figure 4.3: Ensemble mean errors (solid line) and spread (filled) for a MetUM simulation of Hurricane Maria, using the NHC Best Track as the control. For a) track, b) minimum sea level pressure, c) maximum 10 m wind speed. Initialised at 22 September 2017 00 UTC.

mean errors), breaks are made in the time axis to account for periods of no data. By presenting the radar data as a Hovmöller diagrams of ensemble mean error, it is possible to identify any systematic variation of biases in altitude, as well as providing information on the temporal variation.

At a first look, it seems that there is no temporal variation in the vertical structure of the biases. The expansive positive errors, shown in red in Figure 4.4, indicate a consistent over-intensification in the model. An overestimation in the tangential wind (Figure 4.4a) is expected, given the mean over-intensification of the storm shown by the Best Track metrics. There is also a general over-estimation of the radar reflectivity in the model in the storm (shown in Figure 4.4d), which suggests there is too much moisture in the inner core.

Displaying the data in this way also allows for the immediate identification of systematic errors. For example, Figure 4.4b seems to suggest a low-level negative radial wind error and a positive error at higher altitudes, although this is not consistent across all sampled times. A positive value implies that the model simulations are more positive than the observation.

To investigate the kinematic boundary layer structure in more detail, vertical profiles can be produced from a dropsonde analysis. Figure 4.5 exemplifies this type of analysis for Hurricane Maria. The methodology used to produce this figure was explained in Section 4.2.2 - the dropsonde coordinates are transformed into storm-centred coordinates using a normalised radius (r/RMW), and then the profile of the closest model grid-point is used.

The profiles shown here are for the inner core of Maria over the entire study period. Corrob-

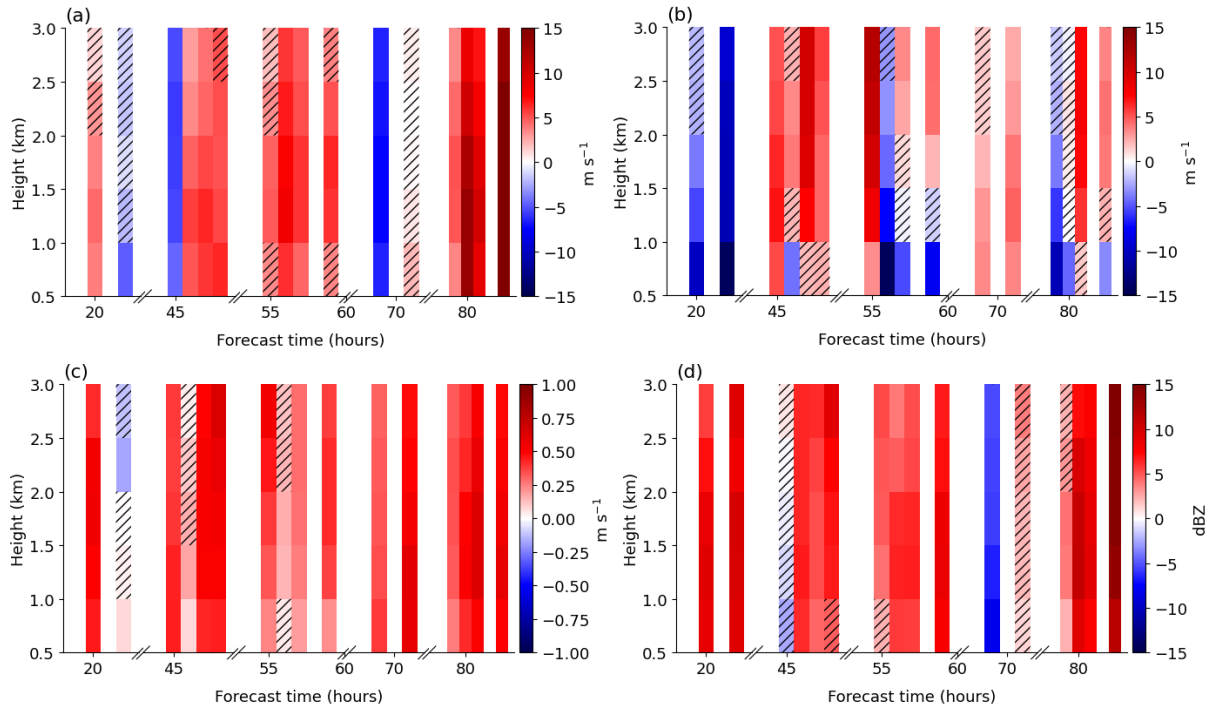


Figure 4.4: Hovmöller time-height diagram of ensemble mean errors (ensemble mean - radar) for Hurricane Maria (2017) within the inner core (0.5 - 1.5 r/RMW). a) Tangential wind (m s^{-1}), b) radial wind (m s^{-1}), c) vertical wind (m s^{-1}), and d) radar reflectivity. Hatching denotes regions where the ensemble spread captures the observed values. Gaps are evident where the data is sparse.

orating the radar analysis, the vertical profiles show an over-intensification in the tangential wind component across all of the storm quadrants. In the western quadrants (Figures 4.5a and 4.5c), the modelled spread overlaps with the observed spread; however, for the eastern quadrants (Figures 4.5b and 4.5d) this is untrue. Similarly, the radial wind profiles seem to match well in the eastern quadrants, with a slight but consistent overestimation of the inflow speed in the lowest 1 km in the ensemble in the western quadrants. The biggest error is in the southeast quadrant (Figure 4.5d), where the modelled radial wind remains negative until the top of the profile but the dropsonde suggests a deep outflow.

By splitting the dropsonde analysis up into quadrants, we begin the evaluation of storm asymmetry. Figures 4.6a and 4.6b summarise the azimuthal distribution of the radial wind at 1.5 km. The results from Figure 4.5 are supported here. For example, in the southeast quadrant, the radial winds are generally negative in the model and positive in the radar. Since both independent sources of observational data agree with each other, this gives us a high confidence that the model is misrepresenting this aspect of the storm on average.

Considering the temporal variation, Figure 4.6c complements the dropsonde analysis in repre-

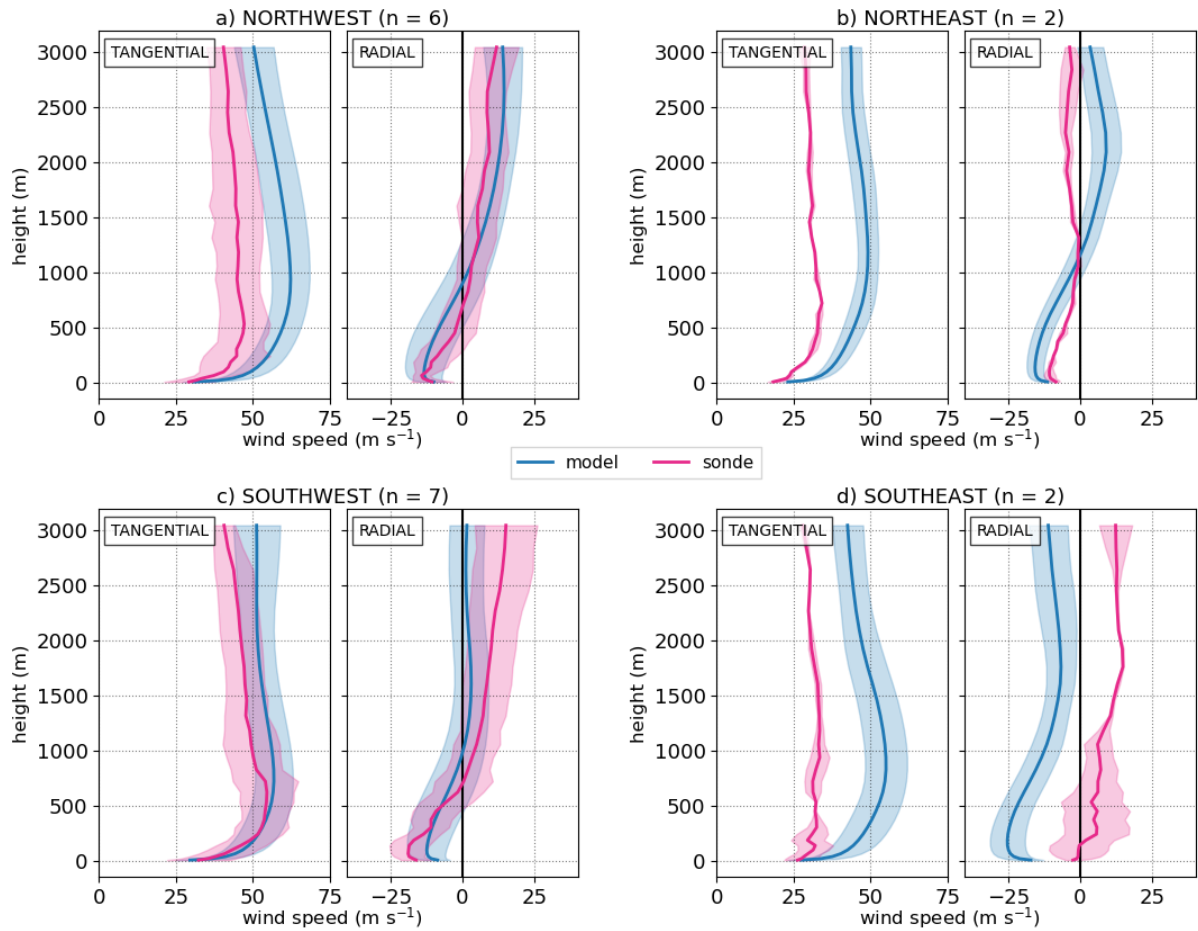


Figure 4.5: Inner core vertical profiles for the mean tangential and radial wind speed (m s^{-1}), for the ensemble (blue) and dropsondes (red) across the study period. The transparent fill denotes the spread. n is the number of dropsondes used. The quadrants are represented as follows: a) northwest, b) northeast, c) southwest, d) southeast.

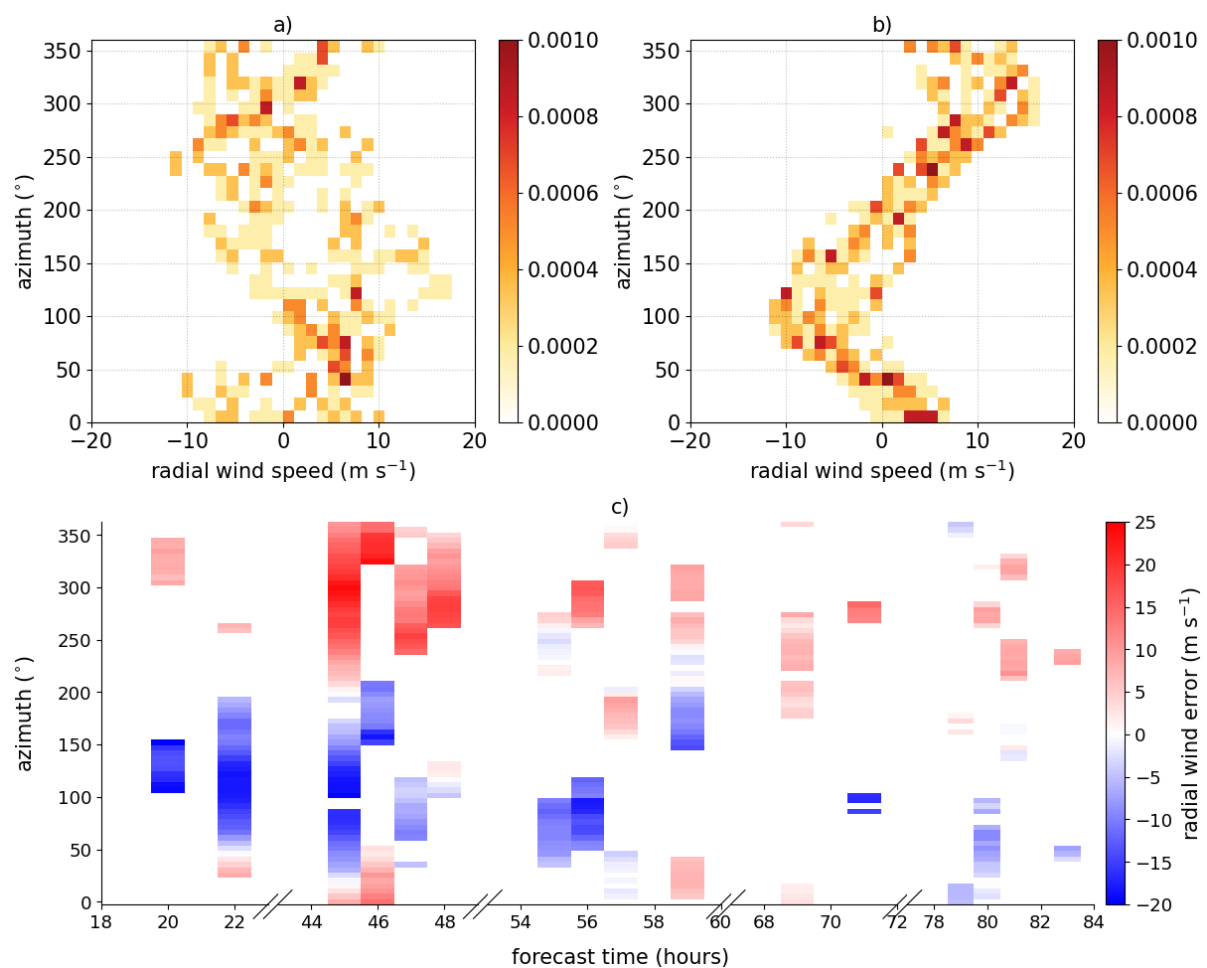


Figure 4.6: (a,b) Contoured Frequency by Azimuth Diagrams (CFAzDs) for the radial wind at the RMW and 1.5 km altitude in Hurricane Maria across the entire study period. (a) airborne tail Doppler radar, and (b) 18-member ensemble mean. (c) Azimuth-time Hovmöller plot of the corresponding radial wind errors (ensemble mean - observations). The same data points are used to produce the top and bottom row of plots.

senting the radial wind asymmetry. However, it also indicates that this error persists throughout the entire forecast period.

When more in-depth horizontal analyses are needed, plan views such as those demonstrated in Figure 4.1 can be used, either using a single radar swathe or by producing a composite of swathes from a single flight mission. This method is simple and may be a first-thought approach to a model evaluation using TDR. However, it is difficult to extract the value of an ensemble using this method, unless either a) a stamp plot is produced, and then there can be an overwhelming amount of data to process, particularly if each plot is from a single radar swathe; or b) the ensemble mean is used, and then a lot of information is lost.

Figure 4.7 maintains much of the value of the ensemble while still being easier to interpret than a stamp plot. In this example, a radar composite is used. There are two good radar swathes, one approximately north-south and the second one east-west. Firstly, Figure 4.7a demonstrates the maximum ensemble uncertainty is between $0.5 - 1 r/RMW$ in the south, and $1 - 1.5 r/RMW$ in the north. In these regions, which define the inner core, the standard deviation sometimes exceeds 8 m s^{-1} .

To put the standard deviation into context, Figure 4.7b shows how close the model is to the observations in standard deviation units. From Figure 4.7b, the ensemble performance can be evaluated in the 2-dimensional (2D) plane. There is an apparent change with radius, where on average the best performance lays within $1.5 r/RMW$ of the storm centre and gets worse in the outer radii. In the outer radius of the southeast quadrant, the values in Figure 4.7 are particularly high (over 3 standard deviations) but the standard deviation itself is relatively low. This result suggests that the model is under-spread in this region.

4.3.1 Combining Methods

The previous sections shed light on how radar and dropsonde observations can be used to extensively evaluate the performance of forecasts in the boundary layer. No previous studies have condensed all available flight-level data for a forecast period into a collection of simple analyses which demonstrate systematic biases in asymmetry and their change over time. To further motivate why this is necessary, in this section, I will investigate how consistent the radar and dropsonde results are with the surface metrics, and whether the best track metrics can be reliably used to infer the forecast quality in the boundary layer.

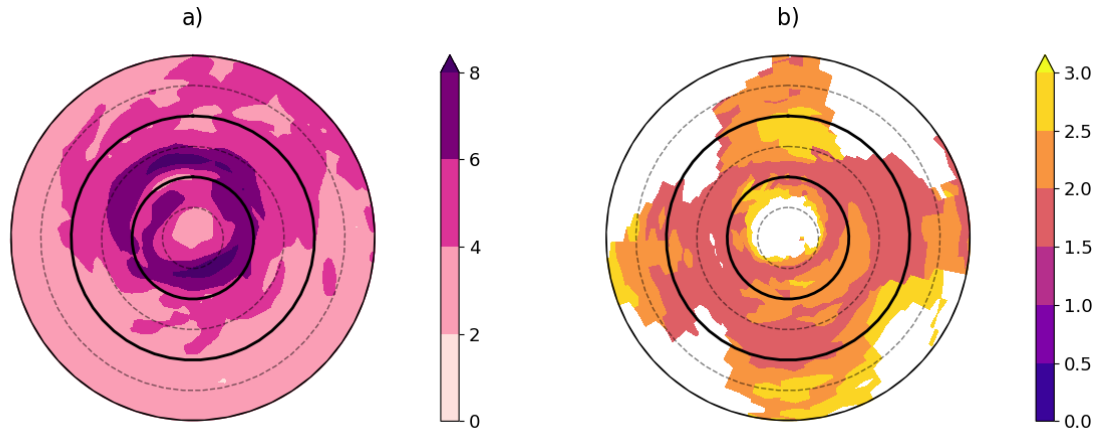


Figure 4.7: a) The standard deviation of the tangential wind speed (m s^{-1}) for the ensemble. b) Number of standard deviations between the ensemble mean tangential wind speed and radar-derived wind speed. Solid black lines denote 1 r/RMW and dotted black lines denote 0.5 r/RMW. Radar swathes were used from 26 September 2017 for demonstration purposes. Gaps in (b) show regions where observational data was not collected.

So far, many of the techniques that have been demonstrated could be applied to deterministic forecasts by using raw values rather than ensemble means. Figure 4.8 draws on the entire ensemble to allow for an evaluation of individual members. The ensemble members were ranked based on the value of their absolute error for each diagnostic, with lower values representing increased forecast skill. The errors were calculated using the methods described in Section 4.2. This ranking technique can be applied to an ensemble of any size, but is demonstrated here for an 18-member ensemble, with member 0 being the unperturbed member.

From a first glance at Figure 4.8, it is clear that there is variability among the ensemble members in terms of forecast skill. It is apparent that the chosen diagnostics are not completely well correlated with each other, as some ensemble members perform well in one diagnostic but poorly in others. It is reassuring that the ‘best’ performing members (which had the lowest overall scores) exhibit some consistency across multiple diagnostics. For example, ensemble member 6 - which was the best performer overall, ranked consistently in the top 50% for every diagnostic except MSLP.

An interesting observation is that v_{10} , which is routinely used as the sole intensity performance indicator, does not seem to be well correlated with the overall rankings. For example, the worst performing ensemble member according to v_{10} was member 16 in this example, which ranked ninth overall.

This discrepancy begins to cast doubt on the quality of v_{10} as a performance indicator for the

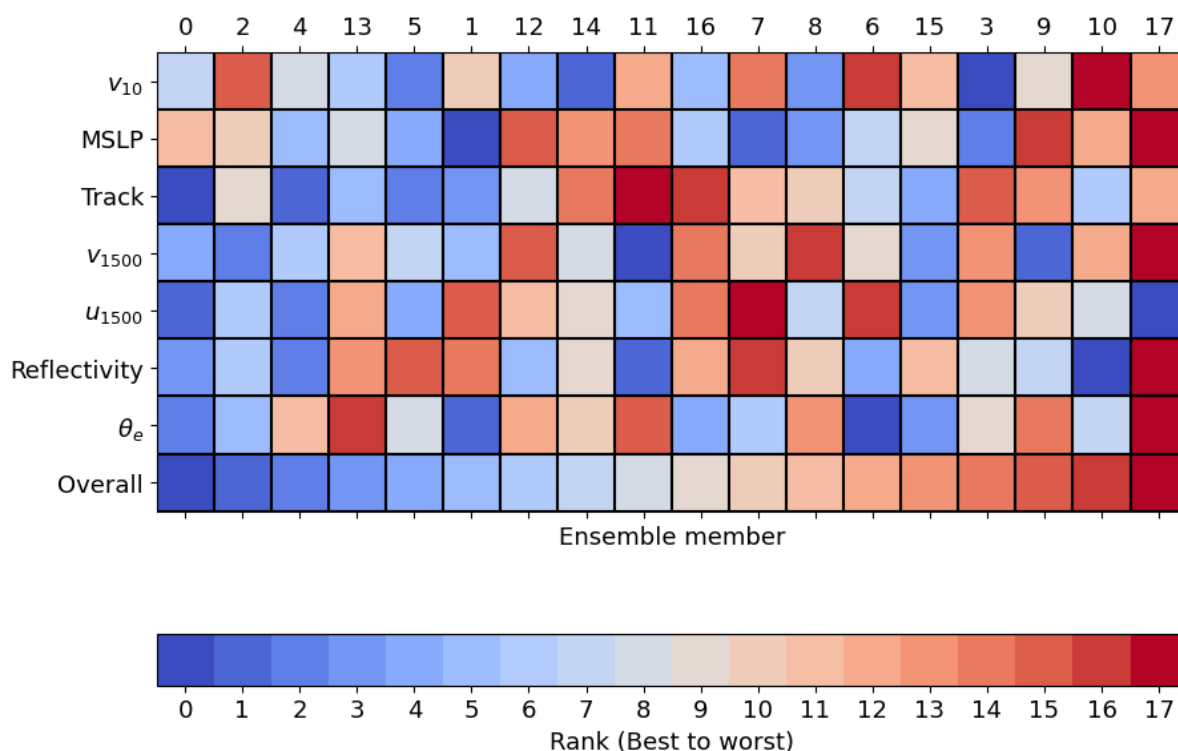


Figure 4.8: An ensemble member ranking system, demonstrated using Hurricane Maria data for T+46. From top to bottom, the ranked diagnostics are: v_{10} - the maximum wind speed at surface level, evaluated against the Best Track; MSLP - minimum sea level pressure, evaluated against the Best Track; the track; v_{1500} - the tangential wind speed at 1500 m, evaluated against radar; u_{1500} - the radial wind speed at 1500 m, evaluated against radar; radar reflectivity at 1500 m, evaluated against radar; and θ_e , evaluated against dropsonde. The boundary layer diagnostics are averaged within the inner core.

overall storm performance. The advantages and limitations of this technique, along with a discussion around the best track metrics, will be explored in more detail in Section 4.4.2.

4.4 Discussion

In the previous section, previously unused analysis techniques were presented to evaluate the vertical and horizontal structure of tropical cyclone boundary layers, as well as temporal variations in the spatial planes. The demonstrated techniques allow for the evaluation of individual ensemble members and their forecast skill, by distilling large quantities of observational and simulation data into easily digestible figures and rankings. Now, we will discuss the advantages and limitations of each analysis technique, which serve to guide future evaluations.

First, The vertical profiles of ensemble mean errors in Figure 4.4 allow for a more detailed look at simulation performance. Demonstrated by the use of surface metrics, tropical cyclone evaluations often neglect the vertical dimension. However, understanding how the performance of the model changes with height is vital, since it provides information which may relate to intensity or size fluctuations.

While Figure 4.4 contains data for the inner core, the annulus can be changes based on the user's needs. For example, the outer radii may be of interest to help to quantify precipitation through the radar reflectivity, or to evaluate the dynamics of the secondary circulation. As another example, while the inner core is the most impactful region, it is the outer radii from which the secondary circulation can entrain dry environmental air in a process known as radial ventilation (Alland et al., 2021b). Since this chapter is a demonstration of new techniques rather than an evaluation in itself, it would be inappropriate to attempt to cover everything, but the example in Figure 4.4 demonstrates how the analysis can be done.

The asymmetry evaluation presented by Figure 4.6 allows for a richer structural analysis which is usually neglected in tropical cyclone forecast evaluations. The CFADs in Figures 4.6a and 4.6b show a clear difference in the radial wind asymmetry between the observation and the model. There seems to be an inverse relationship - in the east there is an outflow in the observations and an inflow in the model. The opposite is true for the northwest. Acknowledging these types of asymmetries can be important for understanding intensity changes. For example, if the radial wind asymmetry is incorrectly represented in the model, the inflow layer could have different

thermodynamic characteristics which would ultimately impact the available potential energy in the inner core (Tang and Emanuel, 2012a), leading to changes in intensity (e.g. Tang and Emanuel, 2012a; Riemer et al., 2010; Alland et al., 2021a).

As was previously mentioned, CFAzDs can be used to represent any diagnostic from any observational source as long as it is in a storm-centred cylindrical coordinate system. Operational forecasters may have more interest in metrics such as total wind speed or reflectivity, which have more obvious impacts. For this example, I use radar data due to the extensive coverage provided by NOAA reconnaissance flight missions.

One issue that can arise is that the coverage of a storm is unlikely to be perfect, unless surveyed by satellite. Because TDR can only retrieve wind data where there are water droplets, the coverage will inevitably be skewed toward precipitating regions of the storm, which may lead to unavoidable biases in the data collection. For example, tropical cyclone rainbands influence the local thermodynamics through evaporation and condensation, but they have also been shown to influence the kinematic diagnostics such as radial and tangential wind (Kepert, 2018). Since CFAzDs are essentially 2D histograms, the frequency contours may also be skewed by these data collection biases. This problem is somewhat accounted for in the technique used here, in which I only use the model data for which there are corresponding data points in the observations. However, this technique does not consider that the distribution of precipitation may be different between the model and observation, which means that regions of limited precipitation may be sampled from the model despite the fact that these areas would not be sampled by TDR.

Ultimately, it is not feasible to adjust the analysis methods to sample like-for-like precipitating regions from the model. The reason for this is that if the precipitation distribution is different, it is likely that the analysis would contain differently angled swathes, which would impact the interpretation of the structural evaluation. The overall structure of the storm is likely to be dominated by azimuthal-mean dynamics, although rainbands can have localised effects (Kepert, 2018). Therefore, these sampling limitations must be considered, particularly if there is a strong rainband with the potential to substantially alter the local environment, but the method presented here remains the most appropriate solution and should still provide a reasonable approximation.

Figure 4.6c shows gaps in data collection, azimuthally and temporally. Now, it is clear to see where the results from the CFAzDs in Figures 4.6a and 4.6b were coming from. The Hovmöller

diagram also gives more information about the temporal variation. In the example shown here, there is not much temporal variation in the errors but for more variable cases such as storms making landfall, the temporal change in asymmetry would be obvious from a plot like this.

Figure 4.7 also addresses gaps in data collection spatially, but lacks the temporal component. When there are so many degrees of freedom, it is important to reduce the information into the relevant components to maximise the value obtained from the simulations. For example, for a broad overview of model performance, the Hovmöller diagram and CFAzDs in Figure 4.6 provide a good summary of the asymmetry. However, studies of the intricate storm dynamics would benefit more from presenting the data in the horizontal plane, such as in Figure 4.7.

Asymmetries can be analysed using the techniques presented in Figure 4.6 but with different quadrant orientations depending on the context. In operational and impact-based evaluations, the standard earth-relative quadrant system is likely the most relevant. However, if a storm is known to be highly influenced by vertical wind shear, or if the wind shear changes significantly in strength or direction throughout the forecast period, then using shear-relative quadrants may be more appropriate for scientific analyses. Similarly, landfall and storm translation can also be used to adjust the quadrants depending on the purposes of the study.

4.4.1 Ensemble Rankings

Next, I will discuss the ensemble ranking methodology and results presented by Figure 4.8. In the previous section, it was acknowledged that overall ranked position according to this analysis technique did not necessarily correlate with the best performing ensemble members when using v_{10} as a performance indicator. An important consideration to make when interpreting Figure 4.8 is that the rankings are relative. They provide a means to compare the forecast skill of different ensemble members within the same dataset, but they do not necessarily indicate the absolute forecast skill of each. What this means is that when a diagnostic is unanimously well predicted across the ensemble, very small differences in the error metrics can result in substantial changes in the ranking. In situations where a datapoint presents as being unrealistic, the user must make use of the other analysis techniques to establish whether there is a large spread in the ensemble. When the ensemble spread is small, it is possible that the ‘anomaly’ is an artefact of the ranking process. Despite this, ensemble members which are consistently better or worse across the boundary layer should still produce a ranking that reflects their relative performance.

For the demonstration in Figure 4.8, the 1.5 km height level was used for the radar diagnostics as it provides information about the middle of the boundary layer, which is not captured by surface metrics. However, the user can choose the height level that is the most appropriate for their research questions. Similarly, the ranking diagnostics were chosen here to represent both the surface metrics, and from the boundary layer: two dynamic features (radial and tangential wind) and two thermodynamic qualities (reflectivity and θ_e). The rankings were equally weighted. By balancing the rankings, this analysis aimed to provide a well-rounded evaluation of overall performance. However, differential weighting can be applied and different variables selected depending on the research question.

4.4.2 Performance Indicators

One of the key questions presented at the start of this paper was regarding the reliability of the surface metrics to predict ensemble performance for the boundary layer. This question started to be addressed in Figure 4.8, in which it was unclear to see a correlation between v_{10} and the overall rank.

To address this question more thoroughly, exploration of the relationship between surface metrics and boundary layer ensemble performance was performed (not shown). A Pearson correlation coefficient uncovered a statistically significant ($P < 0.05$) but weakly positive correlation (0.20) between the overall score and v_{10} , and a weakly positive correlation (0.23) between the overall score and MSLP, when each surface metric was omitted from the overall ranking.

This correlation suggests that while there is a weak relationship between the surface metrics (v_{10} and SLP) and overall performance, they are not reliable predictors of the boundary layer. Reasons for this discrepancy could be explored in more detail, although an in-depth model evaluation is not the aim of the current paper.

A first glance at the correlation coefficients might raise the question around whether the model misrepresents the storm intensity at the surface level. However, the MSLP and v_{10} are also not perfectly correlated in the model, in regards to intensity change. For example, there are cases within the ensemble where the MSLP decreases but v_{10} remains constant or increases slightly. This disagreement between the MSLP and v_{10} can be inferred from Figure 4.8 - in some cases, such as ensemble member 7, the performance for each surface metric can be quite different.

But, just how important is the ensemble performance in the boundary layer relative to the

surface? For operational analyses of risk, such as assessing potential wind damage, perhaps the surface metrics are sufficient - since surface metrics (or estimations of) are more readily available, they may be more practical for operational purposes. Furthermore, the type of post-processing presented here is better suited to ensemble simulations that have enough observational data to evaluate against.

Alternatively, operational forecasters could make use of ensemble evaluation techniques in the boundary layer to explore why a forecast performed more or less well than expected. For example, forecasting the asymmetry of the inflow layer wrongly could result in the radial ventilation of drier environmental air into the storm's core, leading to a reduction in intensity and increased forecasting error. This additional information cannot be provided by the Best Track metrics.

4.5 Concluding Remarks

Throughout this chapter, I have presented novel ways to utilise airborne observations in the evaluation of tropical cyclone forecasts and ensemble simulations. There have been no previous studies condensing the observational data in this way to use for a single case model evaluation. There has been much work on composites of dropsondes (e.g. Zhang et al., 2013; Montgomery et al., 2014; Ren et al., 2019; Ren et al., 2020) and radar composites (e.g. Fischer et al., 2022; Wadler et al., 2023; Fischer et al., 2023); however, to our knowledge there have been no published results using CFAzDs to summarise differences in storm asymmetry, and no tropical cyclone ensemble evaluation work using Hovmöllers to demonstrate systematic inner core biases in altitude over time.

There are several dimensions to consider, such as the horizontal x and y , vertical, temporal, and the ensemble. It is challenging to distil this large amount of data into manageable, digestible pieces of analysis, while maintaining the value added by each dimension. Often, the evaluation of ensemble simulations will come down to single-point measurements compared to the Best Track metrics, represented by the ensemble mean and spread. By evaluating an ensemble (or deterministic forecast) using the surface metrics, the 3D spatial information offered by numerical weather prediction models and airborne observations is deserted.

We have shown that the surface metrics, maximum 10 m wind speed (v_{10}) and MSLP, are not good predictors for overall boundary layer performance for this case study and model set-

up. To make broader conclusions about how well the surface metrics performance can predict boundary layer skill, more work is needed using a composite of case studies and several models or model set-ups. However, this preliminary result suggests that substantial value can be added to forecast evaluation by exploring the boundary layer structure alongside dropsondes and tail Doppler radar.

Techniques that have been presented here include:

- Hovmöller time-height diagrams of ensemble mean errors and spread: allows for the identification of azimuthal-mean biases on the vertical plane and for this bias to be tracked over time.
- Contoured Frequency by Azimuth Diagrams (CFAzDs): provides an overview of how a diagnostic varies azimuthally over the entire forecast period, to allow for a comparison between TDR and model simulations.
- Hovmöller time-azimuth diagrams of ensemble mean errors and spread: complements the CFAzDs by providing quantified errors in each azimuth, enables the tracking of biases in asymmetry over time and provides context for azimuthal data coverage.
- Plan views of ensemble standard deviation, applied to the radar data: provides the user with an overview of ensemble spread and error in the horizontal plane, to enrich the asymmetry evaluation.
- Ensemble rankings: summarises individual ensemble member performance across a range of diagnostics, allowing for selection of members for case study research.

This large range of techniques can lead to a deeper, more comprehensive understanding of ensemble performance in simulating tropical cyclone boundary layers. While this is useful for scientific analyses of tropical cyclone dynamics, it can also be used to identify why forecasts performed less well than expected, and to identify systematic biases in the model for improvement. Furthermore, once the model biases are identified, changes to the model can be tested using these evaluation techniques to ensure that forecast quality is being improved. Overall, this should have a positive impact on the development of tropical cyclone forecasts, and the methods presented here can be applied to any numerical model.

Chapter 5

Impacts of Free Tropospheric Turbulence Parametrisation on a Sheared Tropical Cyclone

5.1 Introduction

In tropical cyclones, turbulent processes play a contributing role in transporting momentum, moisture and heat around the storm (Rotunno et al., 2009). Due to the large horizontal extent of the tropical cyclone, it is often too computationally expensive to run operational forecasting models at a high enough resolution to capture the small-scale turbulence (Rotunno et al., 2009), warranting the need for turbulence parametrisations. For example, ‘turbulence-resolving’ models such as large-eddy simulations typically run at ≤ 100 m horizontal resolution for tropical cyclone studies (e.g. Rotunno et al., 2009; Chen et al., 2021a; Li and Pu, 2021). In fact, recent work by Chen et al., 2021a suggested that to resolve turbulent processes in the tropical cyclone boundary layer, horizontal resolutions as low as 10 m may be the most effective. However, despite recent advances in the in-situ measurement of turbulent fluxes in tropical cyclones (Cione et al., 2020), such observational data is still rare, which means that it is difficult to develop and test turbulence parametrisations for tropical cyclones in operational forecasting models.

Much of the work on turbulence parametrisation (Zhang and Rogers, 2019; Chen et al., 2021b)

has focused on turbulence in the boundary layer, and has established that tropical cyclone intensity forecasts are sensitive to the choice of boundary layer turbulence parametrisation. While many boundary layer parametrisation schemes only consider vertical diffusion, the horizontal diffusion can also play a role in modulating tropical cyclone intensity forecasts (Rotunno and Bryan, 2012). Varying the choice of turbulence parametrisation in the boundary layer has been shown to directly impact the intensity forecasts of tropical cyclones, with lower diffusivity generally producing a more intense storm with a shallower inflow layer (Rotunno and Bryan, 2012; Gopalakrishnan et al., 2013; Zhang and Marks, 2015; Zhang et al., 2017b). It is common for studies of sub-grid scale turbulence to be conducted on an axisymmetric, idealised vortex, which may be further complicated by increased horizontal diffusion to compensate for the omission of resolved radial mixing.

More recently, the impact of such boundary layer parametrisations has been tested on a case study of an asymmetric tropical cyclone experiencing moderate vertical wind shear during a period of intensity change (Zhang and Rogers, 2019). The study demonstrated results whereby smaller vertical diffusivity leads to a stronger storm. Not only did the reduction in diffusivity impact the intensity, it also produced a more resilient vortex which limited the tilt thereby reducing the downdrafts of low-entropy air into the inflow layer (Zhang and Rogers, 2019).

Vertical wind shear is of particular interest due to the import of low-entropy, or low-equivalent potential temperature (θ_e), air from the upper-levels (so-called ‘downdraft ventilation’ - Riemer et al., 2010; Tang and Emanuel, 2012a; Alland et al., 2021a; Ahern et al., 2021) or from the environment (‘radial ventilation’ - Alland et al., 2021b), both of which can contribute to intensity change, typically weakening a storm. Deep layer vertical wind shear (850-200 hPa) can tilt the vortex and can cause the distribution of convection to become more asymmetrical (Corbosiero and Molinari, 2002; Chen et al., 2006; Tang and Emanuel, 2012a). Convective asymmetries caused by vertical wind shear can excite turbulent eddies in the free troposphere through the production of local shear and buoyancy (e.g. Stull, 1988), further encouraging the downward transport of low- θ_e air into the boundary layer.

Although the impact of diffusivity within the boundary layer has been well documented, there is limited research on the relevance of sub-grid turbulence parametrisations within the free troposphere. Operational forecasting models, including that used by the Met Office, use three-dimensional ‘mixing length’ closures to approximate the areal extent of sub-grid scale atmo-

spheric mixing. The mixing length (λ) determines the characteristic scale of turbulence, and the relationship between the parametrised diffusivity and mixing length will be discussed in Section 5.2.3. The Met Office will soon be upgrading their standard tropospheric mixing routine in their operational ‘Unified Model’ (hereafter ‘MetUM’) to include a 3D mixing length reduced by between 1-2 orders of magnitude depending on the operational grid length. Exact details of the current and experimental mixing schemes are detailed in section 5.2.3. Ensuring that the operational MetUM remains robust and effective for forecasting tropical cyclone intensity is one of the main motivations of this work.

The purpose of this study is to evaluate the impact of reduced tropospheric mixing on intensity forecasts of sheared tropical cyclones. I will analyse the decaying phase of Hurricane Maria which was an intense, high-impact tropical cyclone affecting the Atlantic basin in September 2017. The synoptic history of Maria is detailed in Section 5.3.1. Maria experienced a period of moderate deep-layer vertical wind shear of around 12 m s^{-1} on 22 September 2017 according to both the Statistical Hurricane Intensity Prediction Scheme (SHIPS; DeMaria et al. 2005) and the European Centre for Medium Range Weather Forecasting (ECMWF) ERA5 reanalysis (Hersbach et al., 2018), which limited the storm’s intensity and likely contributed to its weakening. The combination of moderate vertical wind shear and storm weakening suggests that Hurricane Maria was likely subject to vortex tilting and subsequent turbulent processes such as downdraft ventilation, making it a suitable case to evaluate the sensitivity to the sub-grid turbulence parametrisation.

We aim to answer two main questions:

- To what extent does tropospheric mixing influence the intensity forecasts of Hurricane Maria (2017) during a period of weakening and moderate to high vertical wind shear?
- How does the choice of sub-grid turbulence parametrisation in the free troposphere contribute to the thermodynamic processes associated with weakening tilted tropical cyclones?

The rest of the paper is organised as follows: Section 5.2.3 will give an overview of the model used and the storm-tracking method applied. Section 5.3.5 will begin by exploring the basic storm metrics such as intensity and track, as well as shear-related conditions such as the vortex tilt and vertical shear magnitude. Allowing for some basic evaluation between the observations

and ensemble means, these metrics will lay the foundations for the following subsections, in which I will systematically compare the azimuthally-averaged and asymmetric structures of two sets of simulations with different turbulent mixing schemes. Analysis of the asymmetric structures will then lead into the more shear-related aspects of the dynamics, such as the ventilation processes and particularly the differences in the entropy. The paper will conclude by summarising the significance of the sub-grid turbulent mixing and providing suggestions for future tropical cyclone forecasting models.

5.2 Data and Methods

5.2.1 Met Office Unified Model

The Met Office Unified Model (MetUM) is described in Section 3.2. For this study, each 18-member ensemble is run at a horizontal resolution of 0.04° (approx 4.4 km), with 70 vertical levels up to 40 km. This horizontal resolution means that there are 380 longitude grid-points (from -80 to -64.82°E) and 550 latitude grid-points (from 16.02 to 37.98°N). By using a domain of this size, we minimise the impacts of the domain boundaries on the storm evolution. The vertical resolution is 10 m near the surface, and it is stretched quadratically with height. The model timestep is 60 seconds.

The regional configuration is convection-permitting and uses a series of parametrisations to represent sub-grid scale processes. In representing microphysical processes, the MetUM contains a warm rain parametrisation based on Khairoutdinov and Kogan, 2000, which was developed based on marine stratocumulus, extended by Boutle et al., 2014b to allow for subgrid variability. For ice microphysics, we use the parametrisation of Field et al., 2007, developed based on mid-latitude and tropical ice clouds.

The ‘boundary layer’ scheme of Lock et al., 2000, is used to calculate the turbulence across the troposphere and is described in Section 3.2. Here, we focus on the stable free troposphere. Boutle et al., 2014a aimed for the blending to relax towards the Smagorinsky scheme above the boundary layer (in the absence of a well-defined length scale). Typically, in our cases this means that the 3D mixing length initially drops down to $\lambda = 40$ m at the boundary layer top and then increases to λ_{max} as an exponential function of the ratio of height to grid size. This operational scheme will be referred to as λ_{high} , reflecting the scale of the mixing that results

from using λ_{max} in the free troposphere.

It seems unphysical that the mid-troposphere should have a much higher mixing length than the lower troposphere. Therefore, for the upcoming experiments, λ in the stable free troposphere is set to the background value of 40 m ubiquitously, removing the reliance on grid size. This experiment will hereafter be referred to as λ_{low} . For each of the schemes (λ_{high} and λ_{low}) an ensemble of simulations was run initialised at 22 Sept 2017 00 UTC (for 120 hours) and at 23 Sept 2017 00 UTC (for 72 hours, to cover the same time period), which will be referred to as the ‘earlier’ and ‘later’ initialisation times respectively. Each pair of experiments (λ_{high} and λ_{low}) is initialised with the same initial conditions from the respective global ensemble member, so the only change is the mixing length. The primary analysis for this work is based on the earlier initialisation time with the full 120-hour simulation; the ensemble initialised 24 hours later serves to validate the results and strengthen the arguments. For the rest of the paper, numerical results and figures will be produced using the earlier (120-hour) simulation, unless specified otherwise. All results presented hereafter have been tested to be robust between both initialisation times.

The tropical cyclone track, tilt and vertical wind shear is calculated as described in Section 3.6.

5.2.2 Distinguishing Ensemble Intensity Divergence Points

In section 5.3.5, I will use the minimum sea level pressure (MSLP) and maximum 10-m tangential wind speed (v) as the basic surface intensity metrics to identify the point at which pairs of simulations begin to ‘diverge’. Although the results presented will not represent intensity bifurcation, there will still be differences in the intensity evolution between the simulations. Since the analysis will focus on understanding why this occurs, it is important to identify an ‘intensity divergence point’ for each pair of ensemble members. A ‘pair’ refers to a member from the λ_{high} simulations and the corresponding member from the λ_{low} ensemble. Dynamic and thermodynamic processes occurring after the intensity divergence point may be a consequence of the changing intensities and subsequent stochasticity, so most of the results presented here will be based on the hours preceding the intensity divergence.

Since the wind-pressure relationship is not linear, I choose to combine the aforementioned common intensity metrics to determine a more robust approximation of the intensity divergence

times:

$$\Delta_i = -(MSLP_{\lambda_{high}} - MSLP_{\lambda_{low}}) \times (v_{\lambda_{high}} - v_{\lambda_{low}}), \quad (5.1)$$

where MSLP is in hPa and v is in m s^{-1} . The intensity divergence time is defined as occurring when $\Delta_i \geq 25$. This value is small enough to capture genuine intensity divergences but large enough to allow for small variability in the intensity.

The ensemble members are then split into three groups based on the value of their maximum intensity divergence. This decomposition will ensure that the signals of more divergent ensemble members do not dominate the potentially weaker signals produced by less divergent members. The groups were determined as ‘least’ ($25 \leq \Delta_i \leq 50$); intermediate ($50 < \Delta_i \leq 100$); and ‘maximum’ ($\Delta_i > 100$). If an ensemble member does not reach the minimum Δ_i of 25 hPa m s^{-1} , it is removed from the analysis. Of 36 ensemble members (between two initialisation times), six did not qualify. The reason for the removal is that the intensity divergence time is a key component of the analysis. Once Δ_i becomes much lower than 25, it becomes difficult to identify a true intensity divergence point due to the inherent variability of the data. It is important to note that all ensemble members across both initialisation times produce the same overall results discussed in section 5.3.1.

5.2.3 Observations

The primary source of observational model verification comes from the metrics provided by the Extended Best Track (part of IBTrACS; Knapp et al. 2010) - primarily the maximum wind speed, MSLP, track (which allows for approximations of the translational speed) and radius of maximum wind (RMW). These metrics can be summarised in Figure 5.1 and will be discussed in more detail in Section 5.3.1. Stepped Frequency Microwave Radiometer data (Uhlhorn et al., 2007), collected in aircraft missions operated by NOAA and the United States Air Force, was independently used to verify the RMW from IBTrACS.

Airborne dual-Doppler radar systems (Reasor et al., 2000), known to measure wind speed with high accuracy (Lorsolo et al., 2013), provide more information about the three-dimensional storm structure of Maria. Figure 5.2f provides an example of the available data. From these flight missions, NOAA (Fischer et al., 2022) have derived estimations of the 2 km RMW, the 2-7 km tilt and an approximate storm centre. These plan views are particularly useful for assessing storm asymmetry and evaluating the approximate size of the system, although it is

important to note that these are composites produced over approximately four hours from an array of flight passes. In some cases, data is missing or not available due to constraints during the mission and from quality control procedures.

Global positioning system (GPS) dropsondes were deployed in most of the NOAA flight missions. The quality controlled data was used to validate the model at the early forecast times prior to intensity divergence. The data provided by the dropsondes is analysed and used for model evaluation in Section 5.3.2. In order to evaluate the model against the dropsondes, I approximate the storm centre from the wind centre fixes calculated from aircraft data (Willoughby and Chelmon, 1982) by the Hurricane Research Division. With a storm centre, it is possible to calculate the radius and azimuth of the sonde. Next, to account for differences in storm size between the model and observations, I normalise by the RMW (r/RMW). For the dropsondes, the RMW is estimated by linear interpolation from the Best Track shown in Figure 5.1. The process is repeated on the model data (using the track described in Section ??) to find the closest relative gridpoint in the cylindrical coordinate system.

5.3 Results and Discussion

5.3.1 Synoptic Overview

In this section, the observed synoptic overview of Hurricane Maria will be described. A detailed model evaluation will follow in Section 5.3.2. The study period for this paper begins at 22 September 2017 00 UTC and ends on 27 September 2017 00 UTC, which catches the most relevant period of storm weakening, taking place after the initial intensification and just after two major landfalls of Hurricane Maria. The purpose of this section is to provide context to the rest of the discussion. Here, I will show that Maria encountered moderate deep layer wind shear, along with a progressively increasing vortex tilt which lined up with an expansion of the inner core and a reduction in storm intensity. By addressing the synoptic history in this way, I motivate the further investigation into the shear-related weakening mechanisms explored in Sections 5.3.4 and 5.3.5.

Throughout the study period, Figure 5.1a shows that Maria moved over the open ocean in a generally north to northwestward direction, becoming approximately northward moving by the 25 September. During this period, Maria was affected by a deep layer of moderate vertical

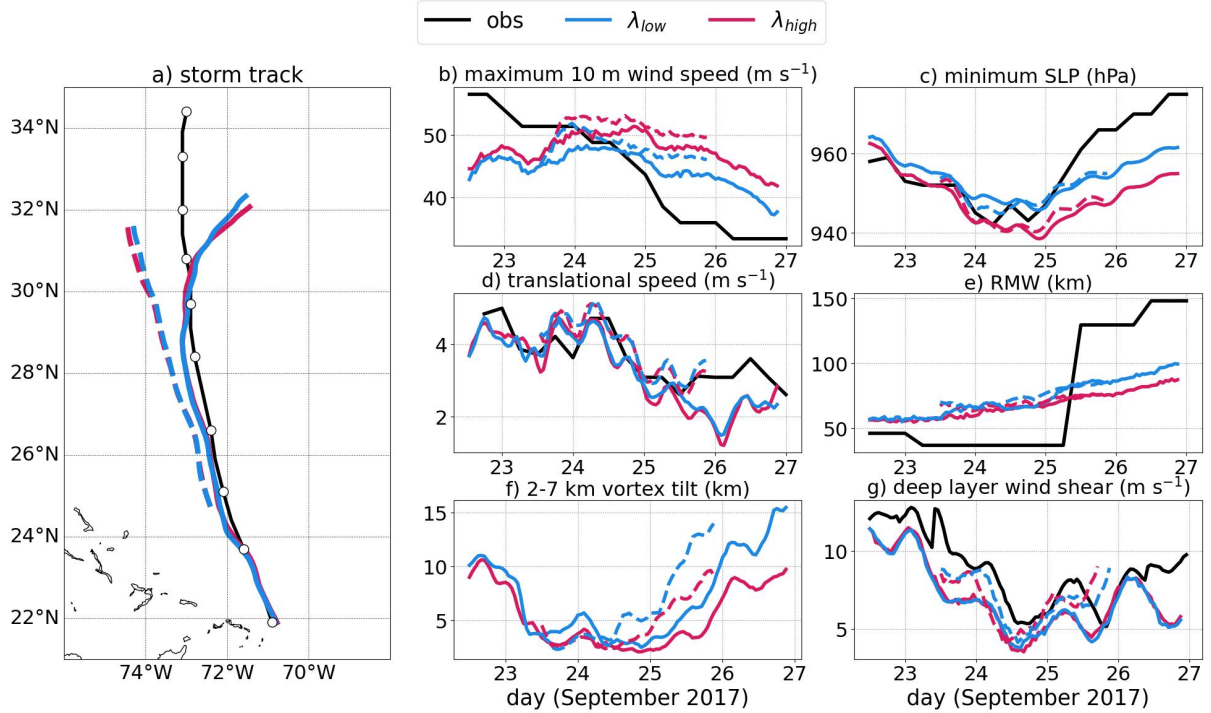


Figure 5.1: Storm metrics of simulations with a high (λ_{high}) and low (λ_{low}) free tropospheric mixing length turbulence parametrisation. Solid lines represent the ensemble means for simulations initialised on 22 September 2017 00 UTC, dashed lines represent the ensemble means for the simulations initialised on 23 September 2017 00 UTC. The black lines denote ‘observations’, which are taken from the NOAA Best Track for a), b), c) and e). The observed translational speed in panel d) is calculated from the latitude and longitude values from the Best Track. The deep layer wind shear in panel g) is calculated from the ERA-5 reanalysis dataset, in a 200-800 km annulus from the storm centre. There is not enough data to calculate a timeseries of observed storm tilt for panel f), but observed point values are discussed in section 5.3.1. Panel a) includes white circle markers every 12 hours from 25 September 2017 00 UTC for the Best Track.

wind shear (Figure 5.1g), which was acknowledged in the National Hurricane Center (NHC) report on Hurricane Maria (Pasch et al., 2019). Moderate vertical wind shear in the context of tropical cyclones is generally defined as being between $4.5\text{--}11\text{ m s}^{-1}$ (Rios-Berrios and Torn, 2017; Nguyen et al., 2019). While there was a sharp decrease in wind shear between the 23 and 24 September, Maria remained in a state of moderate vertical wind shear throughout the study period and experienced a slow increase in shear after 24 September, which likely contributed to tilting the vortex and stunting re-intensification.

Between 22 to 27 September, Maria gradually began to move more slowly and eventually started to weaken, experiencing a steady decline in 10-m maximum wind speed, particularly from the 24 September. While the MSLP remained steady for three days, there was a sharp increase beginning from 25 September. Maria’s MSLP increase coincided with a sizeable inner core

expansion, going from a surface RMW of less than 40 km to over 125 km. The NOAA flight mission 170922H1¹ which ran approximately between 19-23 UTC estimated the 2-7 km tilt to be 13 km, with a RMW at 2 km height of 52.5 km and a maximum wind speed of 46 m s^{-1} . Discrepancies between the tail Doppler radar and Best Track estimates are likely affected by the difference in altitude (surface versus 2 km height) and measurement techniques. It could also be possible that an eyewall replacement cycle took place, which was detected by the airborne radar but not represented by the NHC Best Track at this time. Approximately 24 hours later, another NOAA reconnaissance flight mission (170923H1) demonstrated a distinct drop in the 2-7 km tilt, to 3.9 km.

The NOAA flight missions measured rapid increase in the RMW that occurred on 25 September. Mission 170925H1 operated between approximately 0600 UTC and 1100 UTC and estimated the RMW at 2.5 km height to be 52.5 km. Around 12 hours later, mission 170925H2 estimated the RMW to be 137.50 km.

From the 25 September, observations of tilt from reconnaissance missions were more sporadic, potentially owing to the lack of useful data swathes and a degradation of the eyewall structure. Between approx 1900 UTC and 0000 UTC, NOAA flight mission 170925H2 estimated a center tilt of 27.3 km, which is still lower than the RMW despite being a sharp increase. The apparent rise in the tilt may be attributed to an increase in vertical wind shear, and could be compounded by a loss of resiliency associated with a substantial increase in the RMW. The official NHC report on Hurricane Maria (Pasch et al., 2019) speculated that the wind shear was the primary mechanism preventing Maria from re-intensifying during this period. It is likely that the wind shear also contributed to Maria's weakening, evidenced by the large observed tilt which suggests a lack of vortex resiliency. The extent to which vertical wind shear contributed to the weakening of Maria will be explored further in the next sections. Another environmental factor that may have contributed to Maria's weakening was the progressively cooler sea surface temperatures that were encountered as the storm translated northwards (Figure 5.1a). According to the ERA5 reanalysis (Hersbach et al., 2018), by 24 September 2017 00 UTC, the sea surface temperatures below Maria decreased by 4°C to $\approx 22^\circ\text{C}$ when compared to the start of the simulation (22 September 00 UTC). By 25 September 00 UTC, the storm entered waters of $\approx 20\text{-}21^\circ\text{C}$, where the surface temperatures remained approximately constant until the end of the track shown in

¹The notation of these flight missions is the date (YYMMDD) plus a plane identifier (H; NOAA42 in this case), plus the number of the mission on that day.

Figure 5.1a.

5.3.2 Model Evaluation

On average, the simulations initiated on 22 September at 00 UTC followed the observed track well until approximately T+96, on 25 September 00 UTC, when the storm began to move eastward in the model and slowed to around 2 ms^{-1} translation speed. Conversely, in the simulations initiated on the 23 September at 00 UTC Hurricane Maria continued to move more to the west-northwest throughout the study period, continuously increasing the track error.

Every simulation was initiated with a lower wind speed than observed and began to overestimate wind speed within around 48 hours, and this is supported by the trend shown by the ensemble means in Figure 5.1.

The other intensity metric, MSLP, was more similar to the Best Track at the time of initialisation. On average, the ensemble simulations still missed the storm weakening, leading to a lower central pressure than observed. The simulations initialised on 23 September resulted in both a higher MSLP and higher wind speed when compared to their 22 September counterpart. Table 5.1 summarises the average intensity error in each of the simulations. By T+72, the λ_{low} simulations produced storms with noticeably improved intensities than the λ_{high} tests. It is important to note that the improvement in the intensity forecast was consistent across every ensemble member and both initialisation times.

Table 5.1: Ensemble averages of minimum sea level pressure (MSLP; hPa) and maximum 10 m wind speed (u10; ms^{-1}) forecast error and standard deviation for two tropospheric mixing schemes at T + 72.

| Initialisation time | Run-time | SLP error (λ_{high}) | SLP error (λ_{low}) | u10 error (λ_{high}) | u10 error (λ_{low}) |
|---------------------|-----------|-----------------------------------|----------------------------------|-----------------------------------|----------------------------------|
| 22 Sept. 2017 00 Z | 120 hours | -6.7 ± 7.1 | 0.5 ± 7.2 | 6.6 ± 3.7 | 2.0 ± 4.4 |
| 23 Sept. 2017 00 Z | 72 hours | -16.3 ± 3.8 | -9.3 ± 4.0 | 12.5 ± 2.1 | 9.5 ± 2.8 |

In Section 5.3.1, emphasis was placed on the environment of the storm, particularly the deep layer wind shear, which may have contributed to the weakening of Maria. The ensemble simulations produced a moderate deep layer vertical wind shear (Figure 5.1g) with a trend consistent with the ERA5 reanalysis and with the official NHC report (Pasch et al., 2019) and the magnitude approximately consistent to within $1\text{-}2 \text{ ms}^{-1}$ on average.

We use the 2-7 km tilt metric in this study to provide a direct comparison with the NOAA

flight reconnaissance observations. The modelled tilt shown in Figure 5.1f is generally consistent with the flight observations described in Section 5.3.1. The simulations initialised on the 22 September produced an average vortex tilt of approximately 10 km, comparable to the 13 km measured in-flight. On 23 September, flight missions observed a drop in the vortex tilt to < 5 km, which was captured well on average by all of the ensembles. From 25 September, when the observations became less certain for vortex tilt, all of the ensembles showed a notable increase. However, no ensemble member captured the very large tilt of 27.3 km suggested by the NOAA flight missions on 25 September, but neither did they produce an RMW larger than 130 km. The highest simulated tilt on the 25 September was 10 km, produced by an ensemble member in the λ_{low} test.

Similarly, the observed rapid inner core expansion discussed in Section 5.3.1 was not captured by the ensemble means (Figure 5.1e) but was captured to varying degrees in individual ensemble members. It is likely that the observed storm expansion was linked to the breakdown in the inner core structure consistent with a weakening storm system. The simulations that produced a more similar intensity to the Best Track by the end of the forecast period (λ_{low}) tended to have a slightly higher surface RMW, although it was still much lower than the observed. This may be partly attributable to the differences in storm track in Figure 5.1a, wherein the observed storm moved much further north and encountered cooler waters.

More detailed information on the storm dynamics can be derived from the NOAA reconnaissance flight missions. The tail Doppler radar plan views in Figures 5.2c,e verified that the simulations were producing dynamically consistent storms. For this analysis, I chose to show ensemble member 14 (initialised on 22 September), since this was an ensemble member that exhibited an early intensity divergence that could be attributed with reasonable certainty to changes in the model set-up rather than from a cascade of stochasticity. At the early initialisation times, all ensemble members looked very similar, so this member should be generally representative of the whole group.

Both sets of experiments (Figures 5.2a,b and Figures 5.2c,d) produced similar looking results, with a reasonable sized eye, RMW and eyewall compared to the airborne radar in Figures 5.2c,e. While the distribution of the tangential wind (Figures 5.2a,b,c) is generally consistent, there are some differences in intensity. The λ_{high} simulation (Figure 5.2a) shows the highest wind speeds, which is consistent with the general trend shown in Figure 5.1b. Ideally, the

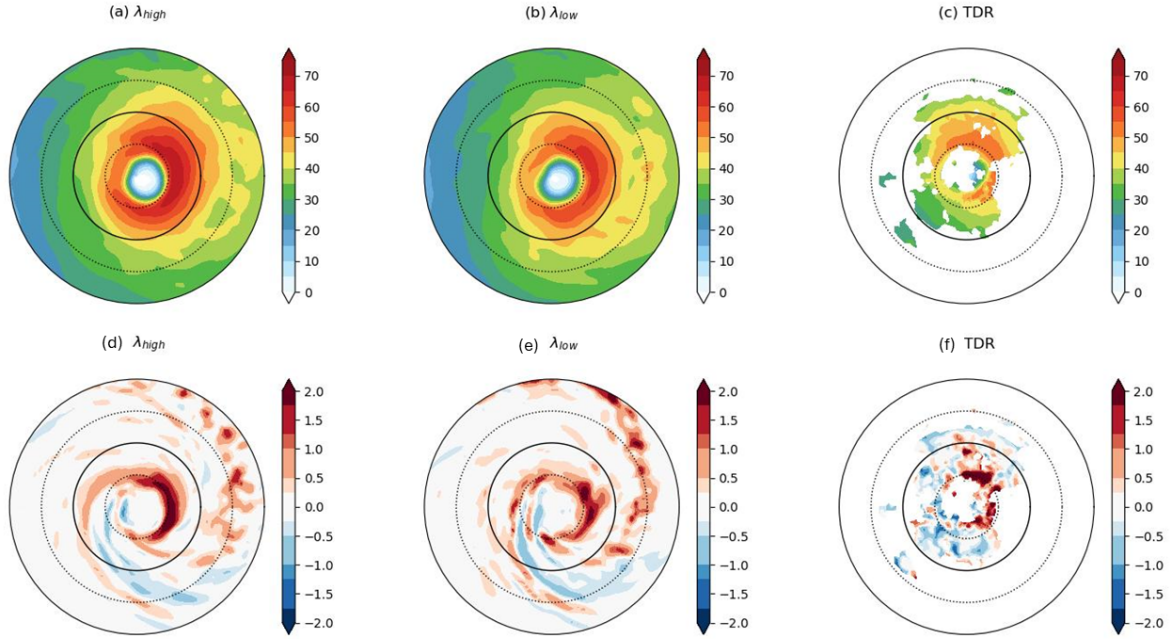


Figure 5.2: A qualitative overview of model performance at T+19 to T+23. (a,b,c) The tangential wind field at 2 km altitude (m s^{-1} ; filled). (d,e,f) The vertical velocity field at 2 km altitude (m s^{-1} ; filled). The dotted circles represent 50 km intervals from the storm centre; the solid circle is 100 km. The complete radius is 200 km. The model data (a,b,d,e) is produced of a mean from 22 September 2017 19:00 UTC and 23:00 UTC. The tail Doppler radar fields (c,f) are produced using the flight missions spanning between the same time period.

simulations would be evaluated against the radar observations at an earlier forecast time to reduce the impacts of the parametrisation differences; however, this analysis is limited based on observation availability.

The radar data can also be used to evaluate the vertical structure of the boundary layer, as described in Chapter 4. Figures 5.3 and 5.4 show the vertical Hovmöller diagrams of the tangential wind and radial wind errors respectively. The simulations generally overestimate the tangential wind across the entire lower troposphere. Figure 5.3b shows that the spread of the λ_{low} simulations better captures the observations than λ_{high} . This finding is confirmed by Figure 5.3c, which shows that the quality of the boundary layer tangential wind forecast across the whole lower troposphere is improved in the λ_{low} simulations, for almost all radar swathes. It is possible that the values around T+70 are of lower observational quality, since these results are inconsistent with the broad trend.

While the radial wind results in Figure 5.4 are more complicated to interpret, from Figure 5.4, it does seem that the quality of the radial wind forecast was also improved in the λ_{low} simulations, but not to the same consistency as the tangential wind.

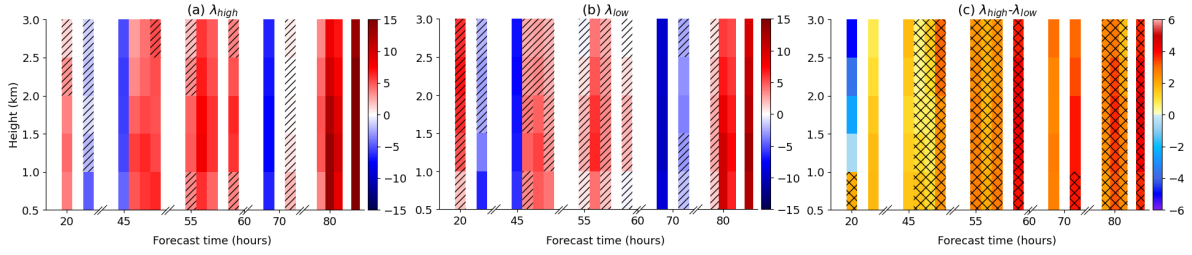


Figure 5.3: Time-height Hovmöller diagrams of the absolute tangential wind errors (ensemble mean - observations). (a) The λ_{high} ensemble mean, regions in which the ensemble spread captures the observations are hatched. (b) The same as (a), but for λ_{low} . (c) $\lambda_{high} - \lambda_{low}$, where the hatching denotes the regions in which λ_{low} has a lower absolute error than λ_{high} .

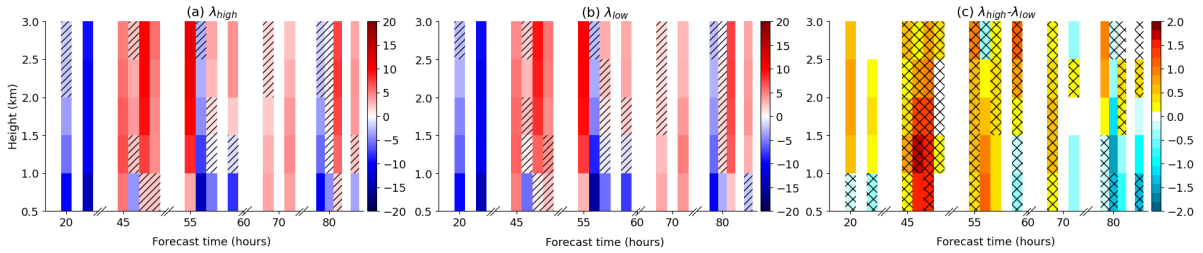


Figure 5.4: Time-height Hovmöller diagrams of the absolute radial wind errors (m s^{-1} ; ensemble mean - observations). (a) The λ_{high} ensemble mean, regions in which the ensemble spread captures the observations are hatched. (b) The same as (a), but for λ_{low} . (c) $\lambda_{high} - \lambda_{low}$, where the hatching denotes the regions in which λ_{low} has a lower absolute error than λ_{high} .

The dropsondes provide insight into the vertical structure of the boundary layer and lower troposphere - the results will be described here and shown in Figure 5.5. For the eyewall region - defined for this analysis as being within 0.75 - 1.25 of the normalised radius (r/RMW), all of the ensembles produced a mean maximum inflow velocity within 5 m s^{-1} of the dropsonde throughout the entirety of the simulation time. In both the model and observations, the inflow tends to reach the maximum magnitude on the order of $20\text{-}25 \text{ m s}^{-1}$ between 100 - 200 m altitude. On average, the depth of the inflow layer (defined as 10% of the maximum inflow) was consistently overestimated in all sets of simulations by approximately 500 m. There was no apparent change in the depth of the inflow layer between the λ_{high} and λ_{low} experiments.

Where available, eyewall dropsondes within the 12-24 hour period after initialisation (to allow 12 hours for model spin-up) provided a mean maximum tangential wind that was comparable to all sets of ensembles, with an average error of $< 4 \text{ m s}^{-1}$, shown in Figure 5.5a. The height of the maximum tangential wind was overestimated in the simulations by a similar degree to the depth of the inflow layer (around 500 m). There were no differences in the height of the maximum tangential wind between the experiments across the entire simulation time (Figures 5.5a,c).

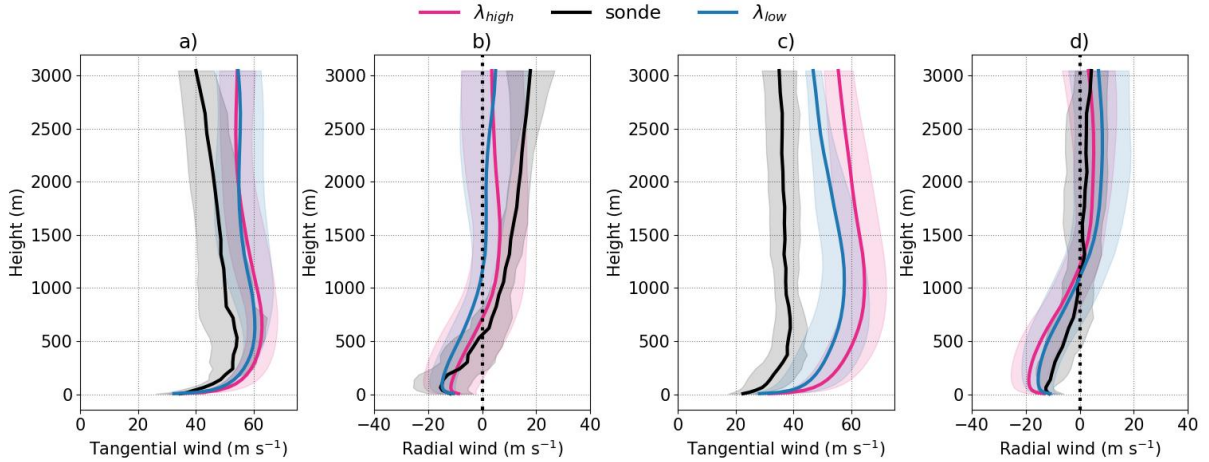


Figure 5.5: Model simulations evaluated against dropsondes, methodology described in-text. (a,b) The tangential and radial wind components respectively (m s^{-1}) between 22 September 2017 1200 UTC and 25 September 2017 00 UTC. For this period, 9 dropsondes were classified as being within the eywall. (c,d) As in (a,b), but between 25 September 2017 00 UTC and 27 September 00 UTC, using 8 dropsondes. The solid line denotes the mean and the transparent fill is the spread.

The dropsonde analysis revealed that all of the experiments over-estimated the depth of the kinematic (wind-based) boundary layer on average. For example, Figure 5.5c, the maximum tangential wind in the dropsondes is around 500 m, whereas in the model it is ≈ 1 km.

By the end of the simulation time, the maximum inflow velocity error remained low; however, the tangential wind error grew (Figures 5.5c,d). The results from the boundary layer structure support the conclusions from the intensity metrics in Figure 5.1b, where the maximum 10 m wind speed error remained higher in the λ_{high} simulations for the entire forecast period. It is useful to analyse intensity metrics from various data sources, since the error is higher in the dropsonde analysis than in the 10 m wind speed for the λ_{high} experiments. Another consideration is that dropsonde soundings are likely to show small-scale features that may not be represented by the model simulations. While averaging over several sondes aims to reduce the signal of this small-scale variability, the ability to represent the general inner core structure is limited by the small sample size.

5.3.3 Asymmetric Storm Structure

Tropical cyclones experiencing moderate-high vertical wind shear tend to exhibit distinctly asymmetrical structures (Corbosiero and Molinari, 2003), often dominated by the azimuthal wavenumber-1 component (Reasor et al., 2000; Riemer et al., 2010; Zhang et al., 2013). In

this section, I will address the convective asymmetries in Hurricane Maria to develop an understanding of how the wind shear is impacting the whole storm system.

Using the vertical velocity as a proxy for convective regions, the model analysis shows convective asymmetry consistent with idealised models (Riemer et al., 2010) and observational studies (Hence and Houze, 2012; Barron et al., 2022), in which generally convective precipitation occurs in the right-of-shear regions and stratiform rainfall occurs left-of-shear (Figure 5.2a,b), although this is not ubiquitous across all storm systems (e.g. Tao et al., 2017). This finding was verified against the tail Doppler radar (Figure 5.2; Fischer et al., 2022), which shows that the observed structure of Maria is consistent with the model simulations at the early forecast times ($T \leq 36$). The vertical velocity fields exhibit an azimuthal wavenumber-1 asymmetry.

The distinctly asymmetric structure can be demonstrated by the depth of the inflow layer in Figure 5.6. During the early forecast times, the storm is travelling toward the northwest while encountering a moderate to strong southwesterly vertical wind shear. Figure 5.6 shows that at the intensity divergence point for a representative ensemble member, the inflow layer is much deeper in the downshear quadrants compared to the relatively shallow upshear quadrants. These results are supported by a detailed dropsonde composite study (Zhang et al., 2013) which suggests that the downshear right quadrant of sheared tropical cyclones tend to have the deepest inflow layers.

Further analysis at the later forecast times suggests that the inflow asymmetry changes as the time progresses. Once the wind shear weakens, the 530-m model level exhibits inflow ubiquitously across all azimuths. Some symmetry is recovered, although the strongest inflow is still situated downshear. Furthermore, the inflow layer depth is decreased at these lead times. This may be a reflection of the general storm weakening. In all cases, changing the mixing length (and thus the diffusivity) within the free troposphere produces no discernible change in the inflow layer depth or strength preceding the intensity divergence points.

Previous work, including full-physics modelling (Zhang and Rogers, 2019) and boundary layer modelling (Kepert, 2012), has investigated the effect of the boundary layer diffusivity on tropical cyclone intensity and structure. In both cases, increased mixing within the boundary layer resulted in a weaker but deeper inflow layer. More specifically, Zhang and Rogers, 2019 investigated the effects of increased boundary layer diffusivity on a sheared tropical cyclone. Along with producing a stronger inflow layer, the storm was also more symmetrical if the boundary

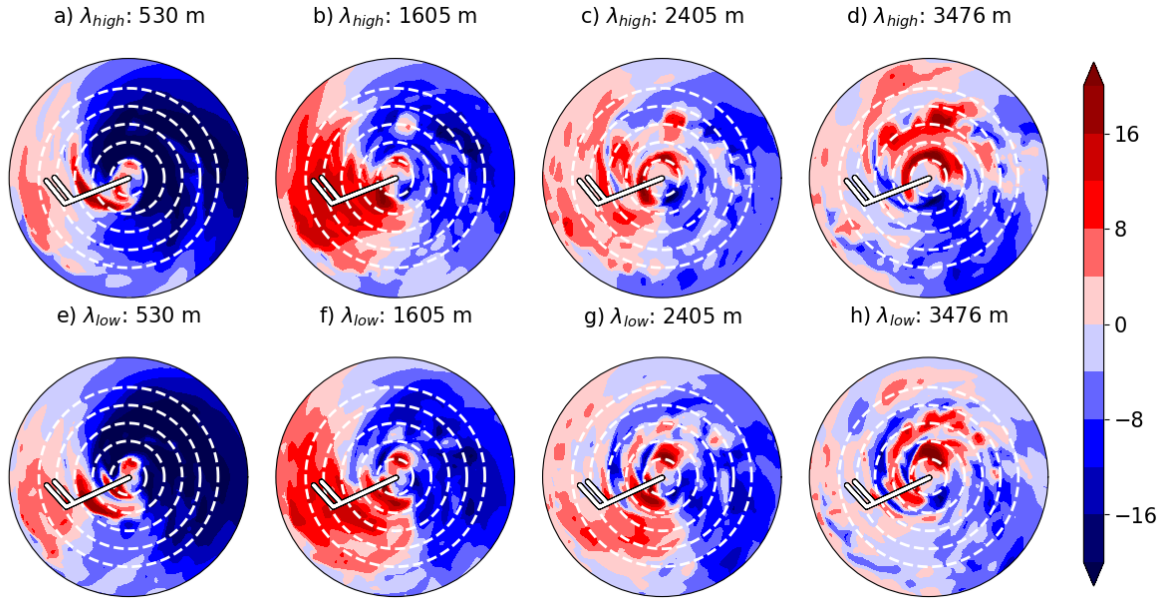


Figure 5.6: Storm-relative radial velocity (m s^{-1}) at different heights at the intensity divergence point (approx T+18) for a representative ensemble member. The high mixing scheme (λ_{high}) is shown in (a)-(d); the low mixing scheme (λ_{low}) in (e)-(h). Dashed contours are at intervals of 25 km radius. The wind barbs represent the deep layer vertical wind shear.

layer diffusivity was reduced.

In tandem with the findings presenting throughout section 5.3.5, the results given in Zhang and Rogers, 2019 show that it is important to consider where the diffusivity is reduced, as changes in the boundary layer versus changes in the troposphere can lead to very different results in terms of storm intensity and resilience to shear. By keeping the boundary layer mixing the same between the λ_{high} and λ_{low} experiments, I have shown that the free-tropospheric mixing can modulate the boundary layer structure.

5.3.4 Vertical Mixing

So far, the data analysis I have presented reveals unexpected results in which more diffusive free-tropospheric environments increase the resilience of tropical cyclones against moderate vertical wind shear, ultimately resulting in a more intense tropical cyclone. Zhang and Rogers, 2019 found that increasing the eddy diffusivity within the boundary layer produced the opposite effect, in which the more diffuse scheme was less resilient to shear and produced a weaker storm. In the case presented by Zhang and Rogers, 2019, the lower boundary layer diffusivity enhanced low-level convergence, increasing the inflow strength and concentrating the convective bursts to

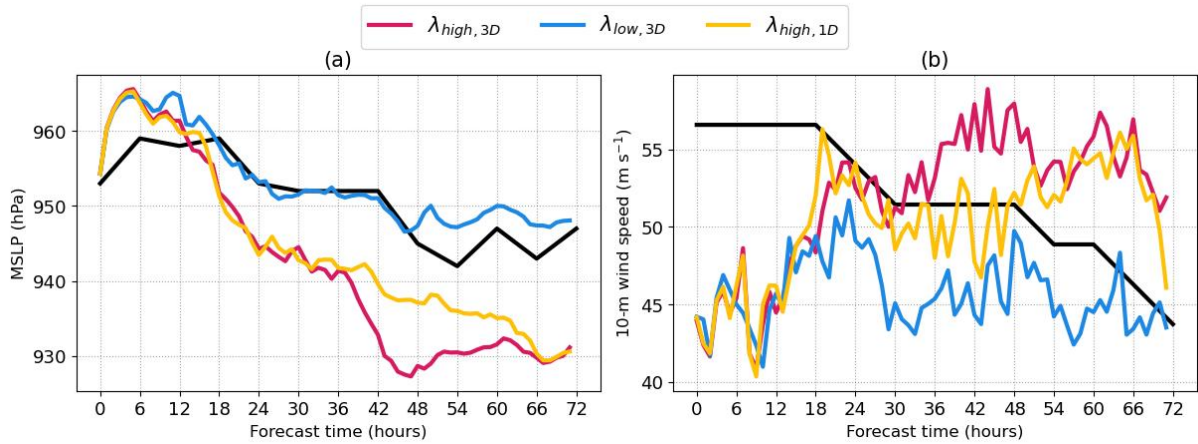


Figure 5.7: (a) Minimum sea level pressure (hPa). (b) Maximum 10-m wind speed (m s^{-1}). The black line is the NHC best track. $\lambda_{high,3D}$ corresponds to a simulation with a high 3-dimensional mixing length. $\lambda_{low,3D}$ is the same, but for a reduced mixing length (described in-text). $\lambda_{high,1D}$ is the same as $\lambda_{high,3D}$ but with no lateral mixing (only vertical).

within the RMW. Additionally, Zhang and Marks, 2015 identified a stronger eyewall updraught in the low diffusivity case, linked to the more pronounced vertical gradients of the diabatic heating rate. Since the experiments I conducted only alter the free tropospheric mixing, the boundary layer convergence is unlikely to be directly impacted, although there may be indirect impacts.

In order to understand these results in the context of the literature, I performed a sensitivity test of ensemble member 14 to evaluate whether it was the vertical or lateral mixing having the biggest impact on the storm intensity. The same model set-up was used as described in Section 5.2.3, except the lateral mixing was switched off for λ_{high} (hereafter $\lambda_{high,1D}$). The results for this experiment are shown in Figure 5.7. For the first 36 hours, $\lambda_{high,1D}$ followed almost the exact same MSLP change as its three-dimensional (3D) counterpart, λ_{high} , and diverged from λ_{low} at precisely the same point, which strongly suggests that the primary control is the vertical mixing. There is a change in intensification rate between 36-48 hours between the three-dimensional and $\lambda_{high,1D}$ simulations, which is likely due to stochasticity. Further simulations would be needed to disentangle these effects. Nonetheless, Figure 5.7 provides strong evidence that the initial divergence is due to changes in vertical mixing.

When considering vertical motions in tropical cyclones, the most significant tends to be the eyewall updraught. The vertical mass flux associated with the eyewall updraught is slightly higher for λ_{high} immediately preceding the intensity divergence point, when compared to the λ_{low} simulations. Although this would typically be more conducive to intensification, it appears

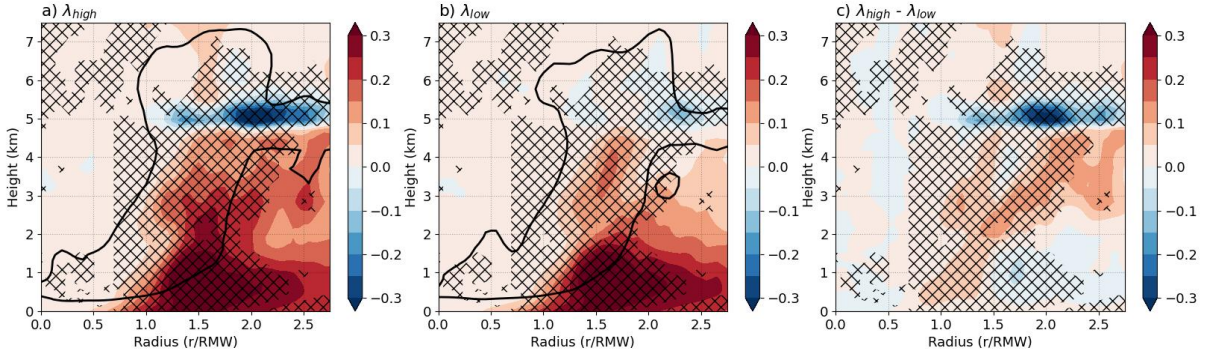


Figure 5.8: Ensemble composite of azimuthally averaged vertical turbulent moisture flux ($\overline{w'q'_t}$) in $\text{g m}^{-2} \text{ s}^{-1}$ in two mixing length (λ) schemes. Negative values (blue) indicate downward transport of moisture. The black solid contour represents the cloud liquid water content at 0.01 g kg^{-1} . The hatching indicates a statistically significant difference in the vertical turbulent moisture flux using the Wilcoxon Rank Sum test, between the experiments. The composite is averaged over the 6 hours prior to intensity divergence. The normalised radius is produced using the surface RMW.

implausible that this change could be a consequence of a more diffusive environment. Due to the scale of the eyewall, much of the vertical transport is handled by resolved processes (w).

To evaluate the role of the diffusive moisture fluxes in more detail, the parametrised vertical turbulent moisture flux is shown in Figure 5.8 and is defined as:

$$\overline{w'q'_t} = -K_m \frac{\delta q_t}{\delta z}, \quad (5.2)$$

where K_m is the diffusivity defined by Eq. 3.1 and q_t is:

$$q_t = q_v + q_l + q_f, \quad (5.3)$$

where q_v is the specific humidity, q_l is the specific liquid water contents, and q_f is the specific frozen water contents.

Analysis of the vertical turbulent moisture flux in Figure 5.8 reveals that the diffusivity remains comparable between the simulations within the boundary layer and low-level environment. Regions where the two simulations are statistically significantly different across a 6 hour time period, according to the Wilcoxon Rank Sum Test (Wilcoxon, 1992), are hatched.

There are two main points to take away from Figure 5.8: the downward flux of moisture is significantly higher in the λ_{high} simulations than in the λ_{low} runs in the main cloud base, and there is also a significantly higher vertical moisture flux in the mid-levels in the λ_{high} runs.

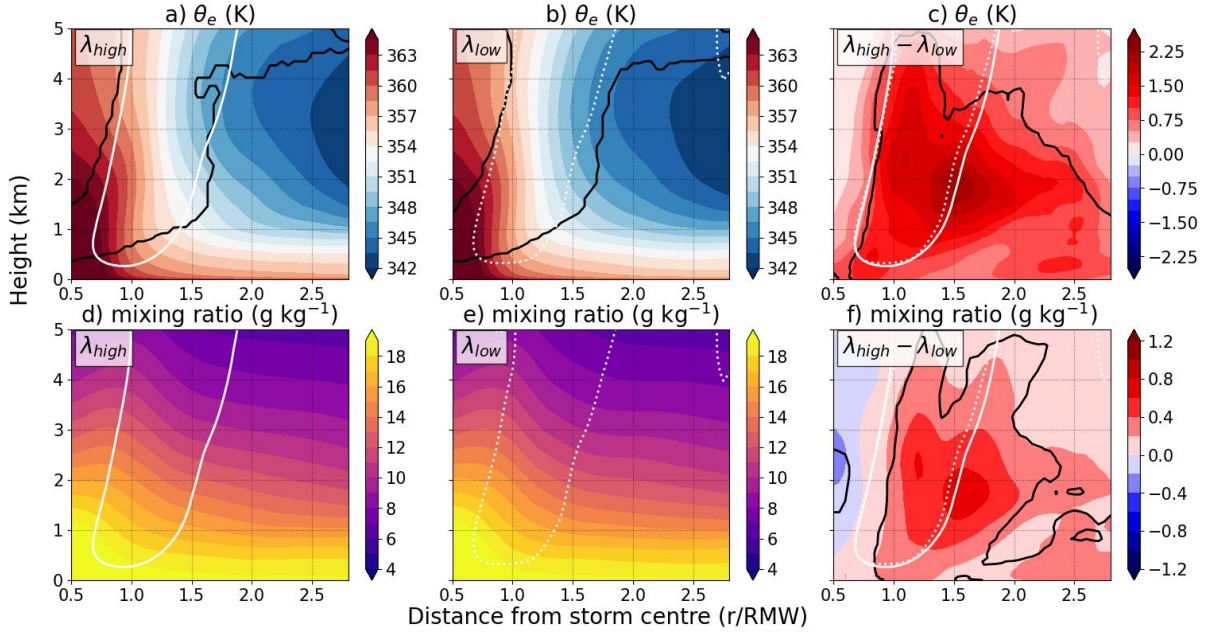


Figure 5.9: Ensemble composites of azimuthally averaged (a-c) θ_e (K) and (d-f) mixing ratio (g kg^{-1}), over a period of 6 hours before intensity divergence. For the θ_e plots in a and b, the black contours indicate a threshold of cloud liquid water cumulative frequency (> 0.001), to provide context into where the cloud layer is. In c and f, the black contours indicate regions of statistically significant difference between the simulations according to a Wilcoxon Rank Sum Test ($p < 0.05$). The unfilled white contours represent vertical velocity $\geq 0.2 \text{ m s}^{-1}$, for λ_{high} (solid) and λ_{low} (dotted). The radius is normalised by the surface RMW.

Overall, this means that the low-entropy mid-levels are receiving more moisture from the cloud layer and the boundary layer in the λ_{high} simulations, which is consistent with the relatively higher θ_e shown in Figure 5.9. For the significantly increased upward flux, the λ_{high} simulations reach up to $0.15 \text{ g m}^{-2} \text{ s}^{-1}$ higher than their λ_{low} counterparts. For the increased downward flux from the cloud base, the λ_{high} runs are up to $0.25 \text{ g m}^{-2} \text{ s}^{-1}$ higher. In the context of a 24-hour period, this can mean a difference of $\approx 13 \text{ kg m}^{-2} \text{ day}^{-1}$ more moisture transported upwards from the lower levels into the mid-levels, and $\approx 22 \text{ kg m}^{-2} \text{ day}^{-1}$ more moisture transported downward from the cloud layer, in the λ_{high} simulations when compared to the λ_{low} ensemble members.

Further supporting the idea of increased moisture transport from the cloud layer, Figure 5.9 shows an ensemble composite of the difference in mixing ratio between λ_{high} and λ_{low} . There is a distinct decrease of moisture in the mid-levels in the λ_{low} members, despite no real change in the inflow characteristics that would indicate either (i) a reduction in the near-surface moisture advection, or (ii) an increase in inflow ventilation (the inward transport of dry air from the environment). Since the peak of the moisture change in Figure 5.9 is along the radially-outward

edge of the eyewall, where the inflow layer turns into updraft, it is possible that the radial wind has some impact on the moisture flux convergence. However, it is difficult to make this conclusion when the inflow characteristics are very similar between the simulations prior to intensity divergence (e.g. Figure 5.6), and the moisture is higher throughout the whole lower-mid troposphere in the λ_{high} simulations.

5.3.5 Downdraft Ventilation

In this section, I will explore the role of downdraft ventilation in the weakening of Hurricane Maria, and analyse how changing the free-tropospheric diffusivity can impact this process. As explained in Section 5.1, downdraft ventilation is a process by which low θ_e (entropy) air can enter the tropical cyclone boundary layer via downdrafts (Riemer et al., 2010; Tang and Emanuel, 2012a; Molinari et al., 2013; Zhang et al., 2017c; Wadler et al., 2018; Alland et al., 2021a). These downdrafts are asymmetrically distributed around the tropical cyclone and can be induced by vortex tilting as a result of environmental wind shear (Riemer et al., 2010).

It is likely that Hurricane Maria was experiencing downdraft ventilation due to the following evidence: Figure 5.1g shows that the storm was under the influence of moderate deep layer vertical wind shear in the MetUM simulations and in the ERA-5 reanalysis, with vortex tilting (Figure 5.1f) from the 25 September aligning well with an increase in minimum SLP (Figure 5.1c). The simulations have demonstrated a distinctly asymmetric structure (Section 5.3.3) with a clear inflow asymmetry that aligns with the shear vectors (Figure 5.6).

Figure 5.9 then suggests that there is a difference in the moisture and θ_e profiles between the two simulations, which implies that the downdraft ventilation process may be represented differently between the more diffusive (λ_{high}) and less diffusive (λ_{low}) ensembles.

By increasing the free-tropospheric mixing length, the cloud layer can become more diffusive (demonstrated by Figure 5.8), thus increasing the sub-grid scale vertical moisture transport between the cloud layer and the local environment. By increasing the downward transport of moisture from the cloud layer, the entropy of the mid-levels - where the θ_e minimum typically occurs (Emanuel et al., 1994) - may be increased. This is confirmed by Figure 5.9, in which all composited ensemble groups display a higher entropy in the λ_{high} simulations.

An important contextual component for this analysis is the presence of a moderate vertical wind shear and wavenumber-1 convective asymmetries discussed in Section 5.3.3. In environments of

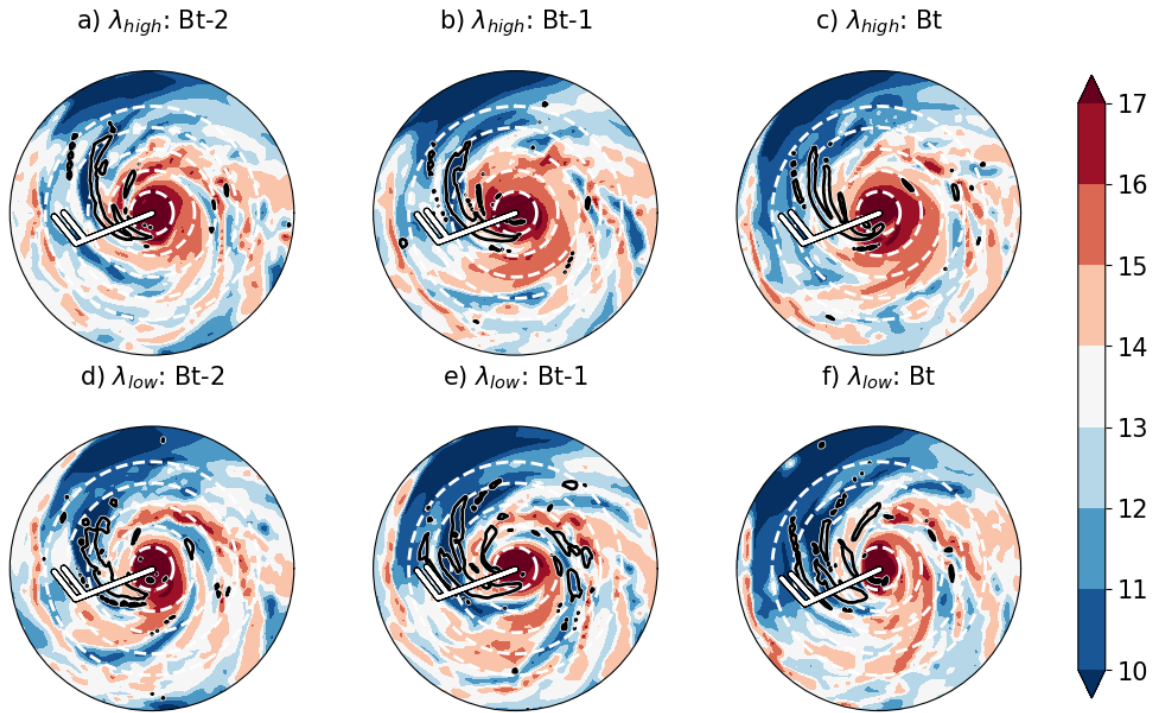


Figure 5.10: Mixing ratio (g kg^{-1}) at 1.5 km for a representative ensemble member. Black contours indicate downward motion of -0.5 m s^{-1} . Three simulation times are shown: time of intensity divergence (t), 1 hour before intensity divergence (t-1) and 2 hours before intensity divergence (t-2). The deep layer vertical wind shear is shown as a wind barb. Dashed white lines denote 50 km radius intervals, beginning with 50 km from the storm centre.

moderate wind shear, low entropy air from the mid-levels can be transported into the boundary layer via downdrafts induced by the asymmetric convective structure (Riemer et al., 2010; Tang and Emanuel, 2012a; Alland et al., 2021a; Wadler et al., 2021). Following Riemer et al., 2010, a plan view at 1.5 km altitude of the representative ensemble member (Figure 5.10) suggests that drier air is being drawn further into the inner core in the λ_{low} simulations and is associated with strong ($\leq -0.5 \text{ m s}^{-1}$) downward motion in the left-of-shear quadrants. This result verifies the presence of downdraft ventilation in the simulations and would explain why the boundary layer θ_e has a higher value in the λ_{high} scheme, despite not being directly impacted by the change in the free-tropospheric mixing parametrisation.

Downdraft ventilation is calculated using the following equation (Alland et al., 2021a):

$$V = \rho w' \theta'_e, \quad (5.4)$$

where ρ is the air density, w' is the perturbation of downward vertical motion and θ'_e is the

perturbation of equivalent potential temperature (relative to their azimuthal means). Only downward vertical motion is considered for this calculation, ensuring that the ventilation diagnostic is not influenced by convective upward motion such as in the eyewall updraft. For these purposes, the downdraft ventilation is averaged within a 150 km radius, which is consistent with the previous study (Alland et al., 2021a), with the inner 50 km removed, and should effectively capture the inner core of the storm without including the impacts of the eye, demonstrated by the RMWs in Figure 5.1e.

Although Figure 5.7 suggests that the primary influence is vertical mixing, for completeness the radial ventilation (the inward transport of anomalously low θ_e) is also calculated within a 150 km radius of the storm centre, according to the following equation from Alland et al., 2021b:

$$V_r = \rho u' \theta'_e, \quad (5.5)$$

where u' is the perturbation of inward radial velocity.

Firstly, the mid-level θ_e differences shown in Figure 5.9 cannot be explained by the radial ventilation in Figure 5.11. While there is some evidence of improved boundary layer recovery (shown by the enhanced negative ventilation in λ_{high} ; Figure 5.11a), within the mid-levels (2-5 km) it is evident that there is more radial ventilation in the λ_{high} simulations compared to λ_{low} . Note that positive values of radial ventilation suggest the inward transport of anomalously low θ_e , so if radial ventilation were the cause of the mid-level moisture differences in Figure 5.9, then the λ_{high} simulations may be expected to have lower θ_e . However, since this is not the case, the downdraft ventilation may be playing the more dominant role. I will now explore this possibility.

Figure 5.12 shows the signal of downdraft ventilation in both sets of simulations. From the full field, shown in Figure 5.12a and 5.12b, it is clear that the downdraft ventilation is at its strongest in the left-of-shear quadrants for both sets of simulations. In the λ_{low} runs, the downdraft ventilation signal peaks around the same altitude as λ_{high} (between 0.5 - 1.5 km), but extends further upward. While this means that the λ_{low} has more ventilation overall, it also suggests that the low θ_e air in the λ_{low} simulations is originating from higher altitudes. From Figure 5.9 and the associated discussion, in which the θ_e minimum was shown to be approximately 3-4 km, it follows that the penetrating θ_e should be even lower in the λ_{low} simulations than if

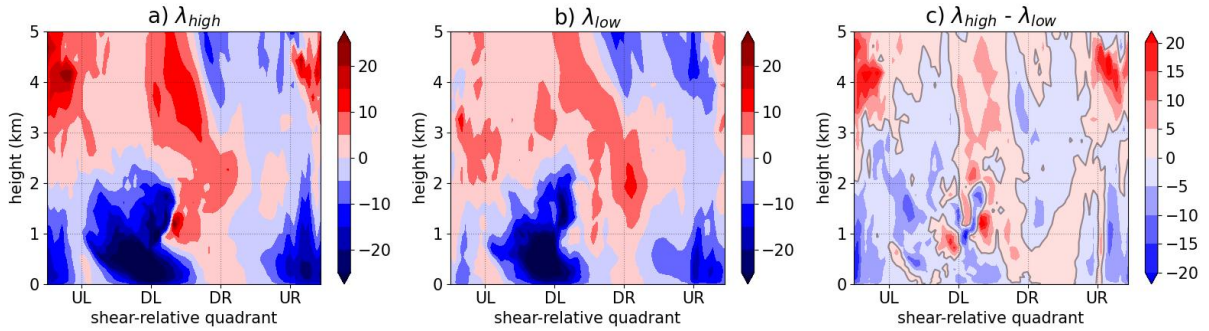


Figure 5.11: An ensemble composite of the radial ventilation in the 6 hours before the intensity divergence point, performed over the inner 50-150 km of the storm. Subplots (a) and (b) are the full field of radial ventilation ($\text{kg K m}^{-2} \text{s}^{-1}$). (c) The difference between (a) and (b), with the grey line denoting the 0 contour. Positive values represent the inward transport of anomalously low θ_e .

the ventilation began closer to the boundary layer.

The structure of the wavenumber-1 ventilation signal is similar to an idealised study by Alland et al., 2021a, in which the left-of-shear regions are dominated by a positive signal (which has a drying effect) and the right-of-shear have a negative signal. Furthermore, the magnitude of the wavenumber-1 component supports the findings of Alland et al., 2021a, producing a signal up to about $\pm 3 \times 10^{-1} \text{ kg K m}^{-2} \text{ s}^{-1}$.

The overall structure of the ventilation in Figures 5.12a,b are also consistent with an observational study by Nguyen et al., 2017, which showed that convective downdrafts in the downshear left quadrant can distribute relatively low θ_e air into the boundary layer, which reduces convection upstream. Nguyen et al., 2017 also found that the downdraft ventilation can contribute to storm asymmetries by suppressing convection upstream.

In Figure 5.12, our results show a much stronger downdraft ventilation signal in the λ_{low} simulations, suggesting that there is an increased transport of anomalously low- θ_e air from the mid-levels into the boundary layer. In the hours leading up to the intensity divergence point, and between 1.5 - 4 km altitude, there is no significant difference between the strength of the downdrafts between the experiments; however, the downward flux of anomalously low θ_e is significantly higher (t-test; $p < 0.05$) for the λ_{low} simulations. This shows that the ventilation signal is a result of the lower θ_e , rather than a consequence of stronger downdrafts.

Further supporting this point, Figures 5.13a and 5.13b show the vertical distribution of the downdrafts is comparable between the λ experiments, but Figures 5.13d and 5.13e demonstrate

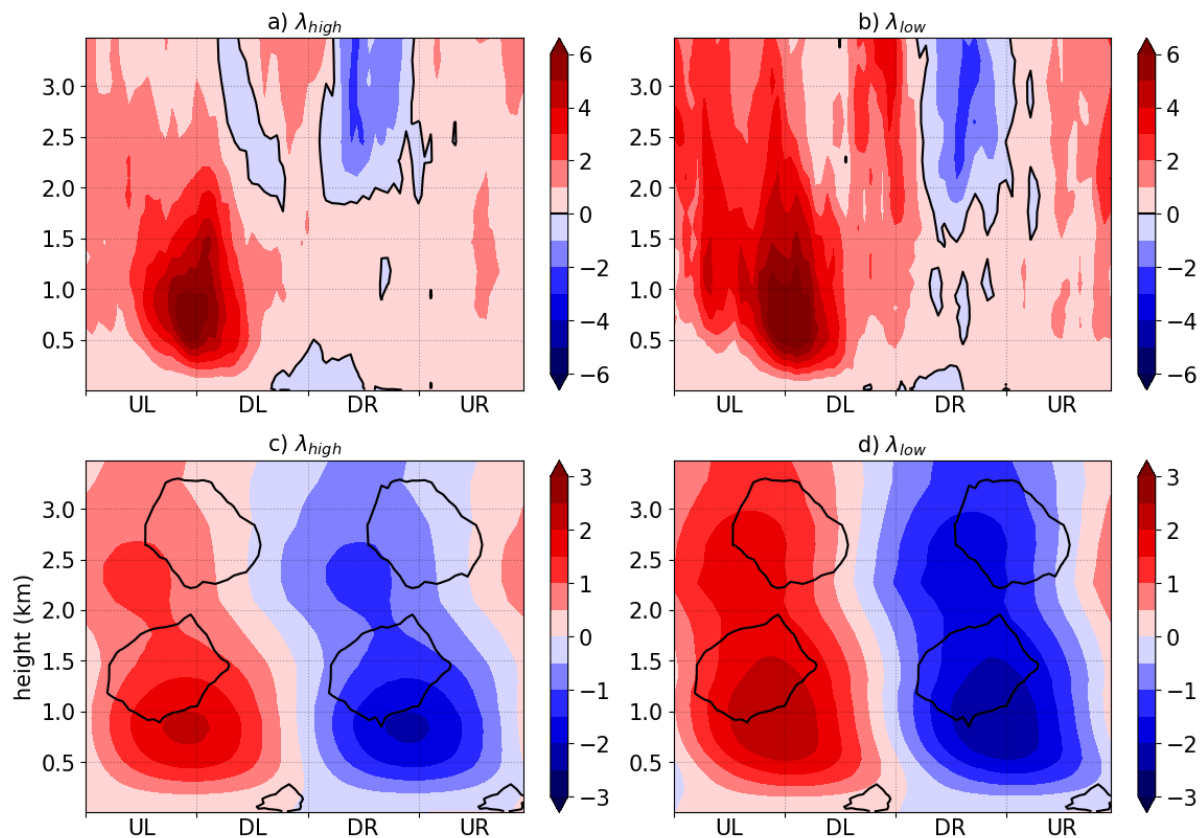


Figure 5.12: An ensemble composite of the downdraft ventilation in the 6 hours before the intensity divergence point, performed over the inner 150 km of the storm. Subplots a) and b) are the full field of downdraft ventilation ($\text{kg K m}^{-2} \text{s}^{-1}$), where the black contour is the 0 line and subplots c) and d) are the wavenumber-1 components ($\times 10^{-1} \text{ kg K m}^{-2} \text{s}^{-1}$), where black contours indicate regions of statistically significant ($p < 0.05$) differences between the two simulations. The radius is normalised by the surface RMW.

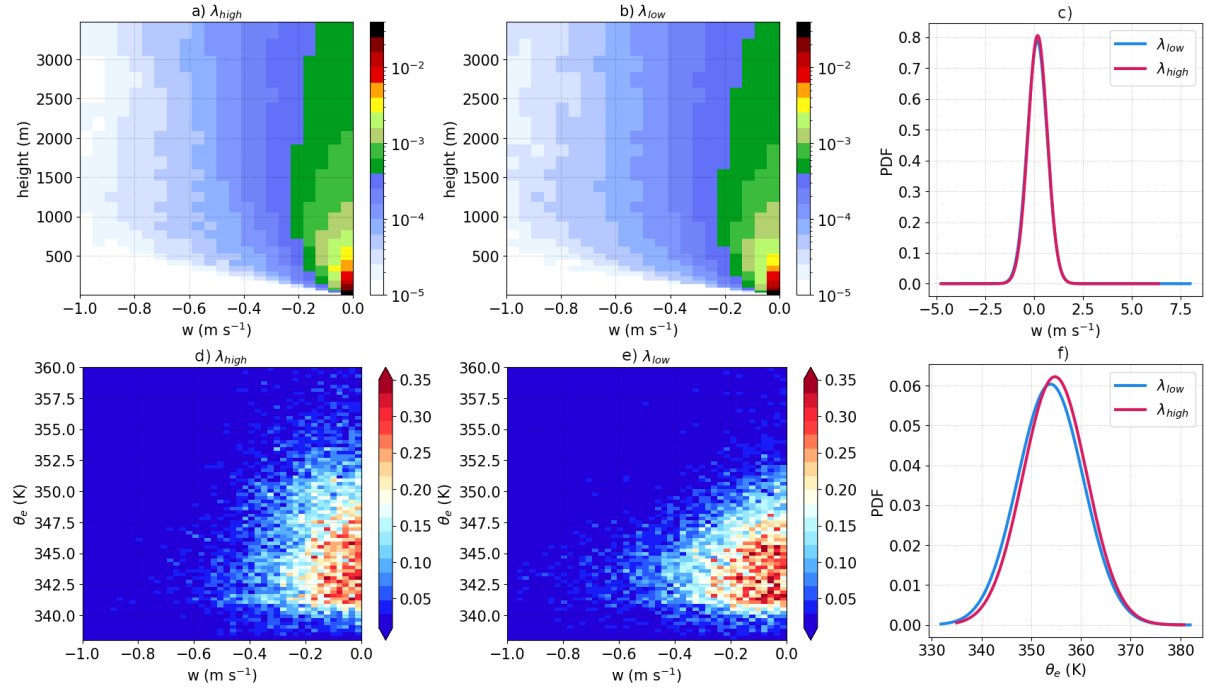


Figure 5.13: An ensemble composite in the 6 hours before the intensity divergence point, performed at 1 km height over the inner 150 km of the storm, removing the inner 50 km to ensure the results were not skewed by the eye. a) and b) are contoured frequency by altitude diagrams of vertical velocity (m s^{-1}) for the λ_{high} and λ_{low} ensemble members respectively. d) and e) 2d histograms, to show the frequency distribution (K m s^{-1}) of θ_e in the downdrafts. c) and f) the probability density function of vertical velocity (m s^{-1}) and θ_e (K) respectively.

that the downdrafts tend to have a much lower θ_e in the λ_{low} simulations. A two-sample Kolmogorov-Smirnov test, which compares the distribution of two independent samples (Hodges Jr, 1958) showed no significant difference ($p < 0.05$) in the distribution of the vertical motion between the simulations. This evaluation was carried out on averaged groups of ensemble members at 1.5 km altitude, and the test was performed over radial and azimuthal averages independently, to find no significant difference in the radial or azimuthal distribution of vertical motion. Overall, the evidence suggests that the main mechanism of weakening is via a lower θ_e in the low-diffusivity simulation within the downdrafts rather than the distribution or intensity of the downdrafts being different. Also note that the statistical distribution analysis took into consideration the upward motion too, suggesting no significant difference in the azimuthal or radial distribution of the updrafts before intensity divergence.

Since the parcels entering the inflow layer of the λ_{low} scheme have a lower entropy compared to those in the λ_{high} scheme, parcels in the λ_{low} simulations would have to either i) spend a longer duration in the inflow layer, ii) have a shallower inflow layer, or iii) be subject to an inflow layer with stronger entropy fluxes from the sea surface, for the parcels to recover their entropy to the

same level as the λ_{high} simulations. If parcels do not sufficiently recover, before entering the eyewall region, this could reduce available potential energy of the eyewall (Tang and Emanuel, 2012a), thereby dampening the most convective region of the storm. It follows that parcels would be more detrimental to the storm's intensity if they entered the inflow layer closer to the eyewall. Within the outer vicinity of the eyewall, the inflow layer has the maximal potential to recover its entropy from surface fluxes (Wroe and Barnes, 2003) due to the strong secondary circulation reducing the convective vertical mass flux of high- θ_e air out of the boundary layer (Wroe and Barnes, 2003). If a low- θ_e parcel enters the inflow within this region, it can very quickly recover its entropy and may not inhibit the eyewall convection (Alland et al., 2021a).

Alland et al., 2021a showed that parcels entering the inflow layer via downdraft ventilation most effectively reduce the convection when they enter in the upshear regions, where they have the highest chance to reduce the areal extent of vertical motion. It is quite clear from Figure 5.12a,b that the λ_{low} simulations have a stronger downdraft ventilation signal in the upshear quadrants than their λ_{high} counterparts, which supports the hypothesis that the downdraft ventilation is a contributing factor to the weaker storm produced by the λ_{low} simulations.

While a parcel trajectory analysis (such as in Alland et al., 2021a) would be the most effective way to prove the hypothesis that λ_{low} parcels which originate from downdrafts tend enter the eyewall region more thermodynamically depleted than their λ_{high} counterparts, this would require data outputted at much higher temporal resolution. Instead, I draw from the data presented above. The change in θ_e and moisture (shown in Figure 5.9c and 5.9f) peak at around 2 km, which suggests the change is not surface-driven. There are also no differences in the sea surface temperature between the schemes.

Figure 5.13 demonstrates that despite the distribution and strength of downdrafts being similar between the experiments, the downdrafts in the λ_{low} simulations have significantly lower θ_e . This is further supported by the ventilation diagnostic in Figure 5.12, in which the downdraft ventilation signal is significantly higher in the λ_{low} simulations.

5.4 Concluding Remarks

The main aims of this study were to quantify to what extent the tropospheric mixing controls the intensity of Hurricane Maria, and to establish how the turbulence parametrisation con-

tributes to these intensity-controlling processes. The most robust conclusion from our results is that reducing the tropospheric mixing length (λ) improved the intensity forecast in this case study. While the changes were made to the 3D mixing length, sensitivity tests showed that the horizontal component made no significant difference to the simulations and that the primary control was the vertical mixing length. All ensemble members in the λ_{low} experiments produced a lower maximum wind speed and a higher central pressure than their λ_{high} counterparts by the end of the simulation time, which reduced the intensity errors when compared to the observed track.

By evaluating the storm environment, it became apparent that Maria was under the influence of shear-related processes contributing to the storm weakening. In this study, it has been shown that a high vertical mixing length in the mid-levels of tropical cyclones can lead to a higher parameterised transport of moisture (upward from the boundary layer and downward from the cloud layer) into the low-entropy mid-levels. This moisture subsequently increases the θ_e of the mid-level air. In moderately sheared tropical cyclones, the transport of this low- θ_e air into the boundary layer via resolved convectively-induced downdrafts (‘downdraft ventilation’) is key to stalling intensification or in some cases, inducing weakening. If the entropy of the mid-levels is greater, then the effectiveness of downdraft ventilation is reduced. I propose that this is part of the reason that the Met Office’s operational forecasting model, which used the λ_{high} settings, produced a stronger storm than the Best Track during the forecast period (22 September - 27 September 2017).

The findings presented here are not in contradiction to the boundary layer study by Zhang and Rogers, 2019, which showed that reduced vertical diffusivity in the boundary layer can produce a more resilient, more intense vortex. Rather, these results complement the previous work by highlighting how the choice of turbulence parametrisation can have different impacts on the storm dynamics based on where the mixing length changes are applied.

Although the conclusions are robust for Hurricane Maria, further work should address the need for more case studies in a diverse set of environments. The primary shear-related processes addressed here (particularly downdraft ventilation) will not be applicable in all tropical cyclones and future research should consider how the tropospheric turbulence parametrisation affects the forecast quality in other stages of the tropical cyclone life cycle. Further work would also benefit from a parcel trajectory analysis, which would require output data of a higher temporal

resolution.

Recent changes to the sub-grid turbulence parametrisation in the operational MetUM, namely the reduction of the free-tropospheric mixing length, are supported by the results presented in this study, in which tropical cyclone intensity forecasts are shown to be improved using a case study of a sheared, weakening tropical cyclone. These results provide confidence that the forecasting quality will be maintained and likely improved by the changes made to the free-tropospheric turbulence parametrisation. While this work is based on the MetUM, many operational forecasting models make use of turbulence parametrisations. The results presented here shed light on the importance of the free-tropospheric turbulence more generally, and should contribute to advances in tropical cyclone modelling.

Chapter 6

The Asymmetric Boundary Layer Wind Structure of a Landfalling Tropical Cyclone

6.1 Introduction

Landfall is the most destructive phase of a tropical cyclone's lifetime, and the potential impact of tropical cyclones becomes more dangerous as the global population rises. Quantifying the distribution of wind speed is particularly important for assessing risk as the boundary layer winds are the main mechanism responsible for generating storm surges (Needham and Keim, 2014), which are one of the most destructive aspects of tropical cyclone landfall. This risk is becoming more important to consider, since the chance of extreme storm surges is correlated with sea level rise (Calafat et al., 2022). High wind speeds are also destructive in themselves, and the distribution of wind can impact precipitation.

In this study, we investigate Tropical Cyclone Veronica (2019), which made landfall in north-western Australia and quickly developed an atypical wind distribution. A change in the maximum wind speed was detected in satellite-borne synthetic aperture radar (SAR) images, moving from the left-of-motion side - common for storms in the Southern Hemisphere (Klotz and Jiang, 2017), to the right-of-motion side as it nears the coastline. Remaining almost stationary for the next 24 hours or so, the wind field continued to become more asymmetrical, leading to an

eyewall break on the offshore side and an expansion of the wind field inland. This asymmetric evolution of the wind field, wherein the wind field expands inland and weakens less slowly than over the sea, despite the storm's proximity to land, challenges our understanding of tropical cyclone behaviour and poses a hitherto unsuspected threat for vulnerable coastal communities.

Veronica is an ideal case study for studying the impacts of landfall on a real tropical cyclone due to the environmental and synoptic conditions which will be summarised now but are discussed in full detail in Section 6.3. For example, Veronica stalled for around 24 hours when it reached the Western Australian coast, which almost completely eliminates the motion-induced asymmetry caused by storm translation. Within the study area (western Pilbara), the topography is relatively homogeneous and mostly low-lying (e.g. Figure 3.5), with a shallow incline up to the highest point, which is still less than 400 m above sea level. The land surface is relatively homogeneous, mainly composed of sandy iron-rich substrate, with a low population density and limited urbanisation which is concentrated around the local ports. The simple topography and land surface characteristics reduce the complications typically associated with landfall case studies.

Studying landfalling tropical cyclones can be extremely complicated due to the inherent heterogeneity of land surfaces, which can impact storm structure and intensity in different ways. For example, increasing surface roughness can accelerate weakening and deepen the boundary layer inflow (e.g. Tuleya and Kurihara, 1978; Kepert, 2001; Kepert, 2012; Hlywiak and Nolan, 2021), as well as modulate the distribution of convection and convergence (e.g. Tuleya and Kurihara, 1978; Chan and Liang, 2003; Chen and Yau, 2003). Complex terrain can pose its own forecasting and modelling challenges, causing large local variability in wind speed (Ramsay and Leslie, 2008), impacts on storm track (Bender et al., 1987; Wu and Kuo, 1999), and distribution of precipitation (Chang et al., 2013). Similarly, soil moisture content can have a direct impact on the amount and distribution of precipitation (e.g. Chan and Liang, 2003; Rao et al., 2019), and varying impacts on storm intensity (e.g. Evans et al., 2011; Kellner et al., 2012; Hlywiak and Nolan, 2021). All of these factors are further compounded by factors such as cyclone translation (e.g. Shapiro, 1983; Corbosiero and Molinari, 2003; Kepert, 2001; Hlywiak and Nolan, 2022) and wind shear (e.g. Chen et al., 2006; Riemer et al., 2010; Zhang et al., 2013).

In some instances, limiting variability by using idealised models is a good option to study isolated aspects of tropical cyclone landfall dynamics. However, it is also important to study landfall in

the context of full-physics operational-type simulations to provide a better understanding into how real tropical cyclone systems interact with their environment.

In this study, I will study Tropical Cyclone Veronica (2019) using the Met Office Unified Model (MetUM) which is an operational forecasting model. In tandem with the MetUM, I will make use of a more idealised model which will assist in attributing the full-physics dynamics to different physical processes. Both the MetUM and the boundary layer model are described in more detail in Section 6.2.

The structure of this paper is as follows: first, the data and methods will be described. Next, there will be a brief section on the synoptic history of Veronica to provide context for the rest of the work. Following the synoptic history, the performance of the MetUM simulations will be evaluated against observations to demonstrate that the model is a reasonable representation of reality. With the context and justification in place, I will go on to investigate the dynamics of Veronica's wind distribution during landfall, which will include an analysis of the changing surface characteristics, the spiral rainband, and vorticity, as well as consideration of environmental wind shear and storm motion. I will aim to answer the following questions:

- 1) How do landfall, environmental vertical wind shear and rainband dynamics contribute to the eyewall break of Tropical Cyclone Veronica (2019)?
- 2) To what extent, and by what mechanism, can eyewall breaks be explained by the synoptic environment?

6.2 Data and Methods

6.2.1 Observations

Veronica was observed by four consecutive passes of a polar-orbiting satellite with synthetic aperture radar (SAR; Mouche et al., 2019) technology, allowing for derivation of the surface wind speeds. In passive microwave satellite imagery provided by the Naval Research Lab (accessible at www.nrlmry.navy.mil), temperatures such as the 91 Hz brightness temperature and 91 GHz polarization-corrected temperatures can be used to imply cloud characteristics of Tropical Cyclone Veronica (2019) during landfall. These observations are used to guide the analysis and model evaluation in Section 6.4.1.

Several automatic weather stations captured surface-level data around Veronica. These are shown in Figure 3.5 and discussed in Chapter 3. From these stations, data is available at least every 30 minutes for surface air temperature, dewpoint temperature, surface wind speed and direction, mean sea level pressure, and precipitation rate. The closest automatic weather stations to Veronica, which are shown on Figure 3.5, are Varanus Island, Karratha, Roebourne and Port Hedland. These measurements were used for model evaluation in Section 6.4.1.

6.2.2 Reanalysis Dataset

The ERA5 reanalysis dataset Hersbach et al., 2018; Hersbach et al., 2020 was used to form an understanding of the larger-scale environment, including the steering flow. The full details of ERA5 are in Chapter 3.

6.2.3 Full-Physics Model

For the full-physics simulations of Veronica, I use the Met Office Unified Model (MetUM) in the regional tropical configuration (RA2-T, Bush et al., 2023). The full details of the MetUM are discussed in Section 3. An 18-member ensemble is initialised on 23 March 2019 00 UTC, using a 2.2 km horizontal resolution and output every 1 hour. For deterministic member 0, I output at higher temporal resolution (10 minutes) to allow for deeper analysis of the dynamics on a shorter timescale. Robustness of the results was also confirmed using a deterministic forecast at 1.5 km horizontal resolution. All simulations were run for a total of 72 hours. The majority of this analysis will focus on the deterministic forecast - the ensemble is used to provide information on the consistency of certain dynamical features, which will be discussed in further detail later.

Boundary Layer Model

To disentangle the dynamical effects of the landfall and of the vortex itself, I use the boundary layer model of Kepert and Wang (2001), hereafter KW01, modified by Kepert (2018) to use an asymmetric pressure field. All simulations were produced with no storm motion, to mirror Veronica's almost stationary state during the period of interest. The boundary layer model of KW01 can use a variety of idealised vortices; for this study I chose to input the asymmetric vorticity field from the MetUM. This vorticity field is used to compute an irrotational wind field (Kepert, 2018), which then becomes the input vortex to the boundary layer model. To investigate the impact of both the landfall and vorticity field on the wind distribution, a series

of experiments were devised and will now be described.

Simulations were run in either an all-sea set-up or using a straight coastline rotated 15° anticlockwise from the x-axis situated 15 km from the storm centre. These values were chosen based on estimations from the coastal geometry of Northwest Australia (e.g. Figure 3.5). For the inland roughness length, the MetUM suggests that a value of approximately 0.035 m would be the most representative, but for completeness I also tried sensitivity tests using 0.1 m and 0.2 m - the results are similar, so are not shown here.

We then performed a series of vorticity tests to determine the sensitivity of the dynamical fields to the degree of anticyclonic vorticity present in the simulations. The rationale for focusing on vorticity will be discussed in more detail in Section 6.4.4. The MetUM field was used as a ‘baseline’ and input for all of the sea and land tests listed above. Two main tests were carried out, including: i) increasing by 50% all anticyclonic vorticity exceeding $2.5 \times 10^{-4} \text{ s}^{-1}$ (Figure 6.1b), ii) removing and interpolating over all anticyclonic vorticity exceeding $2.5 \times 10^{-4} \text{ s}^{-1}$ (Figure 6.1e).

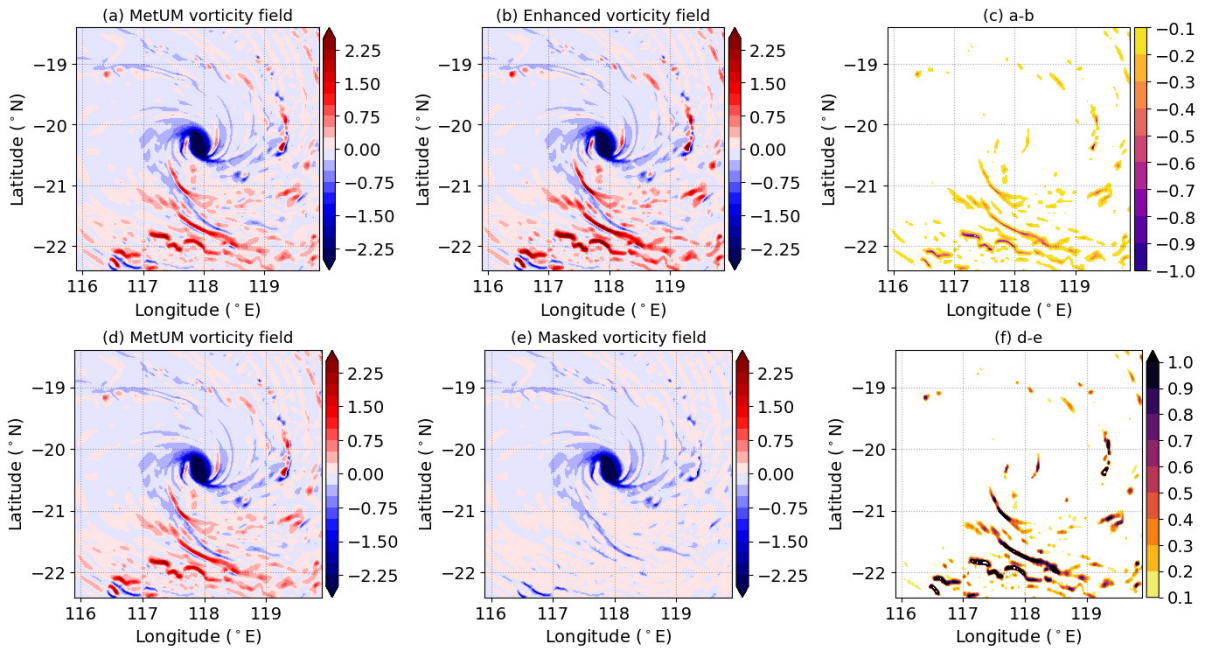


Figure 6.1: Vorticity (10^{-3} s^{-1}). (a,d) The MetUM vorticity field. (b) The MetUM vorticity field with all anticyclonic vorticity exceeding $2.5 \times 10^{-4} \text{ s}^{-1}$ enhanced by 50%. (c) a-b. (e) The MetUM vorticity field with all anticyclonic vorticity exceeding $2.5 \times 10^{-4} \text{ s}^{-1}$ masked and interpolated over. (f) d-e.

As a result, there were six tests that were placed into the KW01 model. These are:

- (1) **Set-up:** An all sea simulation with a symmetric vortex of similar radius of maximum winds (RMW) and intensity to the MetUM vortex
Purpose: A control, to represent symmetric storm dynamics.
- (2) **Set-up:** Same as above, but with a 15° coastline with 0.035 m roughness, 15 km from the storm centre
Purpose: To isolate the impacts of landfall on a symmetric vortex.
- (3) **Set-up:** An all sea simulation using the asymmetric vorticity field from the MetUM as an input (Figure 6.1a,d)
Purpose: To ensure the boundary layer model can reasonably reproduce the MetUM fields.
- (4) **Set-up:** Same as above, but with all anticyclonic vorticity exceeding $2.5 \times 10^{-4} \text{ s}^{-1}$ masked (Figure 6.1e)
Purpose: To evaluate the effect of reduced asymmetric anticyclonic vorticity on the storm dynamics.
- (5) **Set-up:** Same as above, but with all anticyclonic vorticity exceeding $2.5 \times 10^{-4} \text{ s}^{-1}$ enhanced by 50% instead of being masked (Figure 6.1b)
Purpose: To evaluate the effect of increased asymmetric anticyclonic vorticity on the storm dynamics.
- (6) **Set-up:** A simulation using the asymmetric vorticity field from the MetUM as an input, but with a 15° coastline with 0.035 m roughness, 15 km from the storm centre.
Purpose: To determine the impact of landfall on the asymmetric vortex.

6.3 Synoptic history

Tropical Cyclone Veronica was an intense tropical cyclone which affected Western Australia in March 2019. According to the official report (Paterson, 2019), Veronica first obtained the status of a tropical cyclone on March 19, 2019, reaching peak intensity (928 hPa minimum pressure and 59 m s^{-1} maximum winds) on March 21. At this point, Veronica had reached Category 5 on the Australian tropical cyclone intensity scale (World Meteorological Organization, 2022) and Category 4 on the Saffir-Simpson scale (Camelo and Mayo, 2021). By the 23 March, Veronica had weakened slightly as it began to approach the West Australian coast, toward the Pilbara

region. As the storm reached the coast on 24 March, it had maintained a Category 4 intensity on the Australian intensity scale, reaching a minimum central pressure approximately 950 hPa, and maximum winds around 90 kts (46 m s^{-1}).

Figure 6.2a shows that as Veronica neared the coast on 24 March, it stalled and remained almost stationary for around 24 hours. From Figure 6.2b, Veronica can be seen to weaken according to both the maximum wind speed and the minimum sea level pressure from 24 March, which aligns with the coastal influence.

For this study, I focus on the period shown in Figure 6.2 in which Veronica approached and stalled at the coast (23 March - 26 March), weakening by around 30 m s^{-1} from approximately 24 March 00 UTC to 25 March 00 UTC. Figure 6.3b shows the steering-level flow (the mass-weighted mean wind between 850 - 200 hPa, as in Ashcroft et al., 2021) for 24 March 2019 00 UTC in the MetUM global deterministic run. In the lower tropospheric flow, there is an anticyclone propagating eastward from the east Indian Ocean toward western Australia, which is marked by a broad region of anticyclonic vorticity and high surface pressure in Figure 6.3a. It is possible that the propagation of this system and the position of the subtropical jet south of Veronica were producing a blocking effect on the southward movement of Veronica, leading to the reduced motion. The environmental cause of Veronica's stalling (Paterson, 2019) will not be investigated in-depth here, I will instead focus on the storm dynamics that arose as a result.

The large-scale environment shown in Figure 6.3a suggests an asymmetry in the vorticity, whereby there is a large area of anticyclonic vorticity in the south, and more cyclonic vorticity in the north. The flow in Figure 6.3b northwest of Veronica suggests a weak influence of the monsoon trough, which is likely contributing to the larger-scale cyclonic vorticity in this region. This asymmetry will be shown to be an important feature of the synoptic situation and will be explored in more detail in Section 6.4.4.

During the study period, the storm experienced high vertical wind shear according to both the official report (Paterson, 2019) and calculations based on the MetUM global deterministic run, which put the wind shear at values of $\geq 10 \text{ m s}^{-1}$ from the northwest and gradually increasing for the majority of the study period (Figure 6.2c).

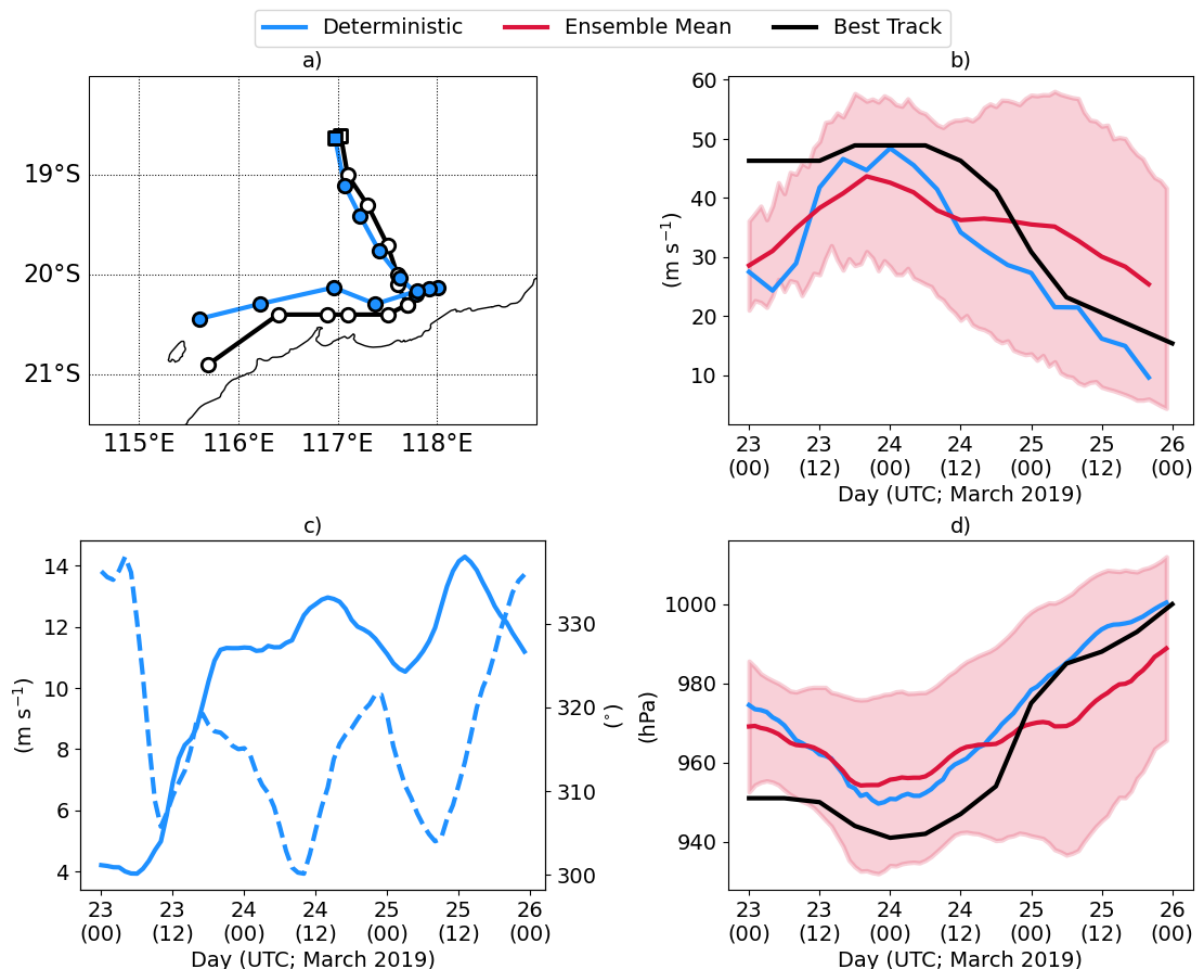


Figure 6.2: a) Best track storm position (black) and modelled storm position (blue) with circles denoting every 6 hours starting at 23 September 2019 00 UTC, where the first point is denoted by a square. b) Best track (black), deterministic (blue) and ensemble mean (red) maximum wind speed (m s^{-1}), with the ensemble spread filled in red. c) Simulated 200–850 hPa wind shear magnitude (m s^{-1} ; solid; left axis) and direction using meteorological convention ($^{\circ}$; dotted; right axis). d) Best track (black), deterministic (blue) and ensemble mean (red) minimum sea level pressure (hPa), with the ensemble spread filled in red.

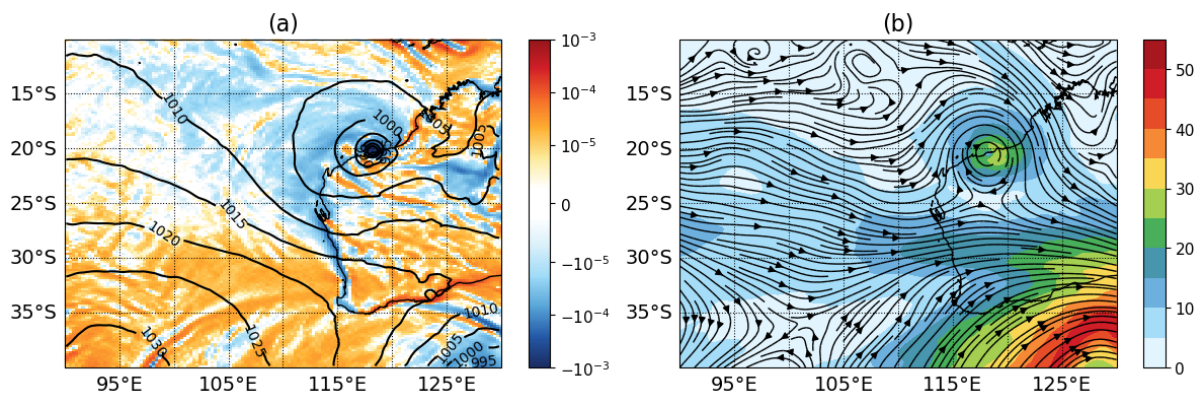


Figure 6.3: MetUM global deterministic forecast at 23 March 2019 00:00 UTC ($T + 24$). (a) Relative vorticity at 850 hPa (filled; s^{-1}), mean sea level pressure (hPa; unfilled contours). (b) Steering-level flow (filled; m s^{-1}) and streamlines.

6.4 Results

6.4.1 Model Evaluation

In this section, the deterministic MetUM simulations will be evaluated against all nearby surface observations to justify the use of the model in investigating the dynamics of Veronica. First, the surface intensity and track metrics will be evaluated against the official best track, then satellite observations will be considered, followed by an analysis of the surface observations.

When comparing the ensemble mean storm position in Figure 6.2a, the model track error is never larger than 0.5° which outperforms average track performance for the Bureau of Meteorology (Paterson, 2019). Around 24 March, it seems that Veronica was slightly eastwardly displaced in the model, which could be due to a slight overestimation in the westerly steering flow shown in the global ensemble mean in Figure 6.3b, discussed in the previous section. While this track error is generally low, the storm centre misplacement needs to be considered when evaluating the model against the satellite and surface-based observations.

The ensemble mean and spread (calculated as the mean difference between every unique ensemble pairing, following Flack, 2023) is shown for the maximum wind speed (Figure 6.2b) and for the minimum sea level pressure (Figure 6.2d). The model was initialised slightly too weak and took approximately 12 hours to spin-up, which is anecdotally typical for tropical cyclones in the MetUM. In general, although the ensemble mean did not capture the maximum storm intensity, the weakening associated with the proximity to land was well captured. Some ensemble members - generally those that over-predicted the southward translation onto land - decayed faster than others, while ensemble members that remained over the sea retained a higher intensity.

Evaluating the deterministic forecast against the satellite observations, Figure 6.4 shows a general agreement in the overall asymmetry between the observations (Figures 6.4a,b,c) and the simulations (Figure 6.4d). For example, all of the satellite observations show a weakness on the northern side, whether this is a lack of deep cloud (Figures 6.4a,b) or a drop in wind speed (Figure 6.4c). While the simulated wind speed (Figure 6.4d) is slightly lower than the SAR-derived wind speeds (Figure 6.4c), the wind distribution is generally consistent. There is a wind speed decrease in the north, with a wind speed maximum in the offshore western part of the storm, and the storm size is realistic. At this forecast time, the modelled wind speed in the northeast (north of -19°N and east of 118°E) is slightly higher than that in the observations.

Possible reasons for this will be investigated in Section 6.5. Note that the times are different between Figures 6.4c and 6.4d due to the modelled storm translating eastwards in the first $T + 24$ -36 hours (shown in Figure 6.2). The chosen time reflects the storm at a more realistic position compared to the observations.

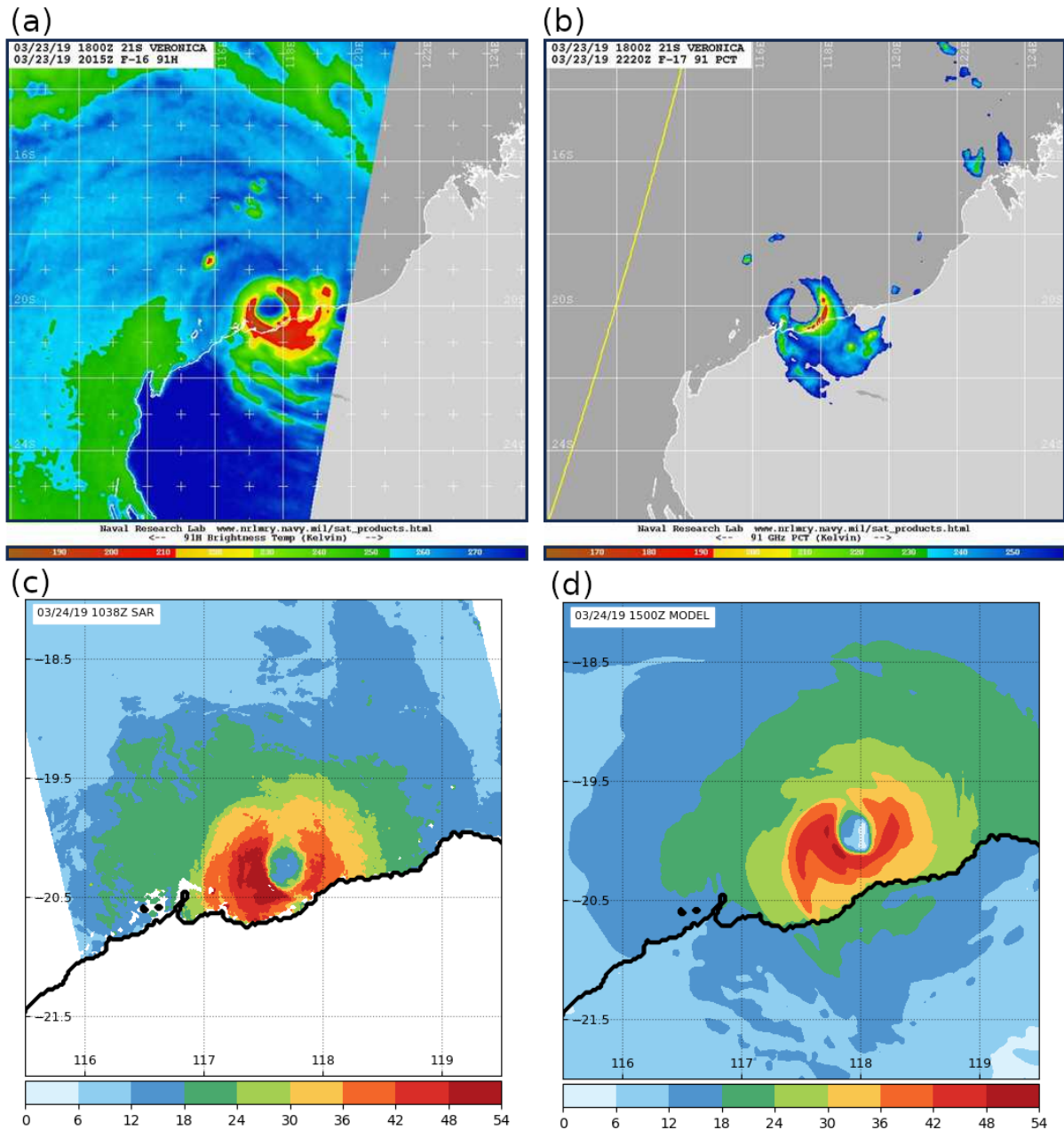


Figure 6.4: (a) Satellite 91 H brightness temperature (K) from the Naval Research Lab on 23 March 2019 20:15 UTC. (b) Satellite 91 GHz polarization-corrected temperature (K) from the Naval Research Lab, on 23 March 2019 22:20 UTC. (c) Satellite-derived SAR 10-m wind speed (m s^{-1} ; Mouche et al., 2019) on 24 March 2019 10:38 UTC. (d) Modelled 10-m wind speed (m s^{-1}) on 24 March 2019 15:00 UTC.

The closest surface observation sites with complete data are (from east-most to west-most):

Port Hedland, Roebourne, Karratha, and Varanus (Figure 3.5). The MetUM deterministic simulation is evaluated against the surface observation sites for the following diagnostics: air temperature, dewpoint, wind speed, wind direction, sea level pressure, and precipitation rate. It can be seen from Figure 6.5 that in general, there is good alignment between the model and the observations. For the Port Hedland site (Figure 6.5i), the SLP had a realistic initialisation and remained very close to the observations until approximately the 24 March 2019, where the model seems to become too intense. This discrepancy is likely due to the misalignment between the modelled and observed tracks; the modelled storm moves too far eastward during this period, which places the storm nearer to the Port Hedland site. However, the general pressure trend is well represented by the model, across all sites (Figures 6.5i,j,k,l).

Trends in the wind speed and direction are also generally well captured across all of the sites (Figures 6.5e,f,g,h), with the highest wind speed being consistently captured at the Roebourne site (Figure 6.5f). Precipitation (Figures 6.5m,n,o,p) is highest at the eastern-most sites and reaches a peak in the Roebourne site during the passage of Veronica at the later forecast times (Figure 6.5n, around the 26 March), which is consistent with the modelled precipitation distribution, suggesting that the majority of precipitation occurred inland in the eastern quadrant of the storm.

In the model there is a distinct trough in the SLP field (e.g. Figure 6.5j at around 25 March 18:00 UTC), which can in some cases be correlated with the peaks in wind speed, just before 26 March. While this was not reflected in the observational data, it is possible that this short-lived feature was the signal of a rainband-like structure, which will be discussed further in Section 6.4.2. Since rainbands can be very narrow, the position can be difficult to reproduce in the model. However, there is further evidence to support the presence of this band outside of the MetUM simulations, such as the banded feature oriented southwest of the storm centre in the satellite data (Figure 6.4a).

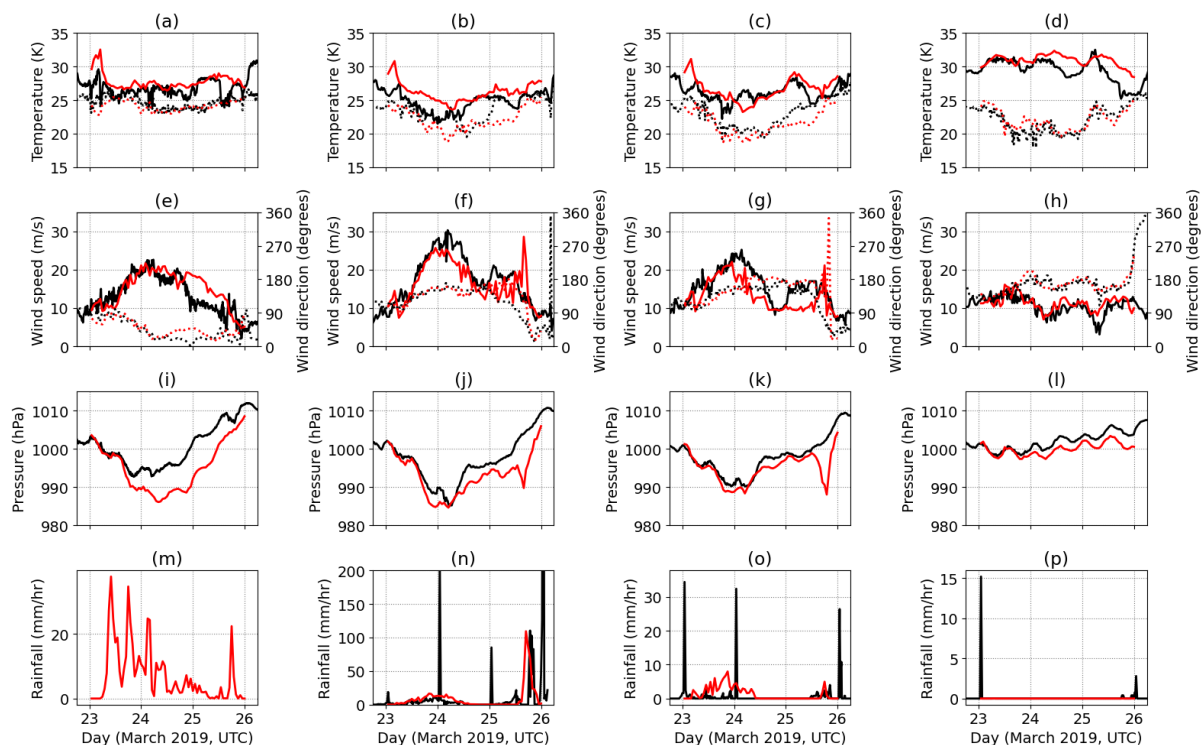


Figure 6.5: Evaluation of MetUM deterministic forecast (red) against the surface observation sites (black). In east to west order (since east is closest to the initial storm landfall), the columns represent: Port Hedland, (a,e,i,m), Roebourne (b,f,j,n), Karratha (c,g,k,o), Varanus (d,h,l,p). (a,b,c,d) Surface temperature (solid; $^{\circ}\text{C}$), dewpoint temperature (dotted, $^{\circ}\text{C}$). (e,f,g,h) Wind speed (solid; m s^{-1}) and wind direction (dotted; $^{\circ}$). (i,j,k,l) Mean sea level pressure (hPa). (m,n,o,p) Precipitation rate (mm hr^{-1}). There were no precipitation measurements available in Port Hedland (m) due to instrument malfunction.

6.4.2 Simulated Storm Evolution

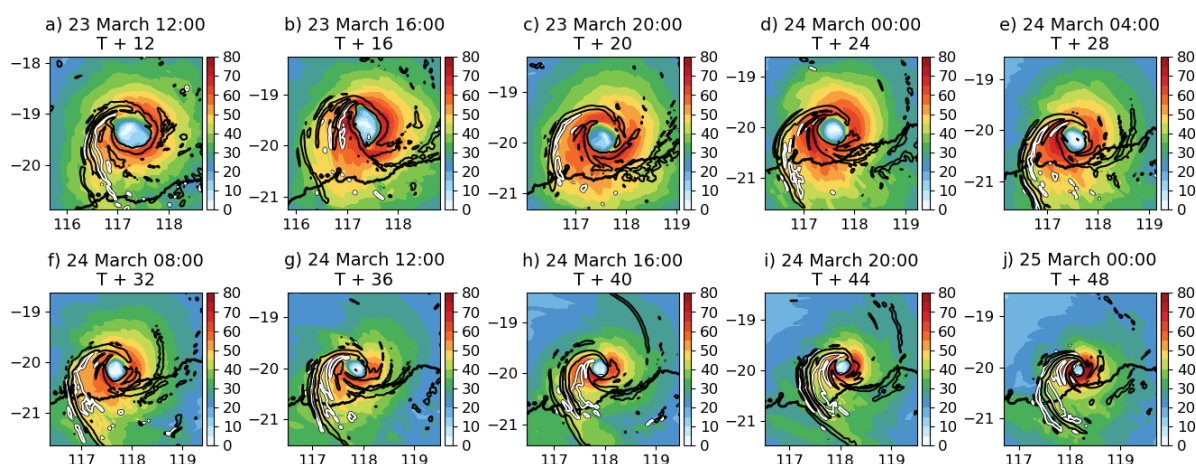


Figure 6.6: Tangential wind (filled contours; m s^{-1}) at 950 hPa, with positive vertical wind in black and downward vertical wind in white contours, at $\pm 0.5 \text{ m s}^{-1}$.

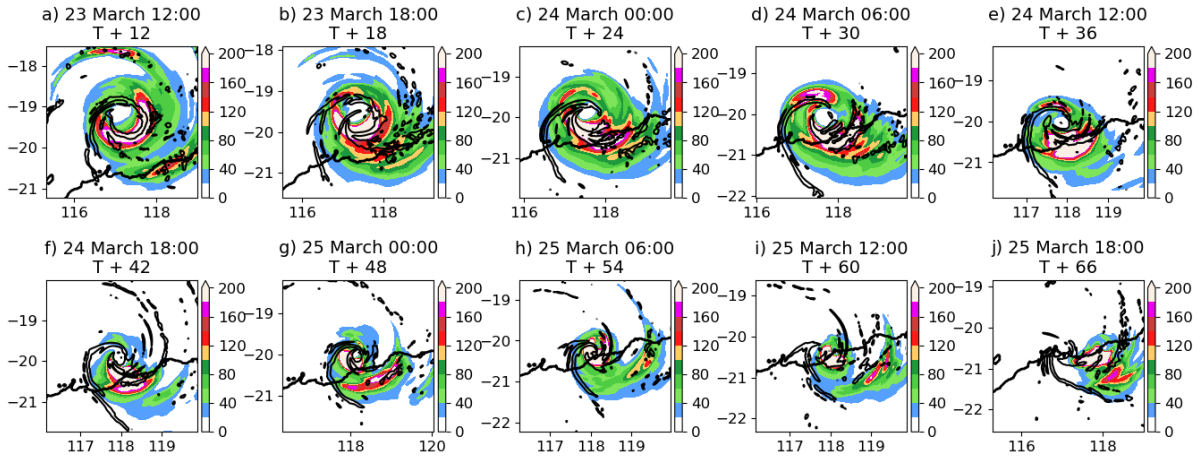


Figure 6.7: 6-hourly rainfall accumulation (filled; mm), with 950 hPa vertical velocity in black contours at 0.5 m s^{-1} . The thick black line denotes the coastline. The y-axis is the latitude in $^{\circ}\text{N}$ and the x-axis is the longitude in $^{\circ}\text{E}$. The plot domain follows the storm centre.

At the start of the simulation time, Veronica presents as a broad, nearly axisymmetric vortex with an RMW of around 75 km. There are two main rainbands, with the primary and dominant rainband spiralling outwards from the northern eyewall into the southwest (front-right) storm quadrant, and a secondary rainband originating from the southern eyewall and spiralling into the northeast (back-left) quadrant. These rainband features can be seen in Figures 6.6 and 6.7, with the primary rainband being present across all simulation times and the weaker rainband sporadically appearing when its intensity fluctuations reach the 0.5 m s^{-1} contour level for vertical velocity.

As Veronica approaches the coast, the eyewall changes shape from relatively circular to polygonal while the inner core decreases in size and the primary rainband becomes more convective, with stronger ascent. Over time, the vertical velocity of the rainband becomes stronger, while the equivalent potential temperature (θ_e) and mixing ratio (q) become lower suggesting that the rainband is becoming thermodynamically depleted. This region of thermodynamically depleted air near the rainband is apparent in Figure 6.8. The evolution of precipitation can be seen in Figure 6.7, which shows a progressively more asymmetric structure as the simulation progresses. The rest of the precipitation within the storm system (stratiform and convective) is concentrated over land in the downshear quadrants, which can be seen in Figures 6.7d-j. This pattern is consistent with observations of precipitation distributions in tropical cyclones in sheared environments (Hence and Houze, 2012).

As the simulation progresses, this spiral band remains connected to the eyewall and extends

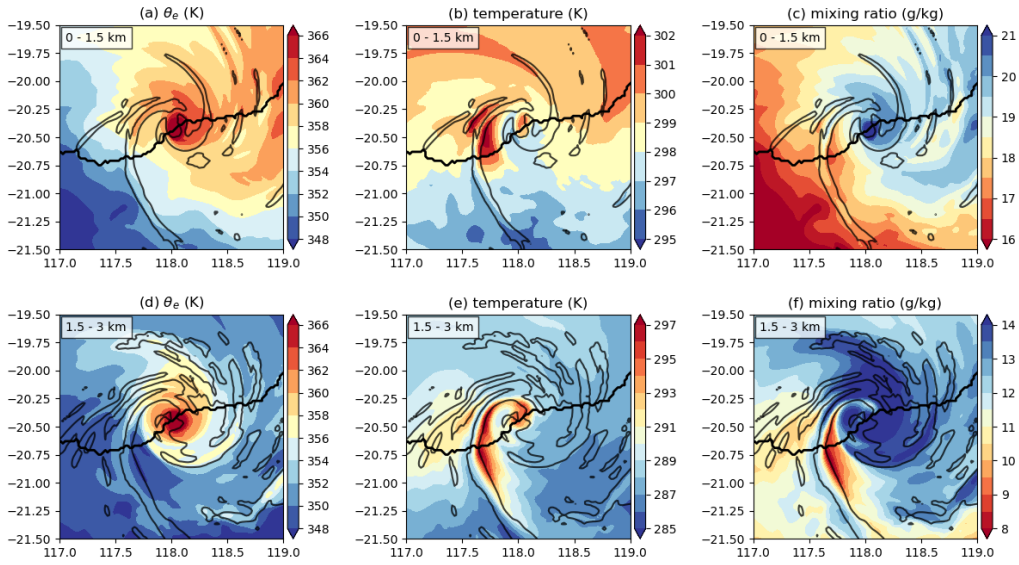


Figure 6.8: Equivalent potential temperature (θ_e ; K) averaged between 0 - 1.5 km (a) and 1.5 - 3 km (d). (b,e) The same as (a,d) but for temperature (K). (c,f) The same as (a,d) but for mixing ratio (g kg^{-1}). During a period of prominent eyewall break (T + 59; 25 September 2019 11:00 UTC). The black contours are the positive vertical velocity (averaged in the same layers) at 0.25 m s^{-1} .

over the land in the south. From as early as T + 15, the western spiral band no longer has a substantial cloud liquid water content. All metrics including the rainfall rate, radar reflectivity, and cloud liquid water content suggest that this band has become relatively dry. The majority of the precipitation and cloud is to the east of the spiral band and updraft, producing a stratiform layer of mixed-phase cloud, with a non-precipitating cirrus shield extending to the west.

Although liquid water and precipitation in the band decrease with time, wind speed, vertical velocity, relative vorticity, and convergence remain high, as shown in Figure 6.9. As the storm slowly moves closer to land, the spiral band starts to become the strongest vertical velocity feature in the lower troposphere, rivaling the main eyewall.

During the development of Veronica's persistent rainband structure, the band became progressively drier, especially to the upwind side which was defined by a downdraft. The majority of the storm precipitation falls in a stratiform region on the southeastern/downshear-left quadrant of the storm, which can be seen in Figures 6.7d-j. With the precipitation being heaviest (and over the greatest area) in the downshear-left quadrant, this suggests that the shear is dominating the distribution of convection (Chen et al., 2006) more-so than the translation is (Shapiro,

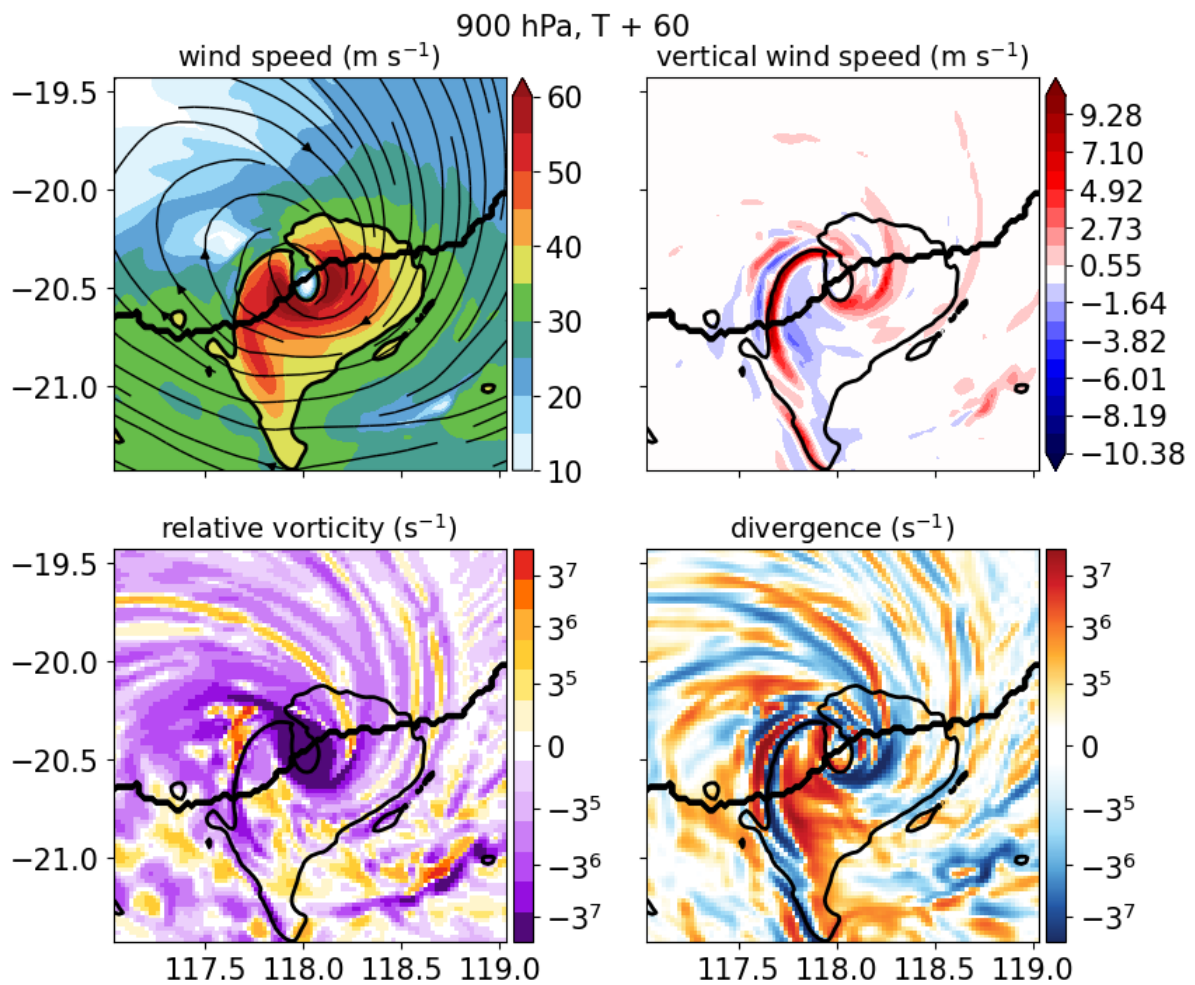


Figure 6.9: Total wind speed (m s^{-1}), vertical wind speed (m s^{-1}), relative vorticity (s^{-1}) and divergence (s^{-1}) for ensemble member 0 at 900 hPa, at 25 March 2019 1200 UTC. The thick black contour denotes the MetUM determined land-sea boundary, where the north side is sea. The thinner contour is the wind speed at 40 m s^{-1} .

1983).

A contrast starts to appear between the drying spiral band and the precipitating stratiform region. Figure 6.8e,f shows a boundary between the higher-entropy air and the thermodynamically depleted spiral band.

Once Veronica is close to the coast, the eyewall becomes elliptical with the long axis oriented in a north-south direction. Figures 6.9a and 6.10d show this, and also demonstrate that the streamlines over the larger storm system become elliptical in shape, with the streamlines expanding out into the northwest quadrants. Whilst near-stationary near the coast, Veronica begins to develop a break or ‘gap’ in the northern eyewall. The 950 hPa tangential wind redistributes, with the wind speeds substantially reducing over the sea and being maintained over land. During this period, Veronica translates very slowly ($< 5 \text{ m s}^{-1}$) and is experiencing moderate-high environmental vertical wind shear from the northwest ($\approx 10\text{-}15 \text{ m s}^{-1}$).

There is a local maximum in the 950 hPa tangential wind field along the inland rainband system (Figures 6.10d,f), which contributes further to the asymmetric storm structure. An asymmetry is also presented in the radial wind field (Figure 6.10b), where the rainband seems to be collocated with a region of ‘outflow’ (or, ‘reversed inflow’, since it does not fit with the classic image of a tropical cyclone outflow). In either case, the flow is diverted radially outwards along the band. Rainbands typically show weaker boundary layer inflow on their inner side (e.g. Powell, 1990; Kepert, 2018), although usually this perturbation is not so strong as to produce radial outflow. Reasons for the unusually strong radial flow perturbation in this case are discussed below.

Throughout the rest of the simulation (not shown), the storm system continues to weaken primarily from the offshore side while maintaining intensity inland and along the rainband. Across the ensemble, 15 out of 18 ensemble members presented a distinct eyewall break in the 950 hPa wind field and of the 3 members that did not, they still began to present an asymmetric wind field that suggests an eyewall break would have formed if the simulations were allowed to run for longer. All of the simulations showed an asymmetric precipitation distribution that was concentrated inland in the downshear-left quadrants, with mixed-phase cloud downwind of the dominant rainband.

6.4.3 Contribution of Rainband, Landfall and Shear

The spiral rainband is a prevalent and consistent feature across the ensemble. Could it be possible that the rainband is contributing to the eyewall break, either through the inflow of thermodynamically depleted air from the rainband into the inner core, or by another mechanism? Figure 6.10 shows azimuth-height sections of the tangential, radial and vertical winds at the RMW (Figure 6.10a,b,c) and plan views averaged across the lowest 1.5 km (Figure 6.10d,e,f). There are two major updraft maxima - the rainband system that spirals outwards from the northern eyewall, and the southern inner core (Figure 6.10c,f). The rainband exists within an increase in the tangential wind and a band of outflow. Note that due to the elliptical nature of the storm center, representing the wind in cylindrical coordinates will give rise to regions of apparent inflow and outflow. However, there is a robust positive signal in the radial wind along the rainband, regardless of its orientation to the storm center. This result is surprising, since idealised simulations (Hlywiak and Nolan, 2022) and observations (Rogers and Zhang, 2023) suggest that in landfalling tropical cyclones the maximum inflow tends to be just offshore as the flow accelerates off the coast.

In terms of the thermodynamics, Figure 6.8 shows the environment during the eyewall break. The equivalent potential temperature (θ_e) is strongly correlated to the mixing ratio at both height levels (0 - 1.5 km and 1.5 - 3 km). It is shown that the inner core θ_e is higher to the north (offshore) and is lower over land. At outer radii, the θ_e is asymmetrically distributed over the east and southeast, which agrees with the general distribution of precipitation. The rainband at this time is relatively dry and warm, which implies diabatic heating. Between 1.5 - 3 km altitude, there is a narrow band of dry air penetrating the inner core from the rainband system; however, this seems to be compensated in θ_e by the local increase in air temperature. Conversely, at the 0 - 1.5 km level, cooler air from the land seems to be entering the inner core but this is compensated by the high mixing ratio. Overall, there is no obvious decrease of θ_e within the eyewall break, either from the rainband or from the land.

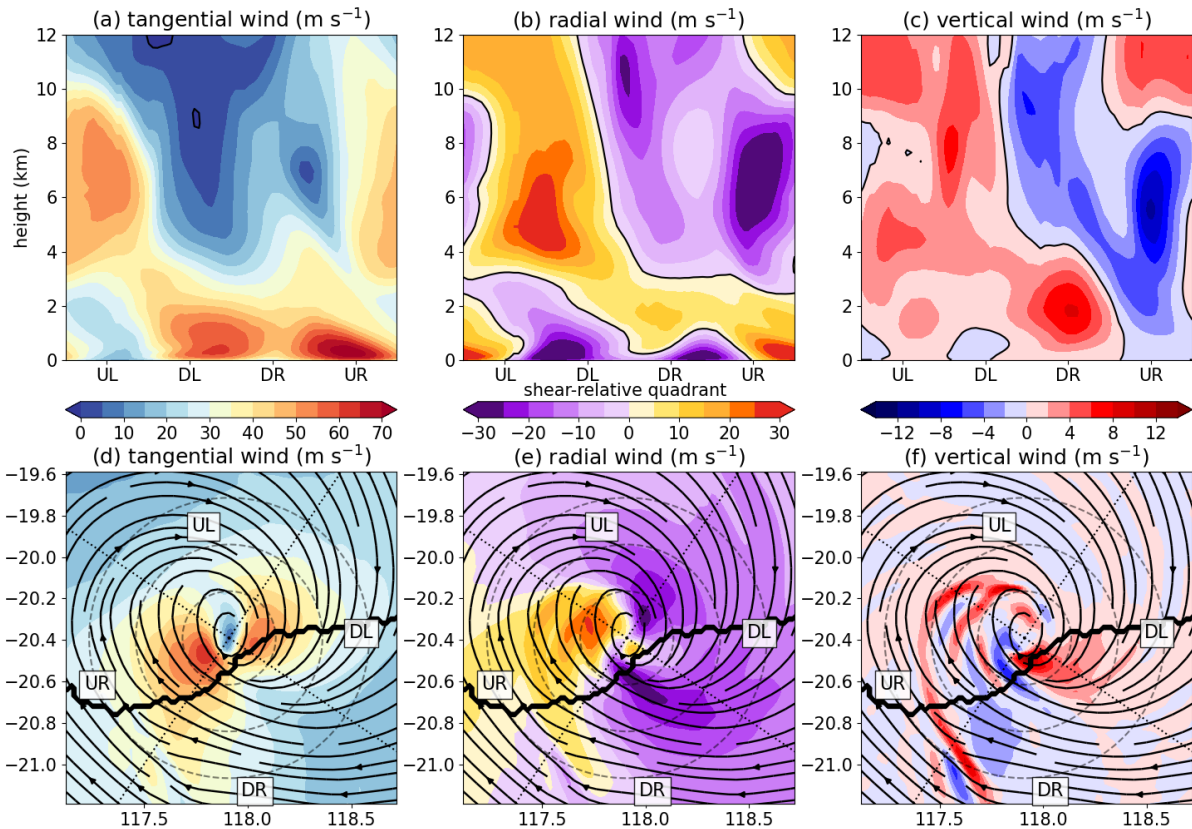


Figure 6.10: (a,b,c) Cross-sections at the RMW (12 km) at 25 March 2019 1200 UTC for tangential wind (m s^{-1}), radial wind (m s^{-1}) and vertical wind (m s^{-1}) respectively. The unfilled contours denote 0 m s^{-1} . (d,e,f) The same fields as (a,b,c) but in a plan-view averaged across the lowest 1.5 km. The coastline is shown as a thick black line. Streamlines correspond to the earth-relative wind field. The shear-relative quadrants are labelled as UL: upshear left, DL: downshear left, DR: downshear right, UR: upshear right. Faint dashed circles denote the radius at 25 km intervals.

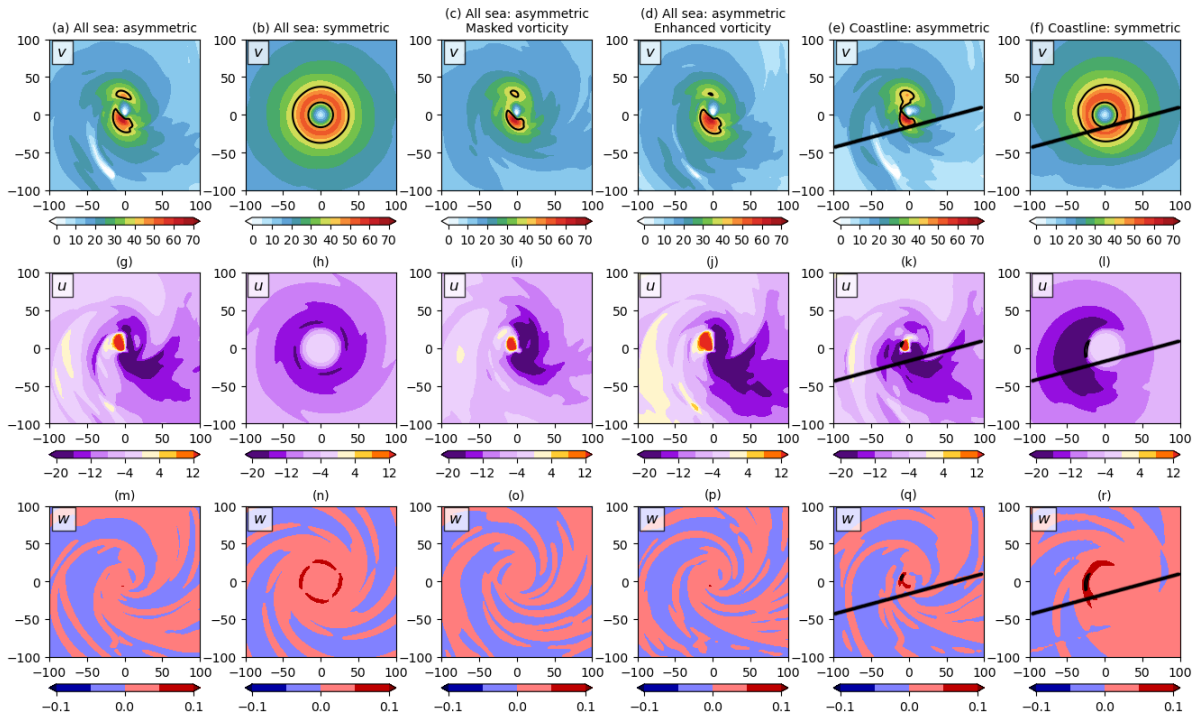


Figure 6.11: Wind fields outputted from the KW01 model at 10 m. (a) - (f) tangential wind (filled; m s^{-1}) with a black contour denoting the 40 m s^{-1} contour level. (g) - (l) The radial wind component (filled; m s^{-1}). (m) - (r) The vertical velocity (filled; m s^{-1}). The thick black line denotes the angle and position of the coastline. Units for the x- and y- axis are in km from the storm centre.

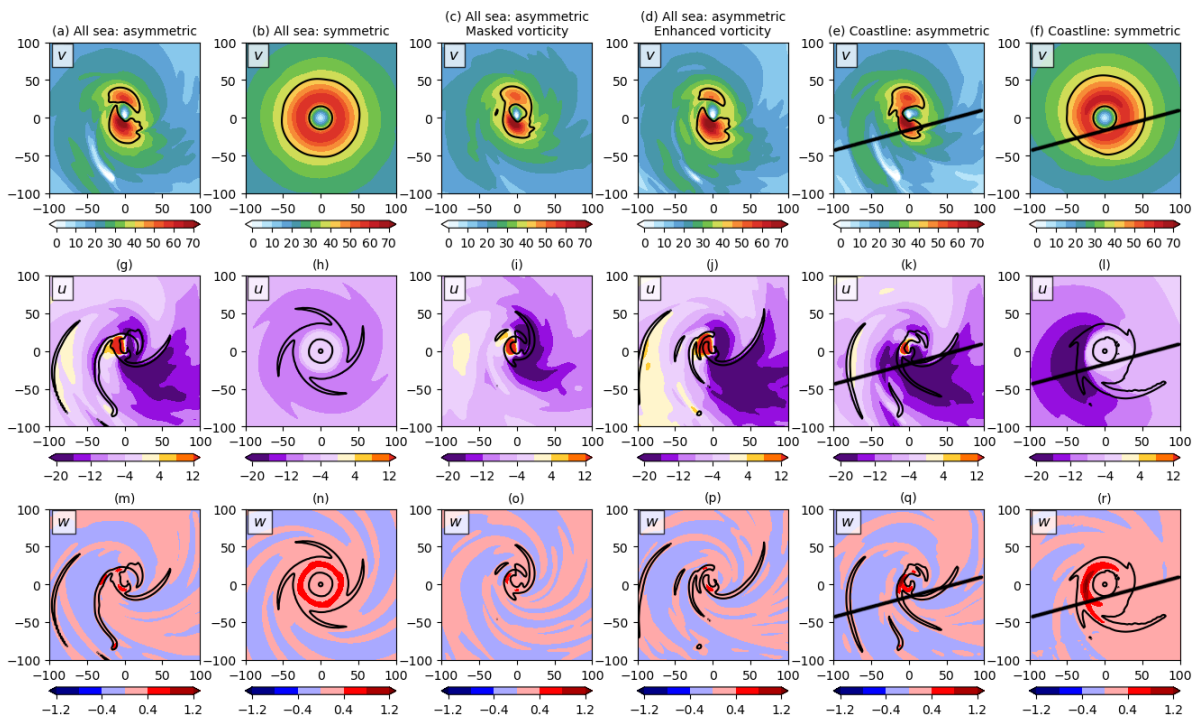


Figure 6.12: As in Figure 6.11, for 298 m altitude. The black contour in (g) - (r) is the vertical velocity at 0.1 m s^{-1} .

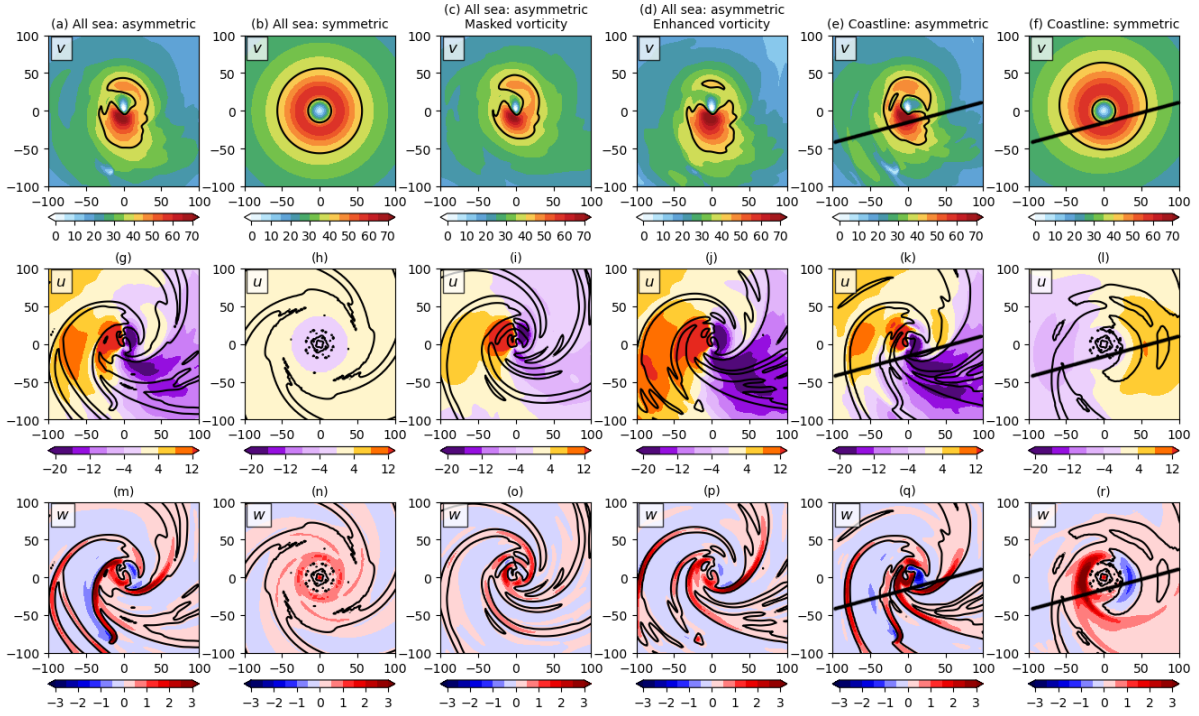


Figure 6.13: As in Figure 6.11, for 1648 m altitude. The black contour in (g) - (r) is the vertical velocity at 0.1 m s^{-1} .

To investigate the effects of the asymmetric environment and the coastline on the eyewall break, I set up a series of experiments using the KW01 model detailed in Section 6.2. The results are shown in Figure 6.11 (10 m), Figure 6.12 (298 m) and Figure 6.13 (1648 m), and are summarised in Table 6.1. At the 10 m level (Figure 6.11), adding a coastline leads to a reduction in the tangential winds over land in both the asymmetric (Figure 6.11e) and symmetric (Figure 6.11f) simulations, with some indication of the offshore flow to the west of the cyclone being strengthened. It is also clear that the addition of the land leads to a substantial asymmetry in the radial wind (Figure 6.11h vs Figure 6.11i), with the inflow velocity peaking offshore, consistent with the findings of Hlywiak and Nolan (2022) and Rogers and Zhang (2023). To a lesser extent, this increased inflow to the west of the cyclone is also shown in the asymmetric simulations including a coastline (Figure 6.11g vs Figure 6.11k), accompanied by a reduction in the outflow to the northwest of the eye.

When compared to the asymmetric all sea simulation (Figure 6.11a), at the 10 m level, it seems that masking the anticyclonic vorticity associated with the rainband feature leads to a more symmetric tangential wind field and an increase in the radial wind within $\approx 50 \text{ km}$ of the storm centre (Figures 6.11c,i). On the other hand, artificially increasing the magnitude of this vorticity

leads to a slightly more asymmetric tangential wind field, with a reduction in the north (Figure 6.11d), increased inflow in the southeast quadrant and increased outflow in the west (Figure 6.11j). These results are an indication that the vorticity is contributing to the eyewall break of Tropical Cyclone Veronica. It should be noted that although only the anticyclonic vorticity linked to the rainband was masked, the rainband also produced cyclonic vorticity. It is not possible to say whether there was a net positive or negative effect on the vorticity from the rainband and that is not the purpose of this analysis. Similar results are shown for the 298 m (Figure 6.12) and 1648 m (Figure 6.13) levels. Next, we will discuss the main differences and key results for these levels.

For all of the asymmetric vortexes, above 298 m, the tangential wind maximum is in the south. This includes the vortex with a coastline (Figure 6.12e). The symmetric vortex with a coastline (Figure 6.12f) does have an asymmetric wind distribution, but with the tangential wind maximum offshore rather than to the south, suggesting that the wind asymmetry shown in the MetUM is not predominantly the result of landfall dynamics. Similarly, the symmetric vortex with a coastline has a radial wind west-to-east through-flow above the surface level (Figure 6.12l and Figure 6.13l), but it is the opposite to the east-to-west through-flow present in the asymmetric simulations (e.g. Figures 6.12g,i,j,k). The symmetric simulation with a coastline suggests a westerly through-flow, whereas the asymmetric simulations suggest an easterly through-flow whether or not the coastline is included. Thus, the through-flow in the MetUM is not consistent with being produced by the dynamics of a landfall.

Similar to the 10 m level, at 298 m and 1648 m, the strength of the anticyclonic vorticity associated with the rainbands and convective features seems to be correlated with the strength of the radial wind. When the vorticity magnitude is increased, the strength of the through-flow also increases (Figure 6.13g vs Figure 6.13d). The opposite is true for the reduced vorticity (Figure 6.12i). This correlation further suggests asymmetric vorticity as a modulating factor.

However, the 298 m level demonstrates that the coastline does seem to play a role in modulating the asymmetry and magnitude of the vertical velocity. Figure 6.12r (the symmetric vortex with a coastline) demonstrates a clear maximum in the vertical velocity in the western quadrants, suggesting a feature spiralling outwards from the northern eyewall to the west and south. Qualitatively, this is consistent with the MetUM simulations (e.g. Figure 6.10c). Furthermore, the coastline has an enhancing effect on the magnitude of the vorticity, likely owing to frictional

convergence. There is also some indication that adding a coastline leads to an increase in the strength of vertical motion just offshore (Figures 6.12q,r). In fact, by comparing the symmetric simulations (Figure 6.12n vs Figure 6.12r), it seems that the coastline contributes to asymmetry in the low-level vertical velocity, shifting the maximum to the northwest quadrant. This feature is important because it correlates with the location of the spiral rainband seen in the full-physics simulations, suggesting a role of frictional convergence in modulating the intensity and position of the rainband.

Within the asymmetric simulations in Figure 6.12, there seems to be weak outflow associated with spiral bands of vertical velocity, particularly in the western quadrants of the storm, suggesting that rainbands can modulate the flow. We will discuss this more in Section 6.5.

To summarise the effects of these various factors on the wind asymmetries in the context of the eyewall break and asymmetric wind distribution, we devised a metric called the ‘eyewall break ratio’. The calculation of the eyewall break ratio is summarised by the schematic in Figure 6.14. Taking the minimum and maximum tangential wind along a constant radius would be inappropriate in this case due to the elliptical shape of the eyewall, which would project onto the calculation. Therefore, the methodology is as follows: the maximum tangential wind is taken from each radial around the storm (there are 72 points in our interpolation), with a maximum radius of 150 km from the storm centre. The eyewall break (EWB) is then calculated from the mean ($\overline{v_{max}}$) and minimum ($\min(v_{max})$) of this dataset, taking the form:

$$EWB = \frac{\min v_{max}}{\overline{v_{max}}}. \quad (6.1)$$

Thus, if the storm is completely symmetrical then the minimum should be equal to the mean, and the ratio would be 1 (no eyewall break). The lower the ratio, the larger the magnitude of the eyewall break. Results are shown in Table 6.1.

Firstly, it must be noted that although imposing a coastline onto a symmetric vortex does lead to some level of asymmetry, the eyewall break ratio only reaches 0.95 even though there are substantial asymmetries in the radial velocity that were absent in the all-sea case.

Looking at the simulations with an asymmetric vorticity field, there is no change in the magnitude of the eyewall break between the all sea simulation and that with a coastline. The major difference between these simulations is the maximum strength of the inflow layer, which

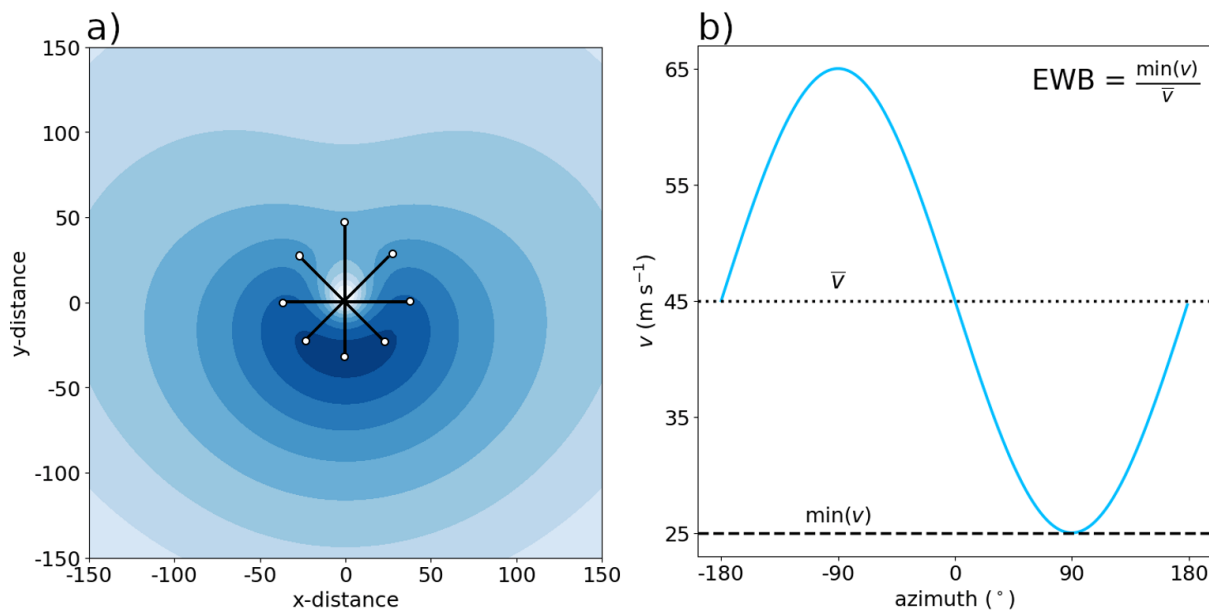


Figure 6.14: Schematic demonstrating the calculation of the eyewall break ratio (EWB). (a) an example asymmetric tangential wind field (v ; filled). The black lines are radials from the storm centre, with a white circle denoting where the maximum wind is. (b) Idealised asymmetric maximum winds from each radial, plotted by azimuth. The eyewall break ratio is the ratio of the minimum tangential wind ($\min(v)$) to the mean (\bar{v}).

increases by 5 m s^{-1} and shifts by 60° cyclonically when a coastline is added. There is also an effect on the maximum outflow, which is shifted anticyclonically by approximately 15° but remains of the same magnitude.

Removing the impact of the coastline (but consider that the effects of landfall and shear on the vorticity are already included due to the nature of the MetUM vorticity field used to input into the KW01 model), and masking the anticyclonic vorticity primarily linked to the rainband, leads to a reduction in all three of the following: the magnitude of the eyewall break, the maximum inflow and the maximum outflow. In contrast, artificially increasing the magnitude of the anticyclonic vorticity strengthens all three.

Table 6.1: The eyewall break (at 1648 m) and radial wind (at 298 m) metrics, calculated within 150 km of the storm centre. The angle, denoted by ϕ , is the azimuth of the eyewall break, the inflow maximum, and the outflow maximum for each dual column respectively.

| Simulation | Eyewall break | | Radial velocity | | | |
|---|---------------|-----------------------|---------------------------|------------------------------------|---------------------------|------------------------------------|
| | ratio | ϕ ($^{\circ}$) | min (m s^{-1}) | ϕ_{min} ($^{\circ}$) | max (m s^{-1}) | ϕ_{max} ($^{\circ}$) |
| All sea: Symmetric vortex | > 0.99 | | -9 | | 2 | |
| Coastline: Symmetric vortex | 0.95 | 285 | -17 | 220 | 9 | 350 |
| All sea: Asymmetric with masked vorticity | 0.7 | 310 | -26 | 150 | 37 | 300 |
| All sea: Asymmetric | 0.66 | 310 | -32 | 150 | 40 | 300 |
| All sea: Asymmetric with enhanced vorticity | 0.6 | 320 | -37 | 150 | 42 | 300 |
| Coastline: Asymmetric | 0.66 | 305 | -37 | 90 | 40 | 285 |

6.4.4 Vorticity Analysis

Although there are existing theories regarding the thermodynamics of eyewall break formation (which will be discussed in detail in Section 6.5.2), current theories do not seem to fully explain the Veronica case. Since the discontinuity is most prominent in the wind fields, it makes sense to take a closer look at the kinematics.

There are several aspects of Veronica’s dynamics which may be explained by exploring the relative vorticity in more detail, including the loss of symmetry of the maximum winds, leading to the development of an eyewall break. Notably, Veronica experienced a progression of cyclonically-rotating polygonal eyewalls, before becoming elliptical and eventually breaking open in the north, on the tip of the ellipse. Polygonal eyewalls have been linked to features such as eyewall mesovortices (e.g. Schubert et al., 1999; Kossin and Schubert, 2001) and vortex Rossby waves (VRW; e.g. Wang, 2001; Cha et al., 2020).

Figure 6.15 shows the wavenumber-2 asymmetry of the 900 hPa relative vorticity at the RMW, where the estimated propagation rate for Figure 6.15a is 21 m s^{-1} and for Figure 6.15b is 26 m s^{-1} . These figures represent approximately 43% and 52% (respectively) of the average maximum tangential wind speed throughout the time period. Veronica is a southern hemisphere storm, so the propagation of the asymmetry (denoted in dotted black lines) is cyclonic and the rate is consistent with previous studies, suggesting values around 50% of the maximum tangential wind (e.g. Reasor et al., 2000; Wang, 2002; Corbosiero et al., 2006).

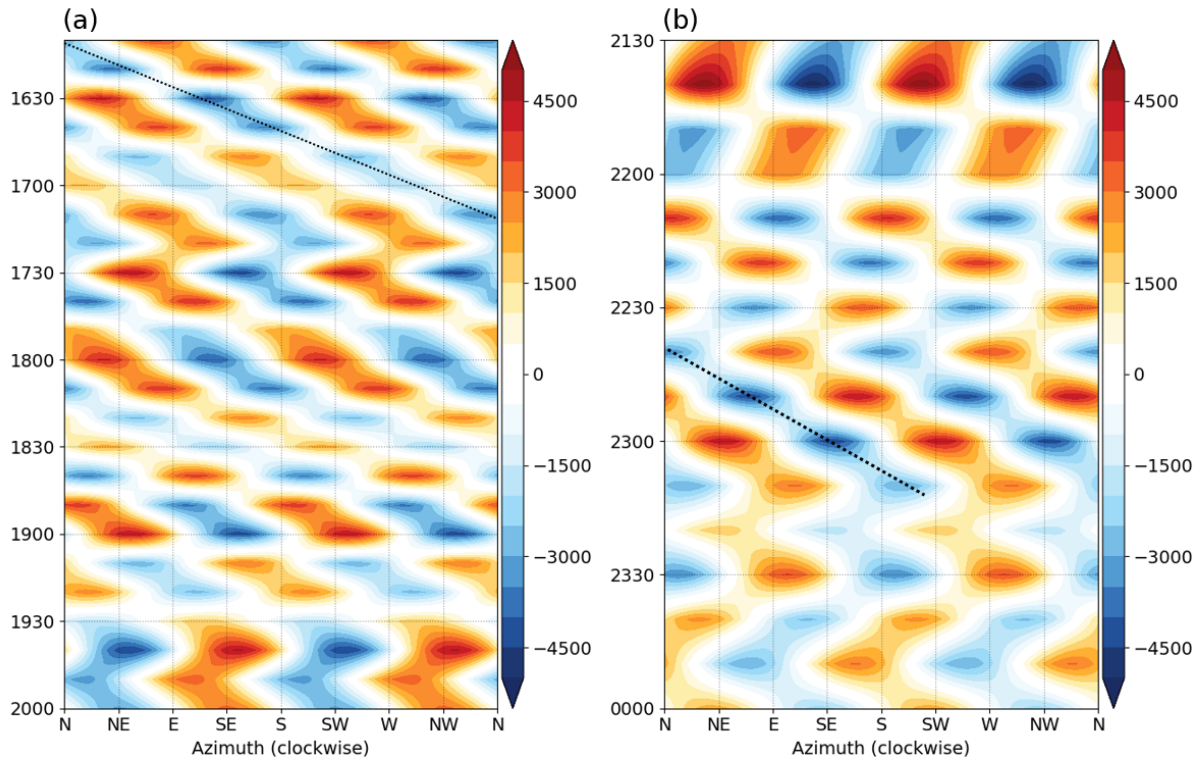


Figure 6.15: Azimuth-time Hovmöller diagram of the wavenumber-2 asymmetry of the 900 hPa relative vorticity (s^{-1}) at the RMW (12.1 km). Times correspond to 24 March 2019, prior to the eyewall break which occurred distinctly in the simulations on 25 March 2019.

To further investigate the role of relative vorticity in the eyewall break of Tropical Cyclone Veronica, I calculate the rotational and divergent components of the flow. If relative vorticity is defined as the curl of the motion vector ($\nabla \times \bar{V}$), then the rotational flow can be reconstructed from the relative vorticity field. I refer to any part of the flow not represented by the rotational component as being the divergent flow. This decomposition follows Helmholtz's theorem (Helmholtz, 1858) and is not in general unique, for there are flows which are both irrotational and nondivergent. The decomposition is here made unique by smoothly masking the relative vorticity to zero far from the storm. By separating the wind field into rotational and divergent flow components, the contribution of the relative vorticity can be diagnosed and quantified. Figure 6.16 shows these results, calculated using the MetUM relative vorticity field (Figure 6.16a) and wind field (Figure 6.16d) at a time during a prominent eyewall break ($T + 59$; 25 September 2019 11:00 UTC). The relative vorticity is re-calculated (Figure 6.16b) from the total flow (Figure 6.16d) to ensure the calculations are consistent with the MetUM outputted field (Figure 6.16a), and the divergence is also calculated in Figure 6.16c.

Figure 6.16e shows that the eyewall break can be reproduced by the rotational flow calculated

from the relative vorticity field. Since the non-linear balance equation for the mass field can be solved from purely rotational fields, the reproduction of the eyewall break in Figure 6.16 suggests that the feature is consistent with balanced flow dynamics. There is evidence that the rainband contributes strongly to the divergent flow (Figure 6.16f) but it does not have substantial signature in the rotational flow (Figure 6.16e), thus it must not be necessary to produce the eyewall break. Overall, the results shown in Figure 6.16e support the hypothesis that the larger-scale relative vorticity is playing a role in Veronica's eyewall break, and that such relative vorticity perturbations are not confined to the eyewall. To expand on this point, it is apparent that there is a north-south relative vorticity gradient across the storm (Figures 6.16a,b), in which there is more anticyclonic vorticity in the southern quadrants compared to the north.

In order to quantify this gradient, I removed the inner 40 km by 40 km of the relative vorticity field in Figure 6.16a to remove the cyclonic perturbation of the inner core, and then I averaged the relative vorticity over each 150 km by 150 km quadrant. By summing over a square in x-y coordinates rather than a quadrant in storm-relative coordinates, I ensure that there are an equal number of grid-points in each quadrant. The results are as follows: the northern quadrants had the highest cyclonic vorticity, with $-1.5 \times 10^{-4} \text{ s}^{-1}$ in the northwest and $-1.1 \times 10^{-4} \text{ s}^{-1}$ in the northeast. In the southeast quadrant, the overall relative vorticity falls to $6.9 \times 10^{-5} \text{ s}^{-1}$. The relative vorticity reaches a maximum in the southwest quadrant, becoming only weakly cyclonic overall, at $-2.1 \times 10^{-5} \text{ s}^{-1}$. The north-south vorticity ratio is therefore 0.331. The impact of the relative vorticity gradient will now be explored in more detail.

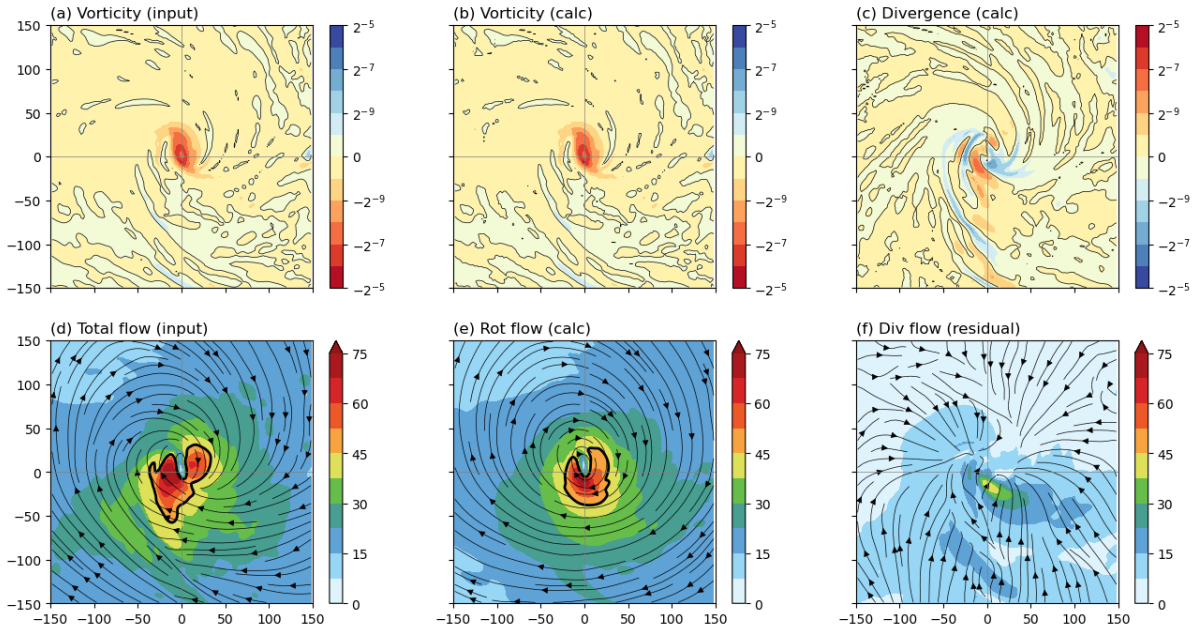


Figure 6.16: (a) Relative vorticity at (10^{-6}s^{-1}) input from the MetUM simulations at T + 59; 25 September 2019 11:00 UTC. (b) Relative vorticity (s^{-1}) calculated from the wind field in (d). (c) Divergence (s^{-1}) calculated from the wind field in (d). (d) Wind speed (filled; m s^{-1}) and streamlines from the MetUM at the same forecast time as (a), where the thick black contours denote the wind speed at 45 m s^{-1} . (e) The rotational flow (filled; m s^{-1}) and associated streamlines, calculated from the vorticity field in (b), where the thick black contours denote the wind speed at 45 m s^{-1} . (f) The divergent flow (filled; m s^{-1}) and associated streamlines, calculated as the residual of (d)-(e). Units for the x- and y- axis are in km from the storm centre and all fields are taken at 900 hPa.

The relative vorticity gradient present in Veronica is likely to be the result of a variety of contributions. At the storm scale, there are the vorticity dipoles which are presumably convectively modulated (since they align with the regions of precipitation in Figure 6.7), predominantly in the south.

The earlier discussed rainband produces strong vorticity perturbations (both positive and negative), with a cyclonic element that emanates from the northern eyewall and down to the south. In some cases, the rainband seems to encourage the elliptical shape of the inner core vorticity, by adding a cyclonic element to the north of the eyewall, which can be seen in Figure 6.16a. However, the cyclonic perturbation caused by the rainband to the south of the storm is dominated by the overall relative vorticity gradient in Figures 6.16a,b and Figure 6.3.

At the larger-scale, Figure 6.3a shows the large-scale environmental gradient of relative vorticity. It is evident that the south is providing more anticyclonic vorticity, potentially related to the eastwards propagation of a high-pressure system in the southwest of the domain. To the

north (and particularly the northwest) of Veronica, Figure 6.3a shows that there is net cyclonic vorticity, which may be related to the monsoon trough.

Considering that there are several factors which may be affecting the relative vorticity (for example, high vertical wind shear, landfall, a prominent spiral band of vorticity, and an asymmetric precipitation distribution), it makes sense to perform a Fourier decomposition in the horizontal plane to disentangle these effects. Following Reasor et al., 2000, a Fourier decomposition of low wavenumbers (0, 1 and 2) is shown in Figure 6.17. Wavenumber-0 (Figures 6.17a and 6.17e) represents the symmetric component. Wavenumber-1 and wavenumber-2 represent the asymmetric components, namely the environmental and the elliptical components respectively. Inferring from the sum of the symmetric and asymmetric environmental component (Figure 6.17f), there is a relative vorticity gradient whereby the southern quadrants have relatively more anticyclonic vorticity. This asymmetry is shown in Figure 6.17b. The wavenumber-2 component projects as an ellipse, which may go some way to explain the elliptical streamlines.

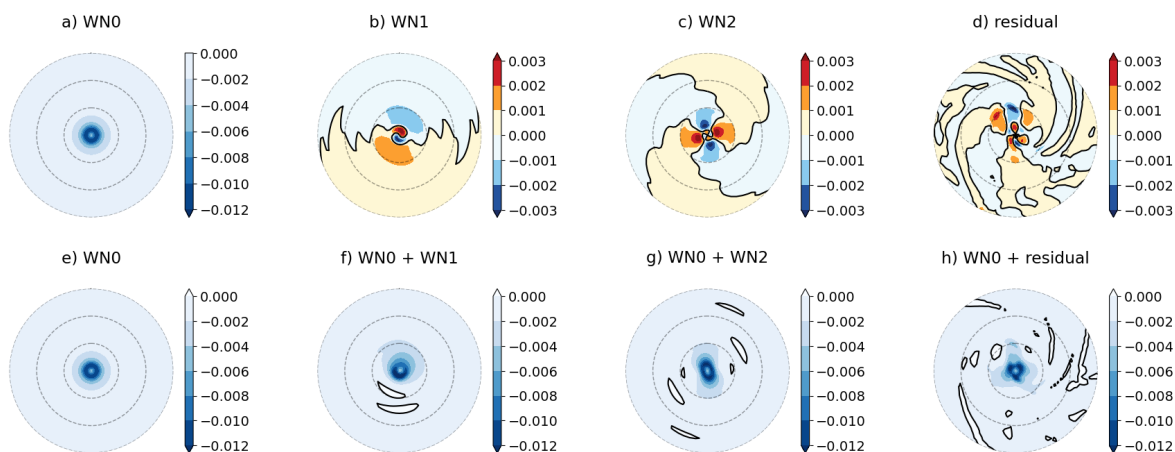


Figure 6.17: Fourier decomposition of the relative vorticity (s^{-1}) at T+59; 25 September 11:00 UTC, during prominent eyewall break (as shown in Figure 6.16). The top row, (a,b,c,d) represent: wavenumber-0, wavenumber-1, waveumber-2, and the residual, respectively. The bottom row (e,f,g,h) as in (a,b,c,d) with the symmetric field (wavenumber-0) included. Each dashed line denotes 50 km radius.

Guided by the wavenumber-1 asymmetry shown in Figure 6.17b and the raw relative vorticity field in Figure 6.16a, I devised an calculation whereby I imposed a north-south vorticity gradient onto a symmetric vortex to determine the effects on the rotational flow (Figure 6.18). Using the north-south vorticity gradient (0.331) calculated from Figure 6.16a, I designed an idealised vorticity gradient (Figure 6.18b) which produces a similar overall gradient (0.35) to the MetUM simulations when imposed onto the full vortex relative vorticity field (Figure 6.18c).

The asymmetric relative vorticity field in Figure 6.18b and its associated rotational flow in Figure 6.18e are intended to represent an idealised environmental gradient of relative vorticity, which is then imposed onto the stronger symmetric relative vorticity field in Figure 6.18a. This gradient is not so large that it distorts the relative vorticity field completely; the summed field in Figure 6.18c still looks nearly symmetric, but it has a noticeable effect on the rotational flow in Figure 6.18f.

This experiment shows that an environmental relative vorticity gradient can produce an eyewall break in the quadrants with a stronger cyclonic flow, and a redistribution of the winds to the quadrants where there is more anticyclonic vorticity. Although the full relative vorticity field in Figure 6.18c is not readily discernible as asymmetry, the velocity field (Figure 6.18f) has a clear visible asymmetry.

To further investigate the impact of relative vorticity gradients on asymmetric wind distributions and eyewall breaks, the experiment in Figure 6.18 was repeated for a series of vorticity gradient magnitudes. These results are shown in Figure 6.19. There is a relationship between the strength of the north-south vorticity gradient and the magnitude of the eyewall break. However, it is also evident from Figure 6.19 that the general wind asymmetry is impacted, with a reduction in the wind speed in the northern quadrants and an increase in the south. Furthermore, the progression shown in Figures 6.19b,d,f,h suggest that a relative vorticity gradient across the whole storm system can produce an elliptical eye and weakly elliptical streamlines, becoming flatter in the quadrants with relatively higher anticyclonic vorticity.

Strengthening the argument that relative vorticity asymmetries can be related to eyewall breaks, Figure 6.20 shows the correlation between the overall north-south vorticity ratio and the magnitude of the eyewall break for a series of experiments, following the methodology of Figures 6.18 and 6.19. The correlation coefficient, using Pearson's correlation coefficient (Pearson, 1901), is > 0.99 .

From this correlation and consistent with the mathematics of the vorticity calculation, it is apparent that there is a strong positive relationship between the vorticity gradient and the magnitude of the eyewall break. In particular, Figure 6.20 shows that as the north-south vorticity gradient increases, so does the magnitude of the eyewall break.

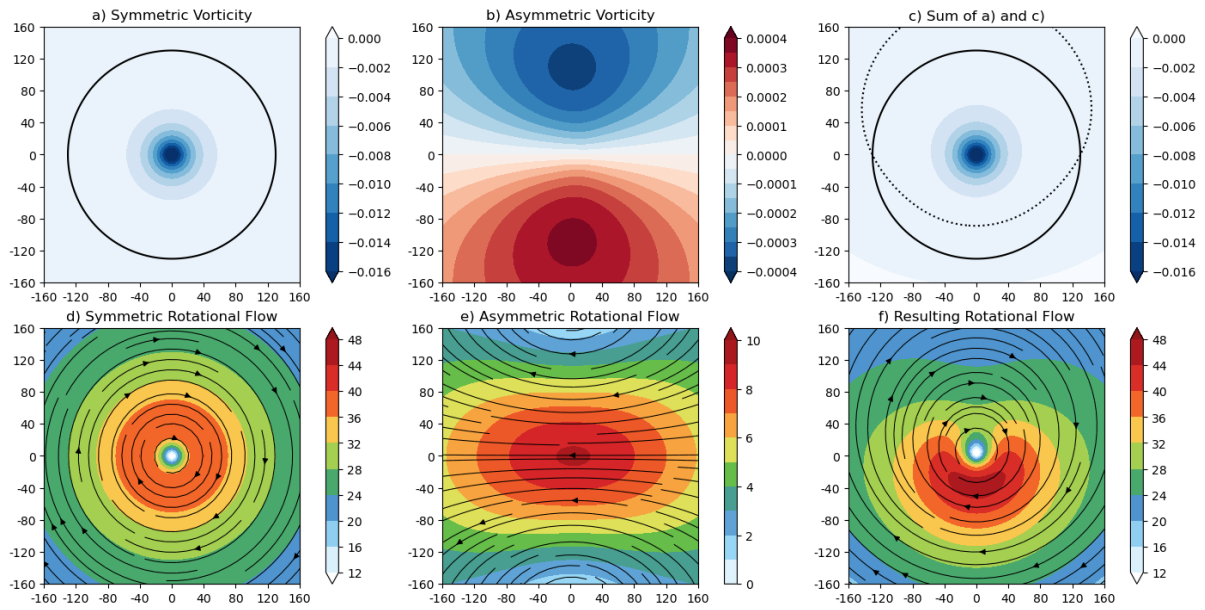


Figure 6.18: (a) Idealised symmetric relative vorticity field (s^{-1}) with a reference contour at $-0.0005 s^{-1}$. (b) Idealised north-south vorticity gradient (s^{-1}). (c) The sum of (a) and (b) with a reference contour at $-0.0005 (s^{-1})$ for (a) (solid) and (c) (dotted). (d) The symmetric rotational flow (s^{-1}) calculated from (a). (e) The rotational flow (s^{-1}) calculated from (b). (f) The rotational flow calculated from (c) (s^{-1}).

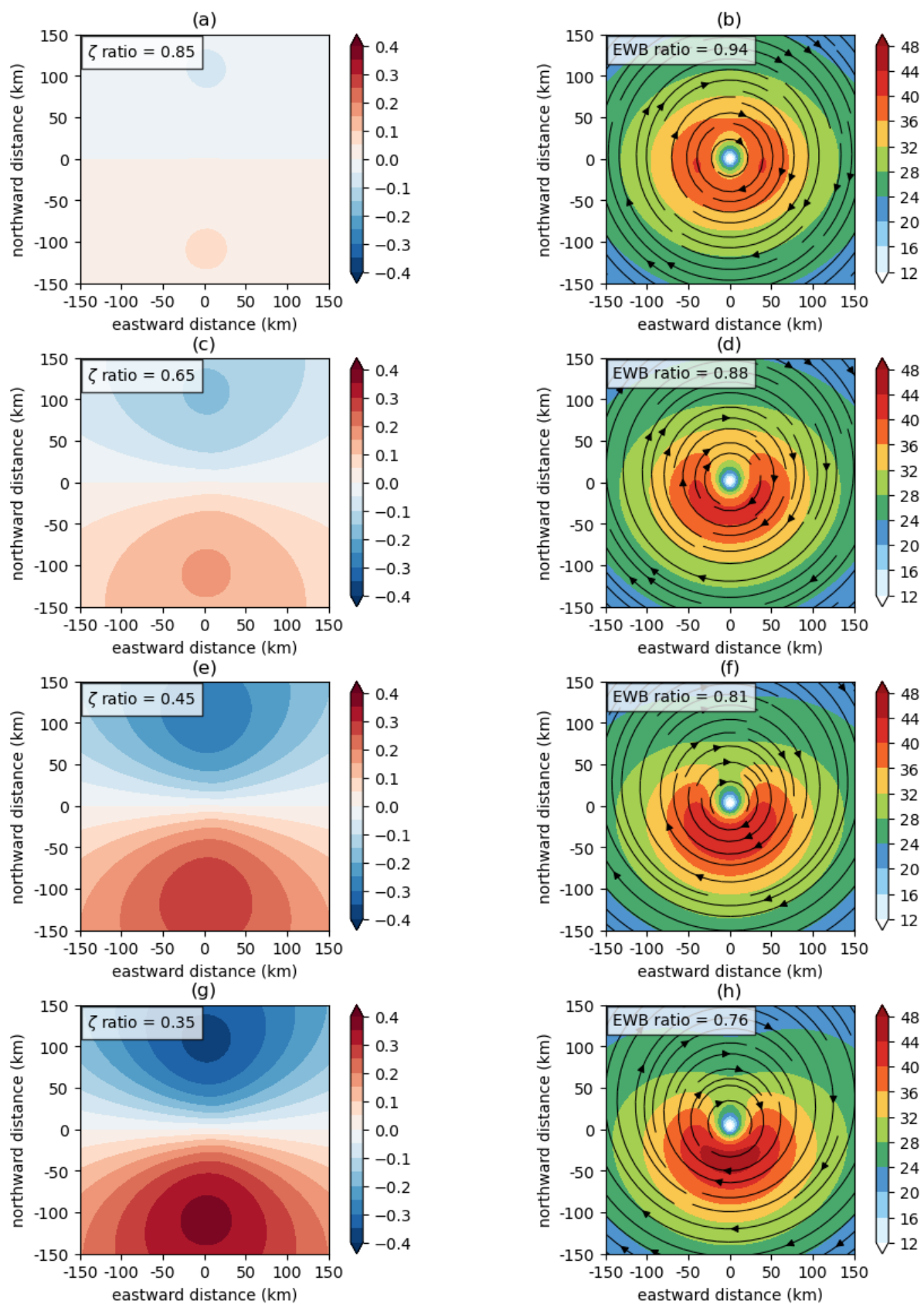


Figure 6.19: (a),(c),(e),(g) Idealised relative vorticity gradients (10^{-3} s^{-1}) with their overall north-south vorticity ratio annotated. (b),(d),(f),(h) The rotational flow calculated from the asymmetric vorticity field the symmetric field (e.g. Figure 6.18c). The eyewall break ratio is annotated. Calculations for the eyewall break ratio and vorticity ratio are described in-text.

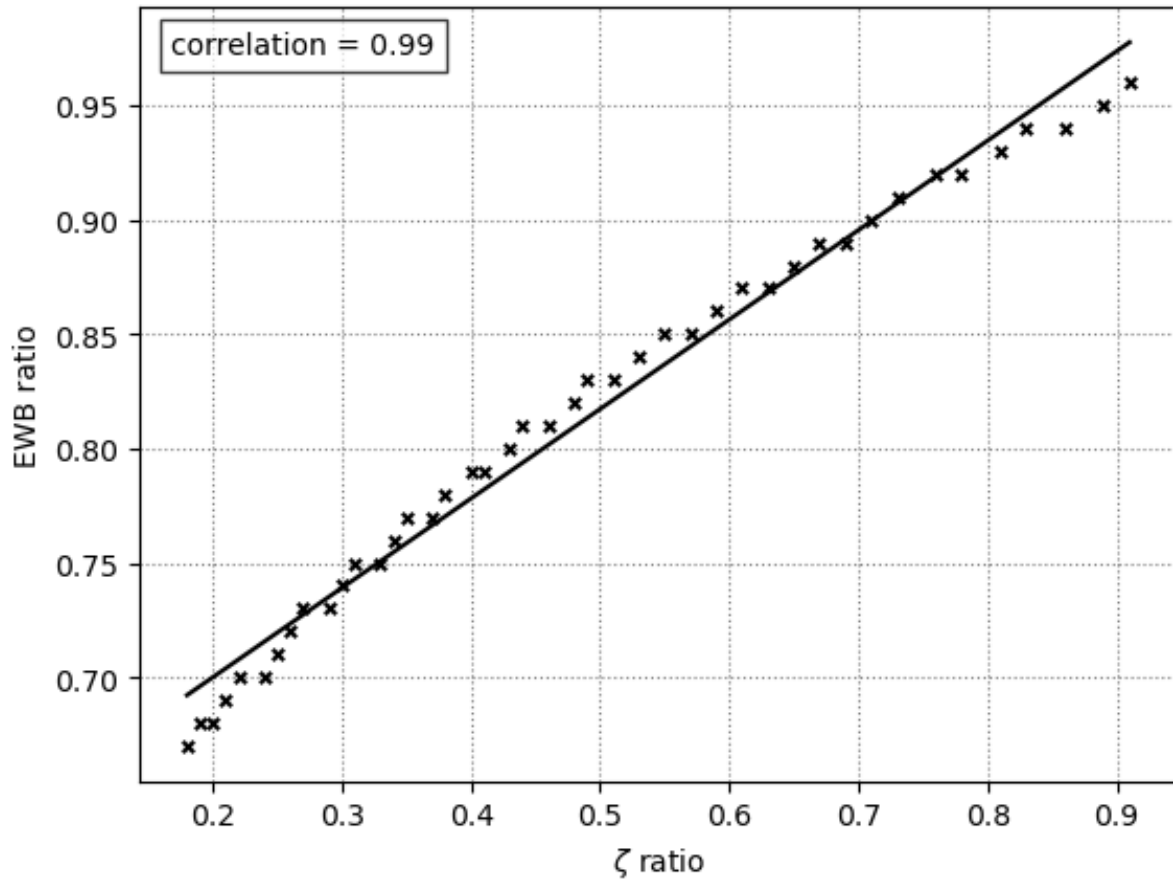


Figure 6.20: Correlation between the north-south relative vorticity gradient (ζ ratio) and the eyewall break (EWB) ratio. Correlation coefficient (annotated) is calculated using Pearson's correlation coefficient (Pearson, 1901) with a confidence level of $> 99.9\%$.

6.5 Discussion

The results presented in the previous sections show that there are multiple influences on the storm asymmetry, which we will now discuss. First, I demonstrated that the rainband structure may be contributing to the eyewall break by outwardly diverting the flow in the west/northwest quadrants, distorting the streamlines in Figures 6.9 and 6.10 into an elliptical shape. The radial wind of this band (Figures 6.10c,f) is structurally different to idealised studies by Hlywiak and Nolan (2022) which show the maximum inflow should be just offshore, attributed to an acceleration caused by the abrupt decrease on frictional stress. There is also disagreement with an observational study over landfall (Rogers and Zhang, 2023), which produced similar results to Hlywiak and Nolan (2022). However, we were able to reproduce these previous results by simulating a symmetric vortex within 15 km distance from a coastline (Figures 6.11l, 6.12l, 6.13l), which suggests that the radial wind in the rainband of Tropical Cyclone Veronica (Figures

6.10c,f) is being dominated by asymmetric processes unrelated to landfall.

It is known that rainbands can modify the flow around a tropical cyclone. For example, Kepert (2018) showed using the KW01 boundary layer model that rainbands can produce local wind perturbations. While the focus was on the azimuthal velocity, the author showed that there was also a local perturbation in the radial wind, in which the inflow velocity was reduced along the inside of the rainband. At the surface level, this impact on the radial wind is supported by observational studies which showed a decrease in the strength and depth of inflow along the inner/upwind edge of rainbands (Powell, 1990; Skwira et al., 2005). I therefore hypothesise, using the results of Kepert (2018) and Skwira et al. (2005), and the analysis shown in Figure 6.10, that the presence of a strong rainband can exert its own influence on the dynamics and can reduce the boundary-layer inflow on its inner edge which, in this case, was strong enough to lead to a narrow band of outflow below about 2 km height. In fact, this ‘outflow’ is likely to be related to convergence into the rainband, rather than being a typical tropical cyclone outflow. The ‘outflow’ along the band is also likely compounded by the through-flow imposed by the relative vorticity gradient, which was shown in Figures 6.13g,i,j,k.

Through idealised simulations using the KW01 boundary layer model (Figures 6.11, 6.12 and 6.13), the strength of convection in the rainband (implied by w) was found to increase in simulations with a coastline compared to those in an all-sea environment. This result suggests that the land plays a role in modulating the convection via frictional convergence and would further support the hypothesis that the radial wind perturbation is related to convergence. Furthermore, having increased convection in this region is consistent with the direction of the strong vertical wind shear. For example, an observational study over storms in the northern hemisphere by DeHart et al. (2014) showed that in sheared environments, convection propagates azimuthally, initiating downshear right, reaching a convective maximum in the downshear left quadrant, and weakening upshear. The results presented here, for example in Figure 6.10, are consistent with these findings when re-oriented for the southern hemisphere.

The relevance of the rainband is supported by simulations shown in Figure 6.13 which suggest that masking (increasing) the strong anticyclonic relative vorticity signatures associated with convection can reduce (enhance) the magnitude of the eyewall break. To clarify, the conclusion is not that rainbands and convection have a net anticyclonic impact on the storm, but that they contain anticyclonic and cyclonic elements. When the overall vorticity gradient is reduced

by masking the anticyclonic regions, the magnitude of the eyewall break is reduced. In the following paragraphs, I will discuss the relationship between relative vorticity asymmetries and eyewall breaks, and the potential sources of vorticity asymmetries in Tropical Cyclone Veronica.

We showed in Figures 6.16 that the general structure of the eyewall break and asymmetric wind distribution can be reproduced numerically from the relative vorticity field using only the rotational flow. Through idealised experiments (Figures 6.18 and 6.19), eyewall breaks were reproduced by imposing a vorticity gradient onto a symmetric relative vorticity field. The eyewall break ratio calculated for the idealised experiments (Figure 6.16f; 0.76) was higher than expected - all of the asymmetric simulations using the KW01 model (summarised in Table 6.1) had eyewall break ratios ≤ 0.7 , which suggests that although the bulk north-south vorticity gradient could reproduce an eyewall break, that there were other contributing factors in the deformation of Veronica's eyewall. Such factors likely include the flow perturbations of the rainband discussed above, and shown in Figure 6.10. Despite this, the experiment in Figure 6.16 did reproduce an asymmetric wind distribution similar to that in Veronica (e.g. Figure 6.9).

There is also a strong correlation between the strength of the vorticity gradient and the magnitude of the eyewall break in the idealised experiments (Figures 6.19 and 6.20), suggesting a positive relationship between relative vorticity and tropical cyclone wind asymmetries. Figure 6.19 showed that as the vorticity gradient became stronger, the overall wind field became more asymmetric, with the highest wind speeds in the quadrants with the most anticyclonic vorticity. This relationship can be explained by the rotational flow produced by the vorticity gradient. The relative vorticity gradient in Figure 6.18b produces a cyclonic gyre in the north and an anticyclonic rotation in the south. In Figure 6.18e, the rotational flow demonstrates why the cyclonic perturbation causes an eyewall break. Due to the nature of the vorticity gradient, the bottom half of the cyclonic perturbation (about 30 km north in Figure 6.18e) produces an easterly flow, which disrupts the westerly tangential wind of the eyewall. Similarly, the top half of the anticyclonic perturbation (about 30 km south in Figure 6.18e) also produces an easterly flow, which enhances the easterly tangential wind in the southern eyewall. This effect takes place across the domain, dampening the tangential wind in the north and enhancing it in the south. The mechanism presented here, along with the strong positive correlation in Figure 6.20, suggests that the relative vorticity gradient was a causal factor in the eyewall break of Tropical

Cyclone Veronica.

Overall, the total effect of a relative vorticity gradient on the wind distribution of a tropical cyclone will depend on the relative intensity of the symmetric (wavenumber-0; e.g. Figure 6.17a,e) and the asymmetric wavenumber-1 (e.g. Figure 6.17b,f) component of relative vorticity, which has been approximated here using the north-south vorticity gradient from a wavenumber-1 like asymmetry (Figures 6.18b and 6.19a,c,e,g) imposed onto a symmetric vortex. As I have discussed, the magnitude of an eyewall break in a real tropical cyclone may also be affected by smaller-scale dynamics, such as rainband-type features.

It is also evident from Figure 6.19 that increases in the relative vorticity gradient can make the streamlines more elliptical, flattening out in the south. This was a feature in Veronica's wind field (Figures 6.9a, 6.10d,e,f and 6.16d). Similarly, from the same figures, Veronica exhibits an elliptical eye. Such a feature begins to become increasingly evident in the idealised simulation in Figures 6.19b,d,f,h as the vorticity gradient increases. These results strongly suggest that the vorticity gradient of Tropical Cyclone Veronica contributed to key dynamics, such as: the eyewall break, the overall wind asymmetry, the elliptical eye, and the elliptical streamlines. Next, we will discuss the potential source of the vorticity gradient.

A Fourier decomposition of the relative vorticity field into the low wavenumbers (0, 1 and 2), shown in Figure 6.17, demonstrated a strong wavenumber-1 asymmetry with anticyclonic vorticity in the south, and cyclonic in the north. This asymmetry broadly lines up with the environment as a whole, whereby an anticyclone is moving eastward in the south of the domain, and the monsoon trough is providing anticyclonic forcing in the north of the domain. There is some evidence for fine-scale relative vorticity inland, likely enhanced by wind shear and frictional convergence; however, the convective vorticity dipoles are propagated azimuthally and tend to contain a stronger cyclonic component (Montgomery and Smith, 2014), which is unlikely to contribute to the overall imbalance of anticyclonic vorticity in the south. Additionally, the ellipticity of the streamlines in the idealised experiment (Figure 6.18f) is less pronounced than in the MetUM (e.g. Figure 6.16d,e), suggesting a contribution from the wavenumber-2 component of relative vorticity (Figure 6.17c).

While it is plausible that vertical wind shear would cause a vorticity asymmetry in TCs, this effect has not been widely studied and the observational evidence is not clear-cut (Figure 2.4 of Section 2.4). Therefore, it is difficult to conclude whether or not the vorticity gradient is

shear-driven. For example, using radar observations Shimada et al. (2024) (Figure 2.4a), Boehm and Bell (2021) (Figure 2.4c) and Reasor and Eastin (2012) (Figure 2.4d) suggest that vorticity dipoles are oriented relative to shear, with the inner-core cyclonic perturbation on the left-of-shear quadrants and the anticyclonic perturbations to the right-of-shear. These studies were all performed in the northern hemisphere, so note that the cyclonic vorticity is positive and that positive asymmetric vorticity left-of-shear in the NH would correspond to right-of-shear negative asymmetric vorticity in the southern hemisphere. Therefore, the results of the inner core vorticity asymmetries are consistent with the Fourier decomposition analysis shown in Figure 6.17. All of these studies also suggest a reversal in the sign of the vorticity dipoles at larger radii, again supporting the findings in Figure 6.17, which places the anticyclonic vorticity perturbation to the right-of-shear (left-of-shear in SH) at larger radii. However, Boehm and Bell (2021) suggest that the strength of the signal is maintained in the second dipole, whereas Shimada et al. (2024) and Reasor and Eastin (2012) indicate a drop in the strength by about 50%. Furthermore, Boehm and Bell (2021) show a third vorticity asymmetry reversal at even larger radii, which is not reflected in the other two studies (Reasor and Eastin, 2012; Shimada et al., 2024).

While these results (Reasor and Eastin, 2012; Boehm and Bell, 2021; Shimada et al., 2024) seem to be generally consistent with Veronica's relative vorticity gradient (Figures 6.16, 6.17), Shimada et al. (2024) also present a different result (Figure 2.4b), which suggests a more downshear-upshear orientation of the shear. Figure 2.4b shows that in steady-state tropical cyclones, the anticyclonic vorticity asymmetry is downshear and the cyclonic component is more upshear. There also seems to be no reversal in the dipole at larger radii in Figure 2.4b. Although Shimada et al. (2024) suggested that the variation in the asymmetry is related to the intensification stage, this suggestion is not supported by the other cases - although Figure 2.4b is based on steady-state tropical cyclones and Figures 2.4a,d are intensifying storms, both Figure 2.4b and the present work on Tropical Cyclone Veronica are based on weakening storms. Therefore, while we can say the results in Figure 6.17b are broadly consistent with the literature in terms of the gradient of vorticity relative to shear, the impacts of shear on the horizontal distribution of vorticity are still not entirely clear.

The environmental gradient presented by the wavenumber-1 asymmetry motivated the idealised numerical analysis in Figure 6.17. By producing an idealised, weaker vorticity gradient similar

to the overall asymmetry, and imposing this onto the vorticity field for a symmetric vortex, we were able to reproduce an eyewall break from the rotational flow. This result suggests that the asymmetric distribution of relative vorticity in the larger-scale environment, specifically the wavenumber-1 asymmetry, plays a key role in producing an eyewall break. The break tends to occur where the cyclonic vorticity is higher, whereas the bulk of the wind field gets redistributed over the region of relatively lower cyclonic vorticity.

It has been shown using simple numerical experiments that an eyewall break can be reproduced by imposing a largescale relative vorticity gradient onto a symmetric vortex. The cause of this vorticity gradient may be complex in reality. In the case of Veronica, I suggest a range of processes that may contribute to the vorticity gradient. For example, the largescale contributions of the eastwardly propagating anticyclone in the south and the monsoon trough providing cyclonic vorticity in the north. More locally, vorticity asymmetries are likely to be modulated by the moderate-strong vertical wind shear, frictional convergence induced by the land, and topographical influences. Overall, I have demonstrated using KW01 boundary layer model that while the imposition of a coastline increases the frictional convergence and convection over land, this does not have a substantial effect on the magnitude of the eyewall break, suggesting the larger dynamical environment is the dominant influence.

However, in this case there is some evidence for the primary spiral rainband contributing to the eyewall break and elevation of the BL wind speeds over land. For example, as previously discussed, the rainband induces an outward flow in the west/northwest storm quadrants, distorting the flow and thus contributing to the elliptical streamlines shown in Figure 6.9. The rainband also contributes to the vorticity budget (which is not shown), primarily through tilting, which creates a spiralling band of cyclonic vorticity emanating from the northern eyewall. This strong perturbation in vorticity at the tip of the eyewall, where we see the break, increases the local vorticity gradient in the inner core. Therefore, while there is an environmental relative vorticity gradient, the rainband still contributes on a local level.

6.5.1 Thermodynamic Contribution

We have presented a dynamical explanation for the eyewall break of Tropical Cyclone Veronica, but thermodynamics are widely accepted to play a direct role in intensity change (e.g. Emanuel, 1986). At the most basic level, tropical cyclones making landfall would be expected to weaken

due to a reduction in surface enthalpy fluxes, particularly the reduction in latent heating. During landfall, thermodynamics can also play a role in the boundary layer and mid-levels. For example, Hlywiak and Nolan (2022) showed that the boundary layer inflow velocity can accelerate as the flow travels offshore, which very likely would transport drier air into the inner core, especially given the extensive desert region in Australia’s northwest. Dry air intrusion during landfall has been shown to induce storm weakening (Kimball, 2006) and rainband systems have been observed to have relatively low surface θ_e signatures (Skwira et al., 2005), which has been linked to the slowed intensification of landfalling tropical cyclones (Kimball, 2006).

Furthermore, Figures 6.10b and 6.10c show a region of strong mid-level inflow collocated with a downdraft at approximately 270° , which could suggest both radial and downdraft ventilation. ‘Ventilation’ here refers to the transport of dilution of the inner core θ_e , either by the radially inward transport of low θ_e from the environment (radial ventilation, e.g. Tang and Emanuel, 2012b; Alland et al., 2021b), or by downdrafts from the dry mid-levels penetrating the inflow layer (downdraft ventilation, e.g. Riemer et al., 2010; Tang and Emanuel, 2012a; Alland et al., 2021a).

If there was a thermodynamic explanation for the eyewall break in this case, following the above discussion, it would be expected that the stronger regions of the storm exist in a higher θ_e environment. Figure 6.8 shows no substantial depletion of the θ_e within the region of the eyewall break, at a time when the eyewall break was already established. In fact, within the inner core the θ_e is asymmetrically distributed over the northern (sea) side of the storm, with a reduction along the landfalling rainband in the south and southwest. This does not immediately appear to be consistent with the suggestion that the eyewall break is a result of thermodynamic depletion by any of the processes listed above.

6.5.2 Other Theories and Cases

A recent study by Fischer et al. (2023) addressed a collapse of upshear inner core convection in a 60-member ensemble. Though not related to landfall, this investigation is relevant due to the shear-relative location of the eyewall degradation, which is consistent with Veronica. The authors indicate that the collapse of convection was related to downdraft ventilation caused by mid-level inflow with a downdraft below, similar to what is shown at around 270° in Figures 6.10b and 6.10c. Despite the similarities in the secondary circulation and the shear-relative

location of the breakdown, I found no evidence to suggest that the depletion of inner core θ_e via downdraft ventilation was a contributing factor to the eyewall break in the case of Veronica (as discussed above).

We now consider the possible impact of VRWs. Wang (2002) found that outer rainband perturbations can contribute to eyewall breaks via the amplification of eyewall VRW, so long as they are in phase with each other. The impact of VRW on the eyewall instability and shape distortion was briefly discussed and supported by Figure 6.15. There are multiple other proposed mechanisms by which VRW can contribute to eyewall distortion. For example, Wang (2001) showed that when there is inner-core inflow associated with VRW activity, the eyewall convection can be enhanced and pushed inward, with the outflow producing the opposite effect. Contorting the inner core in such a way could disrupt the circular nature of the eyewall and can even result in breakdown (Wang, 2001). In the previous sections, I discussed the outflow collocated with the spiral band shown in Figure 6.10e, prior to the eyewall breakdown. The outflow extends into the north-northwest region of the inner core. Following the arguments of Wang (2001), in Veronica the VRW could have been propelled radially outward in the northern eyewall, which would begin to explain the streamlines in Figure 6.9a. However, it is unclear whether this caused an expansion of the eyewall; rather, the eyewall broke apart. The breakdown of eyewalls due to VRW has been documented (Reasor et al., 2000; Corbosiero et al., 2006) and in effect, VRW can contribute both to changes in the shape, and to the breakdown of, tropical cyclone eyewalls.

While it is possible that VRW contributed to instability in the Veronica's eyewall, the VRW activity was present during the polygonal eyewall stage, much prior to the eyewall break. Furthermore, I have demonstrated that a larger scale relative vorticity gradient (which does not seem to be present in the case of Wang (2002)) can produce an eyewall break similar to what is observed in Tropical Cyclone Veronica, without any VRW activity. These results suggest that Veronica was subject to a different eyewall break process, and that multiple factors may lead to the formation of eyewall breaks depending on the environment and internal storm dynamics.

Chen and Yau (2003) present a similar case to Veronica whereby a landfalling tropical cyclone undergoes an eyewall break which is collocated with a spiral band of elevated potential vorticity (PV), although with the possibly significant difference that their storm did not stall on the coast. In this case, the relative location of the eyewall break, the spiral band and the coastline

are different compared to Veronica. There also seems to be no large-scale vorticity gradient, due to the design of their experiment where asymmetries were removed prior to initialisation. Chen and Yau (2003) agree that the spiral band is fuelled by frictional convergence and vertical wind shear, and that it has relevance for the asymmetry of the inner core. Without a direct analysis of their data, I propose that the study by Chen and Yau (2003) is consistent with the findings presented here, in that their rainband contributes to a cyclonic vorticity perturbation within the outer circulation, which is on the same side as the eyewall break, as it was in our simulation of Veronica. In the absence of environmental asymmetries, the rainband perturbation may be enough in itself.

One example of a case which is consistent with the Veronica findings and the relative vorticity theory presented here, is Hurricane Idalia (2023). The radar data is shown in Figure A.1 and the asymmetric tangential wind field mirrors Veronica, but bears an even more remarkable resemblance to the idealised experiment presented in Figure 6.18f, in which a relative vorticity gradient was imposed onto a symmetric vortex. A combination of the radar data in Figure A.1c and the ERA5 reanalysis implies a strong vorticity gradient across Idalia, with the outer-circulation cyclonic vorticity anomaly in the west, and the anticyclonic perturbations in the east. The direction of the vorticity gradient in Idalia is consistent with the results shown here. Furthermore, Idalia was under the influence of easterly shear, meaning that the asymmetries in the wind and vorticity fields relative to the wind shear are similar to those in Veronica, placing the relatively more cyclonic vorticity and eyewall break downshear. This relationship between low-level vorticity anomalies and the direction of wind shear is also consistent with Boehm and Bell (2021).

6.6 Conclusion

Throughout this chapter, we have explored the atypical wind structure of Tropical Cyclone Veronica. As Veronica made landfall on a relatively flat and homogeneous land surface, and remained almost stationary on the coast for approximately 24 hours, this case study presents a unique opportunity to study the impacts of landfall on the storm asymmetry, without the confounding influence of storm motion. Through our analysis, I have found that Tropical Cyclone Veronica displayed an increasingly asymmetrical wind distribution as it approached and remained almost stationary on the coast. Notable atypical features of the wind distribution

include a rotation of the maximum wind speed as the storm approached land; the broadening and maintenance of boundary layer wind speeds over the land; a near-surface eyewall break on the offshore side of the storm; and elevated wind speeds and outflow collocated with a depleted spiral rainband system, which was connected to the region of the eyewall break. Although the increased near-surface inflow and tangential wind acceleration noted by Hlywiak and Nolan, 2022; Rogers and Zhang, 2023 appear to be present, they are not the dominant sources of asymmetry.

The analysis presented here focuses on the eyewall break and the role of the spiral rainband. The spiral rainband was not shown to detrimentally impact the thermodynamics of the inner core within the eyewall break. However, the rainband did have some contribution to the diversion of the flow to the north and northwest of the storm center, at the detriment of the northern eyewall. Along the rainband, the flow seemed to be diverted radially outward from the storm center, which was projected as a low-level outwards wind component. It is likely that this was a result of strong near-surface convergence along the rainband, exacerbated by the increased friction of landfall, which caused an inflection of the flow. Furthermore, the rainband contributed locally within the inner core (just north/northwest of the storm center) to a local vorticity gradient.

Veronica was also under the influence of a large-scale vorticity gradient, with higher cyclonic vorticity in the north and anticyclonic vorticity in the south, which were likely related to i) environmental factors such as the monsoon trough in the north and an eastwardly propagating anticyclone in the south, and ii) the impact of wind shear which can impose anticyclonic vorticity perturbations downshear (Boehm and Bell, 2021). The orientation of the vorticity gradient and eyewall break were consistent with the idealised numerical analysis.

Using a simple calculation, it was shown that an eyewall break could be replicated purely by imposing a weak vorticity gradient onto a symmetric vortex. The break occurs in the region with relatively higher cyclonic vorticity, while the wind speeds in the more anticyclonic sector increase in magnitude. These results present a new paradigm for the development of eyewall breaks and wind asymmetries in tropical cyclones.

As demonstrated by Tropical Cyclone Veronica, such asymmetric wind fields can lead to the maintenance of boundary layer intensity inland while the storm weakens offshore. This study motivates the analysis of the large-scale environment when evaluating risk for landfalling tropical cyclones. While Veronica is just one case, the recent case of Idalia (2023) verified that this

paradigm is consistent with other tropical cyclones. Future work could investigate this further by analysing distinct case studies that present similar asymmetric wind distributions to those presented here. This theory would also benefit from studies which vary the magnitude and direction of vertical wind shear, to evaluate the impact of shear on the vorticity asymmetries and resulting wind fields.

Chapter 7

Conclusions

In nature, tropical cyclones are inherently asymmetric, with the degree of asymmetry closely related to environmental factors such as deep layer vertical wind shear and proximity to land. Despite this, tropical cyclones are often defined by single-value metrics such as the 10-m maximum wind speed averaged over a period of minutes, which is used globally to define storm intensity, and the radius of maximum wind - often used to describe storm size. Operationally, understanding and adequately representing storm asymmetry is vital for quantifying risk to coastal communities, but it is also important for determining storm intensification rates, via processes of weakening (such as the radial and downdraft ventilation of low-entropy air into the inner-core, e.g. Tang and Emanuel, 2012a; Riemer et al., 2010; Molinari et al., 2013; Alland et al., 2021a; Alland et al., 2021b; Wadler et al., 2021) and intensification (such as the provision of cyclonic vorticity to the storm system via stochastic convective updrafts, e.g. Montgomery and Smith, 2014).

While track forecasts of tropical cyclones have been steadily improving, in recent years there has not been the same amount of progress for intensity forecasts (Cangialosi et al., 2020; Gopalakrishnan et al., 2021). This thesis aims to contribute to the improvement of tropical cyclone intensity forecasts by addressing all three pillars of numerical weather prediction, when applied to the complex dynamics of these asymmetric systems. These pillars are: 1) observations and their effective use, 2) numerical representation of the physics that governs the atmosphere, and 3) adequate understanding of the underlying science. I will now list how each results chapter addressed these points, and the research questions set out in Chapter 1.

Pillar 1: Observations (Chapter 4):

- (1) How can in-flight observations be used to effectively evaluate the three-dimensional asymmetric structure of tropical cyclone ensemble simulations?
- (2) How well can single-value surface intensity metrics be used to infer the quality of the ensemble in representing the boundary layer structure?

Pillar 2: Representation of Physics in Models (Chapter 5):

- (3) To what extent does tropospheric mixing influence the intensity forecasts of Hurricane Maria (2017) during a period of weakening and moderate to high vertical wind shear?
- (4) How does the choice of sub-grid turbulence parametrisation in the free troposphere contribute to the thermodynamic processes associated with weakening tilted tropical cyclones?

Pillar 3: Advancing our Knowledge of the Underlying Science (Chapter 6):

- (5) How do landfall, environmental wind shear and rainband dynamics contribute to the eyewall break of Tropical Cyclone Veronica (2019)?
- (6) To what extent, and by what mechanism, can eyewall breaks be explained by the synoptic environment?

In the next section, I will address each question in order, discussing the main findings and contextualising the results with the existing literature.

7.1 Addressing the Research Questions

Chapter 4 was primarily an exploratory chapter, demonstrating how different techniques could be used to evaluate ensemble forecasts in detail, particularly in an asymmetric framework (Q1). The analysis of the correlation between the surface metrics and boundary layer performance (Figure ??) suggested that the single-value Best Track metrics are not wholly reliable indicators of model performance (Q2), and motivated the investigation into three-dimensional model evaluation techniques.

By using the available radar data, I showed that it is possible to identify systematic model biases in vertical and azimuthal representation of the radial wind, which can be extended to

other variables such as tangential wind, vertical wind and radar reflectivity (Q 1). From a single figure (Figure 4.6), I demonstrated a consistent and strong systematic bias in the representation of radial wind asymmetry for Hurricane Maria (2017).

Throughout the evaluation of Hurricane Maria in Chapter 4, it became apparent that the MetUM was under-estimating the weakening that occurred in observations (e.g. Figure 4.3). It has been established that Maria encountered a region of moderate vertical wind shear (e.g. Pasch et al., 2019), which is associated with ventilation pathways that contribute to storm weakening in shear (e.g. Tang and Emanuel, 2012a; Riemer et al., 2010; Alland et al., 2021a; Alland et al., 2021b). I also discussed in Section 2.5 how turbulence can be generated in sheared tropical cyclones through the production of local shear and buoyancy. Following these arguments, I hypothesised that the shear-driven downdraft ventilation process could be directly impacted by the representation of turbulence in the mid-troposphere (Q 3,4). I tested this hypothesis using Hurricane Maria by substantially reducing the free-tropospheric sub-grid turbulent mixing, and showed that the intensity forecasts for Hurricane Maria were significantly improved (Q 4).

By altering the turbulence parametrisation, the vertical mixing was reduced between the top of the inflow layer and the dry mid-levels, and between the dry mid-levels and the stratiform cloud layer. Downdraft ventilation occurs via the resolved transport of dry air from the mid-levels into the boundary layer (e.g. Tang and Emanuel, 2012b; Riemer et al., 2010; Alland et al., 2021a). By reducing the moistening of the mid-levels, the downdraft ventilation process became more efficient and weakened the storm in closer agreement with the observations (Q 3).

The result that a storm with stronger diffusion above the boundary layer is more intense is unexpected. In previous boundary layer studies (e.g. Zhang and Rogers, 2019), increasing the mixing within the boundary layer leads to a less convective, weaker storm with a weaker inflow layer. In our results, increasing the mixing within the free troposphere leads to a stronger storm. The important distinction is the region in which the changes were applied - our results are complementary to the previous study by Zhang and Rogers (2019), and affect different processes within the storm. In tandem, the results suggest that increased diffusivity within the boundary layer is detrimental for storm intensification, whereas increased diffusivity above the boundary layer can be beneficial.

Continuing the theme of asymmetries and intensity change, in Chapter 6, I used a case study along with a full-physics model, boundary layer model, and basic calculations to develop a new

theory for an additional mechanism which explains boundary layer wind asymmetries. Tropical Cyclone Veronica (2019), which made landfall in north-western Australia, was selected to investigate the impact of landfall on the storm's wind structure due to the relatively homogeneous topography and slow storm translation. Veronica should be a good case study to investigate landfall since there are limited impacts of environmental factors such as complex terrain and fast translation, although there was significant vertical shear (Paterson, 2019). Landfall has been shown to strongly impact boundary layer wind structure (e.g. Hlywiak and Nolan, 2022; Rogers and Zhang, 2023) and the analysis in Chapter 6 showed an asymmetry consistent with the landfall studies of Hlywiak and Nolan (2022) and Rogers and Zhang (2023). However, I found that the landfall-induced asymmetry was not the largest source of asymmetry in this particular case. For example, in Chapter 6, I showed that landfall was not producing the dominant effect on Veronica's asymmetry when the storm was closest to the coast. For instance, Hlywiak and Nolan (2022) showed that landfall induces an increased inflow in the region of offshore flow due to the rapid reduction in surface friction compared to that inland, while the flow remains subgradient. As a result, the enhanced convergence contributes to upward motion, promoting the inward transport of absolute angular momentum, thus leading to an increase in tangential wind speeds in the upper boundary layer in the offshore flow region. In contrast, I showed that Veronica had a consistent offshore tangential wind minimum in the boundary layer, along with apparent outflow in parts of the offshore flow (Figure 6.10). These results prompted further analysis into the atypical asymmetric wind structure of Tropical Cyclone Veronica, which we will now summarise.

Throughout this chapter, I built on results by Kepert (2018) that showed that tropical cyclone rainbands can exert an influence on the flow (Q5). I demonstrated that the frictional effects of landfall could increase the low-level convergence into an onshore rainband, leading to a flow into the rainband and radially outward from the storm centre, diverting the flow. Such reduced inflow (or in extreme cases, outflow) along the rainband was likely enhanced by the vorticity-produced through-flow in the mid-boundary layer, further diverting the winds away from the storm centre. It was also demonstrated that Veronica's asymmetric structure could not be attributed to the ventilation of low- θ_e air into the inner core from the rainband, since the region of eyewall degradation had a relatively high θ_e compared to the inland storm quadrants (Figure 6.8).

We discovered that the rainband was not the feature dominating the asymmetric wind distribution of Veronica, although it did contribute to the retardation of the local flow. I showed, using an idealised model and analysis of the rotational flow, that an eyewall break and asymmetric wind distribution could be reproduced by imposing a vorticity gradient onto a symmetric vortex (Q6). The strong positive correlation between the strength of the vorticity gradient and the magnitude of the eyewall break (Figure 6.20) supports that a vorticity gradient was a causal factor in the asymmetric wind distribution of Veronica by the following mechanism: the wind field associated with the vorticity gradient influences the flow, which enhances the tangential wind in the region of anticyclonic vorticity and reduces it in the region of cyclonic vorticity. Although seemingly counter-intuitive, the mechanism can be summarised by Figure 6.18, which shows an enhancement of the tangential wind in the top half of the anticyclonic rotation and a reduction in the lower half of the cyclonic rotation. As seen in Figure 6.3, the large-scale vorticity gradient present in Veronica was likely produced by the monsoon trough north of the storm (providing cyclonic vorticity), and a high pressure system in the south propagating eastwards throughout the study period.

The vorticity gradient theory to explain eyewall breaks appears to be new. Previous work has suggested eyewall breaks to be related to: thermodynamic depletion via downdraft ventilation (Fischer et al., 2023); vortex Rossby wave activity (e.g. Wang, 2001; Wang, 2002; Reasor et al., 2000; Corbosiero et al., 2006); and rainband perturbations of potential vorticity (Chen and Yau, 2003). While it is possible that there are various mechanisms by which eyewall breaks can occur, it would be interesting to re-evaluate some of the existing studies in the new context of a vorticity gradient. The results shown by the idealised studies (Figures 6.18, 6.19) support the asymmetric wind distributions and vorticity gradient in Tropical Cyclone Veronica (e.g. Figure 6.16) and Hurricane Idalia (2023; Figure A.1), suggesting that it is a dynamically consistent theory that is likely linked to many more storms.

7.2 Wider Context

This thesis contributes to the growing idea that storm asymmetry is important for storm intensity change. We will now summarise the major contributions to the field.

Firstly, the parametrisation of turbulence in tropical cyclones has generally been viewed as a boundary layer issue (e.g. Zhang et al., 2017b; Chen et al., 2021a) due to the intense turbu-

lence (Lorsolo et al., 2010) which contributes to intensification via the turbulent surface enthalpy fluxes (Riehl, 1950; Emanuel, 1986; Emanuel et al., 2023). However, I have shown that turbulence above the boundary layer can also contribute to intensity change. While the focus of Chapter 5 was on how the turbulence parametrisation impacts the downdraft ventilation weakening process in tropical cyclones, there were broader implications from this chapter: turbulent processes in the mid-troposphere can modulate tropical cyclone intensity. Consequently, these results force us to reconsider how turbulence is parametrised within the troposphere; tropospheric turbulence should be considered with importance alongside boundary layer turbulence.

There are wider dynamical implications of this work than turbulence parametrisation. With the continuous improvements in computer technology and developments in large eddy modelling, it is likely that the larger scales of turbulence will be resolved in higher-resolution numerical weather prediction models. I have shown that turbulent processes do contribute to overall storm dynamics, particularly intensity. I have proposed one possible mechanism here: the efficacy of downdraft ventilation, which can be increased (decreased) when there is less (more) turbulent mixing, since the dry mid-levels - which are key to downdraft ventilation, can be made moister by turbulent mixing at the top of the boundary layer and at the base of stratiform cloud. Since this work was conducted using turbulence parametrisations, motivation is provided for further studies using turbulence-resolving scales such as large eddy simulations or novel observations from unmanned aerial systems (discussed in Section 3.5) for a more detailed investigation and verification of the role of mid-tropospheric turbulence on tropical cyclone dynamics.

Another major contribution to the study of storm asymmetry is the work on rainband dynamics in Chapter 6. While previous work (Powell, 1990; Kepert, 2018) showed that the depth and strength of the inflow layer are reduced on the inner side of spiral rainbands compared to the outer side, the analysis in Chapter 6 went a step further and showed that landfalling rainbands can exhibit this effect to such a degree that the storm-centred radial wind is reversed, diverting the flow away from the storm centre. This result shows that rainbands can modulate the overall boundary layer flow which can contribute to the asymmetry of eyewalls, but it also contributes more widely to our understanding of tropical cyclone circulations. For example, although the typical ‘in, up and out’ circulation has been acknowledged to improperly represent asymmetric cyclones (Barron et al., 2022), storm-scale radial wind asymmetries are rarely considered in relation to smaller-scale features such as rainbands.

Lastly, in Chapter 6, we developed a theory for a new mechanism for boundary layer wind asymmetry. I showed that large-scale vorticity gradients can be related to a cross-flow across the storm system, contributing to storm-scale asymmetries and static eyewall breaks. Previous work had suggested smaller-scale mechanisms for eyewall asymmetries, such as vortex Rossby waves (Wang, 2001; Corbosiero et al., 2006), downdraft ventilation (Fischer et al., 2023), and local perturbations of potential vorticity (Chen and Yau, 2003). While these theories are viable, our additional large-scale vorticity gradient mechanism presented in Chapter 6 may be able to be used to explain previous cases, and has practical implications for forecasting. For example, large-scale anticyclonic and cyclonic features in the atmosphere are typically well represented in global models. If such large-scale features are within proximity to a tropical cyclone, the mechanism detailed in Chapter 6 can help forecasters to estimate storm-scale asymmetries in the wind field. For example, large-scale cyclonic features can lead to reductions in the storm's tangential wind field by producing an opposing rotational flow (e.g. Figure 6.18). Conversely, adjacent high pressure centres may enhance the storm's tangential wind, by contributing to the rotational flow on that side of the storm.

7.3 Limitations and Future Work Recommendations

While the results presented in this thesis have provided evidence for intensity-modulating mechanisms based on asymmetric processes within tropical cyclones, almost all of the results have been based on case studies. Studying the small-scale dynamics of tropical cyclones requires high precision and attention to detail, making it difficult to analyse a large amount of storms in the amount of detail presented here. Although the model evaluation techniques in Chapter 4 are designed to be relatively easy to implement, reliably testing the correlation between surface metrics and boundary layer performance would require a much larger sample of data. Performing such statistical analyses is also challenging due to the nature of the data - since the data comes from individual flight missions, it is difficult to do systematic analyses between models and observation in the ways set out in Chapter 4. Similarly, ensuring that the model parametrisation changes in Chapter 5 consistently improve tropical cyclone intensity forecasts would require a statistically-testable sample size of simulations. Both of these options would be beneficial to operations and research to better understand and develop numerical weather prediction models in the context of observations, but this is a task most suited to organisations with an archive of

tropical cyclone regional model simulations and advanced supercomputing systems. However, the case study approach herein indicates areas that would benefit from broader investigation.

Although Chapter 5 showed an improvement in tropical cyclone intensity forecasts by changing the turbulence parametrisation, there is still a limited amount of data that can be used to directly validate these changes, such as measurements of turbulence in the lower troposphere of tropical cyclones. With the development of new unmanned aircraft systems (Cione et al., 2024), much more data on tropical cyclone turbulence will soon be available. This new data will allow for validation of the mixing length changes in Chapter 5, but can also be used to improve our understanding of turbulence across the tropical cyclone system which can then be used to inform numerical models.

Similarly, the new unmanned aircraft systems will provide more detailed data on lower boundary layer wind structure, which could be used to build on the studies by Powell (1990), Skwira et al. (2005), and Kepert (2018) on the kinematic impacts of tropical cyclone rainbands. Such analysis could be used to validate the results in Chapter 6 that rainbands can divert the flow and contribute to storm asymmetries.

Evaluation and verification has been a theme across the thesis. To reliably validate the eyewall break theory in Chapter 6, the most robust option would be to analyse radar composites from the NOAA TC-RADAR database (Fischer et al., 2022). This database includes the wind and vorticity fields from NOAA flight missions into primarily Atlantic basin hurricanes, such as the data shown in Chapter 4 and Appendix A.1. The main challenges associated with this analysis would be to ensure some level of uniform azimuthal coverage in the data collection, and to ensure the axisymmetric removal of the inner core cyclonic vorticity when computing the vorticity gradients.

It is worth noting that the eyewall break theory in Chapter 6 revolved around a very idealised set-up, with a perfectly centred vorticity gradient imposed onto a symmetric, stationary cyclone. However, the argument of the largescale vorticity having its own associated rotational flow would stand for every possible orientation, size and structure of such largescale vorticity perturbation. As such, the field would benefit from future work that investigates how different vorticity gradients may impact tropical cyclone dynamics, including the impact of stationary environmental vorticity gradients on translating tropical cyclones.

One of the biggest open questions from the thesis is how vertical wind shear modulates vorticity asymmetries, in the context of larger-scale vorticity gradients. It is difficult to answer this question with observations (as demonstrated by Figure 2.4), since there are variable environmental factors that may contribute to vorticity gradients, such as the distribution of convection, the subtropical jet stream, and proximity to land, other cyclones or anticyclones. Therefore, answering this question (regarding the impact of vertical wind shear on vorticity asymmetries) is best suited to an idealised model such as CM1 (Bryan and Fritsch, 2002), where a series of simulations could be set up removed from the stochastic external impacts of the environment, with the re-addition of an environmental wind shear.

Convection-permitting simulations provide an opportunity to study storm asymmetry in detail, but not without challenges. I showed in Chapter 6 that highly asymmetric boundary layer processes can be well represented by a full-physics model, but it is difficult to attribute specific processes to their causal factors, which is a common issue in meteorology usually addressed by using idealised models. On the larger-scale, the impact of environmental factors such as wind shear and the position of the sub-tropical jet are best investigated using a full-physics, convection-permitting model, which can represent complex large-scale dynamics. Thus, I propose that the best way to study vorticity gradients and the environmental impact on storm asymmetry is to use a combination of convection-permitting models, idealised models, and observations where possible.

7.4 Closing Remarks

Asymmetric dynamics undoubtedly contribute to intensity changes in tropical cyclones. As new observational techniques become available and computing capacity increases, our ability to accurately represent and understand these processes will contribute to the improvement of intensity forecasts. I have developed novel applications of analysis techniques to effectively evaluate model forecasts in three dimensions, such as using Contoured Frequency by Azimuth diagrams, which summarise the systematic biases of model simulations in a single figure. I have shown how reducing the turbulent mixing in the free troposphere of tropical cyclones can directly impact the boundary layer via shear-driven weakening processes involving the downward transportation of dry mid-level air, in contrast to other studies have focused on boundary layer turbulence. Furthermore, I have built on existing research suggesting rainbands influence the

local flow (Powell, 1990; Skwira et al., 2005; Kepert, 2018), and developed a mechanism in which a large-scale horizontal vorticity gradient can produce an asymmetric boundary layer wind distribution and an eyewall break in tropical cyclones. Overall, this thesis presents an analysis of asymmetric tropical cyclone structure, addressing impacts on dynamics and storm intensity, which motivates further research and an operational focus on three-dimensional structure.

Appendix A

Appendix

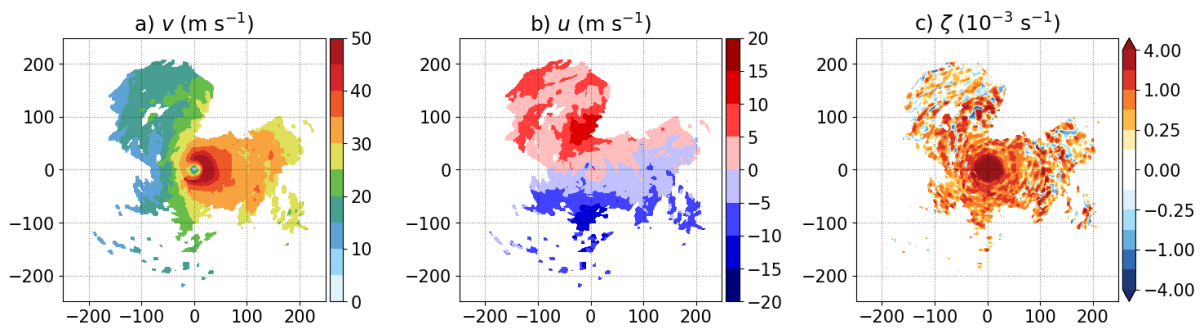


Figure A.1: Hurricane Idalia (2023) radar fields at 1.5 km, composited using five swathes from a NOAA reconnaissance mission on 29 August 2023 over a four hour period from 21:44 UTC. a) Tangential wind, b) radial wind, c) relative vorticity

References

- Ahern, Kyle et al. 2019. Observed Kinematic and Thermodynamic Structure in the Hurricane Boundary Layer during Intensity Change. *Monthly Weather Review* **147**(8), pp. 2765–2785. DOI: 10.1175/MWR-D-18-0380.1. URL: <https://journals.ametsoc.org/view/journals/mwre/147/8/mwr-d-18-0380.1.xml>.
- Ahern, Kyle et al. 2021. Asymmetric Hurricane Boundary Layer Structure during Storm Decay. Part I: Formation of Descending Inflow. *Monthly Weather Review* **149**(11), pp. 3851–3874. DOI: <https://doi.org/10.1175/MWR-D-21-0030.1>.
- Airforce Technology. 2021. *ALTIUS-600 Small Unmanned Aircraft System*. Tech. rep. URL: <https://www.airforce-technology.com/projects/altius-600-small-unmanned-aircraft-system>.
- Alaka Jr, Ghassan J et al. 2017. Performance of basin-scale HWRF tropical cyclone track forecasts. *Weather and Forecasting* **32**(3), pp. 1253–1271.
- Alland, Joshua J et al. 2021a. Combined effects of midlevel dry air and vertical wind shear on tropical cyclone development. Part I: Downdraft ventilation. *Journal of the Atmospheric Sciences* **78**(3), pp. 763–782. DOI: <https://doi.org/10.1175/JAS-D-20-0054.1>.
- 2021b. Combined effects of midlevel dry air and vertical wind shear on tropical cyclone development. Part II: Radial ventilation. *Journal of the Atmospheric Sciences* **78**(3), pp. 783–796. DOI: <https://doi.org/10.1175/JAS-D-20-0055.1>.
- Arakawa, Akio and Vivian R Lamb. 1977. Computational design of the basic dynamical processes of the UCLA general circulation model. *General circulation models of the atmosphere* **17**(Supplement C), pp. 173–265.
- Arndt, Derek S et al. 2009. Observations of the overland reintensification of Tropical Storm Erin (2007). *Bulletin of the American Meteorological Society* **90**(8), pp. 1079–1094.

- Ashcroft, John et al. 2021. The impact of weak environmental steering flow on tropical cyclone track predictability. *Quarterly Journal of the Royal Meteorological Society* **147**(741), pp. 4122–4142.
- Bain, CL et al. 2022. The Met Office winter testbed 2020/2021: Experimenting with an on-demand 300-m ensemble in a real-time environment. *Meteorological Applications* **29**(5), e2096.
- Barron, Nicholas R et al. 2022. Statistical Analysis of Convective Updrafts in Tropical Cyclone Rainbands Observed by Airborne Doppler Radar. *Journal of Geophysical Research: Atmospheres* **127**(6), e2021JD035718. DOI: <https://doi.org/10.1029/2021JD035718>.
- Bender, Morris A et al. 1987. A numerical study of the effect of island terrain on tropical cyclones. *Monthly Weather Review* **115**(1), pp. 130–155.
- BlackSwift. 2024. *VTOL S0 Datasheet*. Tech. rep. URL: <https://techpartnerships.noaa.gov/wp-content/uploads/2024/01/VTOL-S0-Data-Sheet.pdf>.
- Boehm, Annette M and Michael M Bell. 2021. Retrieved thermodynamic structure of Hurricane Rita (2005) from airborne multi-Doppler radar data. *Journal of the Atmospheric Sciences* **78**(5), pp. 1583–1605.
- Bonavita, Massimo et al. 2016. The evolution of the ECMWF hybrid data assimilation system. *Quarterly Journal of the Royal Meteorological Society* **142**(694), pp. 287–303.
- Boutle, IA et al. 2014a. Seamless stratocumulus simulation across the turbulent gray zone. *Monthly Weather Review* **142**(4), pp. 1655–1668. DOI: <https://doi.org/10.1175/MWR-D-13-00229.1>. URL: <https://journals.ametsoc.org/view/journals/mwre/142/4/mwr-d-13-00229.1.xml>.
- Boutle, IA et al. 2014b. Spatial variability of liquid cloud and rain: Observations and microphysical effects. *Quarterly Journal of the Royal Meteorological Society* **140**(679), pp. 583–594.
- Bowler, Neill E et al. 2008. The MOGREPS short-range ensemble prediction system. *Quarterly Journal of the Royal Meteorological Society* **134**(632), pp. 703–722. DOI: <https://doi.org/10.1002/qj.234>.
- Brown, Nick et al. 2020. A highly scalable Met Office NERC Cloud model. *arXiv preprint arXiv:2009.12849*.
- Bryan, George H. 2012. Effects of surface exchange coefficients and turbulence length scales on the intensity and structure of numerically simulated hurricanes. *Monthly Weather Review* **140**(4), pp. 1125–1143.

- Bryan, George H and J Michael Fritsch. 2002. A benchmark simulation for moist nonhydrostatic numerical models. *Monthly Weather Review* **130**(12), pp. 2917–2928.
- Bryan, George H et al. 2017. A simple method for simulating wind profiles in the boundary layer of tropical cyclones. *Boundary-layer meteorology* **162**(3), pp. 475–502.
- Bureau of Meteorology. 2020. *AAPS3 Upgrade to the ACCESS-TC Numerical Weather Prediction System*. Tech. rep. URL: http://www.bom.gov.au/australia/charts/bulletins/opsbull_ACCESS_TC3_External.pdf.
- Bush, M. et al. 2023. The second Met Office Unified Model–JULES Regional Atmosphere and Land configuration, RAL2. *Geoscientific Model Development* **16**(6), pp. 1713–1734. DOI: 10.5194/gmd-16-1713-2023. URL: <https://gmd.copernicus.org/articles/16/1713/2023/>.
- Calafat, Francisco M et al. 2022. Trends in Europe storm surge extremes match the rate of sea-level rise. *Nature* **603**(7903), pp. 841–845.
- Camelo, Jeane and Talea Mayo. 2021. The lasting impacts of the Saffir-Simpson Hurricane Wind Scale on storm surge risk communication: The need for multidisciplinary research in addressing a multidisciplinary challenge. *Weather and Climate Extremes* **33**, p. 100335. ISSN: 2212-0947. DOI: <https://doi.org/10.1016/j.wace.2021.100335>. URL: <https://www.sciencedirect.com/science/article/pii/S2212094721000335>.
- Cangialosi, J. P. 2022. *National Hurricane Center Forecast Verification Report: 2021 Hurricane Season*. Tech. rep. URL: https://www.nhc.noaa.gov/verification/pdfs/Verification_2021.pdf.
- Cangialosi, John P et al. 2020. Recent progress in tropical cyclone intensity forecasting at the National Hurricane Center. *Weather and Forecasting* **35**(5), pp. 1913–1922.
- Cha, Ting-Yu et al. 2020. Polygonal eyewall asymmetries during the rapid intensification of Hurricane Michael (2018). *Geophysical Research Letters* **47**(15), e2020GL087919.
- Cha, Ting-Yu et al. 2021. Doppler Radar Analysis of the Eyewall Replacement Cycle of Hurricane Matthew (2016) in Vertical Wind Shear. *Monthly Weather Review* **149**(9), pp. 2927–2943.
- Chai, Tianfeng and Roland R Draxler. 2014. Root mean square error (RMSE) or mean absolute error (MAE)?—Arguments against avoiding RMSE in the literature. *Geoscientific model development* **7**(3), pp. 1247–1250.

- Chan, Johnny CL and Xudong Liang. 2003. Convective asymmetries associated with tropical cyclone landfall. Part I: f-plane simulations. *Journal of the Atmospheric Sciences* **60**(13), pp. 1560–1576.
- Chan, Johnny CL and RT Williams. 1987. Analytical and numerical studies of the beta-effect in tropical cyclone motion. Part I: Zero mean flow. *Journal of atmospheric sciences* **44**(9), pp. 1257–1265.
- Chang, Chih-Pei et al. 2013. Large increasing trend of tropical cyclone rainfall in Taiwan and the roles of terrain. *Journal of Climate* **26**(12), pp. 4138–4147.
- Charney, Jule G and NA Phillips. 1953. Numerical integration of the quasi-geostrophic equations for barotropic and simple baroclinic flows. *Journal of Atmospheric Sciences* **10**(2), pp. 71–99.
- Charney, Jule G. and Arnt Eliassen. 1964. On the Growth of the Hurricane Depression. *Journal of Atmospheric Sciences* **21**(1), pp. 68–75. DOI: 10.1175/1520-0469(1964)021<0068:OTGOTH>2.0.CO;2. URL: https://journals.ametsoc.org/view/journals/atsc/21/1/1520-0469_1964_021_0068_otgoth_2_0_co_2.xml.
- Chen, Jie and Daniel R Chavas. 2021. Can existing theory predict the response of tropical cyclone intensity to idealized landfall? *Journal of the Atmospheric Sciences* **78**(10), pp. 3281–3296.
- Chen, Shuyi S et al. 2006. Effects of vertical wind shear and storm motion on tropical cyclone rainfall asymmetries deduced from TRMM. *Monthly Weather Review* **134**(11), pp. 3190–3208. DOI: <https://doi.org/10.1175/MWR3245.1>.
- Chen, Xiaomin and George H Bryan. 2021. Role of advection of parameterized turbulence kinetic energy in idealized tropical cyclone simulations. *Journal of the Atmospheric Sciences* **78**(11), pp. 3593–3611.
- Chen, Xiaomin et al. 2021a. A framework for simulating the tropical cyclone boundary layer using large-eddy simulation and its use in evaluating PBL parameterizations. *Journal of the Atmospheric Sciences* **78**(11), pp. 3559–3574.
- Chen, Xiaomin et al. 2021b. Effect of Scale-Aware Planetary Boundary Layer Schemes on Tropical Cyclone Intensification and Structural Changes in the Gray Zone. *Monthly Weather Review* **149**(7), pp. 2079–2095. DOI: <https://doi.org/10.1175/MWR-D-20-0297.1>. URL: <https://journals.ametsoc.org/view/journals/mwre/149/7/MWR-D-20-0297.1.xml>.
- Chen, Yongsheng and MK Yau. 2003. Asymmetric structures in a simulated landfalling hurricane. *Journal of the Atmospheric Sciences* **60**(18), pp. 2294–2312.

- Cheng, Chieh-Jen and Chun-Chieh Wu. 2020. The role of WISHE in the rapid intensification of tropical cyclones. *Journal of the Atmospheric Sciences* **77**(9), pp. 3139–3160.
- Cione, Joseph J et al. 2016. Coyote unmanned aircraft system observations in Hurricane Edouard (2014). *Earth and Space Science* **3**(9), pp. 370–380.
- Cione, Joseph J et al. 2024. “Developing, testing, and transitioning small Uncrewed Aircraft Systems (sUAS) to routinely sample the hurricane boundary layer”. *104th Annual Meeting*. Baltimore, MD: American Meteorological Society.
- Cione, Joseph J. et al. 2020. Eye of the Storm: Observing Hurricanes with a Small Unmanned Aircraft System. *Bulletin of the American Meteorological Society* **101**(2), E186–E205. DOI: <https://doi.org/10.1175/BAMS-D-19-0169.1>. URL: <https://journals.ametsoc.org/view/journals/bams/101/2/bams-d-19-0169.1.xml>.
- Clark, Peter et al. 2016. Convection-permitting models: A step-change in rainfall forecasting. *Meteorological Applications* **23**(2), pp. 165–181.
- Corbosiero, Kristen L and John Molinari. 2002. The effects of vertical wind shear on the distribution of convection in tropical cyclones. *Monthly Weather Review* **130**(8), pp. 2110–2123. DOI: [https://doi.org/10.1175/1520-0493\(2002\)130<2110:TEOVWS>2.0.CO;2](https://doi.org/10.1175/1520-0493(2002)130<2110:TEOVWS>2.0.CO;2).
- 2003. The Relationship between Storm Motion, Vertical Wind Shear, and Convective Asymmetries in Tropical Cyclones. *Journal of the Atmospheric Sciences* **60**(2), pp. 366–376. DOI: [https://doi.org/10.1175/1520-0469\(2003\)060<0366:TRBSMV>2.0.CO;2](https://doi.org/10.1175/1520-0469(2003)060<0366:TRBSMV>2.0.CO;2). URL: https://journals.ametsoc.org/view/journals/atsc/60/2/1520-0469_2003_060_0366_trbsmv_2.0.co_2.xml.
- Corbosiero, Kristen L. et al. 2006. The Structure and Evolution of Hurricane Elena (1985). Part II: Convective Asymmetries and Evidence for Vortex Rossby Waves. *Monthly Weather Review* **134**(11), pp. 3073–3091. DOI: <https://doi.org/10.1175/MWR3250.1>. URL: <https://journals.ametsoc.org/view/journals/mwre/134/11/mwr3250.1.xml>.
- Courtier, Philippe et al. 1994. A strategy for operational implementation of 4D-Var, using an incremental approach. *Quarterly Journal of the Royal Meteorological Society* **120**(519), pp. 1367–1387.
- Courtney, Joseph B et al. 2021. Revisions to the Australian tropical cyclone best track database. *Journal of Southern Hemisphere Earth Systems Science* **71**(2), pp. 203–227.

- Dai, Yi et al. 2021. Tropical cyclone resistance to strong environmental shear. *Journal of the atmospheric sciences* **78**(4), pp. 1275–1293. DOI: <https://doi.org/10.1175/JAS-D-20-0231.1>.
- Davidson, Noel E and Harry C Weber. 2000. The BMRC high-resolution tropical cyclone prediction system: TC-LAPS. *Monthly Weather Review* **128**(5), pp. 1245–1265.
- Davidson, Noel E et al. 2014. ACCESS-TC: Vortex specification, 4DVAR initialization, verification, and structure diagnostics. *Monthly Weather Review* **142**(3), pp. 1265–1289.
- DeHart, Jennifer C et al. 2014. Quadrant distribution of tropical cyclone inner-core kinematics in relation to environmental shear. *Journal of the Atmospheric Sciences* **71**(7), pp. 2713–2732.
- DeMaria, Mark. 1996. The effect of vertical shear on tropical cyclone intensity change. *Journal of Atmospheric Sciences* **53**(14), pp. 2076–2088.
- DeMaria, Mark and John Kaplan. 1994. A statistical hurricane intensity prediction scheme (SHIPS) for the Atlantic basin. *Weather and Forecasting* **9**(2), pp. 209–220. DOI: [https://doi.org/10.1175/1520-0434\(1994\)009<0209:ASHIPS>2.0.CO;2](https://doi.org/10.1175/1520-0434(1994)009<0209:ASHIPS>2.0.CO;2).
- 1999. An updated statistical hurricane intensity prediction scheme (SHIPS) for the Atlantic and eastern North Pacific basins. *Weather and Forecasting* **14**(3), pp. 326–337.
- DeMaria, Mark et al. 2005. Further improvements to the statistical hurricane intensity prediction scheme (SHIPS). *Weather and Forecasting* **20**(4), pp. 531–543.
- Einstein, Albert et al. 1916. The foundation of the general theory of relativity. *Annalen Phys* **49**(7), pp. 769–822.
- Eiter, Thomas and Heikki Mannila. 1994. Computing discrete Fréchet distance.
- Emanuel, Kerry. 2012. Self-stratification of tropical cyclone outflow. Part II: Implications for storm intensification. *Journal of the Atmospheric Sciences* **69**(3), pp. 988–996.
- Emanuel, Kerry et al. 2008. A hypothesis for the redevelopment of warm-core cyclones over northern Australia. *Monthly Weather Review* **136**(10), pp. 3863–3872.
- Emanuel, Kerry et al. 2023. The Surprising Roles of Turbulence in Tropical Cyclone Physics. *Atmosphere* **14**(8), p. 1254.
- Emanuel, Kerry A. 1986. An air-sea interaction theory for tropical cyclones. Part I: Steady-state maintenance. *Journal of Atmospheric Sciences* **43**(6), pp. 585–605.
- Emanuel, Kerry A et al. 1994. Atmospheric convection. Oxford University Press.

- Evans, Clark et al. 2011. Sensitivity in the overland reintensification of Tropical Cyclone Erin (2007) to near-surface soil moisture characteristics. *Monthly Weather Review* **139**(12), pp. 3848–3870.
- Fang, Juan and Fuqing Zhang. 2011. Evolution of multiscale vortices in the development of Hurricane Dolly (2008). *Journal of the Atmospheric Sciences* **68**(1), pp. 103–122.
- Fei, Rong et al. 2021. Contribution of vertical advection to supergradient wind in tropical cyclone boundary layer: A numerical study. *Journal of the Atmospheric Sciences* **78**(4), pp. 1057–1073.
- Field, Paul R et al. 2007. Snow size distribution parameterization for midlatitude and tropical ice clouds. *Journal of the Atmospheric Sciences* **64**(12), pp. 4346–4365.
- Finocchio, Peter M and Rosimar Rios-Berrios. 2021. The intensity-and size-dependent response of tropical cyclones to increasing vertical wind shear. *Journal of the Atmospheric Sciences* **78**(11), pp. 3673–3690.
- Fischer, Michael S et al. 2022. An analysis of tropical cyclone vortex and convective characteristics in relation to storm intensity using a novel airborne Doppler radar database. *Monthly weather review* **150**(9), pp. 2255–2278.
- Fischer, Michael S et al. 2023. A tale of two vortex evolutions: Using a high-resolution ensemble to assess the impacts of ventilation on a tropical cyclone rapid intensification event. *Monthly Weather Review* **151**(1), pp. 297–320.
- Fischer, Michael S et al. 2024. An Observational Analysis of the Relationship between Tropical Cyclone Vortex Tilt, Precipitation Structure, and Intensity Change. *Monthly Weather Review* **152**(1), pp. 203–225.
- Flack, David LA. 2023. Stratification of the vertical spread-skill relation by radiosonde drift in a convective-scale ensemble. *Atmospheric Science Letters*, e1194.
- Goldenberg, Stanley B et al. 2015. The 2012 triply nested, high-resolution operational version of the Hurricane Weather Research and Forecasting Model (HWRF): Track and intensity forecast verifications. *Weather and Forecasting* **30**(3), pp. 710–729.
- Gopalakishnan, S et al. 2021. 2020 HFIP R&D activities summary: Recent results and operational implementation.
- Gopalakrishnan, Sundararaman G et al. 2013. A study of the impacts of vertical diffusion on the structure and intensity of the tropical cyclones using the high-resolution HWRF system.

- Journal of the atmospheric sciences* **70**(2), pp. 524–541. DOI: <https://doi.org/10.1175/JAS-D-11-0340.1>.
- Hanley, Kirsty E et al. 2016. Simulating the 20 May 2013 Moore, Oklahoma tornado with a 100-metre grid-length NWP model. *Atmospheric Science Letters* **17**(8), pp. 453–461.
- Harr, Patrick A and Russell L Elsberry. 1991. Tropical cyclone track characteristics as a function of large-scale circulation anomalies. *Monthly Weather Review* **119**(6), pp. 1448–1468.
- Harris, Lucas M and Shian-Jiann Lin. 2013. A two-way nested global-regional dynamical core on the cubed-sphere grid. *Monthly Weather Review* **141**(1), pp. 283–306.
- Hazelton, Andrew et al. 2021. 2019 Atlantic hurricane forecasts from the global-nested hurricane analysis and forecast system: Composite statistics and key events. *Weather and Forecasting* **36**(2), pp. 519–538.
- Hazelton, Andrew et al. 2022. Performance of 2020 real-time Atlantic hurricane forecasts from high-resolution global-nested hurricane models: HAFS-globalnest and GFDL T-SHiELD. *Weather and Forecasting* **37**(1), pp. 143–161.
- Helmholtz, H von. 1858. Üon integrals of the hydrodynamic equations which correspond to the vortex movements.
- Heming, J T. 2017. Tropical cyclone tracking and verification techniques for Met Office numerical weather prediction models. *Meteorological Applications* **24**(1), pp. 1–8. DOI: <https://doi.org/10.1002/met.1599>. URL: <https://rmets.onlinelibrary.wiley.com/doi/abs/10.1002/met.1599>.
- Hence, Deanna A and Robert A Houze. 2012. Vertical structure of tropical cyclone rainbands as seen by the TRMM Precipitation Radar. *Journal of the atmospheric sciences* **69**(9), pp. 2644–2661. DOI: <https://doi.org/10.1175/JAS-D-11-0323.1>.
- Hendricks, Eric A et al. 2004. The role of “vortical” hot towers in the formation of Tropical Cyclone Diana (1984). *Journal of the atmospheric sciences* **61**(11), pp. 1209–1232.
- Hersbach, H et al. 2018. ERA5 hourly data on single levels from 1959 to present. *Copernicus Climate Change Service (C3S) Climate Data Store (CDS)* **10**.
- Hersbach, Hans et al. 2020. The ERA5 global reanalysis. *Quarterly Journal of the Royal Meteorological Society* **146**(730), pp. 1999–2049.
- Hlywiak, James and David S Nolan. 2019. The influence of oceanic barrier layers on tropical cyclone intensity as determined through idealized, coupled numerical simulations. *Journal of Physical Oceanography* **49**(7), pp. 1723–1745.

- Hlywiak, James and David S Nolan. 2021. The response of the near-surface tropical cyclone wind field to inland surface roughness length and soil moisture content during and after landfall. *Journal of the atmospheric sciences* **78**(3), pp. 983–1000.
- 2022. The evolution of asymmetries in the tropical cyclone boundary layer wind field during landfall. *Monthly Weather Review* **150**(3), pp. 529–549.
- Hock, Terrence F and James L Franklin. 1999. The near gps dropwindsonde. *Bulletin of the American Meteorological Society* **80**(3), pp. 407–420.
- Hodges, Kevin et al. 2017. How well are tropical cyclones represented in reanalysis datasets? *Journal of Climate* **30**(14), pp. 5243–5264.
- Hodges, Kevin I. 1994. A general method for tracking analysis and its application to meteorological data. *Monthly Weather Review* **122**(11), pp. 2573–2586.
- Hodges, KI. 1995. Feature tracking on the unit sphere. *Monthly Weather Review* **123**(12), pp. 3458–3465.
- 1999. Adaptive constraints for feature tracking. *Monthly Weather Review* **127**(6), pp. 1362–1373.
- Hodges, KI and NP Klingaman. 2019. Prediction errors of tropical cyclones in the western North Pacific in the Met Office global forecast model. *Weather and Forecasting* **34**(5), pp. 1189–1209.
- Hodges Jr, JL. 1958. The significance probability of the Smirnov two-sample test. *Arkiv för matematik* **3**(5), pp. 469–486.
- Jekel, Charles F et al. 2019. Similarity measures for identifying material parameters from hysteresis loops using inverse analysis. *International Journal of Material Forming* **12**, pp. 355–378.
- Jones, Sarah C. 1995. The evolution of vortices in vertical shear. I: Initially barotropic vortices. *Quarterly Journal of the Royal Meteorological Society* **121**(524), pp. 821–851.
- Judt, Falko et al. 2021. Tropical cyclones in global storm-resolving models. *Journal of the Meteorological Society of Japan. Ser. II* **99**(3), pp. 579–602.
- Kellner, Olivia et al. 2012. The role of anomalous soil moisture on the inland reintensification of Tropical Storm Erin (2007). *Natural Hazards* **63**, pp. 1573–1600.
- Kepert, Jeff. 2001. The dynamics of boundary layer jets within the tropical cyclone core. Part I: Linear theory. *Journal of the Atmospheric Sciences* **58**(17), pp. 2469–2484.

- Kepert, Jeff and Yuqing Wang. 2001. The dynamics of boundary layer jets within the tropical cyclone core. Part II: Nonlinear enhancement. *Journal of the atmospheric sciences* **58**(17), pp. 2485–2501.
- Kepert, Jeffrey D. 2006. Observed boundary layer wind structure and balance in the hurricane core. Part I: Hurricane Georges. *Journal of the Atmospheric Sciences* **63**(9), pp. 2169–2193.
- 2012. Choosing a boundary layer parameterization for tropical cyclone modeling. *Monthly Weather Review* **140**(5), pp. 1427–1445. DOI: <https://doi.org/10.1175/MWR-D-11-00217.1>.
- 2013. How does the boundary layer contribute to eyewall replacement cycles in axisymmetric tropical cyclones? *Journal of the Atmospheric Sciences* **70**(9), pp. 2808–2830.
- 2018. The boundary layer dynamics of tropical cyclone rainbands. *Journal of the Atmospheric Sciences* **75**(11), pp. 3777–3795.
- Kepert, Jeffrey D et al. 2016. Why is the Tropical Cyclone Boundary Layer Not “Well Mixed”? *Journal of the Atmospheric Sciences* **73**(3), pp. 957–973. ISSN: 0022-4928. DOI: [10.1175/JAS-D-15-0216.1](https://doi.org/10.1175/JAS-D-15-0216.1). URL: <https://doi.org/10.1175/JAS-D-15-0216.1>.
- Khairoutdinov, Marat and Yefim Kogan. 2000. A new cloud physics parameterization in a large-eddy simulation model of marine stratocumulus. *Monthly weather review* **128**(1), pp. 229–243.
- Kimball, Sytske K. 2006. A modeling study of hurricane landfall in a dry environment. *Monthly weather review* **134**(7), pp. 1901–1918.
- Kleist, Daryl T et al. 2009. Introduction of the GSI into the NCEP global data assimilation system. *Weather and Forecasting* **24**(6), pp. 1691–1705.
- Klotz, Bradley W and Haiyan Jiang. 2017. Examination of surface wind asymmetries in tropical cyclones. Part I: General structure and wind shear impacts. *Monthly Weather Review* **145**(10), pp. 3989–4009.
- Klotz, Bradley W. and David S. Nolan. 2019. SFMR Surface Wind Undersampling over the Tropical Cyclone Life Cycle. *Monthly Weather Review* **147**(1), pp. 247–268. DOI: <https://doi.org/10.1175/MWR-D-18-0296.1>. URL: <https://journals.ametsoc.org/view/journals/mwre/147/1/mwr-d-18-0296.1.xml>.
- Klotz, Bradley W. and Eric W. Uhlhorn. 2014. Improved Stepped Frequency Microwave Radiometer Tropical Cyclone Surface Winds in Heavy Precipitation. *Journal of Atmospheric and Oceanic Technology* **31**(11), pp. 2392–2408. DOI: <https://doi.org/10.1175/JTECH-D->

- 14-00028.1. URL: https://journals.ametsoc.org/view/journals/atot/31/11/jtech-d-14-00028_1.xml.
- Knapp, Kenneth R et al. 2010. The international best track archive for climate stewardship (IBTrACS) unifying tropical cyclone data. *Bulletin of the American Meteorological Society* **91**(3), pp. 363–376. DOI: <https://doi.org/10.1175/2009BAMS2755.1>.
- Kolmogorov, A. N. 1941. The Local Structure of Turbulence in Incompressible Viscous Fluid for Very Large Reynolds Numbers. *Doklady Akademii Nauk SSSR* **30**, pp. 301–305.
- Kossin, James P and Wayne H Schubert. 2001. Mesovortices, polygonal flow patterns, and rapid pressure falls in hurricane-like vortices. *Journal of the atmospheric sciences* **58**(15), pp. 2196–2209.
- Landsea, Christopher W and John P Cangialosi. 2018. Have we reached the limits of predictability for tropical cyclone track forecasting? *Bulletin of the American Meteorological Society* **99**(11), pp. 2237–2243.
- Landsea, Christopher W et al. 2008. A reanalysis of the 1911–20 Atlantic hurricane database. *Journal of Climate* **21**(10), pp. 2138–2168.
- Laureano Bozeman, Monica et al. 2012. An HWRF-based ensemble assessment of the land surface feedback on the post-landfall intensification of Tropical Storm Fay (2008). *Natural Hazards* **63**, pp. 1543–1571.
- Li, Xin and Zhaoxia Pu. 2021. Vertical eddy diffusivity parameterization based on a large-eddy simulation and its impact on prediction of hurricane landfall. *Geophysical Research Letters* **48**(2), e2020GL090703.
- Li, Yubin et al. 2014. Numerical study on the development of asymmetric convection and vertical wind shear during tropical cyclone landfall. *Quarterly Journal of the Royal Meteorological Society* **140**(683), pp. 1866–1877.
- Liu, Qingyuan et al. 2021. Storm-scale and fine-scale boundary layer structures of tropical cyclones simulated with the WRF-LES framework. *Journal of Geophysical Research: Atmospheres* **126**(21), e2021JD035511.
- Lock, A. P. et al. 2000. A New Boundary Layer Mixing Scheme. Part I: Scheme Description and Single-Column Model Tests. *Monthly Weather Review* **128**(9), pp. 3187–3199. DOI: 10.1175/1520-0493(2000)128<3187:ANBLMS>2.0.CO;2. URL: https://journals.ametsoc.org/view/journals/mwre/128/9/1520-0493_2000_128_3187_anblms_2.0.co_2.xml.

- Lorenz, Edward N. 1963. Deterministic nonperiodic flow. *Journal of atmospheric sciences* **20**(2), pp. 130–141.
- Lorsolo, Sylvie et al. 2010. Estimation and mapping of hurricane turbulent energy using airborne Doppler measurements. *Monthly weather review* **138**(9), pp. 3656–3670.
- Lorsolo, Sylvie et al. 2013. Evaluation of the Hurricane Research Division Doppler Radar Analysis Software Using Synthetic Data. *Journal of Atmospheric and Oceanic Technology* **30**(6), pp. 1055–1071. DOI: <https://doi.org/10.1175/JTECH-D-12-00161.1>. URL: https://journals.ametsoc.org/view/journals/atot/30/6/jtech-d-12-00161_1.xml.
- Magnusson, Linus and Erland Källén. 2013. Factors influencing skill improvements in the ECMWF forecasting system. *Monthly Weather Review* **141**(9), pp. 3142–3153.
- Magnusson, Linus et al. 2019. ECMWF activities for improved hurricane forecasts. *Bulletin of the American Meteorological Society* **100**(3), pp. 445–458.
- Ming, Jie et al. 2014. Multiplatform observations of boundary layer structure in the outer rainbands of landfalling typhoons. *Journal of Geophysical Research: Atmospheres* **119**(13), pp. 7799–7814.
- Molinari, John et al. 2004. Tropical cyclone formation in a sheared environment: A case study. *Journal of the atmospheric sciences* **61**(21), pp. 2493–2509.
- Molinari, John et al. 2013. Convective bursts, downdraft cooling, and boundary layer recovery in a sheared tropical storm. *Monthly Weather Review* **141**(3), pp. 1048–1060.
- Montgomery, Michael T and Roger K Smith. 2014. Paradigms for Tropical Cyclone Intensification. *Australian Meteorological and Oceanographic Journal*. DOI: 10.22499/2.6401.005.
- Montgomery, Michael T et al. 2006. A vortical hot tower route to tropical cyclogenesis. *Journal of the atmospheric sciences* **63**(1), pp. 355–386.
- Montgomery, Michael T et al. 2009. Do tropical cyclones intensify by WISHE? *Quarterly Journal of the Royal Meteorological Society: A journal of the atmospheric sciences, applied meteorology and physical oceanography* **135**(644), pp. 1697–1714.
- Montgomery, Michael T et al. 2014. An analysis of the observed low-level structure of rapidly intensifying and mature hurricane Earl (2010). *Quarterly Journal of the Royal Meteorological Society* **140**(684), pp. 2132–2146.
- Montgomery, Michael T et al. 2015. Putting to rest WISHE-ful misconceptions for tropical cyclone intensification. *Journal of Advances in Modeling Earth Systems* **7**(1), pp. 92–109.

- Montgomery, Michael T et al. 2019. On the hypothesized outflow control of tropical cyclone intensification. *Quarterly Journal of the Royal Meteorological Society* **145**(721), pp. 1309–1322.
- Mouche, Alexis et al. 2019. Copolarized and cross-polarized SAR measurements for high-resolution description of major hurricane wind structures: Application to Irma category 5 hurricane. *Journal of Geophysical Research: Oceans* **124**(6), pp. 3905–3922.
- Needham, Hal F and Barry D Keim. 2014. Correlating storm surge heights with tropical cyclone winds at and before landfall. *Earth Interactions* **18**(7), pp. 1–26.
- Nguyen, Leon T et al. 2014. Evaluation of Tropical Cyclone Center Identification Methods in Numerical Models. *Monthly Weather Review* **142**(11), pp. 4326–4339. DOI: 10.1175/MWR-D-14-00044.1. URL: <https://journals.ametsoc.org/view/journals/mwre/142/11/mwr-d-14-00044.1.xml>.
- Nguyen, Leon T et al. 2017. Thermodynamic and kinematic influences on precipitation symmetry in sheared tropical cyclones: Bertha and Cristobal (2014). *Monthly Weather Review* **145**(11), pp. 4423–4446.
- Nguyen, Leon T et al. 2019. Assessing the influence of convective downdrafts and surface enthalpy fluxes on tropical cyclone intensity change in moderate vertical wind shear. *Monthly Weather Review* **147**(10), pp. 3519–3534. DOI: <https://doi.org/10.1175/MWR-D-18-0461.1>.
- Nicholls, S. 1985. Aircraft observations of the ekman layer during the joint air-sea interaction experiment. *Quarterly Journal of the Royal Meteorological Society* **111**(468), pp. 391–426.
- NOAA. 2014. *NOAA's Hurricane Research Aircraft*. Accessed on 2023-10-02. URL: https://www.aoml.noaa.gov/hrd/about_hrd/aircraft.html.
- 2017. *Monthly National Climate Report for September 2017*. URL: <https://www.ncdc.noaa.gov/sotc/national/201709> (visited on 05/02/2024).
- 2024. *U.S. Billion-Dollar Weather and Climate Disasters*. DOI: 10.25921/stkw-7w73. URL: <https://www.ncei.noaa.gov/access/billions/> (visited on 05/02/2024).
- Nolan, David S et al. 2021. Evaluation of the surface wind field over land in WRF simulations of Hurricane Wilma (2005). Part I: Model initialization and simulation validation. *Monthly weather review* **149**(3), pp. 679–695.
- Ooyama, Katsuyuki. 1969. Numerical Simulation of the Life Cycle of Tropical Cyclones. *Journal of Atmospheric Sciences* **26**(1), pp. 3–40. DOI: 10.1175/1520-0469(1969)026<0003:

- NSOTLC>2.0.CO;2. URL: https://journals.ametsoc.org/view/journals/atsc/26/1/1520-0469_1969_026_0003_nsotlc_2_0_co_2.xml.
- Ooyama, Katsuyuki V. 1982. Conceptual evolution of the theory and modeling of the tropical cyclone. *Journal of the Meteorological Society of Japan. Ser. II* **60**(1), pp. 369–380.
- Otto, Peter and Joshua Soderholm. 2012. The convective features within and surrounding severe tropical cyclone Larry (2006). *Tropical Cyclone Research and Review* **1**(2), pp. 143–162.
- Pasch, R J et al. 2019. *Tropical Cyclone Report: Hurricane Maria (AL152017)*. Tech. rep. Miami: National Hurricane Center.
- Paterson, Linda. 2019. *Severe Tropical Cyclone Veronica*. Tech. rep. Bureau of Meteorology.
- Paterson, Linda A et al. 2005. Influence of environmental vertical wind shear on the intensity of hurricane-strength tropical cyclones in the Australian region. *Monthly Weather Review* **133**(12), pp. 3644–3660.
- Pearson, Karl. 1901. On the Lines and Planes of Closest Fit to Systems of Points in Space. *Philosophical Magazine* **2**(11), pp. 559–572. URL: <https://doi.org/10.1080/14786440109462720>.
- Powell, Mark D. 1990. Boundary Layer Structure and Dynamics in Outer Hurricane Rainbands. Part I: Mesoscale Rainfall and Kinematic Structure. *Monthly Weather Review* **118**(4), pp. 891–917. DOI: [https://doi.org/10.1175/1520-0493\(1990\)118<0891:BLSADI>2.0.CO;2](https://doi.org/10.1175/1520-0493(1990)118<0891:BLSADI>2.0.CO;2). URL: https://journals.ametsoc.org/view/journals/mwre/118/4/1520-0493_1990_118_0891_blsadi_2_0_co_2.xml.
- Puri, Kamal et al. 2013. Implementation of the initial ACCESS numerical weather prediction system. *Australian Meteorological and Oceanographic Journal* **63**(2), pp. 265–284.
- Ramsay, Hamish A and Lance M Leslie. 2008. The effects of complex terrain on severe landfalling Tropical Cyclone Larry (2006) over northeast Australia. *Monthly weather review* **136**(11), pp. 4334–4354.
- Rao, N Nanaji et al. 2019. Moisture budget of the tropical cyclones formed over the Bay of Bengal: Role of soil moisture after landfall. *Pure and Applied Geophysics* **176**, pp. 441–461.
- Rawlins, F et al. 2007. The Met Office global four-dimensional variational data assimilation scheme. *Quarterly Journal of the Royal Meteorological Society: A journal of the atmospheric sciences, applied meteorology and physical oceanography* **133**(623), pp. 347–362.
- Reasor, Paul D and Matthew D Eastin. 2012. Rapidly intensifying hurricane Guillermo (1997). Part II: Resilience in shear. *Monthly weather review* **140**(2), pp. 425–444.

- Reasor, Paul D et al. 2000. Low-wavenumber structure and evolution of the hurricane inner core observed by airborne dual-Doppler radar. *Monthly Weather Review* **128**(6), pp. 1653–1680.
- Reasor, Paul D et al. 2004. A new look at the problem of tropical cyclones in vertical shear flow: Vortex resiliency. *Journal of the Atmospheric Sciences* **61**(1), pp. 3–22.
- Reasor, Paul D et al. 2013. Environmental flow impacts on tropical cyclone structure diagnosed from airborne Doppler radar composites. *Monthly Weather Review* **141**(9), pp. 2949–2969.
- Ren, Yifang et al. 2019. Hurricane boundary layer height relative to storm motion from GPS dropsonde composites. *Atmosphere* **10**(6), pp. 1–14. ISSN: 20734433. DOI: 10.3390/atmos10060339.
- Ren, Yifang et al. 2020. An observational study of the symmetric boundary layer structure and tropical cyclone intensity. *Atmosphere* **11**(2). ISSN: 20734433. DOI: 10.3390/atmos11020158.
- Riehl, Herbert. 1950. A model of hurricane formation. *Journal of Applied Physics* **21**(9), pp. 917–925.
- Riemer, Michael et al. 2010. A new paradigm for intensity modification of tropical cyclones: Thermodynamic impact of vertical wind shear on the inflow layer. *Atmospheric Chemistry and Physics* **10**(7), pp. 3163–3188. DOI: <https://doi.org/10.5194/acp-10-3163-2010>.
- Rios-Berrios, Rosimar and Ryan D Torn. 2017. Climatological analysis of tropical cyclone intensity changes under moderate vertical wind shear. *Monthly Weather Review* **145**(5), pp. 1717–1738. DOI: <https://doi.org/10.1175/MWR-D-16-0350.1>.
- Rios-Berrios, Rosimar et al. 2023. A review of the interactions between tropical cyclones and environmental vertical wind shear. *Journal of the Atmospheric Sciences*.
- Rogers, Robert et al. 2012. Multiscale analysis of tropical cyclone kinematic structure from airborne Doppler radar composites. *Monthly Weather Review* **140**(1), pp. 77–99.
- Rogers, Robert F and Jun A Zhang. 2023. Airborne Doppler radar observations of tropical cyclone boundary layer kinematic structure and evolution during landfall. *Geophysical Research Letters* **50**(23), e2023GL105548.
- Ronda, RJ et al. 2017. Urban finescale forecasting reveals weather conditions with unprecedented detail. *Bulletin of the American Meteorological Society* **98**(12), pp. 2675–2688.
- Rotunno, R. et al. 2009. Large-Eddy Simulation of an Idealized Tropical Cyclone. *Bulletin of the American Meteorological Society* **90**(12), pp. 1783–1788. DOI: <https://doi.org/10.1175/2009BAMS2884.1>. URL: https://journals.ametsoc.org/view/journals/bams/90/12/2009bams2884_1.xml.

- Rotunno, Richard and George H Bryan. 2012. Effects of parameterized diffusion on simulated hurricanes. *Journal of the atmospheric sciences* **69**(7), pp. 2284–2299. DOI: <https://doi.org/10.1175/JAS-D-11-0204.1>.
- Ryglicki, David R et al. 2021. Observations of atypical rapid intensification characteristics in Hurricane Dorian (2019). *Monthly Weather Review* **149**(7), pp. 2131–2150.
- Ryglicki, David R. et al. 2018. The Unexpected Rapid Intensification of Tropical Cyclones in Moderate Vertical Wind Shear. Part I: Overview and Observations. *Monthly Weather Review* **146**(11), pp. 3773–3800. DOI: 10.1175/MWR-D-18-0020.1. URL: <https://journals.ametsoc.org/view/journals/mwre/146/11/mwr-d-18-0020.1.xml>.
- Saffir, Herbert S and Robert H Simpson. 1974. Hurricane wind and storm surge. *Journal of Waterways and Harbors Division* **100**(1), pp. 1–11.
- Sandu, Irina and Bjorn Stevens. 2021. *Better glimpses of the future with global storm-resolving simulations*. URL: <https://www.ecmwf.int/en/about/media-centre/science-blog/2021/better-glimpses-future-global-storm-resolving-simulations>.
- Schubert, Wayne H et al. 1999. Polygonal eyewalls, asymmetric eye contraction, and potential vorticity mixing in hurricanes. *Journal of the atmospheric sciences* **56**(9), pp. 1197–1223.
- Schwendike, Juliane and Jeffrey D Kepert. 2008. The boundary layer winds in Hurricanes Danielle (1998) and Isabel (2003). *Monthly weather review* **136**(8), pp. 3168–3192.
- Sellwood, Kathryn J et al. 2023. Assimilation of Coyote Small Uncrewed Aircraft System Observations in Hurricane Maria (2017) Using Operational HWRF. *Weather and Forecasting* **38**(6), pp. 901–919.
- Shapiro, Lloyd J. 1983. The asymmetric boundary layer flow under a translating hurricane. *Journal of Atmospheric Sciences* **40**(8), pp. 1984–1998.
- Shimada, Udai et al. 2024. Shear-Relative Asymmetric Kinematic Characteristics of Intensifying Hurricanes as Observed by Airborne Doppler Radar. *Monthly Weather Review* **152**(2), pp. 491–512.
- Skwira, Gary D et al. 2005. Surface observations of landfalling hurricane rainbands. *Monthly weather review* **133**(2), pp. 454–465.
- Slocum, Christopher J et al. 2022. Does ERA5 mark a new era for resolving the tropical cyclone environment? *Journal of Climate* **35**(21), pp. 3547–3564. DOI: <https://doi.org/10.1175/JCLI-D-22-0127.1>.

- Smith, Roger K. 2000. The role of cumulus convection in hurricanes and its representation in hurricane models. *Reviews of Geophysics* **38**(4), pp. 465–489.
- Smith, Roger K and Gerald L Thomsen. 2010. Dependence of tropical-cyclone intensification on the boundary-layer representation in a numerical model. *Quarterly Journal of the Royal Meteorological Society* **136**(652), pp. 1671–1685.
- Smith, Roger K et al. 1990. A numerical study of tropical cyclone motion using a barotropic model. I: The role of vortex asymmetries. *Quarterly Journal of the Royal Meteorological Society* **116**(492), pp. 337–362.
- Smith, Roger K. and Michael T Montgomery. 2010. Hurricane boundary-layer theory. *Quarterly Journal of the Royal Meteorological Society* **136**(652), pp. 1665–1670. DOI: <https://doi.org/10.1002/qj.679>. eprint: <https://rmets.onlinelibrary.wiley.com/doi/pdf/10.1002/qj.679>. URL: <https://rmets.onlinelibrary.wiley.com/doi/abs/10.1002/qj.679>.
- Smith, Roger K. et al. 2009. Tropical cyclone spin-up revisited. *Quarterly Journal of the Royal Meteorological Society* **135**(642), pp. 1321–1335. DOI: <https://doi.org/10.1002/qj.428>. URL: <https://rmets.onlinelibrary.wiley.com/doi/abs/10.1002/qj.428>.
- Stern, Daniel P and George H Bryan. 2018. Using simulated dropsondes to understand extreme updrafts and wind speeds in tropical cyclones. *Monthly Weather Review* **146**(11), pp. 3901–3925.
- Stull, Roland B. 1988. An introduction to boundary layer meteorology. **13**. Springer Science & Business Media.
- Tallapragada, V. et al. 2015. *Hurricane Weather Research and Forecasting (HWRF) Model: 2015 Scientific Documentation*. Tech. rep. 113 pp. National Center for Atmospheric Research. URL: http://www.dtcenter.org/HurrWRF/users/docs/scientific_documents/HWRF_v3.7a_SD.pdf.
- Tang, Brian and Kerry Emanuel. 2012a. A ventilation index for tropical cyclones. *Bulletin of the American Meteorological Society* **93**(12), pp. 1901–1912. DOI: <https://doi.org/10.1175/BAMS-D-11-00165.1>.
- 2012b. Sensitivity of tropical cyclone intensity to ventilation in an axisymmetric model. *Journal of the Atmospheric Sciences* **69**(8), pp. 2394–2413.
- Tao, Cheng et al. 2017. The relative importance of stratiform and convective rainfall in rapidly intensifying tropical cyclones. *Monthly Weather Review* **145**(3), pp. 795–809.

- Tuleya, Robert E and Yoshio Kurihara. 1978. A numerical simulation of the landfall of tropical cyclones. *Journal of the Atmospheric Sciences* **35**(2), pp. 242–257.
- Uhlhorn, Eric W. et al. 2007. Hurricane Surface Wind Measurements from an Operational Stepped Frequency Microwave Radiometer. *Monthly Weather Review* **135**(9), pp. 3070–3085. DOI: <https://doi.org/10.1175/MWR3454.1>. URL: <https://journals.ametsoc.org/view/journals/mwre/135/9/mwr3454.1.xml>.
- Vaisala. 2013. *Vaisala Radiosonde RS41 Measurement Performance*. Tech. rep.
- 2017. *Dropsonde RD94 Datasheet*. Tech. rep. URL: <https://www.vaisala.com/sites/default/files/documents/RD94-Datasheet-B210936EN-B.pdf>.
- Van Sang, Nguyen et al. 2008. Tropical-cyclone intensification and predictability in three dimensions. *Quarterly Journal of the Royal Meteorological Society: A journal of the atmospheric sciences, applied meteorology and physical oceanography* **134**(632), pp. 563–582.
- Wadler, Joshua B et al. 2018. Downdrafts and the evolution of boundary layer thermodynamics in Hurricane Earl (2010) before and during rapid intensification. *Monthly weather review* **146**(11), pp. 3545–3565.
- Wadler, Joshua B et al. 2021. Thermodynamic Characteristics of Downdrafts in Tropical Cyclones as Seen in Idealized Simulations of Different Intensities. *Journal of the Atmospheric Sciences* **78**(11), pp. 3503–3524. DOI: <https://doi.org/10.1175/JAS-D-21-0006.1>.
- Wadler, Joshua B et al. 2023. On the distribution of convective and stratiform precipitation in tropical cyclones from airborne Doppler radar and its relationship to intensity change and environmental wind shear direction. *Monthly Weather Review* **151**(12), pp. 3209–3233.
- Wang, Yuqing. 2001. An explicit simulation of tropical cyclones with a triply nested movable mesh primitive equation model: TCM3. Part I: Model description and control experiment. *Monthly weather review* **129**(6), pp. 1370–1394.
- 2002. Vortex Rossby waves in a numerically simulated tropical cyclone. Part II: The role in tropical cyclone structure and intensity changes. *Journal of the atmospheric sciences* **59**(7), pp. 1239–1262.
- Wang, Yuqing et al. 2015. A statistical analysis of the effects of vertical wind shear on tropical cyclone intensity change over the western North Pacific. *Monthly Weather Review* **143**(9), pp. 3434–3453.

- Wen, Guanhuan et al. 2019. Observed rainfall asymmetry of tropical cyclone in the process of making landfall in Guangdong, south China. *International Journal of Climatology* **39**(7), pp. 3379–3395.
- Wilcoxon, Frank. 1992. Individual comparisons by ranking methods. *Breakthroughs in Statistics: Methodology and Distribution*. Springer, pp. 196–202.
- Willoughby, Hugh E and Marcy B Chelmon. 1982. Objective determination of hurricane tracks from aircraft observations. *Monthly Weather Review* **110**(9), pp. 1298–1305. DOI: [https://doi.org/10.1175/1520-0493\(1982\)110<1298:ODDHTF>2.0.CO;2](https://doi.org/10.1175/1520-0493(1982)110<1298:ODDHTF>2.0.CO;2).
- Wimmers, Anthony J and Christopher S Velden. 2007. MIMIC: A new approach to visualizing satellite microwave imagery of tropical cyclones. *Bulletin of the American Meteorological Society* **88**(8), pp. 1187–1196. DOI: <https://doi.org/10.1175/BAMS-88-8-1187>.
- Wood, Nigel et al. 2007. A monotonically-damping second-order-accurate unconditionally-stable numerical scheme for diffusion. *Quarterly Journal of the Royal Meteorological Society: A journal of the atmospheric sciences, applied meteorology and physical oceanography* **133**(627), pp. 1559–1573.
- Wood, Nigel et al. 2014. An inherently mass-conserving semi-implicit semi-Lagrangian discretization of the deep-atmosphere global non-hydrostatic equations. *Quarterly Journal of the Royal Meteorological Society* **140**(682), pp. 1505–1520.
- World Meteorological Organization. 2022. *Tropical Cyclone Operational Plan for the South-East Indian Ocean and the Southern Pacific Ocean 2022*. Report. World Meteorological Organization, I-4-II-9 (9–21).
- Wroe, Derek R. and Gary M. Barnes. 2003. Inflow Layer Energetics of Hurricane Bonnie (1998) near Landfall. *Monthly Weather Review* **131**(8), pp. 1600–1612. DOI: <https://doi.org/10.1175//2547.1>.
- Wu, Chun-Chieh and Ying-Hwa Kuo. 1999. Typhoons affecting Taiwan: Current understanding and future challenges. *Bulletin of the American Meteorological Society* **80**(1), pp. 67–80.
- Xu, Weixin et al. 2014. Rainfall asymmetries of tropical cyclones prior to, during, and after making landfall in South China and Southeast United States. *Atmospheric Research* **139**, pp. 18–26.
- Young, Kate et al. 2015. A long-term, high-quality, high-vertical-resolution GPS dropsonde dataset for hurricane and other studies. *Bulletin of the American Meteorological Society* **96**(6), pp. 961–973.

- Yu, Chau-Lam et al. 2021. Investigating Axisymmetric and Asymmetric Signals of Secondary Eyewall Formation Using Observations-Based Modeling of the Tropical Cyclone Boundary Layer. *Journal of Geophysical Research: Atmospheres* **126**(16), e2020JD034027.
- Zehr, Raymond M. 2003. Environmental vertical wind shear with Hurricane Bertha (1996). *Weather and forecasting* **18**(2), pp. 345–356.
- Zeng, Zhihua et al. 2010. A statistical analysis of vertical shear effect on tropical cyclone intensity change in the North Atlantic. *Geophysical Research Letters* **37**(2).
- Zhang, Fuqing and Kerry Emanuel. 2016. On the role of surface fluxes and WISHE in tropical cyclone intensification. *Journal of the Atmospheric Sciences* **73**(5), pp. 2011–2019.
- Zhang, Fuqing et al. 2017a. Dynamics and predictability of secondary eyewall formation in sheared tropical cyclones. *Journal of Advances in Modeling Earth Systems* **9**(1), pp. 89–112.
- Zhang, Jun A and Frank D Marks. 2015. Effects of horizontal diffusion on tropical cyclone intensity change and structure in idealized three-dimensional numerical simulations. *Monthly Weather Review* **143**(10), pp. 3981–3995.
- Zhang, Jun A and Robert F Rogers. 2019. Effects of parameterized boundary layer structure on hurricane rapid intensification in shear. *Monthly Weather Review* **147**(3), pp. 853–871.
- Zhang, Jun A et al. 2009. Turbulence structure of the hurricane boundary layer between the outer rainbands. *Journal of the Atmospheric Sciences* **66**(8), pp. 2455–2467.
- Zhang, Jun A et al. 2010. An estimation of turbulent characteristics in the low-level region of intense Hurricanes Allen (1980) and Hugo (1989). *Monthly Weather Review* **139**(5), pp. 1447–1462.
- Zhang, Jun A et al. 2011. On the Characteristic Height Scales of the Hurricane Boundary Layer. *Monthly Weather Review* **139**(8), pp. 2523–2535. ISSN: 0027-0644. DOI: 10.1175/MWR-D-10-05017.1. URL: <https://doi.org/10.1175/MWR-D-10-05017.1>.
- Zhang, Jun A et al. 2013. Asymmetric hurricane boundary layer structure from dropsonde composites in relation to the environmental vertical wind shear. *Monthly Weather Review* **141**(11), pp. 3968–3984. ISSN: 00270644. DOI: <https://doi.org/10.1175/MWR-D-12-00335.1>.
- Zhang, Jun A et al. 2017b. Impact of parameterized boundary layer structure on tropical cyclone rapid intensification forecasts in HWRF. *Monthly Weather Review* **145**(4), pp. 1413–1426. DOI: <https://doi.org/10.1175/MWR-D-16-0129.1>.

- Zhang, Jun A et al. 2017c. Observations of infrared sea surface temperature and air–sea interaction in Hurricane Edouard (2014) using GPS dropsondes. *Journal of Atmospheric and Oceanic Technology* **34**(6), pp. 1333–1349.
- Zhang, Jun A. et al. 2018. Airborne Doppler Wind Lidar Observations of the Tropical Cyclone Boundary Layer. *Remote Sensing* **10**(6). ISSN: 2072-4292. DOI: 10.3390/rs10060825. URL: <https://www.mdpi.com/2072-4292/10/6/825>.
- Zhao, Zhongkuo et al. 2020. Aircraft observations of turbulence characteristics in the tropical cyclone boundary layer. *Boundary-Layer Meteorology* **174**, pp. 493–511.
- Zhao, Zhongkuo et al. 2022. Observations of boundary layer wind and turbulence of a landfalling tropical cyclone. *Scientific reports* **12**(1), p. 11056.
- Zhu, Ping. 2008. Simulation and parameterization of the turbulent transport in the hurricane boundary layer by large eddies. *Journal of Geophysical Research: Atmospheres* **113**(D17).
- Zhu, Shujun et al. 2022. A 4DEnVar-Based Ensemble Four-Dimensional Variational (En4DVar) Hybrid Data Assimilation System for Global NWP: System Description and Primary Tests. *Journal of Advances in Modeling Earth Systems* **14**(8), e2022MS003023.